



Cardiff University

School of Biosciences

Functionalisation and Application
of Gold Nanoparticles for
Enhanced Cellular Targeting and
Imaging Using Four-Wave-Mixing
Microscopy

Nicole Slesiona

Thesis submitted for the award of Doctor of Philosophy (Ph.D.)

School of Biosciences, Cardiff University

Cardiff, February 2024

Supervisors:

1. Prof. Peter Watson

Director for Postgraduate Education, Academic lead of
imaging facilities,

School of Biosciences

2. Prof. Paola Borri

Professor, Coordinator of the European Marie Curie
ETN consortium MUSIQ

School of Biosciences

School of Physics and Astronomy

3. Prof. Wolfgang Langbein

Head of Condensed Matter and Photonics Group

School of Physics and Astronomy

Acknowledgements

I am grateful to my supervisor, Prof. Peter Watson, for his invaluable support and guidance throughout this project. His ability to inspire and challenge me have significantly contributed to my growth in scientific skills. I'm also very thankful to my two other supervisors, Prof. Wolfgang Langbein, whose commitment to scientific precision played an important role in helping my understanding of the complex microscope techniques used in our project, and thank you to Prof. Paola Borri, for translating these complex topics when I couldn't follow at first, the patience, and making the MUSIQ consortium possible.

A big shout-out and heartfelt thanks to Dr. Iestyn Pope and Dr. Lukas Payne in our group for navigating all of us through the maze of advanced imaging modalities and alignment techniques. Your help, along with Dr. David Regan's readiness to tackle any last-minute issues with the microscope, has been a lifesaver more than once. Thanks to the European Union's Horizon 2020 research and innovation program under the Marie Skłodowska-Curie grant agreement No 812992 for funding this project and making this incredible collaboration possible. Meeting each and every one of the members of the consortium was a great experience and created long lasting friendships between us ESRs. A special thank you goes to Dr. Steve Hood, for being ready to make those crucial last-minute tweaks for the secondment at GSK. I would like to thank Paul McGill, Ian Francis and Andy West for making the time on site a great two months.

My thanks also go to Prof. Arwyn Jones' group for their advice during lab meetings. A heartfelt thanks to everyone in the third-floor east group in Biosciences for the laughter and good times shared over lunch and coffee breaks. Freya deserves a special mention for her support, whether it was physically in Cardiff when I was juggling too many things at once and needed an extra pair of hands, or from afar when I needed someone on the ground.

On a personal note, I wish to acknowledge three very special groups of friends I found through my time in Cardiff. To Jack, Kate and Ryan, thank you for making me feel at home in Cardiff. To Carmen, Elena, Martina, and Rhod: you guys made the office more than just a place to work. Thank you for all the adventures, inside jokes and being there when I needed you. To my beloved "Germs" Nina, Anne, and Sven: your friendship means so much to me. No matter the challenge or how busy we were, we always had each other's backs. I'm excited for the day we all reunite and conquer every hiking trail we set our eyes on.

To my family: your endless love and support have been my rock. Even when the world of academia seemed like a maze, you were there cheering me on.

To André, my partner and best friend: where do I even begin? You've been my anchor, teaching me complex physics sometimes until midnight and making sense of the chaos when I thought I couldn't. Your support has been my guiding light. Thank you for sticking with me from the start all the way through to the finish line.

Thank you, each and every one of you, for being part of my journey.

Abstract

Previous research has demonstrated that cross-linking of receptors at the cell surface can drive therapeutic payloads to intracellular locations against the flow of endogenous receptors and ligands, thus improving cellular delivery. Gold nanoparticles (GNPs) are particularly promising for this application due to their customisable surface chemistry, which allows for precise control over ligand density essential for receptor cross-linking.

GNPs exhibit unique optical properties that allow their use as contrast agents in both linear and non-linear biological imaging, offering advantages over traditional fluorophores that are limited by autofluorescence, photobleaching and therefore time-limited imaging. Despite these benefits, imaging GNPs in cellular environments, especially with linear imaging modalities, is complicated by background signals and the need for live-cell compatible sample preparations.

To address these issues, this project utilised Four Wave Mixing (FWM) microscopy, a non-linear imaging method that allows for the background-free visualisation of GNPs. This research has developed and validated a method to quantify ligand density directly on GNPs on a single particle basis using extinction microscopy and single fluorophore bleaching, moving beyond traditional averaged estimates and showing that particle-by-particle quantifications strongly deviate from averaged methodologies. The FWM setup was developed for live cell imaging and demonstrated its utility in tracking GNPs at the single particle level in living cells, marking a substantial step forward in understanding GNP internalisation and receptor cross-linking dynamics. Lastly, previously reported non-colocalisation between GNPs and fluorophores was addressed. We have examined multiple functionalisation procedures using our ligand quantification method and live FWMi, identifying the best functionalisation procedure to be based on utilising pre-functionalised stabilising polymers for functionalisation, resulting in high quality resources for future studies on GNP internalisation.

These advancements pave the way for optimising GNP-based cellular targeting, offering new insights into targeted therapeutic interventions at the cellular level.

Table of contents

Acknowledgements	III
Abstract.....	V
Table of contents	VI
List of abbreviations	X
List of figures	XII
List of Tables.....	XVI
List of symbols	XVII
1 Introduction	1
1.1 Actively-targeted nanomaterials for cancer therapy.....	1
1.2 Lysosomal targeting and receptor-crosslinking.....	2
1.3 Live cell imaging techniques for GNPs.....	5
1.4 Rational nanocarrier design in the context of receptor crosslinking	7
1.4.1 Particle size and shape	8
1.4.2 Choice of target receptor	9
1.4.3 Stabilisation and functionalisation mechanisms.....	11
1.4.4 Ensuring target protein functionality	13
1.5 Ligand valency determination on GNPs.....	14
1.6 Thesis Outline.....	15
2 Fundamentals.....	17
2.1 Optical properties of GNPs	17
2.1.1 Linear optical characteristics of GNPs	17
2.1.2 The dielectric function of GNPs.....	18
2.1.3 Localised surface plasmon resonance.....	20
2.2 Nonlinear optical responses of GNPs.....	22
2.2.1 Nonlinear microscopy.....	22
2.2.2 Four Wave Mixing microscopy.....	23
3 Materials and Methods	26
3.1 Sample Preparation.....	26

3.1.1	Functionalisation procedures of GNP	26
3.1.2	Cell culture	29
3.1.3	Pulse Chase Experiments on HeLa cells	30
3.1.4	Glass cleaning procedure.....	30
3.1.5	Spin-coating procedure.....	31
3.2	Multimodal imaging set-up	31
3.2.1	Extinction	32
3.2.2	FWM.....	32
3.2.3	Confocal fluorescence	34
3.3	Widefield microscope set-up.....	35
3.4	Transmission electron microscopy measurements	35
3.5	Data acquisition and processing	36
3.5.1	Validation of particle functionalisation	36
3.5.2	Wide-field epi-fluorescence microscopy for fixed and live cell imaging	36
3.5.3	Wide-field epi-fluorescence microscopy for single fluorophore bleaching	37
3.5.4	Bleaching step size determination and background correction of single fluorophore bleaching data	38
3.5.5	Wide-field extinction microscopy	39
3.5.6	Superposition of correlative fluorescence and extinction measurements.....	40
3.5.7	FWM measurements.....	41
4	Development of correlative extinction and fluorescence microscopy for ligand density quantification on GNPs	45
4.1	Introduction	45
4.2	Development.....	47
4.2.1	Hot pixel and background signal correction.....	47
4.2.2	Choice of the experimental numerical aperture.....	50
4.2.3	Bleaching step sizes of Alexa647	52
4.2.4	Optimisation of extinction measurements for correlation with fluorescence microscopy	55
4.3	Experimental validation: Results and discussion	62
4.3.1	Determination of number of fluorophores per TfA and number of TfAs per GNP	63
4.3.2	Determination of particle size distribution and crosslinking of particles.....	67

4.3.3	Correlation of fluorescence and extinction signals.....	72
4.4	Limitations and Future Considerations.....	74
4.4.1	Selection of numerical aperture	74
4.4.2	Particle size distributions and oddly shaped particles skew N_{NP} quantification	75
4.4.3	Scatter plots of correlative fluorescence and extinction allow construct quality determination at a glance.....	76
4.5	Conclusions	78
5	Establishing Four-Wave-Mixing imaging in living cells	79
5.1	Introduction	79
5.2	Results and discussion.....	79
5.2.1	2D image analysis of FWMi data and proof of GNP signal.....	79
5.2.2	3D image analysis of FWMi.....	82
5.2.3	Improving FWMi acquisition settings on fixed samples.....	85
5.2.4	Live cell imaging chamber set-up	91
5.2.5	Following GNP internalisation events with the help of live cell FWMi.....	95
5.3	Limitations and Future Considerations.....	102
5.3.1	Live cell FWMi needs further development for faster image acquisition.....	102
5.3.2	The live cell imaging chamber does not create a sterile environment.....	103
5.3.3	A better GNP-Tf conjugate quality is needed for meaningful studies	103
5.3.4	Further assessments of REFL and FWM ^A are necessary to better interpret the data	104
5.4	Conclusions	104
6	Establishing a GNP functionalisation procedure.....	106
6.1	Introduction	106
6.2	Results and discussion.....	107
6.2.1	Functionalisation of GNPs with pre-attached polymers.....	107
6.2.2	Functionalisation of citrate-capped GNPs.....	118
6.2.3	Correlative single fluorophore bleaching, extinction, and FWMi.....	128
6.3	Limitations and Future Considerations.....	138
6.3.1	GNP Functionalisation is Characterised by Significant Variability.....	138
6.3.2	The Order of Functionalisation is likely more Important than the Functionalisation Mechanism.....	138

6.3.3	FWMi aids in identifying GNP constructs in correlative experiments	140
6.3.4	Fluorescence intensities of the constructs differ in cell applications and in single fluorophore bleaching.....	141
6.4	Conclusions	142
7	Thesis conclusions.....	144
7.1	Fluorescence is not necessarily a faithful reporter of GNP localisation.....	144
7.2	For GNP-protein constructs to be used as therapeutics <i>in vivo</i> , sophisticated purification methods are still needed to make sure the internalisation pathway of interest is induced	145
7.3	Specific changes to GNP functionalisation procedures and GNP morphology can be closely monitored with the help of particle-by-particle ligand density determination and FWMi	145
7.4	Live cell FWMi helps with revealing GNP trafficking in living cells but needs to be improved on speed.....	146
7.5	Concluding remarks.....	146
8	Future Directions	149
8.1	Influence of fluorescent labels on the trafficking profile of proteins	149
8.2	Trafficking of mono- and multivalent GNPs in living cells.....	151
9	Bibliography	154
	Publications	i
	Oral and poster presentations	i

List of abbreviations

AOM	acousto-optic modulator
AS	attachment site
BSA	bovine serum albumin
EPR	enhanced permeation and retention
FEME	fast endophilin-mediated endocytosis
GNP	gold nanoparticle
ccMIP	colour-coded maximum intensity projection
CME	clathrin mediated endocytosis
CTAC	cetyltrimethylammonium chloride
CTAB	cetyltrimethylammonium bromide
dGNP	gold nanoparticle expressing directed movement
DI	deionised
DIC	differential interference contrast
DOL	degree of labelling
dH ₂ O	distilled water
DMSO	dimethylsulfoxide
DMT1	divalent metal transporter 1
ESM	extinction suite macro
FF	far field
FOV	field of view
FWM	Four Wave Mixing
FWM ^A	Four Wave Mixing amplitude
FWMi	Four Wave Mixing imaging
H ₂ O ₂	hydrogen peroxide
HP	hot pixel
ID	identification
LSPR	localised surface plasmon resonance
MIP	maximum intensity projection
MNP	metallic nanoparticle
mPEG	methyl-terminated polyethylene glycol
LUT	lookup table

NA	numerical aperture
NF	near field
NHS	N-Hydroxysuccinimide
NP	nanoparticle
OD	optical density
OPN	OPSS-polyethylene glycol-NHS
OPO	optical parametric oscillator
OPT	OPSS-polyethylene glycol-transferrin
PBS	phosphate buffered saline
PEG	polyethylene glycol
PFA	paraformaldehyde
PSF	point spread function
r _{cf}	relative centrifugal force
REFL	Four Wave Mixing reflectance
rGNP	gold nanoparticle expressing random movement
RT	room temperature
SA	streptavidin
sCMOS	scientific complementary metal–oxide–semiconductor
SMCC	Sulfosuccinimidyl 4-(N-maleimidomethyl)cyclohexane-1-carboxylat
SNR	signal to noise ratio
SPR	surface plasmon resonance
SSS	sample step size
TEM	transmission electron microscopy
Tf	transferrin
Tf-Bi	biotin-transferrin
TfA	Alexa647-labelled transferrin
TfR	transferrin receptor
TIR	total internal reflection
UV-vis	ultraviolet – visible

List of figures

Figure 1.1 Schematic Illustration Of Endocytic Mechanisms.	3
Figure 1.2 Recycling of Tf-488 and Tf-Bi-647, and Cellular Retention of Tf-Bi-647(:SA) in HeLa Cells from Moody <i>et al.</i>	4
Figure 1.3 Effects of GNP Curvature, Size, Shape, and Ligand Density.	9
Figure 1.4 Intracellular Trafficking Pathway of Transferrin.	10
Figure 1.5 Reaction Mechanism of EDC-NHS and sulfo-SMCC.	12
Figure 2.1 Lycurgus Cup.	17
Figure 2.2 Comparison of the Real (a) and (b) Imaginary Part of the Dielectric Function for Gold Resulting from Different Models.	19
Figure 2.3 Illustration of Plasmon Formation.	21
Figure 2.4 Transient Changes of the Real ($\Delta\epsilon_R$) and Imaginary ($\Delta\epsilon_I$) Parts of the Dielectric Function of a Single Gold NP Resonantly Excited and Probed at 550 nm for Different NP Diameters as Indicated.	25
Figure 3.1 Schematic Representation of the Optical Components in the FWMi Set-Up.	33
Figure 3.2 Epi-fluorescence Set-Up.	37
Figure 3.3 Extinction Microscopy Set-Up.	39
Figure 4.1 Correlative Single Fluorophore Bleaching and Single GNP Detection for Ligand Quantification on GNPs.	46
Figure 4.2 Comparative Background Correction.	48
Figure 4.3 Calibration of NA for Single Fluorophore Bleaching.	51
Figure 4.4 Bleaching Events of TfA Proteins.	53
Figure 4.5 Bleaching Step Sizes of Alexa 647.	55
Figure 4.6 Utilising Z-Measurements to Differentiate Between GNPs and Debris.	57
Figure 4.7 Sample Preparation for Correlative Measurements on Different Setups.	58
Figure 4.8 Schematic Illustration of the Image Transformation.	59
Figure 4.9 Workflow of Image Transformation of Pre-Registered Common Features in Two Images.	60

Figure 4.10 Fluorescence Intensities of TfA for the Identification of NF Pre and Post Functionalisation.	64
Figure 4.11 Influence of GNP Conjugation Preference on Labelling Rate.	65
Figure 4.12 Distributions of NFs on Free Tf and GNP-Tf Constructs.	66
Figure 4.13 TEM Evaluation of GNPs.	69
Figure 4.14 Extinction Cross Sections of Unconjugated GNPs and GNP-Tf Constructs.	71
Figure 4.15 Characteristics of Construct Samples.	73
Figure 4.16 Scatter Plots of GNP-Protein Constructs for Sample Quality Determination at a Glance.	77
Figure 5.1 2D FWMi Images Reveals Cell Attachment to the Dish Surface and Localisation of GNPs.	81
Figure 5.2 3D REFL Field Reveals the 3D Morphology of Cells.	83
Figure 5.3 3D FWM ^A Data Reveals GNP Localisation in the z-axis.	84
Figure 5.4 The FWMi PSF is Elongated.	85
Figure 5.5 Long Acquisition Times Cause Visible Drifts in FWMi.	86
Figure 5.6 Enhanced Scanning Speed Through Reduced Samples per Row Impacts Data Quality More Significantly Than Shorter Integration Times.	88
Figure 5.7 Optimised Fast Scanning in FWMi Utilising Rapid Integration Times and Reduced SSS Settings Along One Axis.	90
Figure 5.8 Live Cell Imaging Chamber Components.	92
Figure 5.9 DIC Microscopy Shows that HeLa Cells Viability is Maintained Throughout Extended Imaging Sessions Within the Live Cell Imaging Chamber.	93
Figure 5.10 Live Cell FWMi Shows No Adverse Effects on HeLa Cells.	94
Figure 5.11 FWMi Laser Illumination Bleaches Intrinsic Fluorescence of Cells and the Cell Culture Medium.	95
Figure 5.12 Initial Evidence of Successful GNP Internalisation Captured in Live FWMi. ...	96
Figure 5.13 Trafficking Speed Analysis Through Particle Movement in Live Cell Imaging.	97
Figure 5.14 Differential Analysis of GNP Movement: Trafficking versus Brownian Motion.	99

Figure 5.15 Expanded Field of View for GNP Tracking Suggests Localisation within a Sorting Endosome.	100
Figure 5.16 Contrast Inversions in REFL Signal as Indicators of Vesicle Position Relative to the Focal Plane.	101
Figure 6.1 Sulfo-SMCC and NHS Functionalisation Induce Aggregation and Destabilisation in GNPs.	108
Figure 6.2 Differential Binding Patterns of SMCC-GNP and NHS-GNP-TfA Constructs to HeLa Cells.	110
Figure 6.3 Comparative Analysis of GNP Construct Internalisation in Cells Using Axial Colour-Coded Representations of Fluorescence or FWMi Data.	112
Figure 6.4 0.4-SMCC-GNP Constructs Bind Live HeLa Cells But Do Not Internalise.	113
Figure 6.5 Mercaptoethanol-Quenched SMCC-GNP Constructs Exhibit Binding and Accumulation in Live HeLa Cells.	114
Figure 6.6 Size- and Intensity-Differentiated Movement of SMCC-GNP-TfA Constructs Within HeLa Cells.	115
Figure 6.7 Correlating Structures Across Fluorescence, Brightfield, and Extinction Modalities.	116
Figure 6.8 FWMi Analysis Indicates Lack of Internalisation of SMCC-GNP Constructs into HeLa Cells.	117
Figure 6.9 Schematic Overview of Protein Conjugation to GNPs via diS-PEG-NHS and OPSS-PEG-NHS.	119
Figure 6.10 Stages of Particle Aggregation in GNP Functionalisation.	120
Figure 6.11 DMSO/dH ₂ O stabilises GNP more effectively than dH ₂ O/PBS during Functionalisation using diS-PEG-NHS.	121
Figure 6.12 Binding and Internalisation of diS-PEG-NHS Functionalised GNPs in HeLa Cells.	122
Figure 6.13 Orthogonal Views of FWMA verify non-Internalisation of PEG-GNPs and Internalisation of diS-GNPs.	123
Figure 6.14 Stabilisation of GNPs by OPN-Based Functionalisation Evidenced by UV-Vis, Yet Lacking Internalisation in HeLa Cells according to fluorescence imaging.	125

Figure 6.15 OPT-GNP Demonstrates Tf-Specific Trafficking and Uptake Variations in HeLa Cells.....	126
Figure 6.16 Determination of Bleaching Step Size of TfA on OPT-GNP.	129
Figure 6.17 Initial Fluorescence Intensity Indicates Successful GNP Functionalisation.	130
Figure 6.18 Distributions of I(t0) on free TfA and GNP-TfA constructs.....	131
Figure 6.19 Extinction Cross Sections of Unconjugated GNPs and GNP-TfA Constructs.	133
Figure 6.20 Correlation Between Extinction Cross-Section and Fluorescence Rates in GNP-TfA Constructs.	134
Figure 6.21 Sample Quality of OPT-GNP Samples.	136
Figure 6.22 ζ potential of a Particle with Positive Surface Charge.	136
Figure 6.23 Zeta Potential of GNPs.....	137
Figure 6.24 Correlative Analysis of Extinction, Single Fluorophore Bleaching, and FWMi in Spin-Coated OPT-GNP Constructs.	141

List of Tables

Table 4.1 Analysis of BG Corrected Images	49
Table 4.2 Parameters Of Image Transformation.	61
Table 4.3. Visualisation of the GNP-TfA samples created to assess GNP crosslinking using the developed correlative technique.	62
Table 4.4 Updated Visualisation of the GNP-TfA Samples Created to Assess GNP Crosslinking Using the Developed Correlative Technique.	70
Table 6.1 Quantitative 20 nm OPT-GNP and mPEG-GNP uptake by HeLa cells.....	127
Table 6.2 Transformation parameters of extinction and fluorescence to FWMi data on varying samples.	128
Table 6.3 Large 60-OPT-GNP Constructs.....	135

List of symbols

BS	beam splitter
DBS	dichroic beam splitter
FWM_FM1	four wave mixing folding mirror 1
FWM_M2	four wave mixing mirror 2
FWM_M5	four wave mixing mirror 5
FWM_M7	four wave mixing mirror 7
NPBS	non-polarising beam splitter
PBS1	polarising beam splitter 1
PBS2	polarising beam splitter 2
PH (1-4)	pinhole (1-4)
Sig_M1	signal mirror 1
WP	Wollaston prism
C	image transformation matrix
E	electric field
H	horizontal (axis of beam walking)
I_B	bleaching step size (intensity)
$I(t_0)$	intensity at the beginning of the measurement
k	wave number of light in the medium
n	refractive index
\bar{N}	Poisson distribution
N_F	number of fluorophores
N_{NP}	number of particles
p	polarisation
P	polarisation density
R	particle radius
r_e	reference position of the extinction signal
r_f	reference position of the fluorescence signal
t	translation vector

V	vertical (axis of beam walking)
α	polarisability
γ	damping factor
γ_{ib}	damping factor adjusted for interband transitions
ϵ_0	permittivity of free space
$\tilde{\epsilon}$	effective dielectric constant
$\epsilon(\omega)$	dielectric function
$\epsilon_{ib}(\omega)$	frequency dependent dielectric function (interband transitions)
ϵ_m	dielectric function of the medium
ϵ_p	dielectric function inside the particle
ζ	zeta potential
θ_c	critical angle
λ	wavelength
σ_{abs}	absorption cross section
σ_{ext}	extinction cross section
σ_{sca}	scattering cross section
τ	delay time

1 Introduction

1.1 Actively-targeted nanomaterials for cancer therapy

Multidisciplinary research in drug delivery has resulted in the creation of diverse forms of therapeutic nanomaterials that are specifically engineered for the targeted delivery of diagnostic and therapeutic agents. Their effectiveness is dependent on their efficient uptake by target cells. Therefore, a thorough understanding of the cellular internalisation pathways is important for the development of these nanomaterials. In general, there are two classes of cancer targeting nanoparticles (NPs): passively targeted and actively targeted NPs¹. Passive targeting in drug delivery is primarily driven by the enhanced permeation and retention (EPR) effect². This phenomenon results from the poor lymphatic drainage in tumour tissue and the fenestrations in compromised tumour blood vessels³. Fenestrations in blood vessels are pore-like structures found primarily in the endothelial cells of capillaries, specifically in organs with rapid exchange of molecules, facilitating the selective transfer of fluids, solutes, and nutrients between the bloodstream and tissue interstitium³. Active targeting, or ligand-mediated targeting, involves the use of specific molecules capable of binding to receptors predominantly expressed on target cells. A popular strategy to treat cancer is to link drugs to ligands that recognise tumour-specific receptors that are overexpressed at the cell surface. The utilised ligand should thereby induce internalisation following receptor binding to direct the drug inside the cell. This has been shown, for example, with the epidermal growth factor receptor (EGFR)⁴, the folate receptor⁵, and the transferrin (Tf) receptor (TfR)⁶.

Popular NP forms are polymeric NPs (polymerosomes, dendrimers, polymer micelles, nanospheres), lipid-based NPs (liposomes, lipid NPs, emulsion NPs), and inorganic NPs (silica NPs, iron oxide NPs, quantum dots, and metallic NPs)¹. Polymeric NPs are highly variable NP forms that can carry their payload on their surface, or within their polymer matrix. They are made from biodegradable preformed polymers or monomers allowing multiple functions on the same structure as well as co-delivery of more than one therapeutic agent. On the other hand, this class of NPs is prone to aggregation and has been reported to show toxicity⁷. Lipid-based NPs consist of a lipid bilayer with one or more aqueous compartments. Due to the self-assembly formulation of these NPs their synthesis is facile, and they can deliver large payloads to a target site with high levels of bioavailability⁸. However, lipid-based NPs show challenges in manufacturing and scalability, variable protein adsorption, subtherapeutic drug absorption levels, and sometimes slow drug release affecting bioavailability⁹. Inorganic NPs can be synthesised to precisely produce carefully controlled sizes and shapes. Thanks to their physical

and optical properties, they can be used as optical labels or for photothermal therapy, on top of being used as delivery vehicles¹⁰. An in-depth comparison of these NP forms is out of the scope of this work, but for further information refer to Mitchell *et al.*¹¹

Gold NPs (GNPs) have mostly been the focus of research in the field of nanomedicine as opposed to other MNPs due to their inherently low cytotoxicity¹². The optical properties of GNPs, particularly their ability to absorb and scatter light in the visible range, additionally render them as good biological labels. These optical properties depend on their morphology and their surface composition, allowing for tunability and optimisation based on specific requirements both optically and biologically^{13,14}. Therefore, GNPs offer a remarkable opportunity for directed cell targeting and drug delivery as they can be functionalised with a variety of different biocompatible groups simultaneously and they can also be synthesised in a variety of sizes and shapes¹⁵. GNPs can be used to construct highly specific nanocarriers that are able to be used as diagnostic tools, manipulate cellular pathways¹⁶, and eventually kill the targeted cells^{17,18}.

1.2 Lysosomal targeting and receptor-crosslinking

Endocytosis, a fundamental cellular process, mediates the internalisation of extracellular materials and membrane receptors, playing an important role in cellular signalling, nutrient uptake, and immune responses¹⁹. Among the various forms of endocytic mechanisms, clathrin-mediated endocytosis (CME) is the most well-characterised, involving the recruitment of clathrin proteins to form vesicles around the cargo²⁰. Alternatively, caveolin-mediated endocytosis relies on caveolae, flask-shaped invaginations in the plasma membrane, to allow the uptake of specific molecules²¹. There are also clathrin- and caveolin-independent pathways, which include mechanisms such as macropinocytosis and other forms of endocytosis that do not require these coat proteins. Each pathway is defined by distinct sets of molecules and mechanisms that dictate the budding of vesicles from the plasma membrane and their navigation through the cell's internal environment. The specificity and regulation of these pathways ensure the efficient and selective transport of a wide range of cargoes, underlining the importance of endocytosis in cellular physiology and its implications for understanding disease processes and developing therapeutics. Doherty and McMahon have classified the known endocytosis mechanisms in 2009¹⁹ into a comprehensive review and, more recently, Rennick *et al.* have done the same in 2021²². An overview of the currently known pathways is provided in Figure 1.1, which was taken from Rennick *et al.*

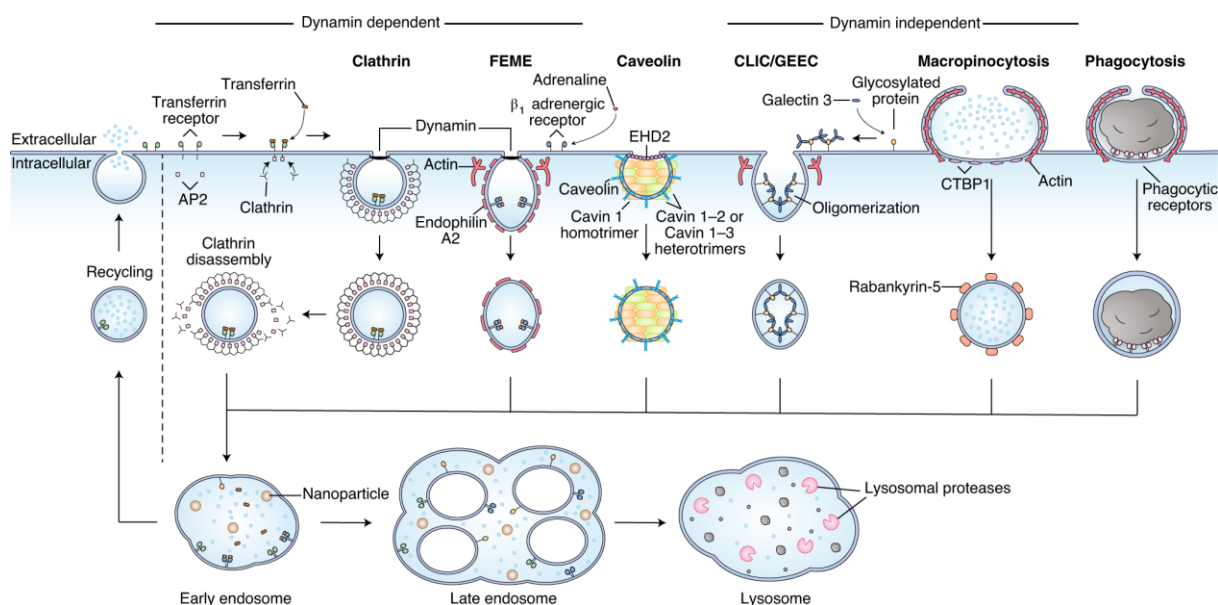


Figure 1.1 | Schematic Illustration Of Endocytic Mechanisms. CME is driven by the adaptor complex, AP2, that recruits clathrin to cytosolic receptor domains, initiating the formation of a clathrin-coated pit. Fast endophilin-mediated endocytosis (FEME) is triggered by ligand–receptor interactions. Both CME and FEME require dynamin to allow scission from the membrane. Formation of caveolae is dependent on caveolin and cavin proteins. Endocytosis involving CLathrin-Independent Carriers and GPI-Enriched Endocytic Compartments (CLIC/GEEC) appears to be a constitutive process and is clathrin and dynamin independent. Macropinocytosis is generally a stimulated pathway involving uptake of large volumes of fluid from the extracellular environment. CLIC/GEEC endocytosis and macropinocytosis are controlled by actin dynamics and different BAR domain proteins. Phagocytosis occurs after a binding event at the cell surface that triggers actin polymerisation and a vesicle forms tightly around the bound material. After internalisation, pathways merge into early endosomes before undergoing sorting, where material may be sent back to the surface or onwards to the late endosome and lysosome. [Figure and caption reproduced from Rennick *et al.*²², reproduced with permission from Springer Nature.]

The deep understanding of these endocytic pathways can be used to design targeted therapeutics. The directed delivery of bioactive molecules to targeted intracellular locations is an important feature to ensure the activity and safety of drugs targeted at subcellular sites of action. Many therapeutics require a controlled delivery to lysosomes as their activation (or deactivation) relies on the therapeutic's or its target's proteolytic degradation, a process called lysomotropic drug delivery^{23,24}. Targeting the lysosome for drug activation has been demonstrated with a number of different drug molecules²⁵. Lysosomes are organelles which contain hydrolytic enzymes that degrade extra- and intracellular components that are also capable of degrading pathogens²⁶. Additionally, they play a role in nutrient sensing and energy metabolism²⁷.

Previous research has demonstrated that crosslinking of receptors at the cell surface can drive therapeutic payloads into the endolysosomal pathway against the flow of endogenous receptors and ligands, improving cellular delivery of drugs based on Tf trafficking¹⁶. Crosslinking receptors on the plasma membrane overrides the native internalisation mechanism and triggers a nonspecific uptake of the crosslinked receptors, which has been shown for the TfR¹⁶, folate

receptor, and EGFR²⁸. Moody *et al.* have shown that fluorescently labelled Tf and Tf-Biotin (Tf-Bi) followed the natural recycling pathway of Tf, whereas signals originating from Tf-Bi crosslinked through streptavidin (SA) accumulated within the cell, indicated by an increase of intensity within the cells after 1 h incubation (see Figure 1.2), and colocalised over time with endolysosomal structures labelled with dextran, indicating their trafficking into lysosomes¹⁶. This mechanism of endocytosis contrasts with the typical receptor-mediated endocytosis, where a single binding event triggers the uptake of the ligand and the receptor. Cellular uptake by receptor crosslinking is only triggered when at least two receptors are crosslinked making this mechanism especially interesting when targeting cells that overexpress the targeted receptor²⁹. This approach is especially compelling for cancer nanotherapy when targeting receptors that in their normal function get recycled back to the plasma membrane or when targeting receptors that are non- or only slowly internalising.

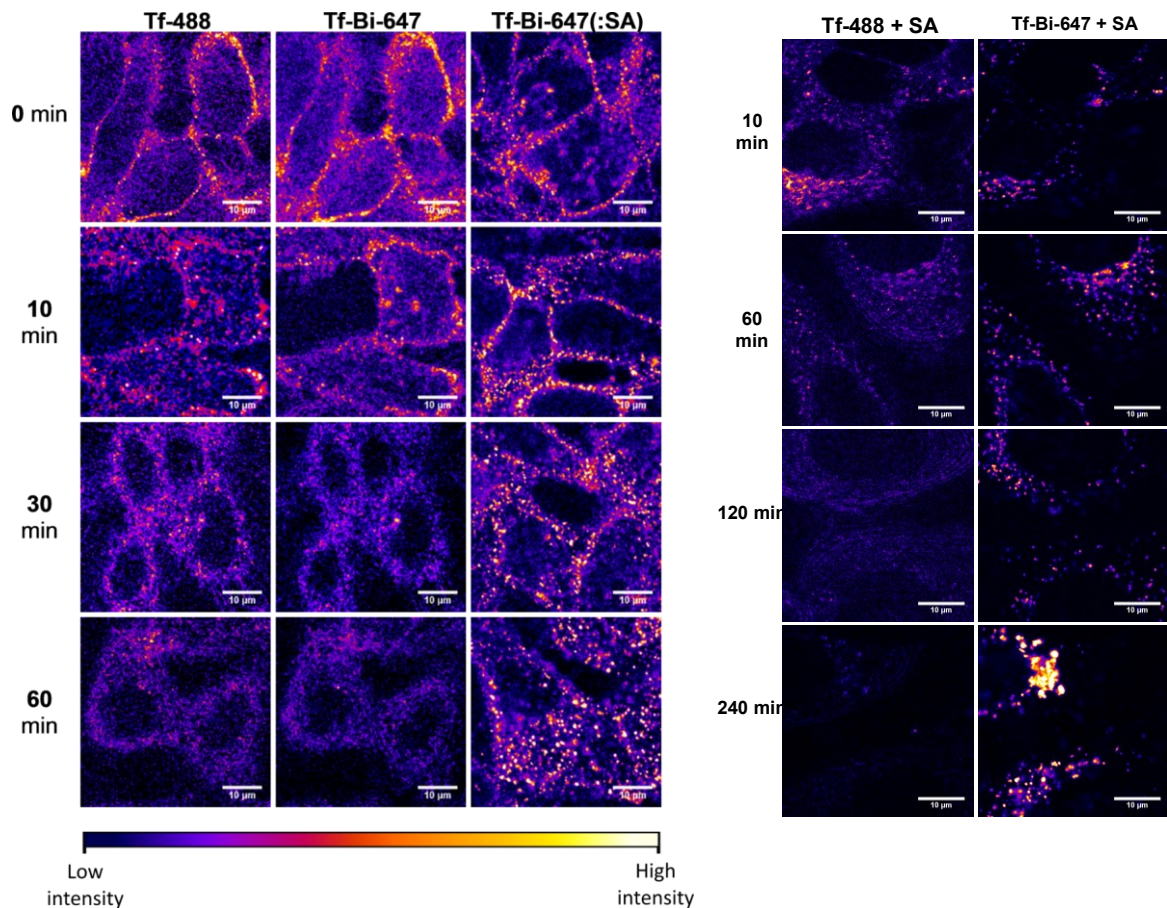


Figure 1.2 | Recycling of Tf-488 and Tf-Bi-647, and Cellular Retention of Tf-Bi-647:(SA) in HeLa Cells from Moody *et al.* Confocal fluorescence images of HeLa cells interacting with Tf-Alexa488, Tf-Alexa-Biotin, and Tfs crosslinked via biotin. Endocytosis was inhibited by placing the cells on ice. After 15 min, the cells were incubated with Tf-Bi-647 and Tf 488 at 10 μg/mL each (columns 1 and 2) or with Tf-Bi-647 alone, followed by SA (column 3) on ice. Afterward, cells were incubated in pre-warmed complete medium at 37°C, and live cells were observed through confocal fluorescence microscopy at specific time points. The images illustrate the recycling of Tf-Bi-647 and Tf-488, both with and without streptavidin, with Tf-Bi-647:SA complexes being retained in intracellular vesicles. Scale bars: 10 μm. [Permission to reprint obtained from Journal of the American Society of Gene & Cell Therapy¹⁶.]

As mentioned earlier, cancer cells adapt their membrane composition to account for their accelerated metabolic rate as they rely on an increased supply of nutrients and energy to support their deregulated cellular proliferation¹⁷. The activation of the receptor crosslinking pathway is likelier in cancer cells, which often overexpress targeted plasma membrane receptors, than in non-cancerous cells with baseline receptor levels. This differential expression makes receptor crosslinking a promising strategy for more selective targeting of cancer cells, potentially enhancing the specificity of cancer therapies. For cancer therapy, receptor crosslinking has been shown with receptors such as Her2^{16,29} and CD20³⁰. The crosslinked receptors enter the endolysosomal pathway resulting in their lysosomal degradation. While the final destination of the crosslinked receptors has been identified to be the lysosome, this mechanism and its exact trafficking profile are still elusive.

In order to fully understand this mechanism, the trafficking pathways that are utilised upon receptor crosslinking at the cell surface needs to be characterised in more detail. For this, a platform is necessary that enables the arrangement of receptor binding moieties to be presented at the plasma membrane that simultaneously allows the tracking of this construct. Generally, the ideal platform on which to control and define ligand arrangement that allows hyper-crosslinking of membrane receptors would be chemically inert and non-toxic. GNPs hold promise as platforms to control ligand surface density and therefore the crosslinking of receptors, and can also be used as trafficking labels. There have been reports demonstrating non-colocalisation between fluorescence and GNP signal of fluorescently labelled GNP-constructs^{31,32}, indicating that it might be beneficial to use the GNP's optical properties as an imaging label in addition to fluorescence microscopy to evaluate their trafficking in living cells.

1.3 Live cell imaging techniques for GNPs

Understanding the pathway and final destination of therapeutic molecules is critical in the development of new drug delivery systems that can improve targeting and reduce off-target effects. The acquisition of reliable translation motion information of these potential drug delivery systems – let alone their rotational dynamics – remains a challenging task especially in scattering environments such as cells³³. What is needed, is a stable optical label that can be tracked reliably over long time frames with high spatial resolution.

GNPs are exceptional imaging labels due to their unique optical characteristics, primarily stemming from their surface plasmon resonance (SPR). SPR occurs when conduction band electrons on the GNP surface oscillate in response to specific wavelengths of light, leading to intense absorption and scattering at those wavelengths³⁴. The conduction electrons are

displaced by the incident electric field which “pushes” the electron cloud toward one side of the particle. As the negative electron charge accumulates on one side of the particle, a positive charge forms on the other that compensates the electron cloud displacement - or in short: a dipole moment is induced. This interaction reaches its peak at certain frequencies known as the localised surface plasmon resonance (LSPR), where noble MNPs exhibit enhanced scattering and absorption, particularly in the visible spectrum, giving them their distinctive colour¹³. The strong scattering and absorption properties of GNPs enhance their visibility under various microscopy techniques.

Despite the optical characteristics of GNP and their intrinsic capability to be used as imaging labels, fluorescence-based methods are predominantly employed to track GNPs, requiring them to be additionally labelled with fluorophores. However, these methods suffer from physical limitations such as photobleaching and quenching. Differential interference contrast (DIC) microscopy has been shown to successfully track gold nanorods as they internalise into cells as well as their rotational behaviour^{35,36}. These methods are fast and don't require an additional label, giving a lot of information about particle movement, but they are limited to gold nanorods as the method requires particles with large aspect ratios to measure their motion. Dark field microscopy has also been used to study GNPs in live cells, which detects the scattering of light, though this method suffers from strong background from any other scatterers in the field of view (FOV)³⁷.

Laser microscopy techniques for GNP detection have been developed, including techniques such as laser-illuminated (hyperspectral³⁸) dark field microscopy to track GNPs, but these techniques generate extensive background in highly scattering environments, limiting them to very thin samples³⁹. Additionally, the GNPs need to be sufficiently large to be visible in those techniques and the employed sizes are reported to internalise less sufficiently or not at all⁴⁰. Heterodyne digital holographic microscopy⁴¹, optical diffraction tomography⁴² and wide-field interferometric phase microscopy⁴³ measure the refractive index distribution of biological samples with high spatial resolution. This has enabled the detection of GNPs, but these methods have limited axial resolution and are not suitable for detailed volumetric reconstructions. GNPs can convert absorbed UV and near infrared light into heat, which is the basic principle that is exploited in photothermal imaging of GNPs⁴⁴. Photothermal heterodyne imaging^{45,46} is capable of imaging GNPs using their photothermal conversion efficiency. However, this method is not background free.

Four-Wave Mixing (FWM) microscopy is a nonlinear imaging technique that is triply resonant to the LSPR that cannot only measure the location of a single NP in a disordered 3D environment, but also provides information about its geometrical anisotropy which enables tracking of the particle rotation and diffusion⁴⁷. In a biological environment, MNPs are the only structures that show changes in their dielectric function following excitation with a pulse of light at their resonance wavelength which can be probed by FWM imaging, making it a completely background free technique⁴⁸. The FWM signal originates from the change in the dielectric function of the GNP induced by the resonant absorption of a pump pulse at the LSPR. The set-up works in a pump probe scheme to first excite the GNP and then measure its response to the excitation using a probe beam. The probe beam arrives at an adjustable delay time after the pump pulse. The FWM signal is extracted from a noisy background through heterodyne detection by recombining the signal with a reference beam while the third-order nonlinearity provides enhanced resolution. The afore described behaviour is imprinted in the dynamics of the FWM signal over delay time between the pump and probe beams⁴⁷⁻⁴⁹. FWM surpasses existing detection methods as it specifically targets the GNPs optical resonance frequency, making it selective to MNPs with a time resolution of sub-milliseconds while being indifferent to autofluorescence and highly scattering environments. This technique, while in principle being theoretically capable of live cell imaging, has yet to be used in combination with live cells.

1.4 Rational nanocarrier design in the context of receptor crosslinking

There is a large number of properties that need to be considered when designing a nanocarrier, a nanoscale vehicle designed to transport therapeutic agents directly to targeted sites within the body. Both constituents, the GNP and the protein within the context of this project, need to be considered and both need to fit the chosen crosslinking agent. For example, an inadequate choice of crosslinkers or reactive groups that are included in the protein's binding sites will generate a non-functional conjugate or may generate a suboptimal version of the therapeutic agent with a negatively affected affinity towards its intended target^{15,18}. On the other hand, the choice of crosslinker can introduce desirable properties to the protein and, for example, enhance its hydrophobic properties and thereby its ability to pass through the cell membrane⁵⁰.

Therefore, having sufficient knowledge of the chemical, structural, and reactive characteristics of each component to be conjugated is important when designing these nanocarriers. Surface reactions on GNPs are critical for determining their physicochemical properties and functional performance. The high surface-to-volume ratio of GNPs enhances their reactivity, making their surface interactions particularly significant⁵¹. Functionalisation of GNPs is a key aspect, often

achieved by binding molecules such as thiols, which form strong covalent bonds with the gold surface, enabling tailored chemical properties for specific applications⁵². Adsorption of ions or molecules onto the surface plays an important role in modifying their catalytic, optical, and electronic properties. GNPs can catalyse redox reactions due to the unique properties of their surface atoms⁵³. The SPR, as mentioned previously, is highly sensitive to changes in the local environment, making GNPs useful in sensing and diagnostic applications⁵⁴. Additionally, surface reactions can influence the charge and stability of GNPs, as seen in citrate-capped nanoparticles stabilized by electrostatic repulsion⁵⁵. These surface interactions can be exploited for bioconjugation, enabling the attachment of biomolecules for use in biomedical and nanotechnology applications⁵⁶. Understanding and controlling these surface reactions is essential for optimising the design and application of GNP-based systems.

Considering the accessible functional groups – including the active site constituents – on the protein surface that will be conjugated to the GNPs is essential to understanding how to build a functional construct for drug delivery¹⁸. If multiple biomodifications are desired, the crosslinkers must be matched to the intended application and ensure that the ligands are attached through different functional groups of the protein⁵⁷. The following section will explore the main aspects one should consider when attempting to design GNP-protein conjugates for cell targeting.

1.4.1 Particle size and shape

Choosing the correct size of the core GNP of the construct is an important step as it will affect the mechanism of internalisation it can induce due to there being a limit to the maximum size of protein/particle a cell is capable of internalising⁵⁸. The properties of the ligand additionally influence the hydrodynamic radius of the construct. The optimal size of functionalised GNPs for cell uptake largely depends on the intended application. GNP internalisation studies suggest a diameter between 20 nm and 50 nm for internalisation by human cancer cell types (such as PK-1, PK.45, Panc-1, HepG2), which offers a balance between effective cellular uptake and potential cytotoxicity as very small GNPs of diameters below 5 nm have been shown to induce apoptosis^{40,59,60}. Particles of diameters of up to 50 nm are typically internalised faster and in larger quantities⁶⁰. In this project, clathrin-mediated endocytosis is the main driver of particle internalisation. Clathrin-coated pits have an average diameter of approximately 100 nm, representing the upper size limit for nanoparticles internalised via this route²². When rationally designing nanocarriers, the clathrin-coated pit size limitation as well as the hydrodynamic radius of the entire construct must be carefully considered.

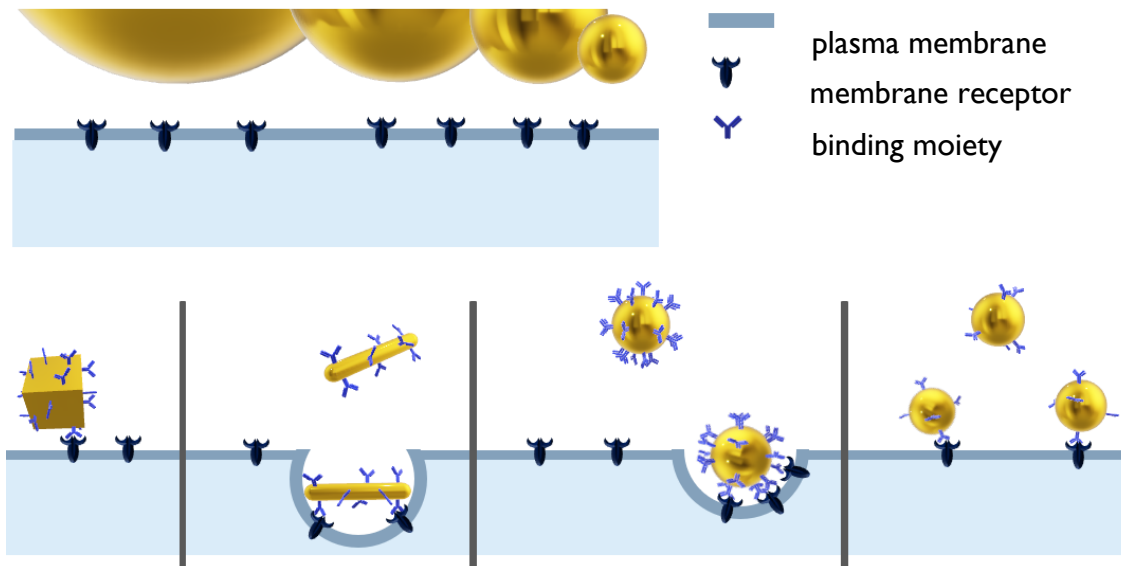


Figure 1.3 | Effects of GNP Curvature, Size, Shape, and Ligand Density. The figure schematically depicts the combined influence of the size and surface curvature (top) and the shape and ligand density (bottom) of GNP on the particle's ability to present binding moieties to the plasma membrane. The larger the particle, the flatter the gold surface seen by the plasma membrane (grey) and the receptors (black), allowing different levels of ligand (purple) presentation.

The ligand valency around GNPs can be influenced by considering the particle's size and shape, a factor that becomes critical in studies aiming to achieve receptor crosslinking. Both parameters largely affect the surface coverage with the desired ligands. Surface ligands are subjected to different levels of electrostatic repulsion and steric hindrance in relation to their own size and charge. As curved surfaces leave more room for bigger ligands, both sterically and electrostatically, they allow a denser adsorption of surface ligands. The average spacing between ligands on curved GNPs with a very small diameter and therefore higher surface curvature increases drastically compared to the average spacing of ligands on planar gold surfaces⁶¹. The effect of surface curvature and particle shape is visually highlighted in Figure 1.3. Furthermore, the ligand valency can be influenced by utilising any of the various bioconjugation approaches offered for GNPs. They are commercially available with a large library of functional groups conjugated to the peptides that are anchored onto their surface. This allows experimenters to choose their preferred approach of functionalisation. The choice of a suitable conjugation reaction is important to ensure the functionality of the ligand and therefore its recognition by its respective receptor^{15,18}.

1.4.2 Choice of target receptor

Choosing a well-studied target receptor when studying uptake mechanisms in cells is advantageous because an extensively researched receptor offers a rich knowledge base that simplifies experimental design and interpretation. Previous studies on the receptor ensure that

new findings can be cross-referenced and validated more easily, strengthening the reliability of the research. The Transferrin receptor 1 (TfR1) is overexpressed in many cancer cells and is an intensely studied receptor^{62,63}. The overexpression is a consequence of an elevated need for iron by cancerous cell types due to accelerated proliferation⁶⁴. This characteristic overexpression can serve as a distinguishing feature between cancerous and non-cancerous cells, positioning TfR1 as a good therapeutic target. TfR1 is the receptor for Tf.

Tf is a protein that regulates iron homeostasis in the human body. Its recycling pathway is schematically shown in Figure 1.4, which is taken from Rodak's Hematology Clinical Principles and Applications (2020)⁶⁵. Each Tf molecule can bind two ferric iron ions (Fe^{3+}) at specific binding sites. In its normal pathway, once iron is bound, the holoTf complex binds TfR1 and undergoes receptor-mediated endocytosis, realised by clathrin-coated pits. Within the endocytic vesicles, the pH drops, triggering a conformational change in Tf that leads to the release of its bound iron. The Fe^{3+} is subsequently reduced to its ferrous (Fe^{2+}) state and transported across the endosomal membrane into the cytosol by the divalent metal transporter 1 (DMT1). After releasing iron, the apotransferrin-TfR1 complex is recycled back to the cell surface. The neutral pH of the extracellular environment triggers the release of apoTf, after which Tf is ready to partake in another cycle of iron binding and transport⁶³.

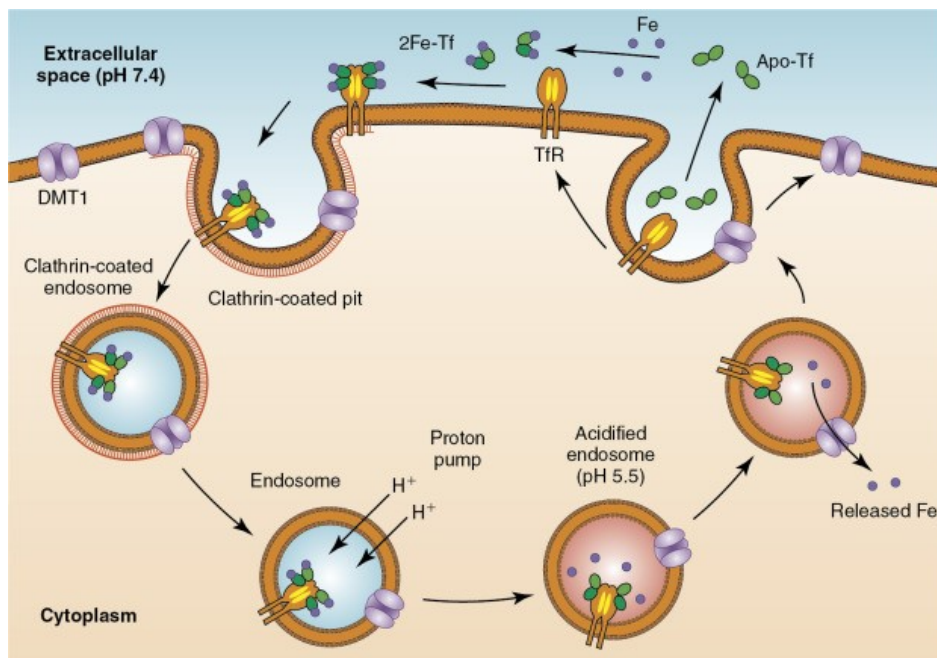


Figure 1.4 | Intracellular Trafficking Pathway of Transferrin. A critical mass of transferrin receptor 1 (TfR) with bound transferrin (Tf) will initiate an invagination of the membrane that ultimately fuses to form an endosome. An influx of hydrogen ions (H^+) inside the endosome causes a drop in pH which releases the iron from Tf, and once reduced, it is transported into the cytosol by divalent metal transporter 1 (DMT1). In the cytosol, iron may be stored as ferritin or transferred to the mitochondria, where it is transported across the membrane by mitoferrin (not shown). The TfR with apotransferrin (ApoTf) is returned to the cell membrane, where the ApoTf releases and the TfR is available to bind more Tf for iron transport into the cell. [Figure and caption reproduced from Rodak's Hematology Clinical Principles and Applications⁶⁵]

1.4.3 Stabilisation and functionalisation mechanisms

To gain insight and access to the afore mentioned pathways, it is necessary to choose an optimal functionalisation mechanism when preparing GNPs with ligands for targeted cell internalisation, as it impacts the efficiency, specificity, and safety of the construct. A well-executed functionalisation ensures that the GNPs are stable, biocompatible, and can effectively reach and interact with the targeted cells or tissues.

The first step of ligand exchange or conjugation procedure on GNPs is determined by the nature of the already attached capping agent. GNPs are capped with a preliminary ligand which is determined by their synthesis procedure. GNP synthesis is realised using gold salts (usually HAuCl) and a reducing agent that reduces the gold salt to neutral gold atoms⁶⁶. Different surfactants (e.g. citrate, CTAC, CTAB) can be used to induce directed growth. This is done by selective adsorption of molecules on different crystallographic planes of the gold seed and can lead to the preferential growth of certain crystallographic facets⁶⁷. Additionally, the presence of these capping agents on the GNP surface provides structural and colloidal stability during and after their synthesis⁶⁸. Unprotected GNPs are prone to aggregation due to the strong van der Waals forces between them. Their aggregation is irreversible and renders them unusable for further experiments⁶⁹. To be used *in vivo*, GNPs need to be stable in physiological aqueous environments containing high concentrations of biologically relevant ion concentrations.

The synthesis capping agents are usually not strong enough to stabilise the GNPs within a cellular environment and, in some cases, are even cytotoxic. Therefore, to ensure the stability and biocompatibility of GNPs, further surface modification and biofunctionalisation are important steps while these characteristics are also influenced by the GNP's geometry^{40,70}. Coating GNPs with polymers, such as polyethylene glycol (PEG) helps prevent aggregation, stabilise the NPs, and improve their colloidal stability⁷¹. Preventing the aggregation of GNPs leads to an extended circulation period in the bloodstream⁷². PEGylation is one of the most common practices in preparing therapeutic GNPs since first being reported for NP coating in 2004⁷³. Furthermore, it has been shown that PEG density will influence the organisation of the polymer on the surface. A low density coating forms a so-called "loose mushroom-coating", whereas a dense coating results in a "brush-formation" that is more accessible for further functionalisation of the polymer⁷⁴. Liu *et al.* have shown that there is an optimal PEG density for different lengths of the polymer to increase the cell viability of functionalised GNPs. They tested 0.55-5 kDa HS- methyl-terminated polyethylene glycol (mPEG), reporting a hydrodynamic radius of 15 to 38 nm, equating to a PEG-layer of 4.4 –16.4 nm with a 6 nm

GNP core⁷⁵. Another study showed that 20 nm GNP expressed increased stability with increasing PEG length, decreasing NP diameter, and increasing PEG mole fraction⁷⁶.

The introduction of chemical moieties through biofunctionalisation enables the attachment of ligands on the GNP surface, facilitating specific binding to desired targets, such as receptors on cells or disease markers⁵⁶. Such chemical moieties can be included on the proximal end of the PEG molecule used for stabilisation of the particle and serve as anchoring points for further functionalisation schemes. N-Hydroxysuccinimide (NHS)-based reaction chemistries have been widely used in conjugation reactions⁵⁷. The reaction mechanism is schematically represented in Figure 1.5A and B. Reagents that contain NHS or sulfo-NHS react with nucleophilic residues in the target protein chain by attacking at the electron-deficient carbonyl of the active ester whereby the NHS (or sulfo-NHS group) is released. The NHS group reacts preferentially with primary and secondary amines forming stable amide and imide linkages. NHS esters can also

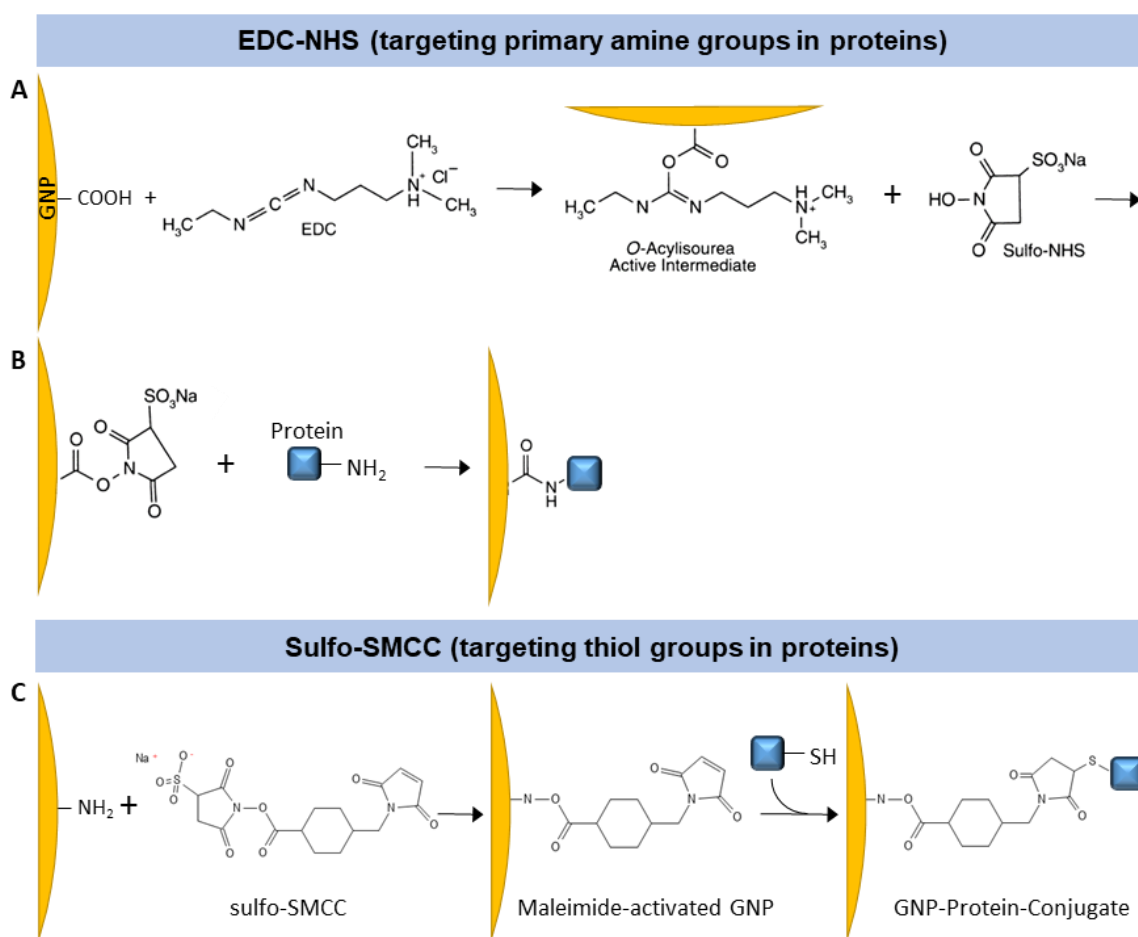


Figure 1.5 | Reaction Mechanism of EDC-NHS and sulfo-SMCC. Schematic illustrations of the reaction mechanism of the chosen functionalisation chemistries. (A and B) When combining EDC with sulfo-NHS, an amine-reactive derivative with active ester groups can be obtained. The mechanism allows for two entry points: (A) -COOH terminated GNPs for EDC activation to conduct the entire mechanism in house or starting with (B) pre-attached NHS groups on GNP for a one step reaction, conjugation to primary amines in the target molecule. Sulfo-SMCC is a bifunctional crosslinker, attaching through NHS one end to amine-terminated GNPs and with a maleimide on the other side that conjugates to sulfhydryls. Reaction scheme modified from Hermanson⁵¹. Representations of GNP and molecules are not to scale.

react with sulfhydryl or hydroxyl groups, but these reactions result in unstable bonds that further react with nearby primary amines or hydrolyse in aqueous environments. Therefore, they react either with the amine residue of lysine, or the α -amines at the N-terminal side of protein chains^{77,78}. Particles with terminal carboxyl groups allow NHS-attachment via EDC(1-Ethyl-3-[3-dimethylami-nopropyl]-carbodiimide hydrochloride)-NHS reaction chemistry.

On the other hand, there are particles available with pre-conjugated terminal NHS groups which allow a one-step reaction (Figure 1.5B). Another possible approach of linking GNP and proteins is to use an NHS ester on one end of a crosslinker and maleimide on the other, such as sulfo-Sulfosuccinimidyl 4-(N-maleimidomethyl)cyclohexan-1-carboxylat (SMCC) (Figure 1.5C). The NHS ester will react with primary amines whereas the maleimide group will react with sulfhydryls. Maleimide is a frequently used functional group in crosslinking agents creating stable thioether bonds. This reaction is specific to sulfhydryl groups in a pH environment of 6.5 to 7.0 and formed by an alkylation reaction between the double bond and sulfhydryl^{79,80}. In this case, GNPs with pre-attached amine groups can be attached to such heterobifunctional crosslinkers reacting with the NHS ester. After purification of the sample, the maleimide-activated GNP can react with cysteine residues in the protein chain of Tf. It should be noted that, in many cases, vendors use NHS esters to attach fluorescence markers to proteins targeting lysine residues in the protein chain which may block possible primary amine reaction sides. In this case, carboxyl groups of aspartic acid and glutamic acid can be targeted by EDC-sulfo-NHS reactions resulting in a reaction scheme as depicted in Figure 1.5A. Here, proteins that do not offer any accessible primary amines can react with the carbodiimide EDC to form an amine-reactive protein derivative that contains active ester groups that further react with sulfo-NHS. This protein derivative can then further be used to react with GNPs with pre-attached primary amine residues⁸¹.

1.4.4 Ensuring target protein functionality

To design a functional therapeutic construct that can bind its target in a cellular environment, the functionality of the ligand that binds the target needs to be ensured. As previously mentioned, it is important to take the protein structure and the amino acids into account that are central to Tf's iron binding site as well as it's receptor binding site¹⁸. Tf has two iron binding sites that are identical in the N and C lobe, respectively. The binding site is comprised of aspartic acid⁶³², two tyrosines Tyr⁴⁵⁷ and another Tyr (number not defined in the references), and one His⁵⁸⁵ that provide a carboxylate oxygen, two phenolate oxygens, and one imidazole nitrogen for Fe³⁺ ion binding^{82,83}. Residues identified as contributing to TfR1 binding are Pro¹⁴²-Pro¹⁴⁵, and Pro¹⁴²-Arg¹⁴³-Lys¹⁴⁴-Pro¹⁴⁵^{83,84}. Wally *et al.* mention lysine as crucial residue

in TfR1 interaction with rare mentions of cysteine⁸³. Amine-directed functionalisation may therefore more likely cause functional impairment of the protein than thiol-directed chemistry. While making sure that the reaction chemistry does not affect the active sites, there need to be enough accessible ligands available for functionalisation. Tf's primary structure, consisting of 679 amino acids in total, include the following primary amine containing amino acid residues: 58 lysines, 27 arginines, 35 asparagines, and 17 glutamines. However, only lysines, being the sole nucleophilic amine of the four, may be relevant; the others might react slowly or not at all under the conditions necessary for the conjugation mechanism⁵⁷. For thiol-directed reaction mechanisms, cysteine is the sole option, 38 of which are present in Tf's amino acid chain.

1.5 Ligand valency determination on GNPs

Receptor-crosslinking, and therefore internalisation, is only achieved when the spatial arrangement of the receptor-targeting ligands allows for sufficient ligand display at the local level of the plasma membrane to interact with the cellular receptors. Thereby, the number of conjugated ligands is an important feature when designing these therapeutic constructs as at least two ligands need to be presented to the cell to allow receptor crosslinking. However, receptor-crosslinking-mediated endocytosis showed to be more effective when more than two ligands are involved²⁹.

The accurate assessment of ligand surface density is important for interpreting data derived from GNP studies, their application as imaging agents, and their advancement into clinical settings. Typically, the quantification of ligands on MNPs starts with estimating the total surface area of the particles either by determining the ensemble's average MNP size using dynamic light scattering^{85,86} or through gas adsorption techniques^{87,88}, scanning electron microscopy⁸⁹, or transmission electron microscopy (TEM)⁸⁹⁻⁹¹. After the assessment of the average NP size, the total number of ligands in the sample is established using methods such as thermogravimetric analysis^{91,92}, optical spectroscopy⁹³, nuclear magnetic resonance^{91,94}, or vibrational spectroscopy⁹⁵. Ligand detachment followed by solution concentration measurement has also been reported^{61,96}. The derived average particle size and total ligand count allow the calculation of ligand density on an average sized MNP within the sample⁹⁷.

Although knowing this density can indicate the success of a conjugation reaction, additional data on sample heterogeneity are important for accurate experimental interpretation. Functionalisation of NPs with ligands typically results in a sample with diverse characteristics, including NPs with different numbers and distributions of biomolecules, ligand-induced NP aggregates, and ligand-only aggregates. Studies have highlighted instances of absent

colocalisation between NPs and presumed surface-bound fluorescent ligands^{31,32}. This complicates the analysis of how functionalised NPs are taken up by cells. For instance, ligand-only aggregates might emit fluorescence mistaken for NP attachment to cell membranes, while cross-linked NPs could become too large for cellular internalisation^{40,97,98}.

Techniques to assess the variability in NP size and the ligand number per NP on an individual basis are currently not available. For NPs, our capability is restricted to averaged measurement approaches that provide an average count of biomolecules attached per particle⁹⁹. Advancing our understanding of experimental outcomes involving functionalised GNPs would be significantly enhanced by creating a methodology capable of identifying the degree of particle crosslinking, determining ligand density individually per particle, and quantifying the components of unconjugated constructs within a sample⁹⁷.

1.6 Thesis Outline

This multidisciplinary project aims at paving the way for an in-depth study of the mechanism behind receptor crosslinking. To allow this characterisation, a method to quantify ligand density on a particle-by-particle basis have been developed. Given the clear differences between the recycling pathway of Tf and TfR1, and TfR1 when crosslinked by a complex containing multiple binding sites towards the receptor, TfR1 was deemed a good model for the GNP internalisation studies of this project. In its normal pathway, assuming physiological concentrations of the protein, only low levels of Tf should be localised in lysosomal structures, while crosslinked TfR complexes will show elevated levels within lysosomes¹⁶. This elevated concentration of Tf-signal within lysosomal structures can therefore serve as a distinguishable validation of inducing the mechanism of interest. The developed methodologies will be studied in human cervical carcinoma (HeLa) cells using GNPs as primary imaging labels to allow FWM microscopy. Bearing the factors of particle size limitations for cell internalisation in mind, 20 nm GNP were chosen for the experiments. The thesis will be structured as follows:

Chapter 2 provides the theoretical background for existing GNP imaging techniques, beginning with a physical description of the optical properties of GNPs, before progressing to explain the principles underlying FWM. It will furthermore describe the importance of understanding internalisation pathways in great detail as well as rational nanocarrier design and how different characteristics of GNP-protein constructs influence their effectiveness as agents with therapeutic relevance.

Chapter 3 details the sample preparation process, the experimental procedures, and the setup of the multimodal FWM system at Cardiff University.

Chapter 4 focuses on the development of a ligand quantification method using extinction microscopy for single GNP detection and single fluorophore bleaching for protein number determination. This method was tested on spin-coated GNP-protein samples. The validation of the developed method was achieved by testing three GNP-protein construct samples with different GNP to protein ratios, confirming that higher ratios lead to particle crosslinking and lower ratios result in singular GNP-protein constructs.

Chapter 5 discusses the upgrade of the FWM imaging modality to include live cell imaging capabilities and its validation for long-term imaging of living HeLa cells.

Chapter 6 evaluates various GNP functionalisation procedures for producing effective GNP-protein constructs capable of internalising into HeLa cells. It explores reaction mechanisms targeting primary amines and thiols in protein chains, GNPs pre-conjugated with stabilising polymers, and in-house functionalisation techniques. The chapter concludes that stabilising polymers pre-attached to proteins yield the highest quality constructs, as evidenced by methods developed in Chapters 5 and 6.

Chapter 7 summarises and concludes the findings from Chapters 4, 5, and 6, placing them in the context of existing research and proposing directions for future investigation.

Chapter 8 proposes two project ideas proceeding from the outcomes of this thesis, offering potential studies for further exploration based on the research conducted.

2 Fundamentals

2.1 Optical properties of GNPs

2.1.1 Linear optical characteristics of GNPs

Unique physical properties can be observed in noble MNPs that cannot be found in macroscopic scales of the same material. The change in physical behaviour is most noticeable in the optical properties of nano sized noble MNPs¹⁰⁰. Scientific research on MNPs dates back at least 150 years to Michael Faraday¹⁰¹. A famous and in this context often mentioned example is the Lycurgus cup (see Figure 2.1). The cup appears a greenish grey colour in reflective light conditions, whereas it appears red when light is transmitted from the inside of the cup. This optical far-field effect of increased absorption and scattering of light at specific wavelengths is caused by the artistic implementation of gold and other MNPs that are interspersed in the glass¹⁰². The optical effect originates in the specific interaction of the MNPs upon irradiation with light. Namely, morphologically dependent collective oscillations of the conduction band electrons are induced when an electromagnetic wave propagates along the particle surface that are known as ‘plasmon’^{13,103}.

These linear optical properties of GNP can be related to the magnitude of absorbed or scattered light by the particle and are physically described by an optical cross section σ_{abs} , an elastic scattering cross section σ_{sca} which in their sum result in the extinction cross section σ_{ext} , which can be described by:

$$\sigma_{\text{ext}} = \sigma_{\text{abs}} + \sigma_{\text{sca}} \quad (2.1)$$



Figure 2.1 | Lycurgus Cup. Lycurgus cup in (left) reflective and (right) transmission light conditions⁹⁷. The optical effect stems from MNPs interspersed in the glass.

These optical cross-sections carry information about the particle's geometric characteristics as well as their composition. In 1908, Gustav Mie presented a theory that described the extinction spectra composed of the combined influences of scattering and absorption effects of spherical particles of different sizes¹⁰⁰.

2.1.2 The dielectric function of GNPs

The dielectric function, represented as $\varepsilon(\omega)$, has two parts - the real part, $\varepsilon_1(\omega)$, and the imaginary part, $\varepsilon_2(\omega)$. The real part deals with how the particles polarise in response to an electric field, and the imaginary part defines how they lose energy, primarily through heat¹⁰⁴.

The observable effects of GNPs in relation to light can be explained using the Drude model, suitable for metals like gold with free electrons¹⁰⁵. The Drude model equation is:

$$\varepsilon(\omega) = 1 - \frac{\omega_p^2}{\omega^2 + i\gamma_b\omega} \quad (2.2)$$

Where, ω_p is the plasma frequency, linked to the density of electrons, γ is the damping factor, related to how the electron oscillations lose energy, and ω is the frequency of the incoming light. To give an intuitive explanation, the Drude model simplifies how electrons behave in metals to explain electrical and thermal conductivity. It describes metals as containing free electrons that move around (plasma frequency) and conduct electricity when an electric field is applied (frequency of the incoming field). However, these electrons can occasionally interact with the fixed atoms in the metal, which slows them down and causes resistance (damping factor).

The Drude model needs some adjustments for describing MNPs correctly because at the nanoscale, different effects come into play¹⁰⁰. The confinement of electrons to a small volume significantly affects their dynamics. This confinement leads to increased electron scattering from the NP's surface. The model needs to incorporate size-dependent damping to accurately describe this enhanced surface scattering effect, which is not observed in bulk metals. This is factored in by adjusting the damping term γ_b , to consider both the inherent damping and the effects of the NP's size¹⁰⁶. This model yields precise outcomes for infrared frequencies; however, it is less effective in the visible spectrum as it does not account for interband transitions in the plasmonic NP¹⁰⁷. Interband transitions describe the movement of electrons from the valence band to the conduction band¹⁰⁸. The conduction band is the range of electron energy levels in a material where electrons are free to move, allowing electrical conductivity.

The valence band comprises energy levels filled with electrons that are bound to atoms and responsible for the chemical properties of the material. If this band is fully occupied, the material is an insulator, but if electrons gain enough energy to jump to the conduction band, the material can conduct electricity¹⁰⁸. To account for the interband transitions, a frequency dependent extra term $\varepsilon_{ib}(\omega)$ has to be included in equation 2.2.

$$\varepsilon(\omega) = \varepsilon_{ib}(\omega) + 1 - \frac{\omega_p^2}{\omega^2 + i\gamma_b\omega} \quad (2.3)$$

And the complex dielectric function can be represented as:

$$\varepsilon(\omega) = \varepsilon_1(\omega) + i\varepsilon_2(\omega) \quad (2.4)$$

For more detailed information, one can refer to Derkachova *et al.*¹⁰⁴, where Figure 2.2 is taken from. It shows the real and the imaginary part of the dielectric function of gold, taking into account the interband transitions as described in equation 2.3.

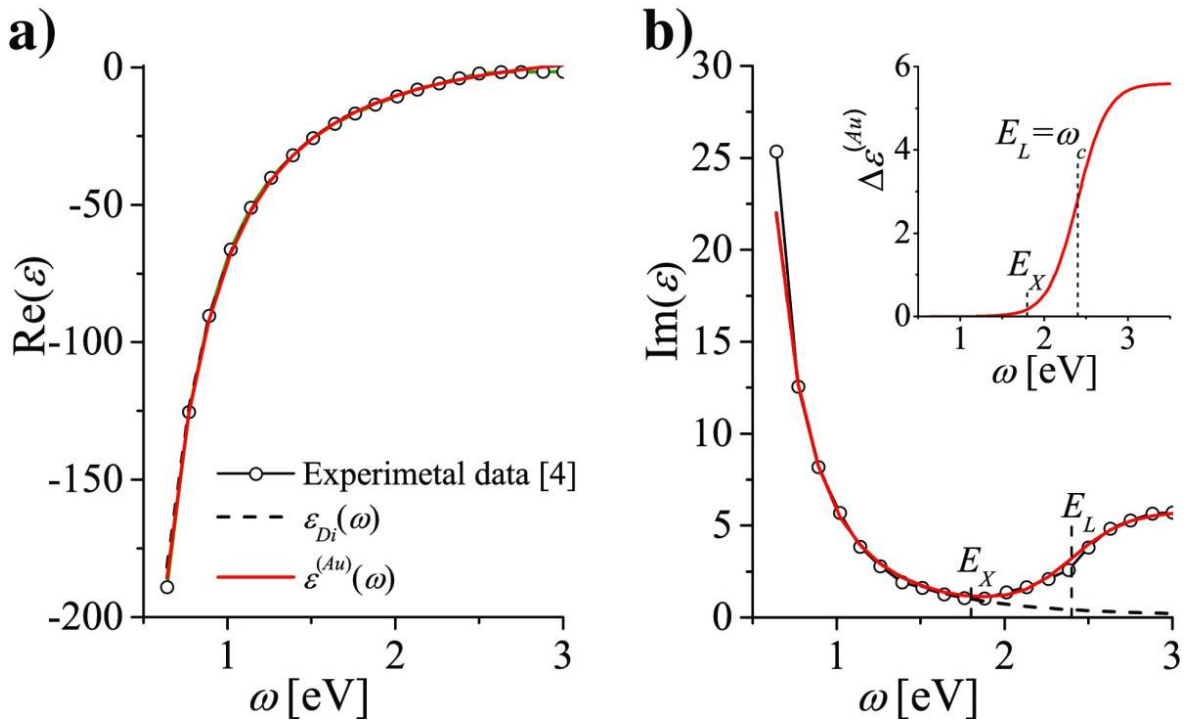


Figure 2.2 | Comparison of the Real (a) and (b) Imaginary Part of the Dielectric Function for Gold Resulting from Different Models. Black dashed lines: $\varepsilon_{Di}(\omega)$ with parameters $\varepsilon_0 = 9.84$, $\omega_p = 9.010$ eV, $\gamma = 0.07$ 2eV. Red solid lines: $\varepsilon^{(Au)}(\omega)$ with the same parameters ε_0 , ω_p and γ but supplemented by $\Delta\varepsilon^{(Au)}(\omega)$ (shown in the insertion) accounting for the interband transitions over 1.8 eV. [Figure taken with permission from Derkachova *et al.*⁹⁹. Reference [4] in the image refers to Johnson *et al.*¹³⁹]

2.1.3 Localised surface plasmon resonance

In an optically isotropic, dielectric medium, when conductive nanostructures are subjected to an oscillating electromagnetic field, plasmonic excitation can be observed. This phenomenon occurs due to the curvature at the interface between the particle and the dielectric medium, leading to the direct excitation of plasmons. The curved geometry of this interface exerts a restoring force on the displaced electrons, generating an opposing dipole moment. This process results in enhanced electromagnetic fields near the particle. The plasmons generated in this context are highly spatially confined, do not propagate, and because of this are considered localised. This is referred to as LSPR with this phenomenon being dependent on the morphology of the nanostructure¹⁰⁹.

The amplitude of the induced electric dipole moment is the highest depending on the polarisability of the NP material. These LSPR bands of enhanced scattering and absorption often occur in the visible spectrum for noble metal NPs which results in their characteristic colour and the effect as visible in the Lycurgus cup (Figure 2.1)^{13,100,102}. The specific equations, for the optical cross sections for particles, from a quasi-static approximation of radius R , σ_{abs} and σ_{sca} can be expressed as

$$\sigma_{abs} = 4\pi k R^3 \left(\frac{\epsilon_p - \epsilon_m}{\epsilon_p + 2\epsilon_m} \right) \quad (2.5)$$

$$\sigma_{sca} = 8\pi k^4 R^6 \left| \frac{\epsilon_p - \epsilon_m}{\epsilon_p + 2\epsilon_m} \right| \quad (2.6)$$

With ϵ_p defining the dielectric function inside the particle, ϵ_m as the dielectric function of the surrounding medium, and k defining the wave number of light in the medium¹¹⁰.

By replacing σ_{abs} and σ_{sca} in equation (2.1) with equations (2.5) and (2.6), it becomes evident that maximal extinction is achieved when the denominator is at its minimum, which is reached at $-2\epsilon_m$.

The frequency at which the relationship described is valid is the LSPR, a predominant feature in the spectra of noble MNPs. As depicted in Figure 2.3 (top), the LSPR is characterised by the collective oscillation of the free electron gas within the NP, triggered by an external electromagnetic field. This oscillation results in a dipole due to the charge separation between the free electrons and the lattice. The intensity, position, and bandwidth of the LSPR are

significantly influenced by the material of the NP, its size, shape, and the refractive index of the surrounding environment (see Figure 2.3, bottom)¹³. The asymmetry of the UV-Vis spectra is characterised by a plateau at shorter wavelengths. This feature is attributed to the absorption caused by interband transitions within the NPs.

Other than size, the optical properties of plasmonic NPs are significantly influenced by the medium surrounding them. This effect on the spectra of plasmonic NPs is evident when observing their absorption spectra in mediums with varying refractive indices, showing a red shift and an increase in the intensity in the LSPR wavelength when the refractive index of the medium increases⁵⁴.

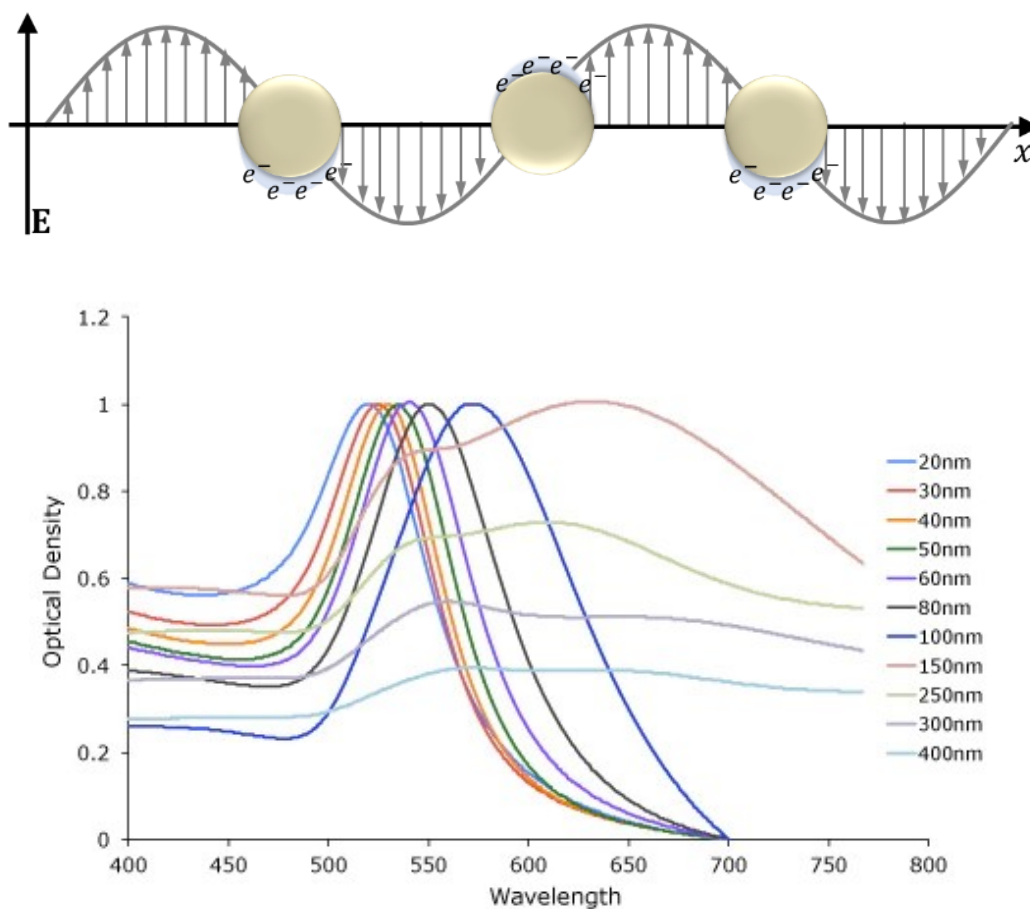


Figure 2.3 | Illustration of Plasmon Formation. (Top) Schematic illustration of conduction electron oscillation in MNPs in the quasistatic approximation⁸⁵. In this process, the conduction band electrons in the metal undergo collective oscillation when they interact with light. The oscillation amplitude reaches its peak at the surface plasmon resonance frequency, a value dependent on the nanoparticle's shape, size, and the dielectric properties of the surrounding environment. (Bottom) UV-Vis spectra of spherical GNPs of different sizes, exemplifying the size-dependency of the LSPR position. [Bottom figure taken from Cytodiagnosics¹⁵².]

2.2 Nonlinear optical responses of GNPs

2.2.1 Nonlinear microscopy

Nonlinear optics is a branch of optics that deals with the behaviour of light in nonlinear media, where the response of the material to the electromagnetic field of the light is nonlinear. This nonlinearity typically becomes significant at very high light intensities, such as those provided by lasers. Unlike in linear optics, where the response of a medium is directly proportional to the electric field of the light, in nonlinear optics, the response can depend on the square, cube, or higher powers of the electric field¹¹¹.

Most nonlinear optical behaviours are explained through the concept of polarisation, which is related to the applied electric field. In linear optics, the polarisation density P in a dielectric medium is quantified as $P = \frac{dp}{dV}$. This equation denotes the variation in the dipole moment dp within a given volume element dV in the substance. This polarisation is linearly dependent on the magnitude of the applied electric field E and can be expressed by the following equation, known as the first order susceptibility¹¹²:

$$P(t) = \epsilon_0 \chi^{(1)} E(t) \quad (2.7)$$

The nonlinear polarisation of the medium is described by:

$$P(t) = \epsilon_0 [\chi^{(1)} E(t) + \chi^{(2)} E(t) + \chi^{(3)} E(t) + \dots] = P^{(1)}(t) + P^{(2)}(t) + P^{(3)}(t) + \dots \quad (2.8)$$

Here, ϵ_0 defines the permittivity of free space, and χ^2 , χ^3 are the second-order and third-order nonlinear susceptibility of the medium, respectively. These susceptibilities are tensors, and their values depend on the properties of the material and the frequencies of the interacting waves¹¹².

One of the most studied nonlinear optical phenomena is second harmonic generation, where two photons of the same frequency interacting with a nonlinear material are combined to generate a new photon with twice the frequency of the original photons. The efficiency of this process is governed by the second-order susceptibility χ^2 .¹¹¹

Nonlinear optics include a variety of phenomena besides SHG, including third harmonic generation, four-wave mixing, two/three photon luminescence, CARS, and more¹¹¹.

2.2.2 Four Wave Mixing microscopy

This project uses phase-resolved triply resonant FWM microscopy to detect and reveal the pathway of GNPs within a cellular environment. It uses a third-order nonlinear optical process that is characteristic to noble MNPs, which will be further elaborated in this section. Central to understanding this technique is the concept that χ^3 nonlinearities alter the dielectric function of the material under examination.

The optical set up uses three laser beams that all operate at the same wavelength, a scheme that is also called degenerate. These equal frequencies ($\omega_1 = \omega_2 = \omega_3 = \omega_p$), are close to the LSPR of the GNPs. The beam sequence arrives at the sample in a pump probe scheme with an adjustable delay time in the picosecond regime between the two fields. The absorption of the pump beam causes ultrafast changes in the real and imaginary parts of the dielectric function of GNPs, which have been shown on the FWM set up with GNP diameters ranging from 5 nm to 40 nm⁴⁹. The model accounts for the transient changes in electron and lattice temperatures within the GNPs, including considerations of both intraband and interband transitions. These transitions are critical for understanding the energy absorption and scattering mechanisms at play, which in turn influence the NPs' optical properties. This set-up was developed by the Biophotonics and Quantum Optoelectronics group at Cardiff University. The set-up itself with its optical parts will be explained in more detail in the methods section and explanations in this section are based on the descriptions of Masia *et al.*⁴⁹.

The pump and probe fields in the FWM imaging scheme are represented as E_1 and E_2 , respectively. The induced polarisation p at the particle can be described by

$$p = \varepsilon_0 \varepsilon_p \alpha E_2 \quad (2.9)$$

where α defines the polarizability of a spherical GNP that is much smaller than the wavelength that excites it. The polarizability of a GNP in this regime was defined in equation (2.5) and can now be written as follows:

$$\alpha = 4\pi\varepsilon_0 R^3 \left(\frac{\varepsilon_p - \varepsilon_m}{\varepsilon_p + 2\varepsilon_m} \right) = 4\pi R^3 \tilde{\varepsilon} \quad (2.10)$$

with $\tilde{\varepsilon}$ defining the effective dielectric constant.

When the NP is excited by the intensity-modulated pump field E_1 , there is an alteration in the dielectric function. This modification, that is referred to as $\Delta\tilde{\epsilon}$, leads to the generation of a FWM field E_{FWM} which is directly related to the change in polarisation. Since $\Delta\tilde{\epsilon}$ changes in proportion to the intensity of the pump, denoted by $I_1 = |E_1|^2 = E_1 E_1^*$, the resulting FWM signal is therefore linked to E_{FWM} and is proportional to $E_1 E_1^* E_2$. This relationship highlights the third-order nonlinearity characteristic of the process.

On the electronic level, the absorption of the pump beam leads to the formation of a non-equilibrium electron distribution with a fast energy transfer from the oscillating electrons to single electron excitation. There is a thermalisation of the hot electron gas through electron-electron scattering that in turn leads to a lattice thermalisation. Finally, through heat diffusion into the environment, the lattice cools down¹⁰⁶. These dynamics take place over a few hundreds of picoseconds and they are plotted in Figure 2.4 as measured by Masia *et al.*⁴⁹.

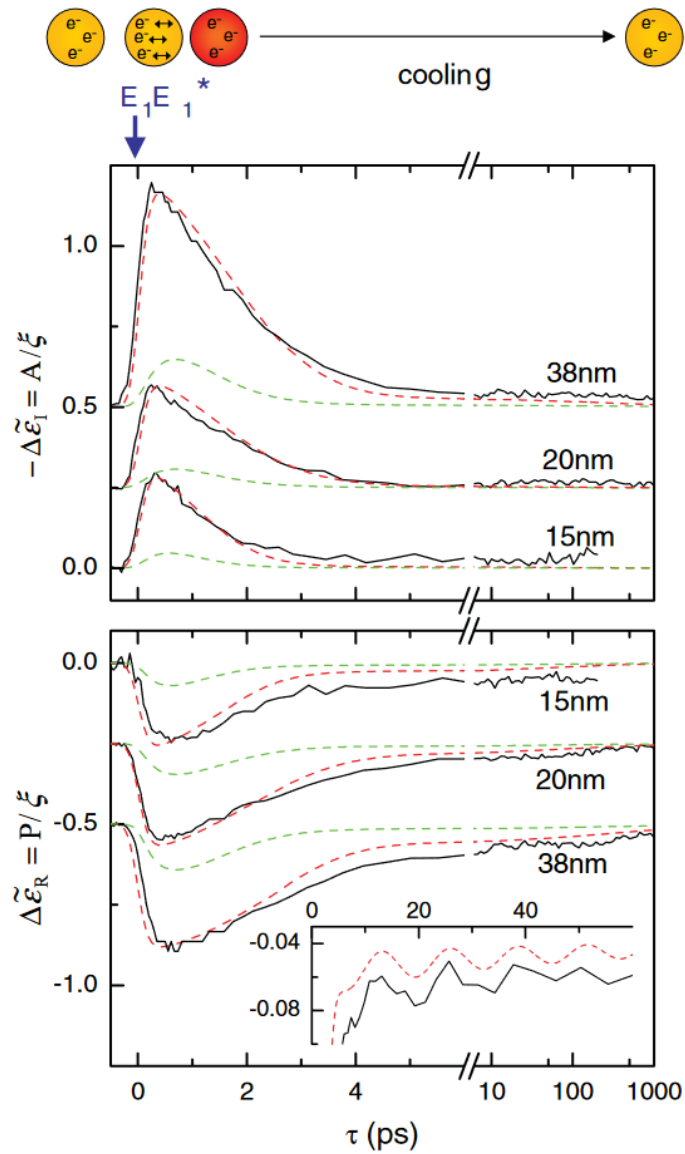


Figure 2.4 | Transient Changes of the Real ($\Delta\tilde{\epsilon}_R$) and Imaginary ($\Delta\tilde{\epsilon}_I$) Parts of the Dielectric Function of a Single Gold NP Resonantly Excited and Probed at 550 nm for Different NP Diameters as Indicated. Pump (probe) fluence is 0.60 J/m^2 (0.11 J/m^2) for the 15- and 20-nm NPs and 0.65 J/m^2 (0.05 J/m^2) for the 38-nm particle. Acquisition time per point is 200 ms. Dashed lines are corresponding calculations, with the green lines neglecting the heating by interband absorption. Curves are vertically displaced for clarity. The top sketch illustrates the SPR excitation by the pump (E_i) and the subsequent heating and cooling dynamics monitored by the probe. The inset shows coherent phonon oscillations for the 38-nm NP. [Figure and caption from Masia *et al.* with permission.⁴⁹]

3 Materials and Methods

This chapter incorporates content that has been previously published in

N. Slesiona, L. Payne, I. Pope, P. Borri, W. Langbein, P. Watson, Correlative Extinction and Single Fluorophore Bleaching Microscopy for Ligand Quantification on Gold Nanoparticles. *Adv. Mater. Interfaces* 2023, 10, 2300568.⁹⁷

3.1 Sample Preparation

3.1.1 Functionalisation procedures of GNP

The functionalisation procedures in the method section do not mention concentrations as different samples were functionalised using different concentrations of crosslinkers, particles, quenchers, and/or proteins. The concentrations will be mentioned in the main text of the chapters when discussing and comparing the samples.

3.1.1.1 functionalisation using GNPs with pre-attached NHS-groups

Spherical 20 nm GNP with a coating of a stabilising polymer (unknown) and pre-attached NHS residues were purchased freeze-dried from Nanopartz (California, USA) to which human, Alexa647-labelled Tf (TfA) (5 mg/mL, Invitrogen™, California, USA) were conjugated following the suggested procedure by the vendor. In short, the vendor recommends 100 mg in 1 mL phosphate buffered saline (PBS) (BupH™, Thermo Scientific, Germany) of a 150 kDa antibody to load 20 mg onto the particles. The needed amount of TfA was diluted into 1 mL PBS which was adjusted to a pH of 8. The solution was added to the freeze-dried particles. The particles were resuspended by sonication in an ultrasonic bath (FB15047 Fisher Scientific, UK) for 30 seconds, followed by 30 seconds of shaking by hand, repeating both steps three times. The reaction was left for 30 min at 30°C on a shaker. The sample was then purified by centrifugation at 12,000 relative centrifugal force (rcf) for 10 min, the supernatant discarded, and the particles resuspended in 1 mL 1% PBS 0.1% Tween 20 (Sigma-Aldrich, Darmstadt, Germany) solution. The purification step was conducted three times in total, whereby after the last step of supernatant removal 1 mL PBS was added. The functionalised particles were stored in the fridge at 4°C until usage.

3.1.1.2 EDC-NHS reaction

Spherical GNPs of 20 nm core diameter with pre-attached carboxyl groups (Nanopartz, California, USA) were taken from stock (30 nM) which was sonicated prior to use to ensure uniform dispersion and detachment of GNP from tube walls. The NPs were centrifuged at

12,000 rcf for 20 min to produce a pellet. The supernatant was removed, and the pellet resuspended in MES buffer (pH 6, (BupH™, Thermo Scientific, Germany). This wash step was repeated twice with a final resuspension of the GNPs in MES buffered saline. 1-Ethyl-3-(3-dimethylaminopropyl)carbodiimide (EDC, Pierce™, Thermo Scientific, Darmstadt, Germany) was added together with sulfo-NHS (Thermo Scientific, Germany). The reaction was left on a shaker at room temperature (RT) for 15 min, followed by a centrifugation step at 12,000 rcf for 20 min. The supernatant was removed and replaced with PBS. The sample was subjected to another round of centrifugation, after which the supernatant was replaced with PBS containing TfA at concentrations as stated in the main text. The sample was left on a shaker at RT for 2h and protected from light. To quench the reaction, hydroxylamine was added to a final concentration of 50 μ M. The sample was washed by centrifugation at 12,000 rcf for 20 min three times, replacing the supernatant with PBS buffer in an equivalent volume.

3.1.1.3 sulfo-SMCC reaction

Spherical GNPs with an average diameter of 20 nm and a proprietary hydrophilic polymer coating featuring terminal amine groups (2 attachment sites (ASs) per nm^2 as specified by the manufacturer) (Nanopartz™ Ntracker™, California, USA), were employed in this project. For the conjugation process, TfA (Invitrogen™, California, USA) was conjugated to the GNPs using sulfo-succinimidyl-4-(N-maleimidomethyl)-cyclohexane-1-carboxylate (sulfo-SMCC) (Thermo Scientific, Darmstadt, Germany). Initially, GNPs were conjugated to the NHS functional group of sulfo-SMCC in a 100:1 sulfo-SMCC to amine residue excess, and the mixture was left on a shaker at RT for an hour before being purified by centrifugation at 12,000 rcf for 20 min. Subsequently, 90% of the supernatant was replaced with PBS (pH 7) containing TfA and incubated for 2 hours at RT on a shaker, shielded from light. After incubation, centrifugation at 12,000 rcf for 20 min was repeated to eliminate unbound TfA, discarding 90% of the supernatant and resuspending the GNPs in a 1% PBS and 0.01% Tween20 solution. Where sulfo-SMCC's remaining maleimide groups were quenched, mercaptoethanol (Thermo Scientific, Darmstadt, Germany) was added at a 100:1 mercaptoethanol:AS ratio and left to react for an hour at RT, shielded from light. This step was omitted in reactions that did not employ quenching. Following three centrifugation and supernatant removal steps, the GNP-TfA constructs were resuspended in PBS to their original volume and briefly sonicated for 1 second between each centrifugation to ensure proper resuspension. The functionalised GNPs were then stored in the dark at 4°C, for up to one month.

3.1.1.4 Dithiol-PEG-NHS

20 nm GNPs (BBI solutions, Crumlin, Wales; Sigma-Aldrich, Darmstadt, Germany) were subjected to centrifugation at 12,000 rcf for a duration of 10 min. Following centrifugation, the supernatant was carefully removed and replaced with an equivalent volume of distilled water (dH₂O) or dimethylsulfoxide (DMSO) (Thermo Scientific, Darmstadt, Germany). Next, PEG-NHS (Sigma-Aldrich, Darmstadt, Germany) was dissolved in DMSO at a concentration of 20 mM. DMSO was chosen as the solvent to prevent the hydrolysis of the NHS group. The PEG-NHS solution was then mixed with the GNPs at varying molar ratios to test for the best outcome of functionalisation. This mixture was allowed to incubate for 1.5 hours at RT. After the incubation, a second round of centrifugation was performed at 12,000 rcf for 10 min. The supernatant was removed, and the same volume of PBS or dH₂O was added to remove excess NHS-PEG-thiol. Subsequently, TfA in PBS (final conc. 62.5 nM) was added to the GNPs, and the mixture was allowed to incubate for 3 hours. Finally, another two rounds of centrifugation at 12,000 rcf for 10 min were conducted, followed by resuspension of the particles in dH₂O with an equivalent volume. The functionalised GNPs were stored in the dark at 4°C until usage for a maximum of one month.

3.1.1.5 ortho-Pyridyldisulfide-PEG-NHS

Prior to functionalising the GNPs, TfA was conjugated to OPSS-PEG-NHS (OPN) (Iris Biotech, Marktredwitz, Germany). A 10 mM OPN solution was prepared by dissolving the OPN in 100mM sodium bicarbonate buffer (pH 8.6). The prepared OPN solution was added to TfA at a molar ratio of 150:1 (OPN:TfA) immediately after preparing the solution. The mixture was incubated overnight at 4°C in a dark environment. Following incubation, a dialysis was performed to eliminate unreacted reagents. The reaction mixture (1 mL) was transferred to a 20kDa MWCO dialysis membrane (Slide-A-Lyzer™, Thermo Scientific, Darmstadt, Germany) and dialyzed against 3×1 L PBS at 4°C for 24 hours in the dark. The dialysis buffer was changed three times during this 24-hour period. The OPSS-PEG-TfA (OPT) concentration was quantified by BCA assay (Pierce™, Thermo Scientific, Germany). This involved preparing protein standards using Bovine Serum Albumin (BSA) and a serial dilution of OPT in a 96-well plate. The BCA working reagent was added to each well. After incubation at 37°C for 30 min, absorbance was measured at 590 nm using a FLUOstar OPTIMA microplate reader (BMG Labtechnologies, Ortenberg, Germany). Protein concentrations were determined by comparing sample absorbance to the BSA standard curve. Blank wells with PBS were included for background correction. The conjugates were stored in the dark at - 20°C until needed.

GNPs suspended in citrate of 20 nm and 60 nm diameter (Sigma-Aldrich, Darmstadt, Germany) were functionalised with OPT. For this, the GNPs were centrifugated three times at 10,000 rcf (20 nm GNPs), or 900 rcf (60 nm GNP) for 30 min and 95% of their supernatant removed and replaced with 10 mM citrate to the original volume supplemented with 0.01% Tween20 after the first two rounds of spinning. After the third round, the particles were added to OPT and incubated for 2h at RT, while protected from light. The concentrations of the constituents were formulated as follows: one TfA per 40 nm², i.e. 32 TfAs per 20 nm particle (surface area: 1260 nm²), and 283 TfAs per 60 nm particle (11,310 nm²). After this, 2kDa mPEG-SH (Sigma-Aldrich, Darmstadt, Germany) was added for PEG-backfilling at a ratio of 4 PEGs/nm². The constructs were incubated overnight in the dark at 4°C. The next day, two washing steps were conducted, spinning the particles down at the speeds as stated above and removing approx. 95% of the supernatant, replacing it with PBS supplemented with 0.01% Tween20. After a third round of centrifugation, the particles were resuspended in PBS with an equivalent volume and stored at 4°C in the dark until further use.

3.1.2 Cell culture

HeLa cells, a human cervical carcinoma cell line, were obtained from the American Type Culture Collection (ATCC, USA). The cells were cultured in cell culture petri dishes (Ø10 cm) with Dulbecco's Modified Eagle Medium (Gibco™, UK) supplemented with non-essential amino acids and GlutaMAX™ with 10% (v/v) fetal bovine serum (Life Technologies, UK) at 37°C and 5% CO₂ in a humidified incubator. The cells were regularly checked for infections and growth under a brightfield microscope. Upon reaching a confluency of 80% the HeLa cells were passaged in sterile culture conditions typically in a time frame of 4 days. Passaging was done in a cell culture hood under sterile conditions. Prior to and following any work in the cell culture hood, all surfaces were disinfected with 70% ethanol. In the passaging procedure, the cells were washed with 1 mL of 0.25% trypsin (Thermofisher, UK) followed by a 5 min incubation step with 1 mL of 0.25% trypsin at 37°C to detach the adherently growing HeLa cells from the culture dish. The cells were resuspended in 9 mL culture media and plated onto new petri dishes (Ø10 cm) in 1:10 and 1:20 dilution for continuous culturing. For next day experiments, the cells were plated on Ø35 mm glass bottom dishes (MatTek, USA) to a concentration of 5,000 cells per mL to a total of 2 mL. Cells were passaged to a maximum passage number of 25. The cell concentration of the resuspension was determined via counting the average cell number in a haemocytometer. Prior to counting, the chamber and cover slip were washed with 70% alcohol. After fixing the cover slip in position, 10 µL of the cell suspension was added to the hemocytometer and the cell number determined by counting the

cells in the four corners of the gridded square (1 mm²) and averaged. This average was multiplied by 10⁴ to estimate the number of cells per mL and the necessary dilution of the suspension was calculated using the following equations:

1) Number of cells per ml = Average cell number per square x Volume of square (ml)

2) Volume of cell suspension (ml) = Desired cell number per ml / Number of cells per ml

3.1.3 Pulse Chase Experiments on HeLa cells

Pulse-Chase experiments in HeLa cells were conducted to determine the fate of free TfA and TfA-functionalised GNP. The day after plating the cells onto Ø35 mm glass bottom dishes (MatTek, USA), the HeLa cells were serum-starved by removing their normal growth media and adding 500 µL fresh, non-supplemented and serum-free FluoroBrite DMEM (FB), (Life Technologies™, California, USA). All incubation steps were conducted at 37°C and 5% CO₂ in a humidified incubator. After 30 min incubation and aspiration of the media, the cells were incubated in FB containing either TfA or construct for 30 min. Subsequently, the cells were incubated in normal growth media for varying chase times that are stated for each experiment within the main text. After the incubation time the media was replaced by FB supplemented with non-essential amino acids and GlutaMAX™ with 10% (v/v) fetal bovine serum (Life Technologies, UK) for imaging in live cell experiments, or by 4% paraformaldehyde (PFA) to fix the cells for 30 min, followed by two washing steps of PBS. Fixed cells were then mounted on a glass slide using Mowiol. The cells were then imaged in epifluorescence and in transmission on an inverted wide field microscope, or on the FWM set up.

3.1.4 Glass cleaning procedure

Prior to spin-coating TfA, GNP-TfA, or GNP onto coverslips, the coverslips and glass slides for later mounting were cleaned by a hydrogen peroxide (H₂O₂) procedure as follows: First, the coverslips were marked to allow reliable identification of the same area on two different set-ups. For this, a diamond pen was used to scratch a crosshair into the surface. This procedure was developed within this project and is further detailed in Section 4.2.5. The glassware was then scrubbed with acetone (Carl Roth, Karlsruhe, Germany) and submerged in toluene (Carl Roth, Karlsruhe, Germany). The coverslips were sonicated (Ultrasonic Bath 3510 MTH, Branson) for 20 min after which they were immersed in acetone for another round of sonication for 20 min. The glassware was then thoroughly rinsed with DI water and placed in a clean beaker filled with DI water and placed into a microwave to bring to a boil. Additionally, a toothpick was placed in the beaker to prevent sudden release of vapor due to superheating.

Once at boiling temperature, the microwave power was reduced to gently boil for 3 min. After letting the glass cool down, the coverslips were submerged in 30% H₂O₂ for final sonication for 20 min. The glassware was then stored in fresh H₂O₂ until usage.

3.1.5 Spin-coating procedure

A hydrogen peroxide-cleaned cover slip (24x24 mm, thickness 0.16-0.19 mm, Menzel-Gläser, #1.5, Braunschweig, Germany) was positioned on the chuck of a spin coater (WS-650MZ-23NPPB, Laurell, USA) and secured by vacuum. The procedure involved spinning the disc for 35 seconds at 2000 rpm, followed by an additional 30 seconds at 4000 rpm. At the onset of rotation, 20 µL of the sample was dispensed onto the centre of the cover slip. Due to their size, single TfAs and GNP-TfA constructs are smaller than the resolution limit of diffraction-limited optical imaging systems, rendering their fluorescence signals as spots determined by the microscope's point spread function (PSF). The PSF size depends on the objective's numerical aperture (NA), the wavelength of illumination, and the refractive index of the medium. If two nano-objects are closer together than the size of the PSF, they are indistinguishable as separate structures. To reduce the occurrence of such overlaps, TfA, GNP, and GNP-TfA constructs were diluted to a concentration of 10⁹/mL prior to spin-coating. The resulting density was approximately 0.035 particles/µm², translating to an average particle separation of about 5 µm, assuming an even distribution. Diamond scribe markings were made on the cover slip before spin-coating to allow reidentifying of specific areas across different microscopy platforms. For imaging, the sample was attached to a glass slide, spin-coated side facing the slide, using a 0.12 mm thick adhesive gasket (Grace Bio-labs SecureSeal) modified to include channels for injecting index-matching oil, essential for extinction microscopy.

3.2 Multimodal imaging set-up

Bright field, Extinction, FWM microscopy, DIC and confocal fluorescence were conducted on the same multimodal imaging set up. The set up consists of a Nikon Ti-U inverted microscope with a set of microscope objectives. Wide-field illumination is provided by a halogen tungsten lamp (V2-A LL 100 W; Nikon, Tokio, Japan) with a set of bandpass filters available in the illumination path. Additionally, different polarisers and sliders are available that can be inserted into the optical pathway for dark field illumination and DIC microscopy. Two condensers were available, an oil condenser of 1.1-1.34 NA, and a long working distance dry condenser of 0.52 NA, as well as two tube lenses of 1x and 1.5x magnification. The samples are moved by an xyz piezoelectric stage (NanoLP200, MadCityLabs, Madison, WI, USA) with a range of 200 µm. Images were acquired with a water-cooled scientific Complementary Metal–Oxide–

Semiconductor (sCMOS) camera (PCO Edge 5.5, Excelitas, Waltham, MA, USA), with 2560×2160 pixels and 16-bit digitisation, 0.54 electrons per count, and a full well capacity of 30 000 electrons. For FWM (and CARS) measurements, a laser beam can enter the microscope through its right port. The microscope and its optical components were operated remotely by a custom-written software called MultiCARS which is implemented in LabWindows CVI (written by W. Langbein, Cardiff School of Physics and Astronomy).

3.2.1 Extinction

A technique for measuring the extinction cross sections of individual NPs was developed in our group and is further described in Payne *et al.* employing Extinction Suite Macro (ESM) as analysis software¹¹³. In this method, transmission images of GNPs are obtained using wide field microscopy using a lateral shift and a rapid reference method. This way, a large number of frames can be obtained in a short period of time. These frames are averaged and subtracted, creating a differential transmission image Δ . From this, the extinction cross sections of each particle in the FOV can be calculated by

$$\sigma_{ext} = \int_{A_i} \Delta dA,$$

with A_i denoting the area used in which the particle is centred. The high number of frames lead to exceptionally high sensitivity, even for very small NPs down to 5 nm and a shot noise limited cross-section sensitivity of 0.4 nm^2 . Wavelength-dependent measurements are possible with the available band-pass filters in the excitation light path. Wide-field extinction measurements are recorded using the 100 W halogen lamp as illumination source. The 1.34NA oil-immersion condenser (Nikon MEL41410) and 1.45 NA oil immersion objective (Nikon MRD00405) are used coupled with the 1x tube-lens.

3.2.2 FWM

FWM is a third-order nonlinear phenomenon that arises from light-matter interaction of three interacting light waves that generate a fourth wave that can be modulated in the presence of plasmonic NPs. The Four Wave Mixing imaging FWMi scheme consists of such three optical pulses of 150 fs duration (80 MHz repetition rate) with the same centre frequency close to the LSPR of spherical GNP at 550 nm that are denoted as pump, probe, and reference. All three beams are generated by the same laser source, stemming from an optical parametric oscillator (OPO, Inspire HF 100, Spectra Physics, Newport, CA, USA) pumped by a Ti:Sapphire laser (Mai Tai HP, Spectra Physics, Newport, CA, USA). To aid with visualisation of the setup, a schematic overview of the involved optical components is provided in Figure 3.1. The laser

power of the set-up was regulated by modulating the radio-frequency wave amplitude with Acousto-Optic Modulators (AOMs, ASM-802B67, IntraAction Corp. Illinois, U.S.A), with output power measurements between the Dichroic Beam Splitter (DBS1) and the microscope port. The output beam from the OPO is initially linearly polarised in a horizontal direction (H) in respect to the laboratory's reference system. This beam first goes through a polariser (P) and a $\lambda/2$ plate ($\lambda/2-1$) to adjust the power of the beam. This serves as an initial attenuation factor. The beam then goes through prism pulse compressor, which is used to adjust for chirp caused by the optics in the beam path. Following the pulse compressor, the beam passes through another $\lambda/2$ ($\lambda/2-2$) waveplate. This waveplate rotates the beam's linear polarisation by 45 degrees. After this, the beam enters a polarising beam splitter (PBS1), where it is divided into two separate beams (50:50 split). One of these is a H polarised transmitted beam, and the other is a vertically polarised (V) reflected beam. These two beams have equal intensity and serve different functions: The V polarised (reflected) beam acts as pump and excites the GNPs at the

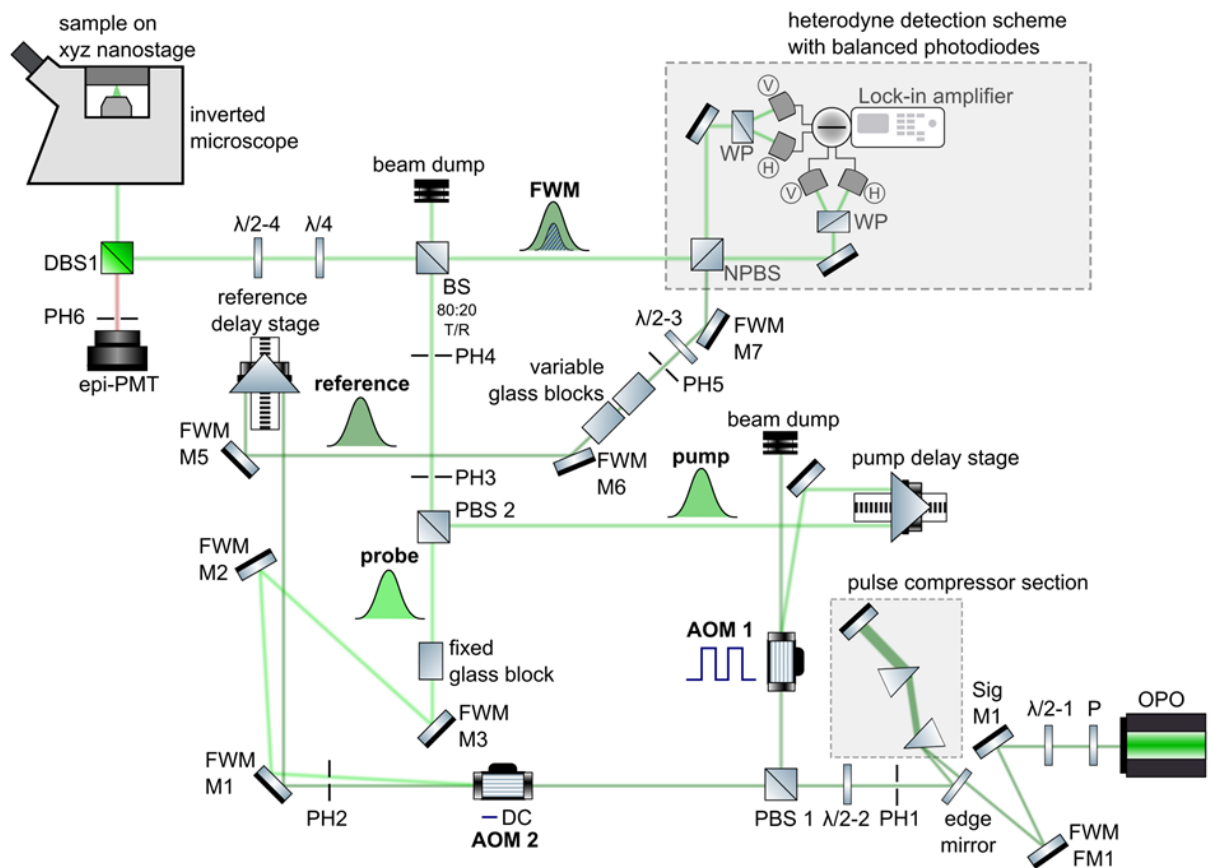


Figure 3.1 | Schematic Representation of the Optical Components in the FWMi Set-Up. This figure provides a schematic overview of the optical components utilised in the FWM setup, part of a multimodal imaging system that also includes CARS and IGOR modalities. The illustration focuses exclusively on the components relevant to FWMi. Components not depicted are either not integral to the FWMi pathway or do not require adjustment during alignment. All components that are subject to adjustment in the FWMi configuration are specifically highlighted and labelled in the schematic. A comprehensive description of the entire setup is provided in the main text of the document as well as the alignment procedure.

LSPR. The change in the NP's optical properties is resonantly probed by the H polarized (transmitted) probe beam. The delay time τ between the pump and the probe beams is adjustable thanks to a motorised delay stage (M403.8, Physik Instrumente (PI) GmbH, Karlsruhe, Germany) that is incorporated into the pump beam's path. The pump and probe beams are recombined using a second polarising beam splitter (PBS2) and then directed by a non-polarising beam splitter (BS) with an 80:20 transmission-reflection ratio. A pair of $\lambda/2$ ($\lambda/2-4$) and $\lambda/4$ waveplates is employed to transform these beams into circularly polarised light at the sample plane. These recombined beams are further reflected by DBS1 into the right port of the Nikon Ti-U inverted microscope stand. The pump and probe pulses are combined and focused onto the sample by a high NA microscope objective. This generates a FWM field that is proportional to $E_1 E^* E_2$. This FWM field (FWM^A), along with the reflected probe field (REFL), are collected in reflection by the same microscope objective, travel back through the waveplates and are transmitted by the BS. As a result, if the probe is reflected by a planar sample surface without any NP, the REFL returns V polarised in the laboratory system. The reference beam, which is also temporally adjustable using a motorised delay stage (M403.6, Physik Instrumente (PI) GmbH, Karlsruhe, Germany), is polarised at a 45-degree angle by $\lambda/2-3$ before being recombined with the epi-detected signal via a non-polarising beam splitter (NPBS) to achieve equal photocurrents on V and H diodes of the balanced detector. A Wollaston prism then vertically separates the H and V polarisations. The interference between the epi-collected FWM field and the reference field is detected using two pairs of balanced silicon photodiodes (Hamamatsu S5973-02), which provide polarisation-resolved detection. The detection scheme distinguishes the FWM field from the pump and probe pulses, using a heterodyne technique. The heterodyne detection scheme, characterised by radio-frequency shifts combined with lock-in amplification, stands as a cornerstone of the experimental setup, facilitating the differentiation of pump, probe, and FWM signals. Sharing an identical wavelength and being both focused and collected by the same objective lens, these signals are indistinguishable based on wavelength or propagation direction. The heterodyne technique enables us to overcome this challenge by modulating the frequencies of the interacting light beams, thereby allowing for the isolation of specific signals based on their unique frequency shifts. For more detail on this, please refer to Borri *et al.*^{114,115}. The system measures both the amplitude and phase of the REFL and the epi-detected FWM^A.

3.2.3 Confocal fluorescence

To allow simultaneous measurement of confocal fluorescence with FWMi, a dichroic mirror (DBS1) was used to spectrally separate the fluorescence signal from the FWM fields, all which

were collected by the same objective. DBS1 has a cut at 600 nm, where it reflects shorter wavelengths and transmits longer ones. The fluorescence was excited by the laser beam that was used for FWM. The light then passes through an adjustable confocal pinhole (PH6) before reaching a photomultiplier detector (Hamamatsu H10770A-40) with an additional bandpass filter (Semrock FF02-650/100) which transmits light within the 600-700 nm wavelength spectrum. To allow confocal imaging, the pinhole was set at 1 Airy unit.

In confocal fluorescence microscopy, adjusting the pinhole to different Airy unit settings directly impacts the optical sectioning capability, the signal-to-noise ratio and the resolution of the acquired image. The Airy unit is a measure related to the diffraction pattern produced by a circular aperture, with one Airy unit being the diameter of the first diffraction disk. Setting the pinhole to a smaller diameter (less than 1 Airy unit) increases the optical sectioning ability of the microscope at which point the resolution is diffraction limited. This means the microscope can more precisely isolate a thin section of the specimen, reducing the amount of out-of-focus light that reaches the detector. The result is a sharper image with higher contrast¹¹⁶. This update of confocal fluorescence was available before the onset of the project but was not aligned for use until later in this project.

3.3 Widefield microscope set-up

Wide-field epi fluorescence as well as bright field measurements were conducted on an inverted Olympus IX73 microscope and a Prior Lumen200Pro light source using filter set (89000, Chroma, Vermont, U.S.A.). Fluorescence emission can be separated with using a multiband dichroic filter set (#89000, Chroma, Vermont, U.S.A.). The emission was detected with a sCMOS Camera (Hamamatsu ORCA-flash 4.0 V2, 30,000 full well capacity, 1.4 electrons read noise, and 0.46 electrons per count) at a 2×2 binning readout on all images corresponding to a 130 nm image pixel size. Camera and filter settings were operated utilizing the HCImage software package (Hamamatsu).

3.4 Transmission electron microscopy measurements

Transmission electron microscopy was conducted by Dr. Thomas Davies as follows: Samples were prepared by wet dispersion. 5 x 10uL drops were added sequentially, by blotting onto 300 mesh copper grids coated with holey carbon film. Samples were analysed using a JEOL JEM 2100 LaB₆ TEM operating at 200 kV.

The resulting images were then analysed in ImageJ to determine the particle diameter of GNP samples as well as to determine the sphericity of the GNPs.

3.5 Data acquisition and processing

3.5.1 Validation of particle functionalisation

3.5.1.1 UV-Vis measurements of GNP

UV-vis spectra were recorded to calculate the resulting particle concentration after functionalisation. GNP and GNP-TfA spectra were measured with a NanoDrop 1000 spectrophotometer (Fisher Scientific, UK) using the vendor's operation software. The spectra were measured in 3 nm increments of wavelength. The obtained raw data was plotted and evaluated using Origin 2023.

3.5.1.2 Zeta (ζ) potential measurements

ζ potential measurements were performed with ZEN3600 Malvern Instruments Ltd. and were conducted in disposable folded capillary cells (DTS1070). In the Zetasizer software, the parameters were set as follows: (1) Material: Gold (Malvern), (2) Dispersant: Water at a Temperature of 25 °C (Viscosity 0.8872 cP, refractive index: 1.330), (3) equilibration time for temperature stabilisation: 120 sec, (4) Measurement: 3 measurements with no delay in between with at least 10 runs per measurement. The mean of the measurements was calculated and plotted using Origin 2023.

3.5.2 Wide-field epi-fluorescence microscopy for fixed and live cell imaging

Epi-fluorescence and bright-field measurements of live and fixed cells were conducted on the microscope described in section 3.3. After treatment in live-cell pulse chase experiments or after fixation, samples were imaged either with 1 sec in live cell experiments or 3 sec in fixed cell experiments. Alexa647 was the only fluorophore used during this project, so a ET645 nm/30 nm was chosen as the excitation filter and the ET705 nm/72 nm as the emission filter. Cell experiment data was acquired using a 100x, 1.4 NA oil immersion objective. All FOVs were acquired in epi fluorescence mode first, followed by a bright field image for reference.

3.5.2.1 False colour overlays and axial colour coding

Epi-fluorescence data were utilised to generate false-colour overlays, combining fluorescence with brightfield images of the same FOV, allowing the analysis of GNP internalisation via the fluorescent tag of TfA. This image processing was conducted using the ImageJ software, where brightfield data were displayed in grayscale with adjusted contrast to enhance the visibility of the cellular structure. The fluorescence signal was visualised using the "Fire" look-up table

(LUT) to depict intensity variations. In time-lapse studies, representative epi-fluorescence frames were selected to create a composite false-colour overlay for individual frames. Additionally, z-stacks of epi-fluorescence data contributed to creating maximum intensity projections (MIPs), which further served in constructing false-colour overlays that mapped the distribution of fluorescent signals across FOV, again employing the “Fire” LUT for this purpose.

For two-dimensional representations of z-depth, z-stacks of epi-fluorescence data underwent temporal colour coding in ImageJ, utilising the “physics” LUT. The resulting RGB image was then either directly used as an image for analysis or it was superimposed with a brightfield image of the same FOV by separating the RGB image into its constituent channels and superimposing them back in their respective colour channels together with the brightfield image in greyscale for a more detailed analysis.

Orthogonal representations of z-stack data were created using the VolumeViewer Plugin¹¹⁷ within ImageJ. For better visualisation, the data was stretched in z by a factor of 5 with further settings at: Mode: Max Projection (2); Interpolation: Tricubic smooth (2); Sampling: 1.

3.5.3 Wide-field epi-fluorescence microscopy for single fluorophore bleaching

Wide-field epi fluorescence measurements were carried out using the inverted Olympus IX73 microscope, detailed in Section 3.3 and illustrated in Figure 3.2. For these experiments, the ET645 nm/30 nm and ET705 nm/72 nm filters were selected for excitation and emission, respectively. A 100× oil immersion objective with a variable NA ranging from 0.6 to 1.3 was employed,

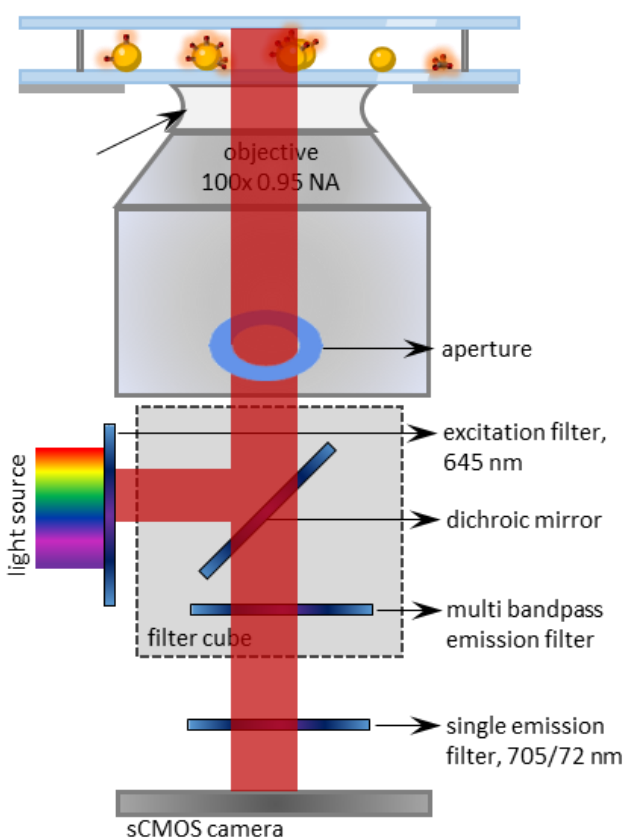


Figure 3.2 | Epi-fluorescence Set-Up. Wide-field epi fluorescence set-up with a 645 ± 15 nm excitation filter and a 705 ± 36 nm emission filter. Emission is detected using a sCMOS camera. A 100× oil immersion objective with an adjustable NA of 0.6-1.3 is used (set to 0.95 NA to avoid total internal reflection, which resulted in background due to limited spectral filtering of the reflected excitation). Representations of components and the sample are not to scale. [Figure and description adapted from Slesiona *et al.*⁹²]

with the NA adjusted to 0.95. This adjustment aimed to prevent total internal reflection (TIR), which was identified as a source of significant background noise due to residual filter transmission. The IX73's fly-eye illuminator lacks an aperture iris, which would have allowed for the control of illumination NA while maximising emission collection NA for optimal signal acquisition. To quantify the number of fluorophores per TfA and the number of TfA molecules per GNP, time series measurements of spin-coated TfA and GNP-TfA samples were performed with a 3-second integration time. A consistent excitation intensity was ensured by using a red fluorescent slide (ThorLabs -FSK6), adjusting the lamp to yield an average signal of 50,000 counts with a 50 ms exposure. Photobleaching was minimised by focusing the sample in brightfield contrast at the lowest light intensity, without any filters. Bleaching traces and initial fluorescence intensities $I(t_0)$ were extracted using the custom Extinction Suite macro (ESM)^{113,118}, which automatically identifies individual fluorescence signals within the FOV. $I(t_0)$ data were plotted as histograms in Origin 2023, with binning settings specified within each figure description in the main text.

3.5.4 Bleaching step size determination and background correction of single fluorophore bleaching data

To eliminate background, such as hot pixels (HPs), a background image was recorded from an average of 20 frames taken under the same acquisition conditions but in the absence of fluorescence excitation. This image was then subtracted from the photobleaching time-series. The analysis, conducted using ESM, involved calculating the fluorescence intensity of individual spots, summing the signal across the PSF over time to identify photobleaching steps. For each fluorescent spot, the intensity was summed within a 4-pixel radius of its peak, and a local background, derived from data within an 8-pixel radius, was subtracted. ESM indexed each spot with an ID (identification) number, enabling correlation with its respective extinction spot for correlation analysis. The methodologies behind the analysis software and its computational processes are elaborated in Payne *et al.*¹¹³ The manual assessment of photobleaching steps allowed the quantification of the average number of fluorophore ligands per TfA, which was necessary for estimating the TfA to GNP ratio. The number of fluorophores per TfA was calculated using the histograms of fluorophores per protein, and running the implemented Poisson fit function within Origin 2023 which is accessed by the script access code `nlf_Poisson(x,a,b)`¹¹⁹.

3.5.5 Wide-field extinction microscopy

Following photobleaching measurements, the chamber of the sample (development detailed in Section 4.2.5) was filled with silicone oil, index matched to glass ($n = 1.52$), to mitigate background caused by surface roughness in extinction measurements. Extinction microscopy was performed as described by Payne *et al.*¹²⁰.

Briefly, measurements were carried out on the multimodal imaging set-up described in section 3.2 and schematically represented in Figure 3.3, utilising a 100x 1.45 NA oil objective (Nikon lambda series, MRD01905) paired with a 1× tube lens and a 1.34 NA condenser. A 550 ± 20 nm bandpass filter (Thorlabs FB500-40) was employed in the illumination pathway. Extinction images were captured using a cooled sCMOS camera at its full sensor resolution of 2560×2160 pixels, setting the exposure time to 12 ms per frame at an 82 Hz frame rate, achieving an average signal of approximately 22,000 photoelectrons (pe). Differential transmission images were obtained by imaging the area of interest twice: once with particles in the reference position and again after shifting the sample laterally by 1.3 or 2 μm . Background images were taken by blocking the illumination path. For enhanced extinction cross-section sensitivity, 1280 frames were collected

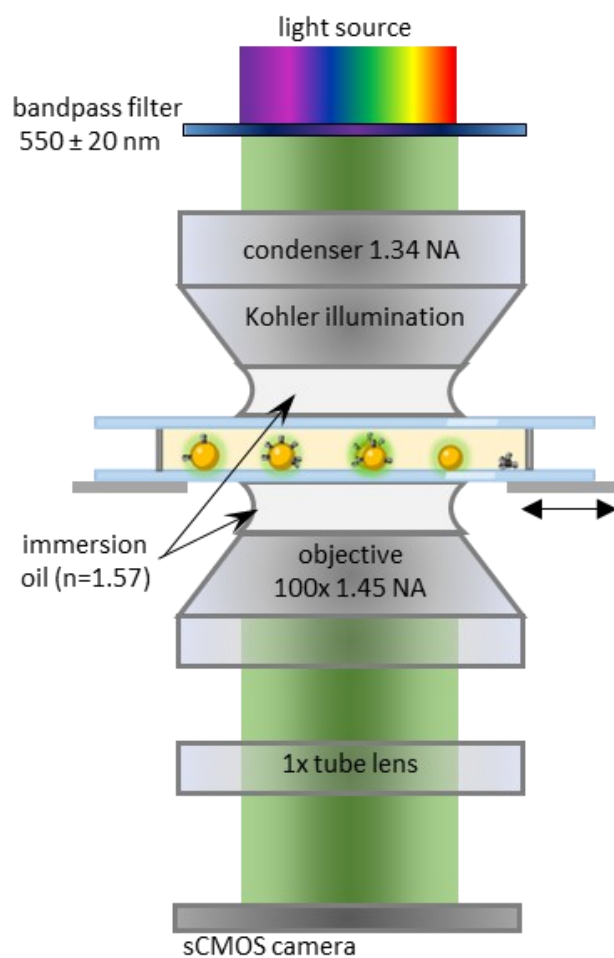


Figure 3.3 | Extinction Microscopy Set-Up. Under Köhler illumination, a sample's transmission is captured on an sCMOS camera, employing a 1.34 NA condenser and a 100x 1.45 NA objective. To perform differential measurements, the sample position is laterally adjusted using a piezoelectric stage. A bandpass filter of 550 ± 20 nm was chosen to ensure maximum extinction of the incident light by the GNPs. Representations of components and the sample are not to scale. [Figure and description adapted from Slesiona *et al.*⁹²]

for each shifted position, with 128 frames sequentially captured at a fixed sample position before cycling the position 10 times to minimise slow drift effects in illumination and sensor stability. The resulting σ_{ext} data exhibited a noise level of 15 nm^2 . Particle size estimation from the σ_{ext} was performed using MiePlot v4.6.18, simulating σ_{ext} for GNPs in oil ($n = 1.52$) and

averaged across the wavelengths 535, 545, 555, 565 nm, reflecting the selected illumination bandpass filter range. The extinction image calculation, following Payne *et al.*'s description¹²⁰, was conducted by averaging all frames at each shifted position, realised by ESM which automatically identifies extinction signals and performs signal calculations within the FOV. These signals were plotted as histograms in Origin 2023, with specific binning settings detailed within the experiment's figure descriptions in the main text.

3.5.6 Superposition of correlative fluorescence and extinction measurements

Correlative fluorescence bleaching and extinction data were analysed using ImageJ. Due to the acquisition of extinction and bleaching measurements on different microscopy systems, it was necessary to align extinction images with fluorescence images to account for discrepancies in scaling, shear, rotation, and translation. This alignment was achieved using an image transformation software developed within the group. Based on a number N of common features identified by their coordinates of fluorescence (r_f) and extinction (r_e) signals, the software determines a transformation

$$\mathbf{r}_f = \mathbf{C}\mathbf{r}_e + \mathbf{t}$$

where \mathbf{t} is a translation vector, and the matrix \mathbf{C} rotates, shears, and scales the axes. The transformation parameters are determined by minimising the standard deviation S between r_f and the transformed r_e , given by

$$S = \sqrt{\frac{1}{N} \sum |\mathbf{r}_f - (\mathbf{C}\mathbf{r}_e + \mathbf{t})|^2}.$$

With a minimum requirement of $N=3$ matching features, the transformation achieves exact alignment, resulting in a standard deviation (S) of 0. This alignment allows the transformed image to be accurately overlapped with its reference image for subsequent correlation analysis. The methodology behind this registration process is detailed in by Pope *et al.*¹²¹ The co-localisation of extinction and fluorescence signals within these overlaid images was then manually evaluated to identify the presence of constructs, such as GNP-protein conjugates. These detected constructs were subsequently analysed in Origin 2023 by plotting $I(t_0)$ against their σ_{ext} values. This analysis allowed the assessment of potential crosslinking, the quantification of fluorophores per GNP, and the determination of the number of GNPs per construct, providing valuable insights into the structural and functional characteristics of the conjugated constructs.

3.5.7 FWM measurements

3.5.7.1 Alignment

It is crucial that the pump and probe pulses have matching chirp along their beam paths. This allows them to be equally pre-compensated and maintain Fourier-limited pulses at the sample. To achieve this, glass blocks are inserted in the beam path to adjust the chirp accordingly. Since the reference beam does not pass through the microscope objective, glass blocks with known group-velocity dispersion were added to its path as well. The exact amount of glass added is tailored to the objective/tube lens combination being used. This step aligns the chirp introduced by the microscope optics with that of the reference beam, maximising the interference between the reflected FWM field and the reference field at the detector.

The FWM alignment procedure ensured spatial overlap of the reference, pump, and probe beams both in *direction* and *position*. The alignment included several steps which will be briefly summarised in the following. To follow the beam walking procedure visually, please refer to Figure 3.1. The probe, pump and reference beams are aligned independently. While one beam path is being aligned the other beam paths are blocked using servo-controlled shutters.

Mirrors Sig_M1 and FWM_FM1 were used to align the signal beam (combined pump, probe and reference beams) through pinhole 1 (PH1) and pinhole 2 (PH2), ensuring the signal beam enters the optical setup consistently on a day-to-day basis. Subsequently, the pump and probe beams were separated using a polarising beam splitter (PBS1), adjusted independently to align through pinholes 3 (PH3) and 4 (PH4), and recombined with another polarising beam splitter (PBS2). Two external cameras (not shown within the scheme in Figure 3.1), which visualise the near field (NF) and far field (FF) directional space by observing the partially transmitted (FF) and reflected (NF) beam from optical elements within the setup, are used to view the beams during the alignment procedure. The uc80viewers software is used to view the signals from the cameras. First, the probe beam was aligned using the mirrors FWM_M2 and FWM_FM1. The alignment of the probe beam through pinholes PH3 and PH4 was iterated until the central spots of PH3 and PH4 overlapped in both the NF and FF cameras. The overlap position was marked within the uc80viewers software, and these coordinates used when aligning the pump beam. The pump beam is aligned by iteratively adjusting PBS1 and PBS2 until the central spots of PH3 and PH4 overlap the coordinates of the central spots from the probe beam in both the NF and FF cameras.

To overlap the reference beam with the probe (pump) beam a reflective gold film is mounted in focus at the sample position on the microscope. The gold film reflects the probe beam back

towards the heterodyne detector system. A removable alignment mirror is placed in front of the Wollaston prism (WP) in the heterodyne detector system to reflect the probe beam back along the probe alignment path where it can be viewed on the NF and FF cameras. The position of the back reflected probe beam is marked on the image from the alignment cameras displayed in the uc80viewers software. The reference beam, which is also reflected by the removable mirror onto the NF and FF cameras, is aligned onto the marked position of the back reflected probe beam by adjusting mirrors FWM_M5 and FWM_M7. Once the probe and reference beams have been overlapped the mirror is removed from the heterodyne detection system.

Subsequently, the photodiodes in the heterodyne detection system were corrected for dark current and the dc offset from the reference beam balanced. The diodes are balanced by rotating thin (170 μm thick) glass plates located between the WP and the diodes. As the glass plate is rotated the amount of transmitted light varies allowing the diodes to be balanced.

As well as the spatial overlap of the beams their temporal overlap is equally as important. Firstly, with both the probe and reference beams on the reference delay is varied to find the maximum reflection signal from the gold film. This reference delay is taken to be zero i.e. when the probe and references pulses are in temporal overlap. Secondly, with both the pump and reference beams on the pump delay is varied to find the maximum reflection signal. This is referred to as the pump zero-time delay i.e. when the pump is in temporal overlap with the reference (and by the previous step the probe). It is important to note that once the reference delay has been determined, the objective focus should not be changed since this will change the temporal overlap of the probe (pump) and reference pulses. Instead the sample position should be moved through the objective focus using the piezo x,y,z stage. For this reason, the reference delay is optimised every time the sample is exchanged, or the objective z-position is adjusted.

The pump-probe delay was set to 0.5 picoseconds using the pump delay stage, a duration previously identified as optimal for generating strong signals from 20 nm GNPs. Final steps included the acquisition of the phases of the two sidebands from the pump modulation, and the carrier, in the lock-in detection. For this, the interference of the pump and reference beam were monitored. By tuning the $\lambda/4$ waveplate, the detected modulations in the V and H channels were equalised in magnitude. The lock-in acquisition software provides the measured offset phase for both V and H. The users compare this value with the carrier phase, and sets a value into the software to enable the correct evaluation of amplitude and phase modulation from the two sidebands. Finally, polarisation resolved imaging was realised by monitoring the interference between the pump and the probe, maximising to the vertical component of the FWM signal and minimising the horizontal part through the rotation of $\lambda/2$ and $\lambda/4$ waveplates.

3.5.7.2 FWM microscopy of fixed and live cells

After alignment, the sample was mounted onto the microscope stage. This was either a 100× magnification oil-immersion objective with a 1.45 NA (Nikon CFI Plan Apochromat lambda series) for fixed cell imaging, or a 60× magnification water-immersion objective with 1.27 NA (Nikon CFI Plan Apochromat lambda series) for live cell imaging. The laser power was adjusted and calibrated for each experiment using the AOMs. The nominal laser powers that were employed were measured before they entered the microscope port and are stated with each experiment within the figure descriptions. For orientation, a DIC image was recorded after imaging the area of interest in FWMi.

3.5.7.3 Regularisation

Subsequent to data acquisition, the FWM data was transformed into a format suitable for processing using the MultiCARS software. The FWM dataset includes both spatial and amplitude data across various scan channels: the x-axis scan channel, the y-axis scan channel, the amplitude channels of H and V REFL, H and V FWM^A, and the fluorescence channel. The acquired information is reformatted into a multi-dimensional Cartesian data cube. Each voxel within this cube, which is a three-dimensional equivalent of a pixel, represents a signal value in amplitude and phase, or equivalently as real and imaginary parts, for the FWM and reflected probe fields in 3D space. For example, an image is created by reading out the x and y value linked to an amplitude of either of the signal channels, such as REFL. After regularising, the data can be exported either as a bitmap or ASCII file for further analysis.

3.5.7.4 Image analysis of FWMi data

FWM^A data were utilised to generate false-colour overlays, combining FWM^A with brightfield images of the same FOV, allowing the analysis of GNP localisation. This image processing was conducted using the ImageJ software, where REFL data were displayed in grayscale. The scaling information of the presented mV ranges are stated with all figures in the main text. Z-stacks of FWM^A data were used to create maximum intensity projections (MIPs), which were further used in creating false-colour overlays that mapped the distribution of GNPs across the FOV in 2D.

For two-dimensional representations of z-depth, z-stacks of FWM^A data underwent temporal colour coding in ImageJ, utilising the “physics” LUT. The resulting RGB image was then either directly used as an image for analysis or it was superimposed with a REFL image of the same FOV by separating the RGB image into its constituent channels and superimposing them back

in their respective colour channels together with the brightfield image in greyscale for a more detailed analysis.

Orthogonal representations of z-stack data were created using the VolumeViewer Plugin¹¹⁷ within ImageJ. For better visualisation, the data was stretched in z by a factor of 5 with further settings at: Mode: Max Projection (2); Interpolation: Tricubic smooth (2); Sampling: 1.

To analyse tracks of particle movement, the Manual TrackMate Plugin¹²² was used. The GNP under study was marked on each frame within the plugin interface. From this information, the plugin generated the GNP track. The program was then used to plot particle displacement, speed, and mean intensity of the signal over time.

To determine the number of GNP signals/mm² within cells, z-stack frames at $z = 1.2 \mu\text{m}$ were selected. The area covered by cells was selected using the polygon selection tool within ImageJ and measured. The number of signals within the FOV was determined using the “Find Maxima” tool and the number of signals/mm² calculated. Subsequently, the $z = 0 \mu\text{m}$ of the same FOV was selected and the selection inverted, to determine the number of signals outside of cells per mm² in the same manner. This served to quantify off-target binding of GNP-TfA constructs.

4 Development of correlative extinction and fluorescence microscopy for ligand density quantification on GNPs

This chapter incorporates content that has been previously published in

N. Slesiona, L. Payne, I. Pope, P. Borri, W. Langbein, P. Watson, Correlative Extinction and Single Fluorophore Bleaching Microscopy for Ligand Quantification on Gold Nanoparticles. *Adv. Mater. Interfaces* 2023, 10, 2300568.⁹⁷

The figures and text presented herein are included as part of this comprehensive discussion. While the published paper provided a focussed analysis of the fully developed technique, the details within this chapter go deeper into the development of the techniques described, offering additional insights and elaborations beyond what was included in the journal article. As evidenced in the author contribution statement of the publication: I was responsible for the majority of the work, performed all experiments, acquired and analysed all data, compiled all figures, authored the initial and final draft, and managed all aspects of the writing process. This expanded exposition in the thesis aims to provide a more thorough and nuanced understanding of the research conducted.

The automated extinction and fluorescence analysis software Extinction Suite Macro (ESM) was written by Dr. Lukas Payne. Dr. Francesco Masia and Dr. George Zorinians developed the image transformation script (detailed in section 4.2.5). Transmission Electron Microscopy was conducted by Dr. Thomas Davies.

4.1 Introduction

The current standard for ligand quantification on GNPs relies on averaged estimations, typically calculating the total protein concentration of a sample and its average particle size. These parameters are used to calculate the average ligand density on GNPs of average size, and it is assumed that this density is consistent across all particles in the sample⁹⁹. At present, there is no method to evaluate the parameters quantifying a sample's polydispersity of NP size and number of ligands bound to the NP on a particle-by-particle basis. To draw educated conclusions from data derived from experiments where functionalised GNPs are used, it would be beneficial to develop a method that is capable of determining the level of particle crosslinking, the ligand density on a particle-by-particle basis, and the number of unconjugated construct constituents.

In this work, the quantification is realised by a correlative analysis of fluorescence and extinction microscopy images of GNP constructs, here using functionalised spherical GNPs decorated with human *holo*-Tf fluorescently labelled with TfA. The development of this technique will be detailed and data showcasing its functionality will be shown and discussed.

Fluorescence information and quantification of the number of fluorophores contributing to the fluorescence of a single TfA are obtained by image-based and time-resolved single molecule bleaching analysis. This is then used to quantify the number of TfA per GNP (Figure 4.1). Wide-field extinction microscopy allows the determination of the size and the estimated number of GNPs contributing to the extinction spots. Extinction microscopy is a method to quantitatively measure MNP sizes of hundreds of particles simultaneously using commonly available optical components. MNP sizes are then retrieved by an automated analysis, which allows a high-throughput characterisation of particles in the nanometre range^{113,120}. An image transformation software is used to create matching fluorescence and extinction images of the same area to analyse the co-occurrence of extinction and fluorescence signals. The analysis produces a quantifiable output in respect to the number of attached TfA per GNP, the fraction of successfully functionalised GNPs vs. unconjugated GNPs vs. free TfA in a sample, and the number of GNPs that have been crosslinked by the reaction procedure. The method is also capable of generating a measure for how many TfAs have been crosslinked without a GNP present in the aggregate. These aggregates might be misinterpreted as successfully internalised

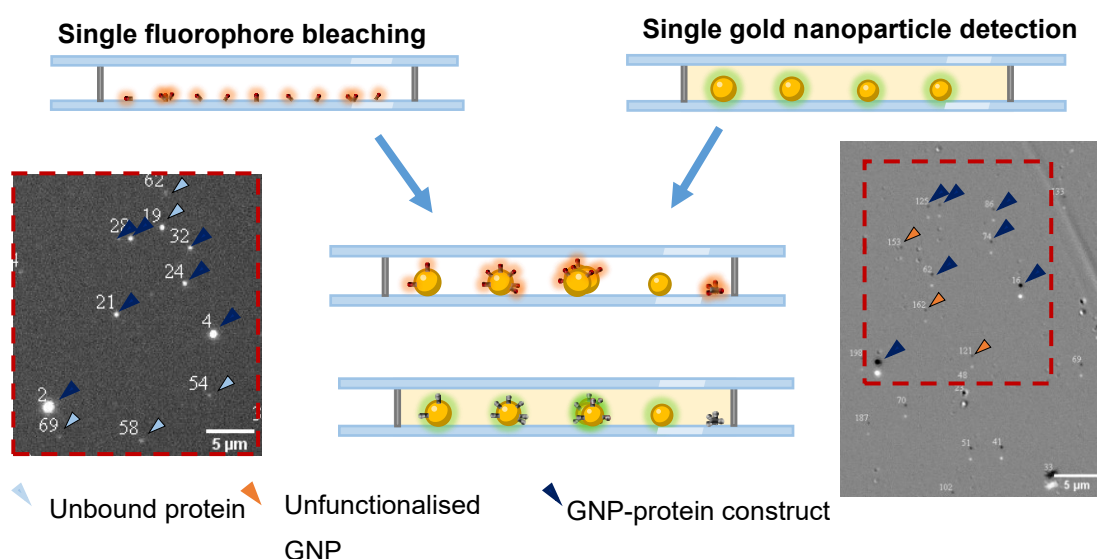


Figure 4.1 | Correlative Single Fluorophore Bleaching and Single GNP Detection for Ligand Quantification on GNPs. Schematic illustration of the procedure of correlative fluorophore bleaching and GNP detection. The figure contains a representation of (top left) a sample of fluorescently labelled proteins under fluorescent excitation and (top right) a sample of bare GNP subjected to extinction microscopy. When subjecting a sample of GNPs functionalised with such proteins to both imaging modalities, the ligand density of GNPs can be assessed at the single particle level.

particle-ligand constructs if only fluorescence-based microscopy measurements are utilised to detect their location. Our analysis overcomes these limitations and can provide information to guide the optimisation of the functionalisation reaction using for example different concentrations of ligands, cross-linkers, and particles.

4.2 Development

4.2.1 Hot pixel and background signal correction

In fluorescence microscopy, background signals play an important role in influencing the quality and interpretability of acquired images. Background signals may stem from non-specific light emissions that can obscure or distort fluorescence signals from labelled components of a sample. Imperfections in optical components can introduce stray light or scatter into the image as well. In the case of our experiments, the use of a 1.45 NA immersion oil objective for epi-fluorescence measurements can produce background signal by total internal reflection (TIR)^{123,124}. Hot pixels (HPs) are another phenomenon generating background signal that does not originate from the sample but from the camera sensor itself¹²⁵. These are pixels that give a higher readout than they should in relation to the photons that reach it and can create bright spots in an image where there should be no signal above the noise.

The extent of these background phenomena within the generated data on the microscope equipment used for this work was tested. For this, a spin-coated sample of TfA was measured on an epi-fluorescence microscopy set-up. The data was analysed using an analysis software called ESM^{113,118} (refer to Section 3.2.1 for more information), written and developed by Dr. Lukas Payne, to extract the fluorescence intensity of individual spots, spatially summed over the PSF either from a single frame or from an image stack (z-stack or time-lapse). The software aids with identifying signals originating from the fluorescent label on TfA, assigns each signal with an ID number, and provides a table of signal intensities of the individual signals for further evaluation. As visible in Figure 4.2A and B, which show fluorescence images of spin coated TfA proteins, HPs caused a significant issue in our experiments.

After analysing the data using ESM, it was observed that a lot of HPs (see signal IDs 109, 23, 144, 43) can be observed alongside TfA fluorescence (see signal IDs 55, 142, 37), hampering the automated analysis (Figure 4.2C and D). ESM has a built in in-band spatial frequency filter that is designed to dismiss such HPs, but it was not able to pick up the HPs as fast spatial frequencies to filter out during evaluation. In microscopy, fast spatial frequencies correspond to very fine details or edges within an image, with rapid intensity changes over small spatial areas (such as between two pixels where one is a HP and the other is background noise). HPs

appear as such high-frequency components due to their sharp contrast against the surrounding area¹²⁵. Therefore, ESM should be able to identify these HPs, but it was not for these data sets. The reason for this was likely that the HPs appeared pairwise in the images, giving the HPs an assumed PSF. This caused the evaluation software to analyse the HPs as signals, crowding the evaluation plots with unusable data points.

The main problem with HPs in the images was that the evaluation software uses a proximity filter to exclude signals that are too close to one another^{118,120}. This filter was implemented to account for background signals and requires sufficient space around each signal to ensure accurate analysis. When signals are too close, the software dismisses them to avoid false readouts. The high number of HPs in the data led to the exclusion of many valid fluorescence signals, compromising the accuracy of single fluorophore bleaching experiments. To address this, careful equipment selection and post-acquisition image processing were essential. To allow faster processing and analysis of future GNP-TfA samples, two different image correction

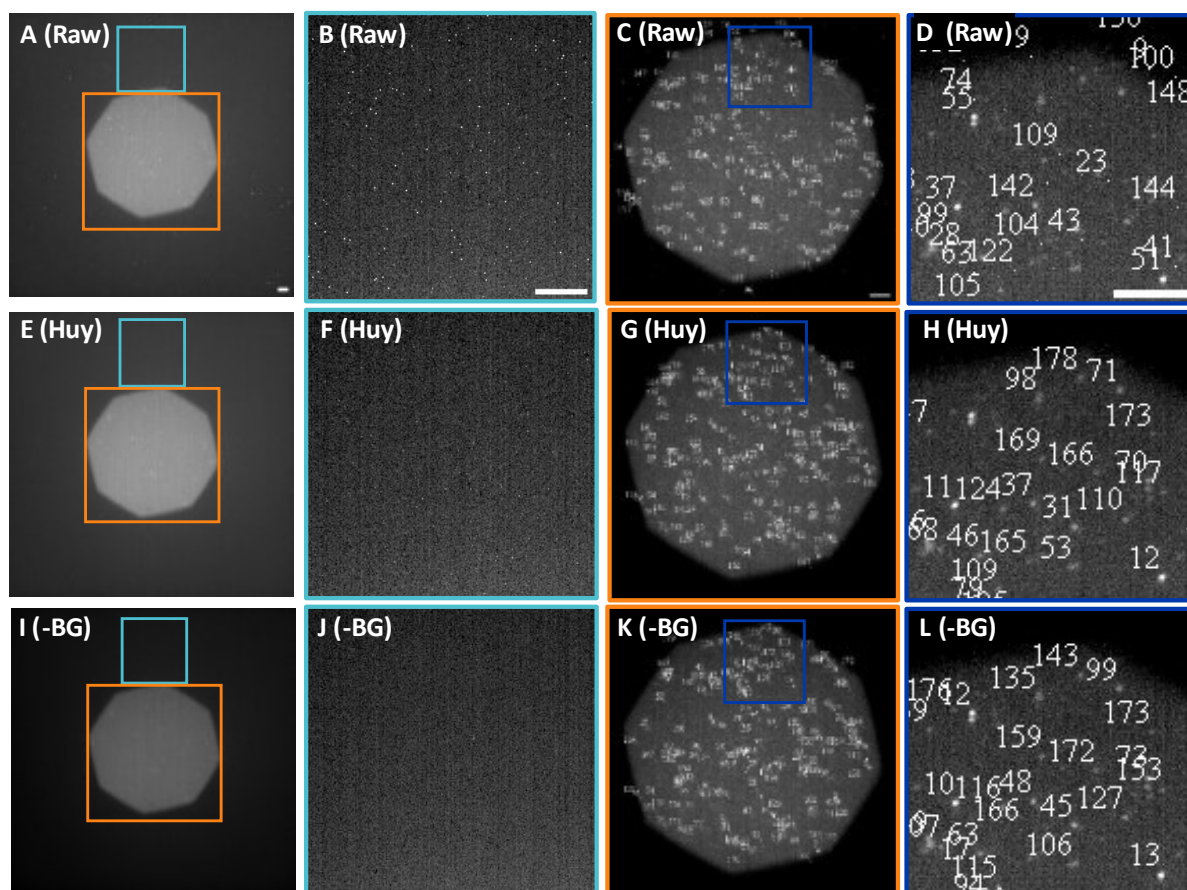


Figure 4.2 | Comparative Background Correction. Epi-fluorescence images of a glass slide with spin-coated TfA show significant amounts of HPs. This figure shows attempts at corrections by different background correction techniques. To ensure uniformity in comparison, all corrections were performed on an identical dataset. (A-D) Raw epi-fluorescence data. (E-H) Data after HP correction using the Huygens software (Huy)) and (I-L) after dark current subtraction (-BG). The regions highlighted in light blue within panels A, E, and I are magnified in B, F and J, highlighting the presence of HPs. Scale bars: 5 μm .

methodologies were tested to eliminate the HPs. This included the built-in HP correction of Huygens Software (Scientific Volume Imaging) and dark sensor subtraction.

The Huygens software uses an algorithm to identify HPs. This is easiest with data sets of multiple frames as the HPs are likely to appear at the exact same spot for every frame, showing up as “hot columns” in XZ projections. The software replaces hot columns with the median of their nearest neighbours. The images in Figure 4.2E and F have been corrected using the Huygens software. The number of HPs is largely reduced, though some bright spots are still visible, but they did not seem to negatively impact the automated analysis (Figure 4.2G and H). Prior to BG correction more than two thirds of all signals identified by ESM were HPs (Table 4.1). Image processing with the Huygens Software led to a significant reduction of HPs and an increase of correctly identified fluorescent signals by 342.3% (52 compared to 178). Given that not all details of Huygens’ algorithm are published, further post-acquisition correction methods were developed to allow for more control and knowledge about the processing the acquired data is subjected to.

Table 4.1 | Analysis of BG Corrected Images.

The table delineates the fluorescence signals detected by ESM after HP correction using Huygens and BG subtraction, by showing the number of detected signals, of evaluated HPs and correctly identified signals.

Correction Method	# of detected signals	# of eval. HP	# of correctly identif. sigals
None (raw)	158	106	52
Huygens	182	4	178
BG subtract	179	8	171

Therefore, a more commonly used method of BG correction was tested, namely that of dark sensor subtraction. Dark sensor subtraction involves acquiring an image with the same acquisition settings as the actual data but without fluorescence excitation. The resulting image is then subtracted from the actual fluorescence data, which should eliminate the HPs. As mentioned above, HPs are a sensor defect that is pixel specific and, therefore, HPs should appear at the same spots in the dark sensor image as in the acquired fluorescence data. The advantage of this approach is that there is no further alteration to the data than simple subtraction. The results of this BG correction are visible in Figure 4.2I-L and Table 4.1. Visually, dark sensor image subtraction was indistinguishable from the Huygens correction software and resulted in a similarly good identification of fluorescence signals with 171 accurately identified fluorophores (see Table 4.1). Given the ease of operation and reduced raw data modification, dark sensor subtraction was deemed the most suitable correction method moving forward.

4.2.2 Choice of the experimental numerical aperture

In order to reduce background caused by TIR, the previously used 1.4 NA 100x oil objective was replaced by an oil objective with 100x magnification and an adjustable NA. TIR occurs when a light beam that travels through a medium with a higher refractive index hits the boundary with a medium of lower refractive index at an angle greater than the critical angle, leading to the light being reflected back into the original medium instead of refracting through the boundary. The critical angle θ_c is defined by:

$$\theta_c = \arcsin\left(\frac{n_2}{n_1}\right)$$

where n_1 and n_2 are the refractive indices of the denser and the less dense medium, respectively, with $n_1 > n_2$ ¹²⁶. While being an unwanted artefact for this experiment, there are imaging set ups, such as total internal reflection fluorescence microscopy, that use this principle to selectively excite fluorophores near a surface, leading to minimised background and enhanced resolution of specimens close to an interface¹²⁴.

To determine the optimal NA for bleaching experiments, an adjustable NA oil objective was tested at different NA settings to discern the effects of lower and higher NA settings when otherwise using the same optical components and acquisition settings. For this, a H₂O₂-cleaned coverslip was marked using a black felt-tip marker for measurements on an epi-fluorescence setup and measurements performed at 0.6, 0.95 and 1.3 NA. The highlighter pen's fluorescence was used to compare the relative background and signal intensities to emphasise the achieved signal to noise (SNR) at different NA settings. The highlighter fluorescence served as a well-defined, uniform source, allowing for consistent evaluation of signal intensities and background levels under different imaging conditions. To mitigate the impact of bleaching in the imaged area, measurements were conducted across different regions along the marked trajectory. For consistency, images were captured using identical settings (3 sec integration time, utilising the same filter set used for TfA measurements), with a partially closed microscope aperture, and ensuring the marked region occupied approximately half of the FOV (Figure 4.3A-C). This would, in theory, allow to distinguish up to three groups of signal intensities: signals originating from inside aperture background (the part of the FOV not blocked by the closed aperture), outside aperture-background (the part of the FOV blocked by the closed aperture), and the signal (the area within the FOV marked with a fluorescent identification label).

An NA setting of 1.3 yielded a strongly visible signal from the marker, the non-marked area and the aperture-blocked area (Figure 4.3A). To compare these signal intensities, the grey value

distribution of all pixels was plotted for each image, respectively (Figure 4.3D-F). This resulted in three distinct peaks in the image's grey value distribution: at 20.4, 33.9, and 119.5 photoelectrons per second (pe sec^{-1}) according to multiple peak fit analysis. These peaks are indicative of two sources of background (inside and outside aperture), and the signal from the marker line.

The source of background light in these measurements likely includes bleed-through of reflected (TIR) illumination light into the detection path. The bleed-through of reflected illumination light (inside aperture background) likely arises from incomplete blocking by the emission filters. Conversely, the distribution from the measurement of the same sample obtained at 0.95 NA (Figure 4.3B) shows two distinguishable peaks at 15.9 and 40.3 pe sec^{-1} , respectively (Figure 4.3E). The image acquired with 0.6 NA shows no sufficient signal (Figure 4.3C), which is visible within the distribution of signal intensities in Figure 4.3F. The

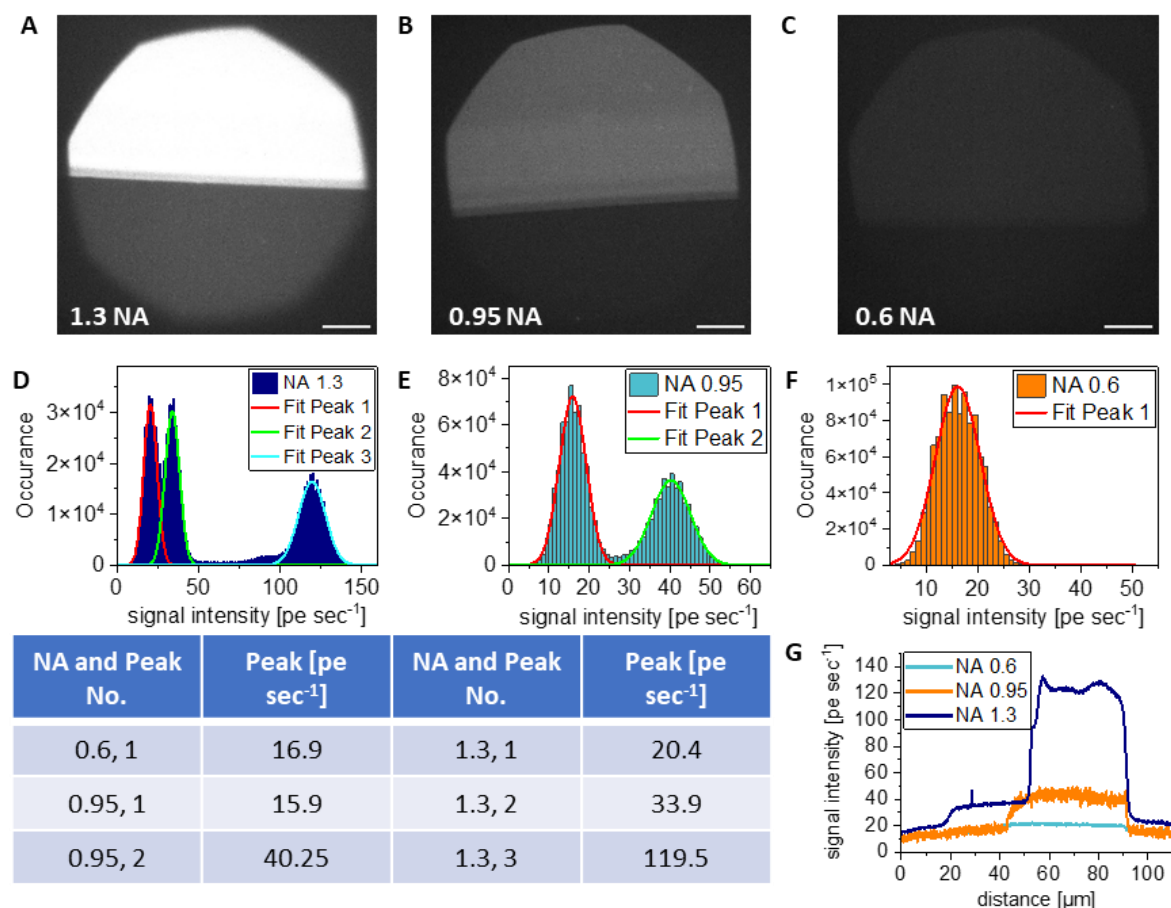


Figure 4.3 | Calibration of NA for Single Fluorophore Bleaching. The images depict the calibration of the objective NA to minimise background caused by TIR. Panels A-C depict fluorescence measurements of a coverslip marked with a felt tip marker acquired with (A) 1.3 NA, (B) 0.95 NA, and (C) 0.6 NA. All images in (A-C) are scaled the same ($m = 0, M = 110 \text{ pe sec}^{-1}$). Histograms in (D-G) reflect the distribution of fluorescence intensity values of all pixels of the corresponding fluorescence images acquired with (D) 1.3 NA, (E) 0.95 NA, and (F) 0.6 NA including a multi peak fit analysis. The table in (G) gives information about the peak centres of the histogram peak fits. The plots in (H) depict the fluorescence intensity value along the lower left corner to the upper right corner of each fluorescence image. Scale bars: 20 μm .

distribution shows a single peak, centred at 16.9 pe sec^{-1} without a second peak, suggesting a lack of sufficient light collection capabilities of the objective with the employed acquisition settings.

Figure 4.3A (and D) demonstrate a notable improvement in signal peak separation from background fluorescence at an NA of 1.3 (in TIRF mode) with an SNR of 3.5 (inside aperture background vs. signal peak) compared to epifluorescence (NA below 1) with an SNR of 2.5 (background peak vs. signal peak). To mitigate this issue, additional optical filters, such as a notch filter designed to block the specific wavelength of the illumination light, could be incorporated into the setup. This would further suppress the background contribution from reflected illumination, potentially improving SNR. The findings highlight the importance of carefully considering the interplay between illumination, emission filtering, and background contributions when optimising imaging conditions.

While TIRF microscopy generally has a better SNR, the bleed-through of reflected illumination light must be addressed to fully exploit its advantages. Based on the results presented, an NA setting of 0.95 was chosen for subsequent experiments, as this setting minimised background noise while maintaining adequate signal intensity. In all following experiments, the intensity of the excitation light was normalised by measuring a fluorescent test slide, adjusting the lamp intensity to an average signal of 50,000 counts (76% sensor saturation) at 50 ms exposure time at the start of each measurement day to ensure consistency.

4.2.3 Bleaching step sizes of Alexa647

To test the development for single fluorophore bleaching thus far, a spin-coated sample of TfA was measured on a wide-field microscope in epifluorescence using an NA of 0.95. The resulting data was background corrected by dark current subtraction and then analysed using ESM. The fluorescence intensity over time was measured to determine the mean bleaching step size I_B of Alexa647 on Tf. ESM allows for such timelapse analyses, providing signal intensity over time information for each identified signal. To determine the intensity level of each bleaching step, the fluorescence values within a single intensity plateau were averaged. The bleaching step size was then subsequently calculated by subtracting the averaged intensity level of one bleaching plateau by the subsequent plateau value. The mean photobleaching step size I_B allows to calculate the number N_F of fluorophores per TfA or GNP-TfA construct, by dividing the fluorescence intensity $I(t_0)$ detected for an individual spot in the image at the initial time point t_0 in the fluorescence intensity over time sequence by I_B , so that

$$N_F = \frac{I(t_0)}{I_B} \quad (4.1)$$

Figure 4.4A shows an exemplary intensity-over-time profile resulting from the photobleaching experiments, which reveals distinct photobleaching steps that are quantified in Figure 4.4B. For a visual representation, the individual time points in B are depicted in Figure 4.4C and D (signal ID 34). The background signal intensity at the final time point was measured at a negligible 1.6 pe sec^{-1} , underlining the validity of the BG correction method. A closer examination of the I_B s shows the following values: $193.9 \text{ pe sec}^{-1}$, $164.1 \text{ pe sec}^{-1}$, $122.1 \text{ pe sec}^{-1}$, and $134.7 \text{ pe sec}^{-1}$. These values show strong variability and do not remain constant. The variability in noise within photobleaching traces complicates the accurate identification of steps and their positions. Noise fluctuates unpredictably with changes in the number of active fluorophores as reported by Tsekouras *et al.*¹²⁷ Such variations in single fluorophore intensities have been documented in past research by other groups¹²⁸ and have more recently been quantified by Steen *et al.*, where their study demonstrated that individual Alexa647 dye molecules emit an average of $10,348 \pm 1,358$ photons per 100 ms ¹²⁹. This was achieved by immobilizing single dye molecules on DNA origami structures to ensure that measurements reflected the emission from individual fluorophores rather than potential clusters. Incorporating an approach to determine the number of fluorophores per protein using single-molecule immobilisation on DNA origami

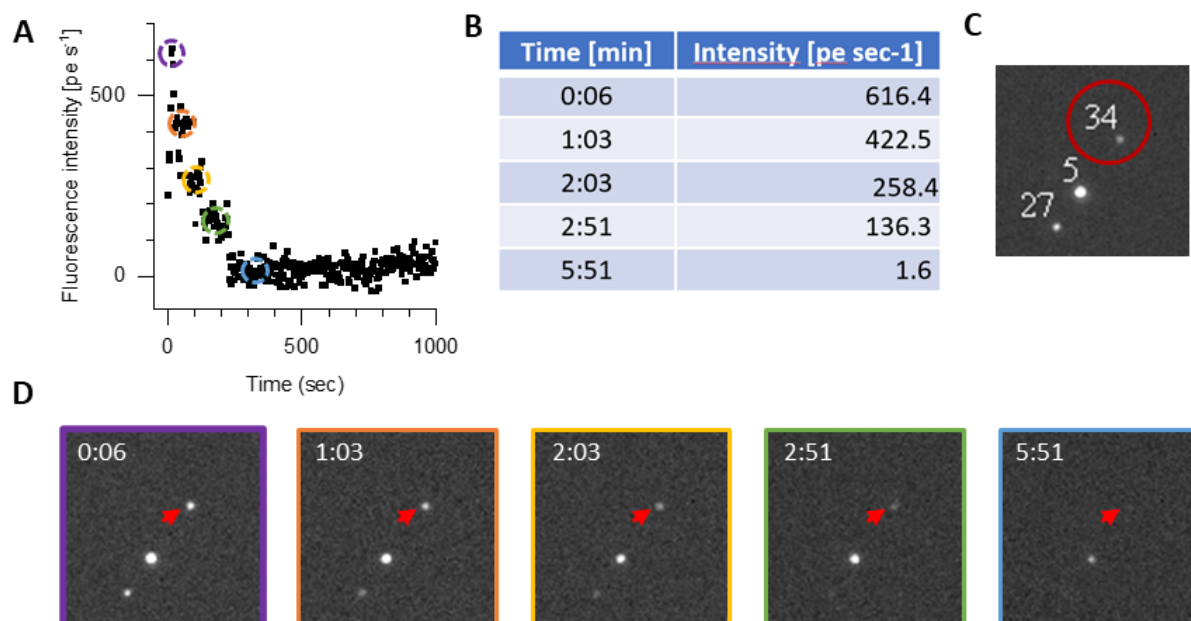


Figure 4.4 | Bleaching Events of TfA Proteins. The figure depicts an imaging session of fluorescence intensity over time to identify bleaching step sizes of individual TfA using an inverted widefield fluorescence microscope. (A) Fluorescence intensity over time of an exemplary TfA molecule showing steps of photobleaching. (B) Table of fluorescence intensities at specific time points of of this TfA molecule as analysed by ESM. (C) Fluorescence image of the analysed TfA molecule (ID 34). (D) Fluorescence image of the fluorescence intensity at the time intervals detailed in (B).

would have been a valuable enhancement to this project as well. This method ensures that an individual protein is being analysed. By taking advantage of the precise spatial control offered by DNA origami, this approach would provide accurate quantification of fluorophores per protein, significantly improving the reliability and clarity of the results.

Another potential reason for this variability may include the influence of the local electronic environment the fluorophore is subjected to (i.e. what residue the fluorophore is attached to and therefore its surrounding residues) and the orientation of the fluorophore within the illumination path^{132,133}. Additionally, fluorophores can undergo blinking where they intermittently enter a non-fluorescent state at random time intervals and frequency¹³⁴. The variable frequency and duration of these states in combination with a long exposure time (here 3 sec) can lead to variations in the total intensity measured over the applied integration time. Furthermore, in experiments where polarised light is used, a possible explanation for this variability is Förster Resonance Energy Transfer (FRET). FRET is a distance-dependent process where energy is transferred non-radiatively from an excited donor fluorophore to an acceptor via dipole–dipole coupling over a range of 1–10 nm. It typically occurs between spectroscopically distinct fluorophores (heteroFRET) but can also occur between identical fluorophores with a small separation between their spectral excitation and emission peaks (homoFRET)¹³⁰. The process affects spectroscopic properties such as fluorescence intensity, lifetime, and quantum efficiency, providing valuable information about molecular interactions¹³¹. However, since homo-FRET occurs under polarised illumination, it cannot be considered in this set of experiments, as no polarisers were used.

To further investigate this phenomenon, the I_B s of Alexa647 attached to TfA were examined across multiple FOVs. Additionally, the I_B values of TfA conjugated to a GNP were examined to determine if the presence of the GNP had an influence on the signal intensities of the fluorophore. The measurements revealed a substantial variability of I_B values, as shown in Figure 4.5. Unconjugated TfA showed a mean I_B of 150 ± 79 pe sec⁻¹, and GNP-TfA a mean I_B of 142 ± 48 pe sec⁻¹. Combined populations resulted in a mean I_B of 146 pe sec⁻¹, which was used in the following analyses. It should be noted that plasmonic NP are known to alter fluorescence intensity depending on the distance of the fluorophore to the NP¹³⁵. Fluorophore quenching has been shown to affect a fluorophore to a distance of up to 15 nm for GNP of 10 nm diameter with a steep decrease in its effects the larger the distance between fluorophore and GNP¹³⁶. For this reason, the I_B was assessed for TfA associated with a GNP, though no such quenching was apparent within the data.

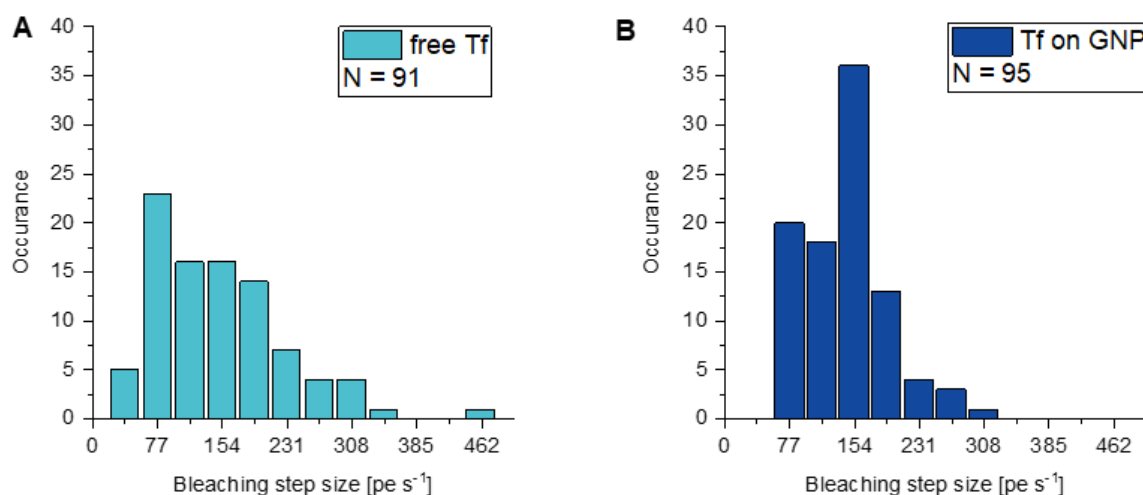


Figure 4.5 | Bleaching Step Sizes of Alexa 647. Histograms of bleaching step sizes I_B of Alexa 647 attached to (A) free Tf and (B) Tf conjugated to GNPs (GNP-Tf) to determine whether the presence of a GNP in close vicinity to the fluorophore has an influence on fluorophore intensity and its bleaching step size. Tf showed a I_B of 150 ± 79 photo-electrons per second (pe s^{-1}) (mean \pm standard deviation), and GNP-Tf of $142 \pm 48 \text{ pe s}^{-1}$. Bin size: 77 pe sec^{-1} . [Figure and description from Slesiona *et al.*⁹²]

The GNPs utilised in these experiments came with a proprietary polymer corona to stabilise them against aggregation in cellular environments for *in vitro* applications, that may prevent or reduce fluorophore quenching due to the GNP. The exact nature of this polymer is not disclosed by the vendor but general *in vitro* studies of GNP make use of PEGylation at molecular weights of 500-5000 kDa, resulting in a polymer thickness of 4-16 nm^{75,137}. In addition to the polymer thickness, the protein may act as a spacer between the polymer coating and the fluorophore, adding up to 4 nm distance¹³⁸ depending on how TfA attaches to the polymer and the location of the fluorophore on TfA. The resulting total distance of 8-20 nm from the GNP may limit the effect of quenching on the detected intensities. Additionally, excitation rates are also affected and in general enhanced in the vicinity of GNPs due to an enhanced local electric field¹³⁹. While it is somewhat surprising that the observed I_B s are similar for free TfA and GNP-TfA, it is possible within our mechanistic understanding.

4.2.4 Optimisation of extinction measurements for correlation with fluorescence microscopy

The extinction cross-section of a molecule or particle quantifies how effectively it absorbs or scatters light at a specific wavelength. It represents the effective area a particle presents to an incoming light beam, and determines the total light removed from the incident light¹⁴⁰. For NPs, particularly MNPs with strong scattering cross-sections, the extinction cross-section is a key parameter for characterisation. This parameter is especially effective to determine the size of

NPs with dimensions comparable to or smaller than the wavelength of visible light, where diffraction effects dominate¹⁰⁹.

Extinction microscopy is used to detect and size NPs in the nanometre range by calculating the extinction cross section from transmission images captured through wide-field microscopy¹¹³. A sample of spin-coated and thus immobilised NPs is imaged at two slightly shifted positions, referred to as the signal and reference positions. These positions differ by a small lateral shift of a few micrometres. Differential transmission images are created by averaging thousands of frames per position and subtracting one from the other, producing images where each particle appears as a paired intensity drop (black spot) and peak (white spot), due to the shifted reference method, creating an image as visible in Figure 4.6 (orange arrow). The high number of frames used to produce the differential image allows for effective background subtraction, enabling individual measurements to be analysed without requiring calibration samples¹²⁰. ESM can then be used to analyse the FOV and determine the size of each individual MNP quantitatively by comparing the measured extinction cross section to theoretical models. ESM has been benchmarked against TEM imaging and developed within the group, with acquisition parameters tailored to achieve high sensitivity and reproducibility. For further details, refer to previous work conducted within the group^{113,120,141}.

In extinction microscopy, the presence of even the smallest impurities on glassware can generate significant signals, hampering differentiation from genuine GNP signals. Despite employing H₂O₂-cleaned glassware, the presence of surface contaminants is nearly impossible to prevent. These impurities will affect accurate differentiation between GNPs and background signals during evaluation of the resulting data with ESM, similar to HPs in fluorescence data. The presence of surface impurities can trigger the proximity restriction implemented within the software, causing genuine GNP signals to be discarded from analysis. To address this, a method for differentiation based on the optical behaviour of signals across multiple z-planes has been developed. Specifically, genuine GNP signals typically blur when imaged below their precise z-position and diminish in intensity above it, as demonstrated in Figure 4.6. Conversely, impurities are identified by a unique 'contrast flipping point' – a reversal in signal contrast from black to white when imaged at a z-plane transition from below to above the impurity. This optical characteristic is a robust measure for distinguishing between dielectric debris and actual GNPs to reliably discard non-valid datapoints from analysis. Nonetheless, the distinction of debris against GNP is done by manually scanning through the data, which considerably extends the time needed for analysis. Therefore, adopting an H₂O₂ cleaning protocol for all microscopy glassware is highly recommended to reduce the number of such impurities significantly.

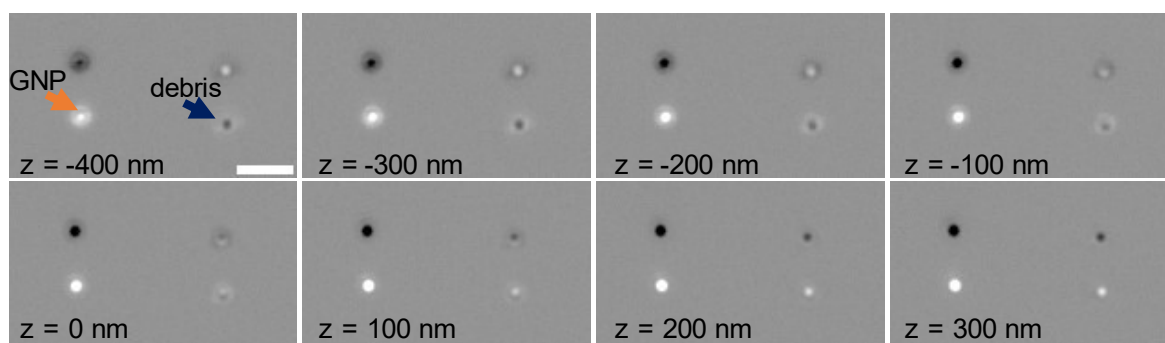


Figure 4.6 | Utilising Z-Measurements to Differentiate Between GNPs and Debris. This figure demonstrates the use of z-stacks in extinction data acquisition to differentiate GNPs (orange arrow) from debris (blue arrow). The displayed images show a series of z-planes, ranging from -400 nm to +300 nm relative to the sample surface. The GNP exhibits either blurring or a reduction in intensity across these z-planes. In contrast, the debris signal is characterised by a notable inversion point of black and white values when the imaging plane traverses from below the sample surface to above, observable between the -100 nm and +100 nm frames. This specific flipping behaviour serves as a reliable criterion to distinguish between GNPs and debris particles in extinction microscopy.

4.2.5 Development of a sample substrate for correlative measurements and oil injection

Extinction and fluorescence bleaching studies are conducted on two separate microscopes with different stages, sensor sizes, and magnifications. After fluorophore bleaching, the sample was dismantled from the fluorescence microscope and mounted onto the extinction microscopy set-up. In the absence of distinguishable markers on the sample, the primary challenge was that transitioning the sample between the two microscopes introduced uncertainties when trying to identify the exact regions that were previously subjected to bleaching (Figure 4.7A). To solve this, the glass cover slip was scratched using a diamond pen prior to spin coating to create a marker layout reminiscent of a targeting crosshair (Figure 4.7B). Following the spin-coating procedure with bare GNPs, the marked cover slip was attached to a glass slide using an adhesive gasket. Initial extinction measurements revealed an extensive number of signals from surface irregularities, as depicted in Figure 4.7C. Likely, these stem from an uneven glass substrate surface, as well as small impurities or imperfections in the glass. The number of these additional signals complicated the differentiation between GNPs and non-particles and rendered the use of ESM for automated analysis impossible.

To address this issue, it was hypothesised that the introducing index-matched oil could mitigate the problem by filling any surface irregularities. Such surface irregularities are marked in the zoomed areas of Figure 4.7C and E. These circular structures could be small pockets in the glass surface filled with air that vanish when filled with index-matched oil. Therefore, the adhesive gasket was modified to create a channel, to allow for a controlled infusion of oil after fluorophore bleaching (Figure 4.7D). It was necessary to allow the injection after the bleaching

Development of correlative extinction and fluorescence microscopy for ligand density quantification on GNPs - Development experiments, as the oil would introduce a significant amount of background signal in fluorescence measurements. There was substantial improvement and reduction of unwanted signals as visible in Figure 4.7E, permitting future use of automated analysis using ESM. Four FOVs on four different samples were examined by extinction in both air and oil to establish that the oil infusion did not lead to particle displacement, which would obstruct subsequent correlative analyses and no such particle displacement was evident. GNP signals have been marked by blue dotted circles within Figure 4.7C and E to show that GNPs remained at the same position after oil injection.

The scratches allowed for correlative measurements between the two microscopes as the crosshair design allowed for identification of the same location based on the geometry of the shape of the scratch and oil injection worked well by capillary effects.

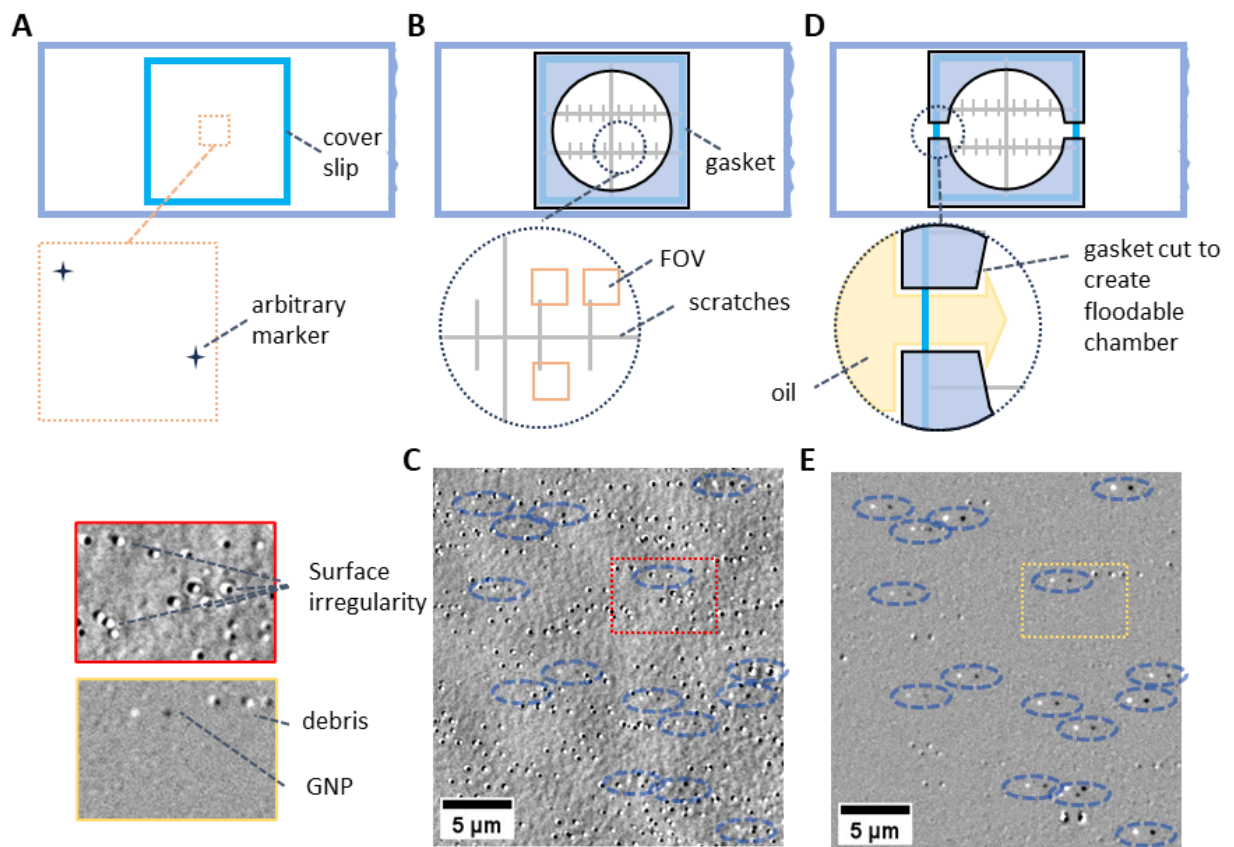


Figure 4.7 | Sample Preparation for Correlative Measurements on Different Setups. (A) Correlative measurements of fluorescence and extinction were originally conducted by identifying arbitrary markers on the sample surface. (B) Scratches were introduced to aid with identifying the same region on a sample repeatedly and reliably. (C) Exemplary extinction measurement in air showing extensive background signals. (D) The adherent gasket used to glue the sample cover slips onto the glass slide was cut to allow oil injection after fluorescence measurements. (E) Extinction measurement in oil of the same region as shown in (C) show markedly reduced background signals. Zoomed areas of C and E show surface irregularities (vanish after addition of oil), debris, and GNP.

4.2.6 Image transformation for correlation analysis

Mounting the samples onto different microscope stages introduces tilt, distortion, and rotation to the two different data sets, which were minimised by utilising the above-described scratched coverslip. Nonetheless, to allow superposition and correlative analysis of data sets of single GNPs and fluorescently labelled proteins, a precise image transformation was necessary to ensure signal overlap. To resolve these spatial discrepancies, a MATLAB script was used that was written within the group to transform one of the images. It works based on the registration of pre-entered common features in two images and returns the parameters of a transformation matrix together with a transformed image that can be overlapped with its reference for correlation analysis, as schematically shown in Figure 4.8. The script includes a vector-based image transformation software that can be used to produce images that can be colour-merged for correlation analysis. The details of this transformation software are further explained in Section 3.5.6. Following the optimisation for correlative analysis, a proof-of-concept measurement was conducted to show the capability of this method to produce data sets of fluorescence and extinction that can be overlapped with one another for further analysis.

20 nm GNPs were functionalised with TfA and spin coated onto a coverslip. The sample was measured in both fluorescence (Figure 4.9A), followed by extinction (Figure 4.9B). The data sets were then evaluated using ESM separately and then the extinction image was transformed to spatially correlate the signals to one another.

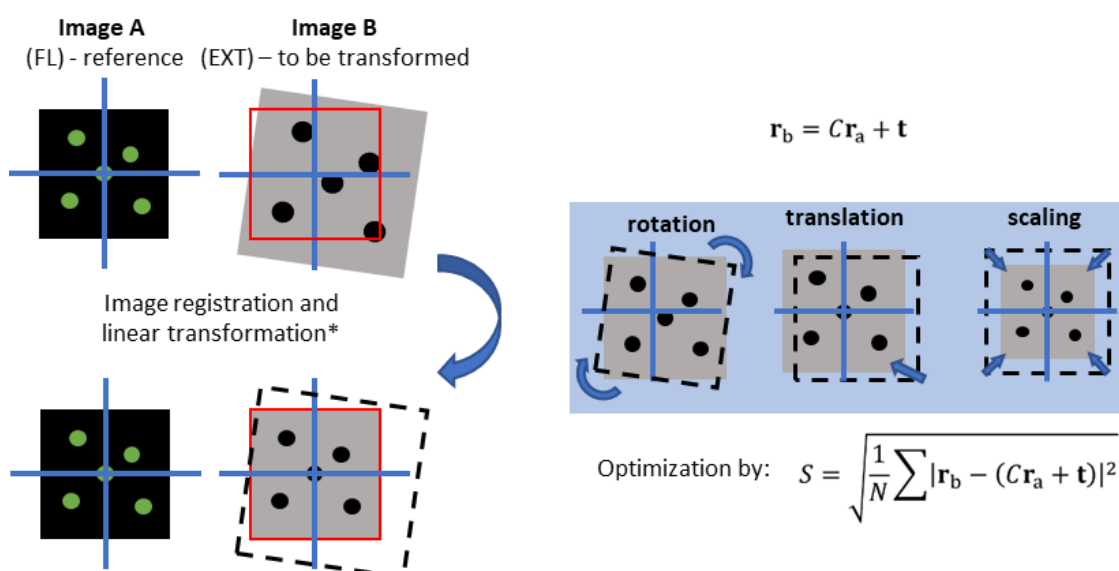


Figure 4.8 | Schematic Illustration of the Image Transformation. Visual representation of the mathematical procedure during image transformation. The software works based on a user input of the xy coordinates of at least three common features in the reference image and the image to be transformed, denoted r_a and r_b . The software calculates a transformation matrix C (rotation, shear, and scaling) including the parameter t (translation vector) and also generates the transformed image. The fit is optimised by minimising the standard deviation between r_a and r_b .

Subsequently, the extinction data was transformed using the transformation software (Figure 4.9C) using the coordinates of fluorescence and extinction as common features as highlighted in Figure 4.9A and B. The transformation software yields the computed values of the function, as detailed in Table 4.2. Error S, a measure to qualify the goodness of the transformation (0 = perfect alignment, 1 = poor alignment), was calculated to be $8E-14$, demonstrating a perfect alignment of this dataset. To achieve the alignment of the data set shown here, a translation of -187.5 pixels in the y-axis and 0.05 pixels in the x-axis was necessary. These values may vary between measurement areas depending on how well the same area was centred when finding the same area on both set ups with the help of the scratched markings. The extinction image was scaled by the image transformation, effectively halving its size by a factor of 0.497 in the

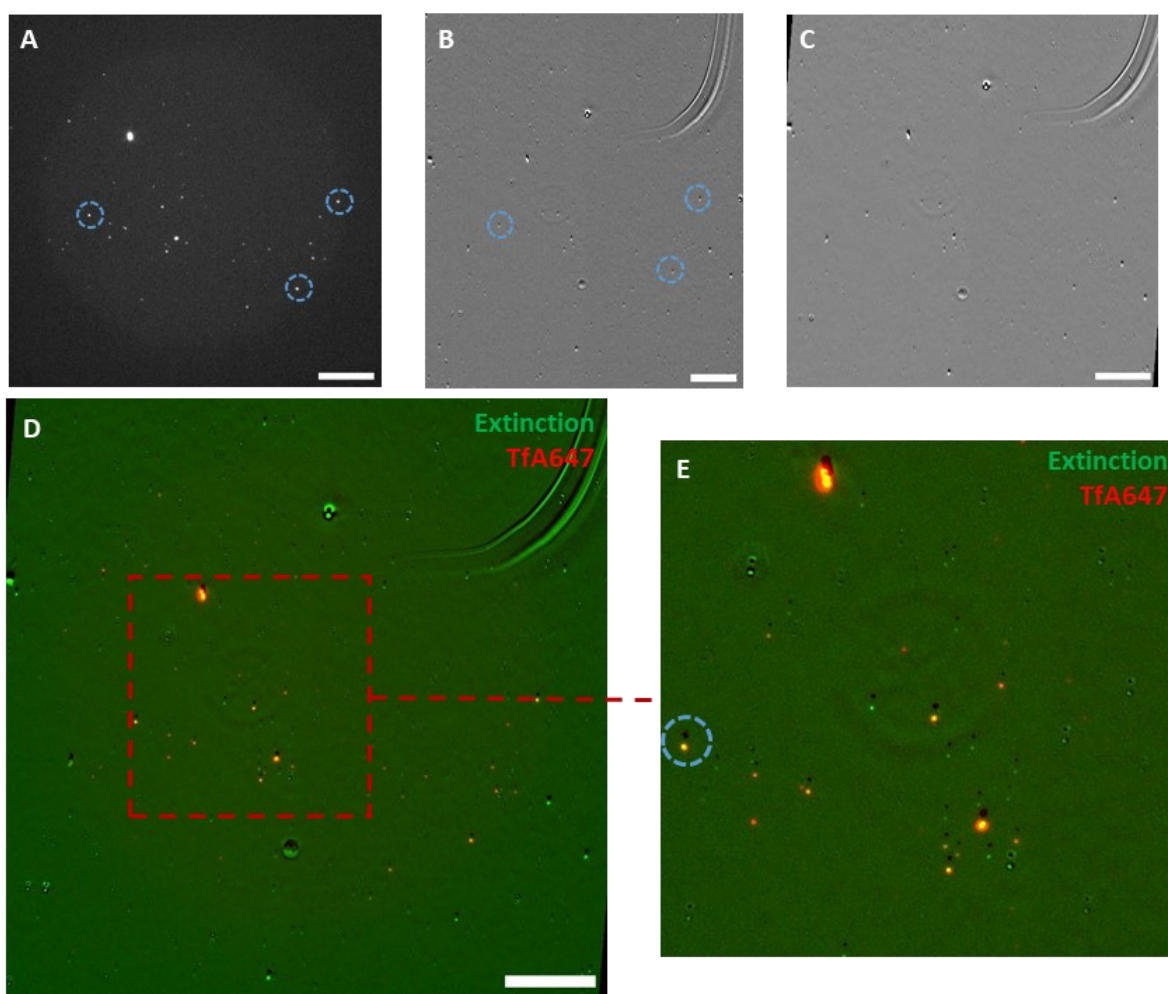


Figure 4.9 | Workflow of Image Transformation of Pre-Registered Common Features in Two Images. (A) The reference image, a frame from a fluorescence bleaching experiment (fluorescence, FL) of spin-coated GNP-Tf constructs, displays three fluorescence signals (blue circles) used to calculate the transformation parameters required for alignment. (B) The extinction image (EXT), acquired at the same sample position identified by visible scratches, shows the fluorescently labelled GNPs, also marked by blue circles. (C) The transformed extinction image, after the calculated transformation parameters have been applied, is aligned with the fluorescence image. (D) False-colour overlay of the fluorescence image (red) and the transformed extinction image (green). (E) A zoomed view of the overlay in (D) reveals matching fluorescence and extinction signal patterns, confirming the successful transformation and alignment. This enables the evaluation of the number of successfully functionalised GNPs. Scale bars: 20 μm .

x-axis and a factor of 0.496 in the y-axis. The FOV of both images is similar in size visually, but fluorescence images were acquired with a 2x2 pixel binning while the extinction data was not binned. Pixel binning was applied during fluorescence imaging to minimise the size of the resulting datasets. The acquisition times of bleaching experiments extended until all fluorescence signals within the FOV were photobleached, with one image

Table 4.2 | Parameters Of Image Transformation. The table details the parameters calculated by the transformation values. The meaning of each parameter is detail in the main text.

Parameter	Value
Error S	0.000000
x coordinates of the translation vectors	-187.511
y coordinates of the translation vectors	0.041
scale x	0.497
scale y	0.496
angle x	4.434
angle y	94.715
Real parts of of matrix C eigenvectors	0.495
	0.495
Imaginary parts of of matrix C eigenvectors	0.039
	-0.039
Determinant of matrix C	0.247
chi	1

captured every three seconds. Some datasets required acquisition times of up to 3 hours, resulting in exceedingly large data files that posed challenges during analysis. To mitigate this issue and reduce the data size, 2×2 pixel binning was implemented. Therefore, scaling values close to 0.5 were expected.

The angle parameters describe the rotation between the two images. Within the data sets generated during this project only a small degree of rotation needed to be applied to realise the fit conditions. The values for this specific field of view were $x = 4.4^\circ$ and $y = 4.7^\circ$. Within the project, these parameters did not fluctuate for scaling, and only showed a variation of up to 2% for the rotation.

The eigenvectors can be looked at to provide additional insights into the transformation, indicating a slight scaling effect (real parts: 0.495) along with a minor rotational component (imaginary parts: 0.039 and -0.039). The determinant of matrix C serves as an internal calculation factor needed to validate the user's input of xy-coordinates. If the input consists of more than three coordinates, it results in an overdetermined linear system. In such cases, the software calculates the coefficients C and t by least squares (refer to Figure 4.8 for the equation). The determinant, in this scenario, would equate to 0, with $Error\ S \neq 0$. Lastly, the parameter χ informs the user about the sign of the determinant. A value of 1 signifies that both coordinate systems are aligned. Conversely, a value of -1 implies a mirror flip in one of the images.

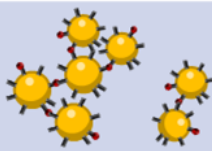
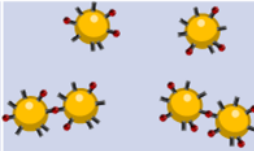
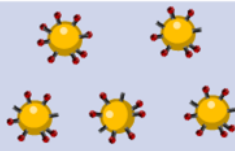
Overlaying the transformed extinction data with the fluorescence image reveals clearly visible correlation of fluorophore and GNP signals discernible as yellow signals resulting from superimposed green signal from extinction (GNPs) and red fluorescence signals (Figure 4.9D and E).

At this stage, the developmental phase for correlative analysis was deemed advanced enough to continue with a more elaborate experiment to fully compare the capabilities of this method that would allow a rigid testing of its limitations and advantages. In summary, the effect of background signals was minimised to optimise the evaluation of fluorescence intensity and bleaching dynamics. Additionally, a sample preparation workflow was established that allowed a reliable correlation of the same area for imaging as well as allowing for oil injection after fluorescent measurements to improve GNP visibility. The transformation was confirmed to return consistent values that resulted in data fit for correlative analysis.

4.3 Experimental validation: Results and discussion

After completing the development of correlative single fluorophore bleaching and extinction measurements, samples of GNP-TfA were prepared to test whether the developed technique would allow to discern differences in functionalised GNP samples as a result of varying functionalisation reaction conditions. Three GNP-TfA constructs were prepared, differing in their ratios of proteins to attachment sites (ASs) on the GNPs. These ratios were formulated as follows: 0.04 TfA per AS in sample 1 (denoted in the following as 0.04-TfA-GNP), 0.4 TfA per AS in sample 2 (0.4-TfA-GNP), and 1 TfA per AS in sample 3 (1-TfA-GNP). Table 4.3 details the sample characteristics for reference. It was assumed that these conditions should

Table 4.3. Visualisation of the GNP-TfA samples created to assess GNP crosslinking using the developed correlative technique. GNPs (yellow circles) are attached to proteins (red circles).

Sample	1 High level of crosslinking	2 Medium level of crosslinking	3 Low level of crosslinking
Visual representation			
NP diameter [nm]	20	20	20
attachment sites per GNP	2500	2500	2500
ratio of attachment sites to TfA	0.04	0.4	1

produce measurably different particle populations in terms of GNP crosslinking. This was assumed because a shortage of protein per binding site should force the particles to bind to the same protein when the likelihood of a GNP finding “its own” reaction partner is very low, leading to particle-protein constructs that consist of multiple GNPs. In the case in which there is an abundance of reaction partners, the likelihood of crosslinking is reduced, but there is a higher chance of variability in ligand density between the particles.

4.3.1 Determination of number of fluorophores per TfA and number of TfAs per GNP

As mentioned previously, the mean photobleaching step size I_B (calculated in section 4.2.3) allows to calculate the number N_F of fluorophores per TfA or GNP-TfA construct, by dividing the fluorescence intensity $I(t_0)$ detected for an individual spot in the image at the initial time point t_0 in the fluorescence intensity over time sequence by I_B . Figure 4.10A shows the histogram of $I(t_0)$ for a sample containing only free TfA. To interpret this histogram in terms of the number of fluorophores, the histogram bins were set to 146 pe sec^{-1} (so the I_B of Alexa647). This bin setting creates a distribution plot for N_F , which represents the number of fluorophores per TfA molecule. In the histogram, the highest occurrence corresponds to TfA molecules conjugated to a single fluorophore, though it should be noted that Tf molecules without fluorophores cannot be detected, as they do not emit fluorescence. The average number of fluorophores per protein $\overline{N_F}$ was determined by fitting the data to a Poisson distribution, which is used to estimate the number of times an event occurs within a specified time or space and can be used to describe the random labelling of fluorophores on proteins. The manufacturer specification states a degree of labelling (DOL) of between 1 to 3 fluorophores per TfA, with the ensemble measurement for this lot given as 2. However, the Poisson fit yielded $\overline{N_F} = 1.17$, indicating that while the ensemble measurement suggests an average of 2 fluorophores, most detectable TfA molecules in the sample had a DOL of 1. The same approach can be applied to samples with GNP-TfA constructs to assess whether there is a preference of GNPs for TfA with specific fluorophore labelling densities. The distribution of unconjugated TfA (TfA that did not bind to GNPs) after the functionalisation was analysed. The possible outcomes of such reactions are schematically depicted in Figure 4.11. If unconjugated TfA molecules show a higher average N_F after the conjugation reaction, this would indicate that GNPs preferentially bind TfA molecules with lower labelling densities.

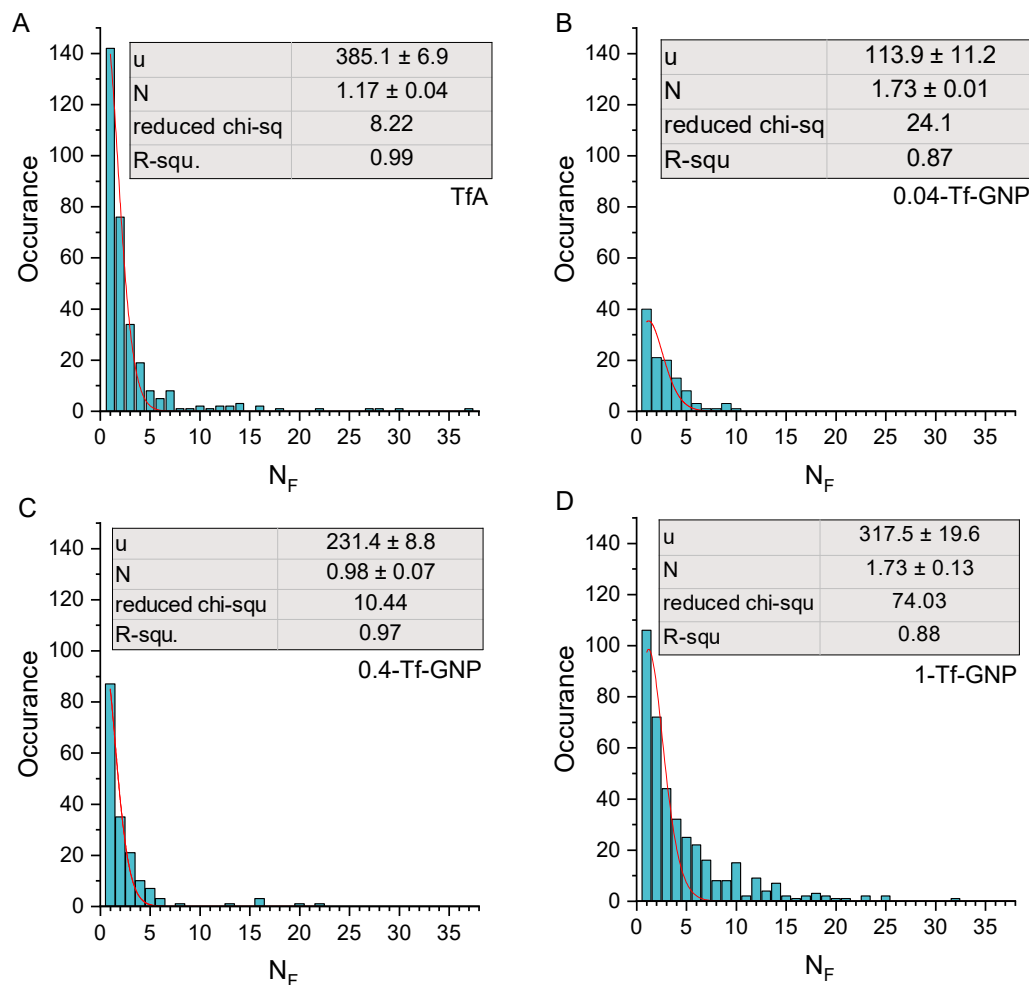


Figure 4.10 | Fluorescence Intensities of TfA for the Identification of N_F Pre and Post Functionalisation. Distributions of number of fluorophores (N_F) on (A) free TfA, and residual unconjugated TfA in (B) 0.04-Tf-GNPs, (C) 0.4-Tf-GNPs, and (D) 1-Tf-GNPs. These figures and their fits indicate the likeliest fluorophore count on a given TfA molecule under investigation within the sample. The data was fitted to a Poisson distribution, yielding a \bar{N} of 1.17 in the control (free TfA), 1.73 in 0.04-Tf-GNPs, 0.98 in 0.4-Tf-GNPs, and 1.73 in 1-Tf-GNPs with the respective amplitude of each fit given by u (= scaling factor). Changes in \bar{N} reflect a change in the fluorophore population on TfA after conjugation, indicating preferential binding of GNPs to Tf with either a low DOL (\bar{N} of the sample higher than the control) or a high DOL (\bar{N} of the sample lower than the control). The distribution of 1-Tf-GNPs shows deviations from the fit, indicating relevant aggregation of Tf. The reduced chi-square and R-square values are included as an indicator of the goodness of the fit by two different weights. [Figure and description adapted from Slesiona *et al.*⁹²]

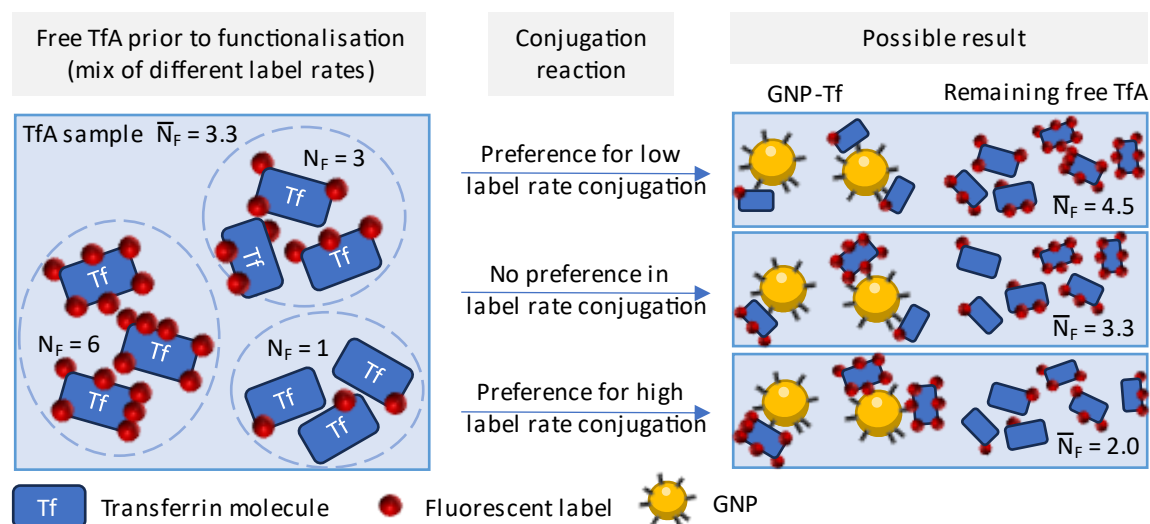


Figure 4.11 | Influence of GNP Conjugation Preference on Labelling Rate. This schematic depicts a TfA sample before functionalisation, with an \bar{N}_F of 3.3, but with diverse DOLs (N_F) across the individual TfA molecules. GNP affinity for specific labelling rates on TfA can be inferred by performing a Poisson fit on free TfA after functionalisation. A preference for lower DOLs by GNPs would result in a higher post-conjugation N_F , whereas a lack of preference would leave N_F unchanged. Conversely, a preference for a higher DOL TfA would decrease N_F relative to the initial value.

Conversely, a lower N_F value after conjugation would suggest that TfA molecules with a higher number of attached fluorophores are more likely to bind GNPs. This observation would point to an influence of fluorophore density on the efficiency of GNP-TfA conjugation.

The Poisson fit for unconjugated TfA after the functionalisation yielded \bar{N}_F values of 1.73 for 0.04-Tf-GNPs, 0.98 for 0.4-Tf-GNPs, and 1.73 for 1-Tf-GNPs (Figure 4.10B-C). This suggests an increase of \bar{N}_F after GNP functionalisation. This change in the population of remaining free TfA could be explained by either a) a low level of crosslinking between the proteins, or b) predominant binding of single fluorophore-conjugated protein to GNPs, removing these proteins from the remaining free-TfA pool.

These changes also provide insights into the functionalisation outcomes. Figure 4.12 shows the N_F distributions of a control TfA sample and GNP-TfA constructs. 0.04-Tf-GNPs and 0.4-Tf-GNPs (B and C) show broad distributions of N_F of GNP-Tf constructs and residual free TfA within the sample. This indicates that the available reaction sites on the GNPs were not fully saturated during functionalisation. This incomplete saturation may increase the probability of crosslinking, where two GNPs bind to the same TfA molecule. A large fraction of constructs in these samples have N_F values that exceed 15 fluorophores, indicating GNP crosslinking via the same Tf molecule. 15% of the signals of 0.04-Tf-GNPs correspond to constructs or multimers with more than 15 attached fluorophores, 26% of 0.4-Tf-GNPs, compared to 7% in 1-Tf-GNPs.

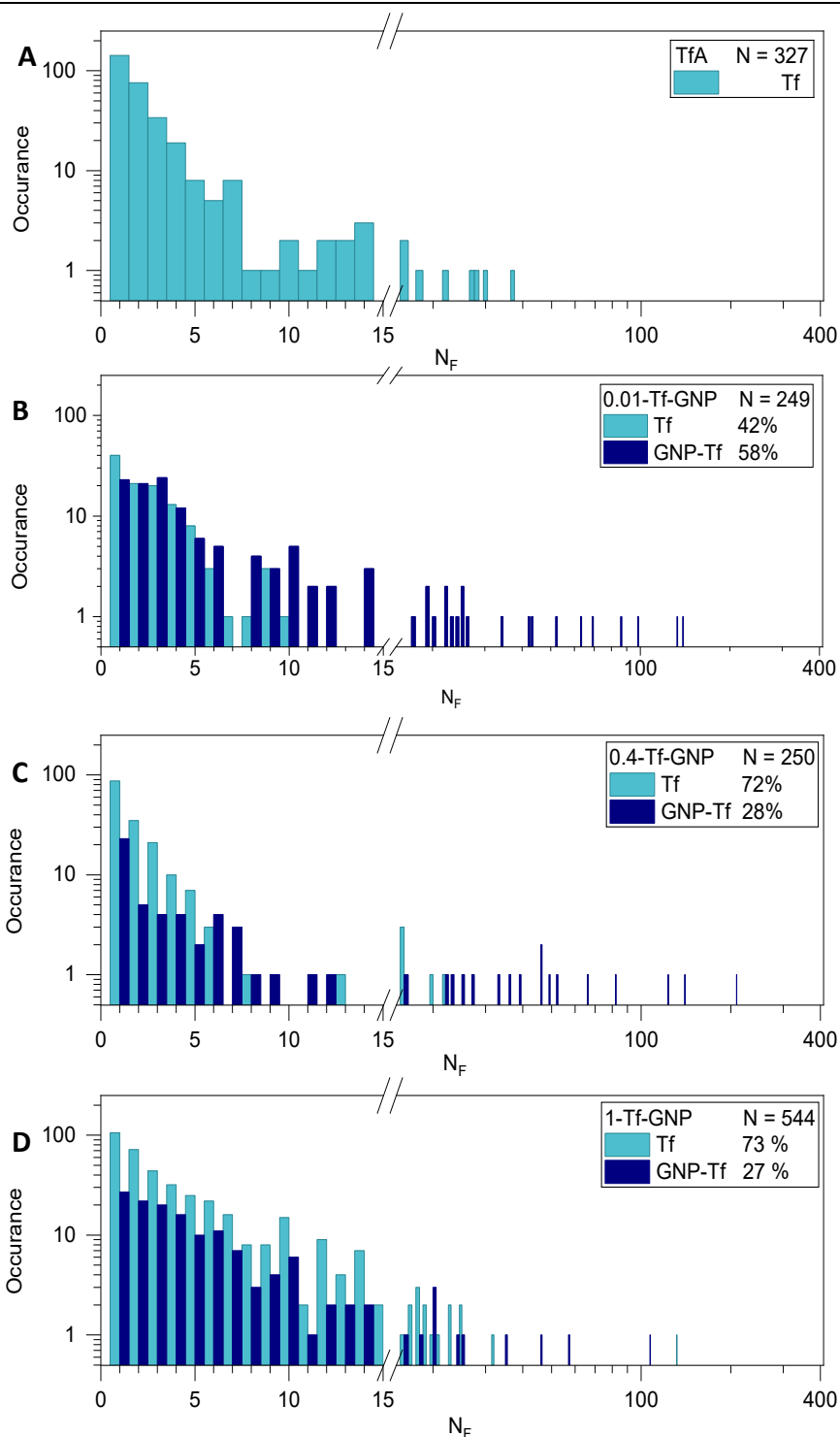


Figure 4.12 | Distributions of N_F s on Free Tf and GNP-Tf Constructs. Distribution of N_F of free Tf (light blue) and GNP-Tf constructs (dark blue) on a sample containing free Tf (A), 0.04-Tf-GNPs (B), 0.4-Tf-GNPs (C), and 1-Tf-GNPs (D) to assess the functionalisation reaction in terms of fraction of successfully conjugated TfA (dark blue) and unconjugated protein (light blue). Changes in the population of unconjugated Tf to higher values indicates crosslinking between the proteins as a result of the reaction conditions, while high values of N_F indicate a high degree of labelling of the GNPs or crosslinking of the functionalised GNPs, Fractions of GNP-Tf represent fluorescent particles only i.e. do not include non-fluorescing particles. Data show initial $I(t_0)$ from time course experiments in epifluorescence mode (from the first frame with 3 sec integration time). The graph's x-axis is linearly scaled between the values of 0-15, and transitions to logarithmic scale after the break, starting at a value of 15.1. The first tick following the break on the logarithmic scale is positioned at 20. [Figure and description adapted from Slesiona *et al.*⁹²]

Figure 4.12B-D revealed a higher occurrence of residual free TfA with a high DOL in GNP-TfA samples compared to the control TfA sample (Figure 4.12A). This indicates that the functionalisation reaction may have caused the TfA molecules to cross-link with one another, producing TfA-agglomerates with high fluorescence intensities. Crosslinking between the proteins is possible, assuming that a portion of the conjugation molecule, sulfo-SMCC, was not removed by the intermediate purification step between particle activation and TfA addition. Sulfo-SMCC is a heterobifunctional reagent which is frequently used for crosslinking proteins with an N-hydroxysuccinimide polyethylene (NHS) end on one side of the reagent and a maleimide group on the other. The NHS ester is capable of creating stable amide linkages with the primary amine groups present on the GNP. The maleimide group can interact with sulfhydryl groups in proteins⁵⁷. As a consequence, any residual unconjugated bifunctional crosslinkers may bind to primary amines in the protein structure at one end and to thiols at the opposite end. It is important to highlight that the GNP construct samples utilised in these experiments underwent purification through centrifugation, a standard practice for purifying MNPs following biomolecule functionalisation¹⁴². Despite this purification process, a significant proportion of fluorescence signals were not colocalised with GNPs across all samples (42%, 71%, and 72%).

Whether these unbound proteins are a result of inadequate purification or detachment from the GNPs over time following the functionalisation process remains unclear. If these samples were used in trafficking studies on living cells, many of the fluorescence signals observed in the images could potentially originate from free proteins or their aggregates, rather than from the intended GNP constructs. This could complicate the interpretation of the data and lead to inaccurate conclusions about the localisation and behaviour of the GNP constructs within the cells. This persistence of TfA agglomerates raises concerns about the purity of GNP-TfA constructs and suggests that additional or alternative purification techniques, such as size-exclusion chromatography or more stringent washing protocols, might be necessary to achieve higher sample purity.

4.3.2 Determination of particle size distribution and crosslinking of particles

As described previously, the size of MNPs can be determined quantitatively by measuring the σ_{ext} of individual NPs with the help of extinction microscopy. Spin-coated samples of GNP-TfA were imaged by widefield extinction at the same areas that were previously photobleached, followed by correlative analysis of the two data sets with the help of the image transformation. This was done to verify the presence and size of GNPs on a particle-by-particle or construct-

by-construct basis. This served to determine the number of particles N_{NP} contributing to an extinction signal. Multiple GNP within the PSF (i.e. from dimers, trimers, etc.) will cause the detection of stronger σ_{ext} values. The number of GNP contributing to such a signal can be calculated from the ratio between the measured σ_{ext} and the average cross section value of a single particle σ_{sp} .

$$N_{NP} = \frac{\sigma_{ext}}{\sigma_{sp}} \quad (4.2)$$

At this stage, an unexpected outcome for the 0.04-Tf-GNP sample was noticed. The average σ_{ext} was significantly smaller than expected for 20 nm GNP. The expected σ_{ext} of GNPs of 20 nm diameter can be calculated as described in section 3.5.5 to be of 547 nm². The measured σ_{ext} of individual GNPs showed a mean value of 156 ± 85 nm² for 0.04-Tf-GNPs, and 566 ± 374 nm² in the other two samples. The values for 0.4-Tf-GNPs and 1-Tf-GNPs were in accordance with the nominal diameter from the manufacturer while the σ_{ext} for 0.04-Tf-GNPs corresponded to 14 nm GNPs, well below the value of 20 nm stated by the manufacturer. It should be noted that different batches of 20 nm particles were used for functionalisation for 0.04-Tf-GNPs, and for 0.4-Tf-GNPs and 1-Tf-GNPs.

It was therefore necessary to validate these results with a second technique. The GNP batches were imaged using a TEM, which allows for a second step of validation. TEM served not only to verify the diameter of the particles, but also their sphericity. The sphericity needed to be validated, because at a constant volume but varying aspect ratios of the GNP, σ_{ext} can vary by up to 20% for aspect ratios of 0.8-1.2, which would have an impact of up to 7% on the size evaluation in extinction microscopy¹²⁰. Figure 4.13A-C shows TEM images of the GNP batch used for 0.04-Tf-GNPs (N=305) followed by a histogram of the GNP diameter determined by image analysis of this data set, and Figure 4.13D-E shows images of the batch that was used for 0.4-Tf-GNPs and 1-Tf-GNPs, also followed by a histogram of the this batch's GNP size distribution (N=297) in Figure 4.13F. It became apparent that the particles used to make 0.04-Tf-GNPs were indeed smaller than the ones used for sample 0.4-Tf-GNP and 1-Tf-GNP. Therefore, the functionalisation ratio of TfA per AS needed to be recalculated for 0.04-Tf-GNPs. The corrected ratios of TfA to AS are stated in Table 4.4, and 0.04-Tf-GNPs are denoted as 0.01-Tf-GNPs from here on to reflect the corrected ratio. The samples were deemed comparable even in the light of the samples being made of particles of different sizes as the original parameter of comparison (comparing ligand density and particle crosslinking based on

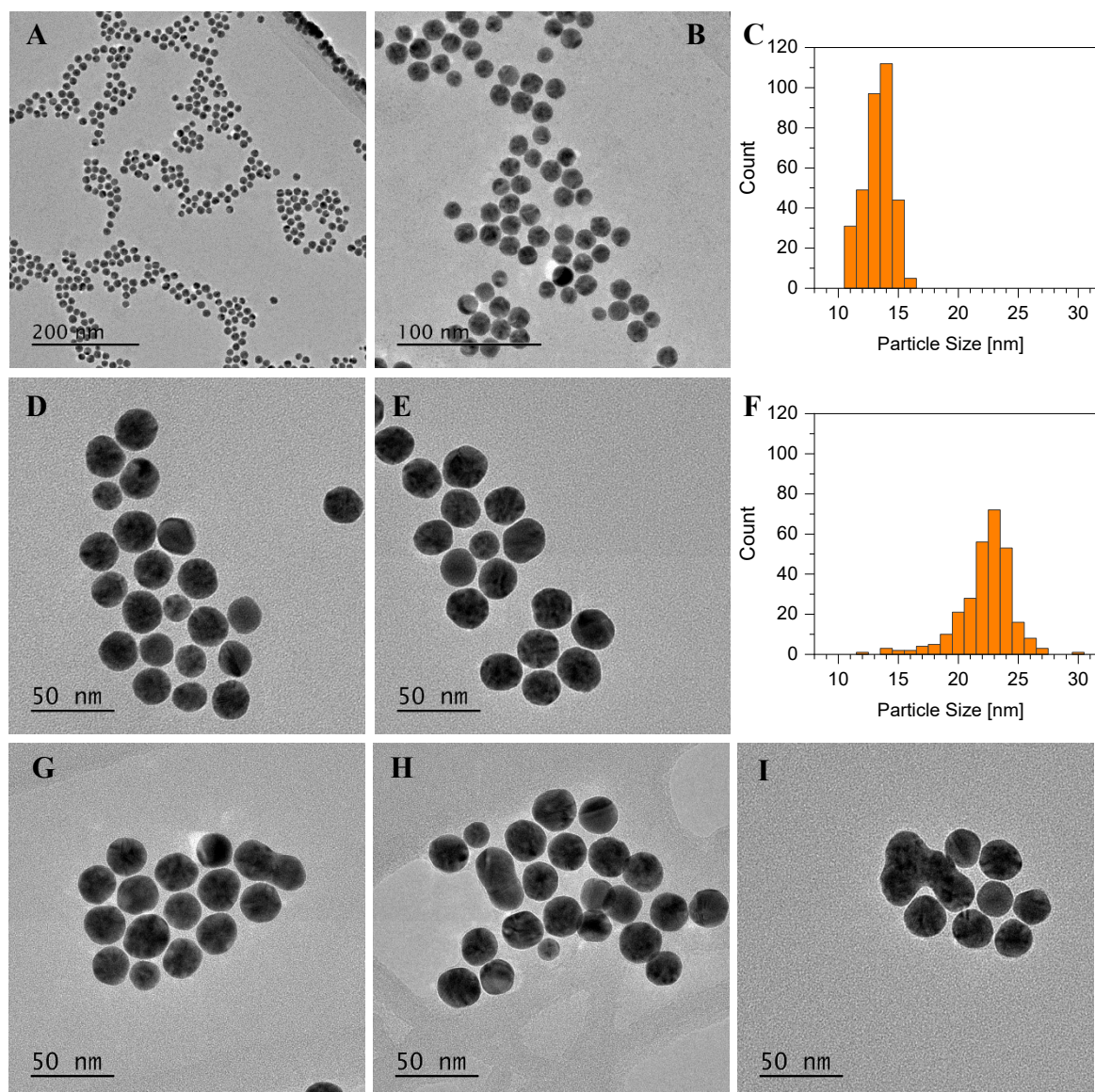
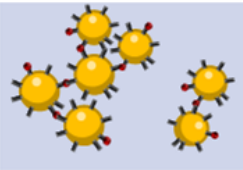
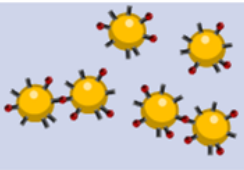
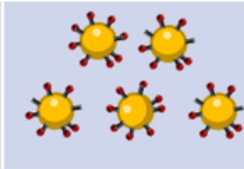


Figure 4.13 | TEM Evaluation of GNPs. The TEM images show the GNPs used for 0.4-Tf-GNPs (panels A and B, $N = 351$) and 0.4-Tf-GNPs and 1-Tf-GNPs (panels D and E, $N = 297$) to compare size differences of the GNPs batches used for the experiments presented in this chapter. This comparison was deemed necessary after extinction measurements indicated a smaller GNP size in the batch that was used for 0.04-Tf-GNPs. The resulting images were analysed using the particle analysis plugin of ImageJ, showing a mean diameter of 13.3 nm and a distribution with a standard deviation of 1.3 nm for particles used for 0.04-Tf-GNPs (panel C). The particles used for 0.4-Tf-GNPs and 1-Tf-GNPs show mean diameter of 22.7 nm and a distribution with a standard deviation of 2.3nm (panel F). Examples of asymmetric particles are shown in panels G-I. These sizes are consistent with the observed extinction cross sections considering the variability of the gold dielectric function by surface scattering as mentioned in the main text. [Figure and description from Slesiona *et al.*⁹²]

Table 4.4 | Updated Visualisation of the GNP-TfA Samples Created to Assess GNP Crosslinking Using the Developed Correlative Technique. GNPs (yellow circles) are attached to proteins (red circles). [Figure and description adapted from Slesiona *et al.*¹¹³]

Sample	1	2	3
Visual representation			
NP diameter [nm]	14	20	20
attachment sites per GNP	1230	2500	2500
ratio of attachment sites to TfA	0.01	0.4	1

different ratios of TfA to AS) was still valid. This outcome further shows the power of the newly developed technique, showing its capability to determine an accurate particle size without the user's prior knowledge of the particle's physical characteristics and therefore serves as additional independent validation. Furthermore, GNPs show no strongly non-spherical particles in the batch that was used for 0.01-Tf-GNPs, and only a small fraction (4%) of such particles in the batch used for 0.4-Tf-GNPs and 1-Tf-GNPs (Figure 4.13G-I), according to TEM. Therefore, signals originating from dimers and multimers can statistically be linked to the functionalisation procedure rather than oddly shaped particles.

Figure 4.14 shows the histograms of N_{NP} measured for the GNP-TfA constructs (Figure 4.14B-D) and on a control sample using unconjugated 20 nm GNPs prior to functionalisation (Figure 4.14A). The results have been separated into GNPs associated with (GNP, orange) and no association with (GNP-TfA, dark blue) fluorescence by the correlative fluorescence-extinction analysis. The results showed that 28% to 64% of GNPs in all construct samples did not colocalise with fluorescence signals (Figure 4.14B-D) despite the excess of protein to AS and amount of unconjugated protein still present in the sample (Figure 4.12D). One potential explanation for this might be an instability of the bonds created by sulfo-SMCC, which could tend towards dissociation during each successive purification step by centrifugation. Another reason could be the formation of a "soft corona" of TfA around the particles. Protein corona formation around GNPs occurs upon their exposure to proteins and/or biological fluids, leading to the loose adsorption of proteins on their surface¹⁴³. This process may result in a "hard"

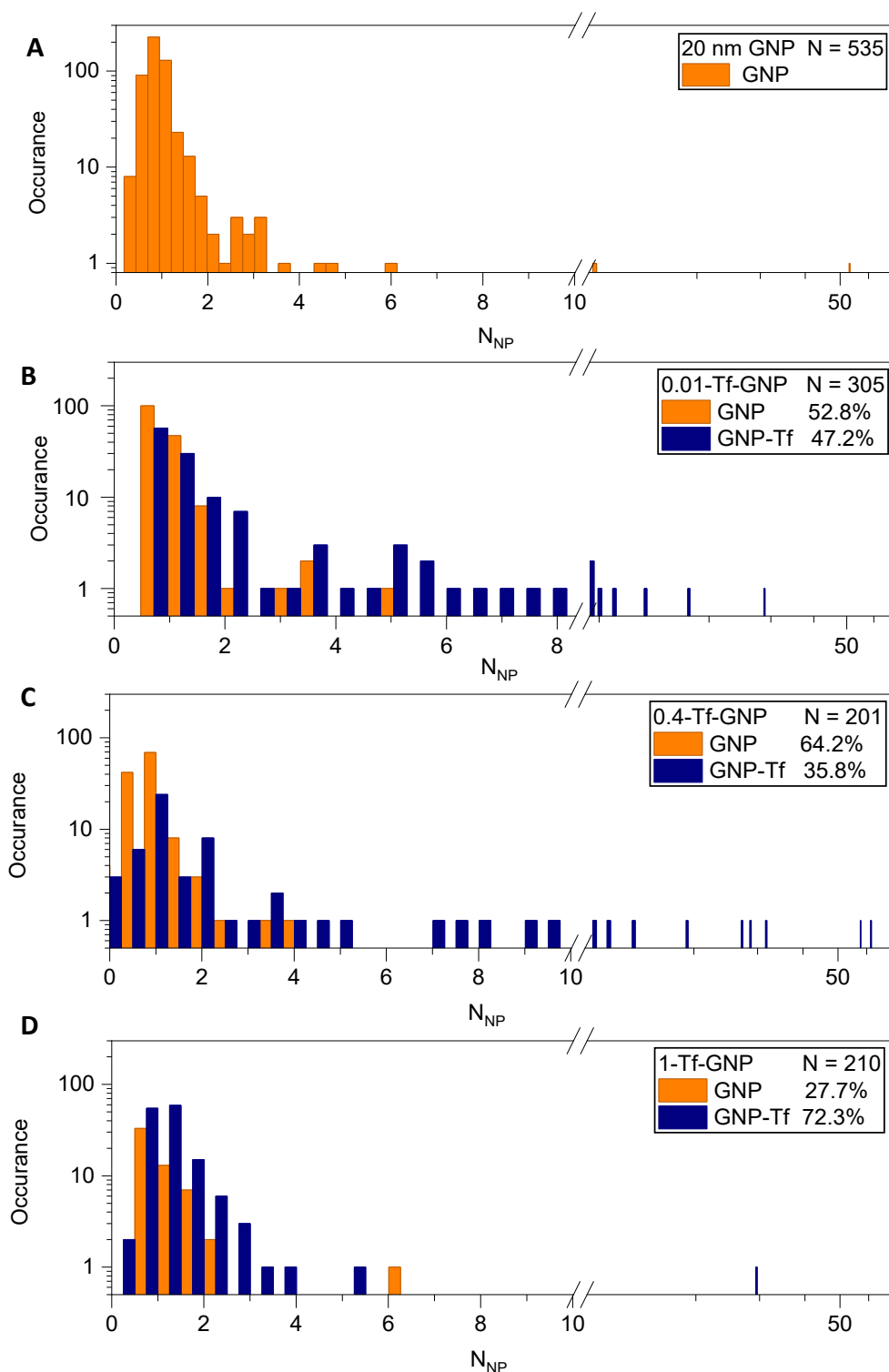


Figure 4.14 | Extinction Cross Sections of Unconjugated GNPs and GNP-Tf Constructs. Histogram of N_{NP} measured on unconjugated 20 nm diameter GNPs prior to functionalisation (A), GNP-Tf constructs 0.01-Tf-GNPs (B) 0.4-Tf-GNPs (C), and 1-Tf-GNPs (D) following cross-correlative analysis. For the GNP constructs, the results have been separated into GNPs without (GNP, orange) and with (GNP-Tf, dark blue) fluorescence, based on the correlative fluorescence-exciton image analysis to compare changes in GNP cluster populations. Populations of higher N_{NP} values indicates crosslinking between the GNPs or GNP aggregation following the functionalisation reaction. was determined using single GNP extinction cross-sections $\sigma_{sp} = 156 \text{ nm}^2$ in (B), and 566 nm^2 in A, C, and D. The graph's x-axis is linearly scaled between the values of 0-9 (B) or 0-10 (A, C and D), and transitions to logarithmic scale after the break continuing at 9.1 (B) or 10.1 (A, C, and D). The first tick following the break on the logarithmic scale is positioned at 20. [Figure and description adapted from Slesiona *et al.*⁹²]

corona of tightly bound proteins and a "soft" corona of loosely attached biomolecules, significantly altering the GNPs' biological identity and interactions with cells^{143,144}. If free TfA formed a protein corona around the constructs, it might be bound strong enough to stay associated with the construct (soft corona) during purification by centrifugation, but not during spin coating when samples were prepared for imaging, due to the strong shear flow. This would cause the loosely bound TfA molecules to detach from the GNP-Tf constructs and appear on the spin-coated samples as residual free TfA.

The variability of multimer particle distribution ($N_{NP} > 1$) was similar for 0.01-Tf-GNPs and 0.4-Tf-GNPs (Figure 4.14B,C) but notably lower for 1-Tf-GNPs (Figure 4.14D), aligning with the hypothesis that inter-particle crosslinking varied with the ligand to AS ratio on the particles. 1-Tf-GNPs showed a reduced fraction of unfunctionalised particles (28%) compared to 0.01-Tf-GNPs and 0.4-Tf-GNPs (53% and 64%, respectively), indicating an increased likelihood of functionalisation when TfA is in higher excess to GNP, as typically advised in sulfo-SMCC crosslinker functionalisation protocols. Additionally, the observed fractions of unconjugated GNPs could be influenced by fluorophore degradation that does not affect protein presence, potentially occurring during sample preparation or while adjusting focus under low light in bleaching studies. Hence, this analysis should be viewed as a conservative estimation of ligand density on GNPs, where the actual density may be underestimated but not overestimated.

4.3.3 Correlation of fluorescence and extinction signals

Additional insights into the functionalisation process can be gathered from correlating fluorescence and extinction signals of GNP-TfA on a single particle level. This was achieved by plotting the constructs' extinction cross-sections against fluorescence intensities, as depicted in Figure 4.15A-C. The analysis revealed that 0.01-Tf-GNPs (Figure 4.15A), characterised by the lowest TfA to GNP ratio, displayed an accumulation of σ_{ext} within the 100-400 nm² range, alongside fluorescence intensities spanning 100-1000 pe sec⁻¹.

At higher values of extinction and fluorescence, a linear relationship was observed between fluorescence intensity and σ_{ext} , indicating a direct correlation. Given the size distribution of the GNPs, as illustrated in Figure 4.14B, σ_{ext} values within the 100-400 nm² range are indicative of either single GNPs or GNP dimers, which are shown to have a broad range of fluorescence values. This variability suggests a distribution of GNPs with a DOL of 1 to 10 fluorophores, reflecting the variation in the number of TfA molecules attached to each GNP. To provide a clearer understanding of these findings, σ_{ext} and fluorescence values in Figure 4.15 are also expressed in terms of N_{NP} and N_F , respectively.

The variability in photobleaching step size for each fluorophore can be substantial, suggesting that the actual distribution of the number of fluorophores per GNP is probably narrower than initially assumed. As σ_{ext} increases, the distribution of fluorescence values averages out, indicative of GNP multimers within the PSF that likely stem from NP crosslinking. This results from ensemble averaging of single-particle variability in size across the multimer. 1-Tf-GNPs (Figure 4.15C), show σ_{ext} values that point to constructs composed of 1-3 GNPs, and a broad range of fluorescence values (100-2000 pe sec^{-1}), corresponding to 1-15 fluorophores, highlighting significant variability in DOL across these constructs within the same sample. This sample exhibited reduced GNP crosslinking while maintaining a wide range in the number of fluorophores attached to each particle. 0.4-Tf-GNPs show a behaviour that combines the observations made in 0.01-Tf-GNPs and 1-Tf-GNPs, showing both a population of single GNPs bound to varying numbers of TfA and a linear correlation observed among crosslinked particles (Figure 4.15B).

Figure 4.15D shows the fractions of unconjugated TfA, conjugated GNP-TfA constructs, and unconjugated GNPs across the samples, highlighting that an increased TfA ratio in the reaction steps reduces the occurrence of unconjugated GNPs. The notable presence of unconjugated protein, particularly in the 1-Tf-GNP sample, makes the relatively low fraction of conjugated constructs unexpected. One plausible explanation could be a rapid hydrolysis of the sulfo-SMCC crosslinker in aqueous environments, potentially compromising the efficiency of conjugation. Conducting the reaction at lower temperatures may have mitigated this hydrolysis¹⁴⁶, suggesting that hydrolysis could precede the interaction between unconjugated particles and their potential binding partners. Additionally, the significant amount of

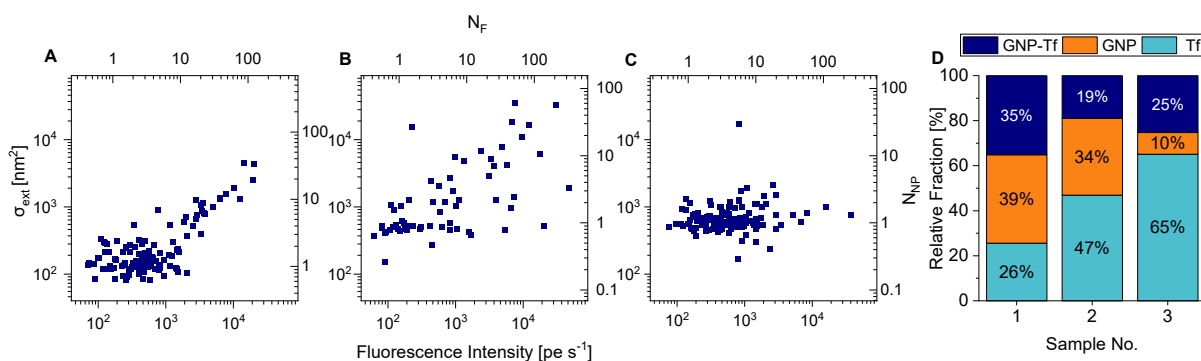


Figure 4.15 | Characteristics of Construct Samples. Correlation of extinction cross-section and fluorescence intensity $I(t_0)$ for GNP-TfA constructs from (A) 0.01-Tf-GNPs, (B) 0.4-Tf-GNPs, and (C) 1-Tf-GNPs to evaluate sample quality at a glance. Larger extinction cross sections indicate a higher number of crosslinked particles while higher fluorescence intensities indicate a higher number of bound TfA. (D) Fractions of unbound protein (light blue), unconjugated particles (orange), and successfully TfA-conjugated GNPs (dark blue) of each sample. [Figure and description from Slesiona *et al.*¹¹³]

unconjugated protein observed might also result from the proteins' tendency to form a soft corona around NPs. This soft corona could subsequently be separated from the construct during the spin coating process, further contributing to the high levels of unconjugated protein, as described previously. Additionally, there is a potential risk of proteins being trapped between nanoparticles during the centrifugation process.

Despite these challenges, it is evident that the purification process, aiming to yield a pure and stable population of functionalised nanoparticles, requires optimisation prior to conducting cell internalisation studies. The cross-correlation analysis introduced in this study offers a valuable tool for evaluating the efficiency of purification strategies across conjugated samples, ensuring their readiness for subsequent applications.

4.4 Limitations and Future Considerations

4.4.1 Selection of numerical aperture

As described in Section 4.2.2, an NA of 0.95 was chosen for all bleaching experiments as it minimised background signals caused by bleed-through of reflected illumination light into the detection path. However, following discussions with peers in the field after completing all experiments and analysis, it became evident that an NA of 1.3 would have been a better choice due to a greater separation between signal and background fluorescence, as particularly visible in Figure 4.3A. This suggests that an NA of 1.3 would have been more suitable for achieving optimal results in these experiments and an easier workflow when distinguishing single molecule fluorescence from background signal. Although there was no signal bleed-through contributing to background noise, the peaks of signal and background fluorescence in Figure 4.3B showed limited separation between weak signal intensities and brighter background signals. Using the higher NA of 1.3 would have provided a clearer distinction of weak signals, which is especially important in single-fluorophore studies.

These observations highlight the importance of carefully evaluating imaging conditions, balancing background suppression with the need for effective signal discrimination. Future experiments of the nature as described within this work should select imaging parameters that maximise signal clarity.

4.4.2 Varying DOL on TfA render the developed method an averaged estimation.

The DOL on TfA showed strong variability between 1-30 fluorophores per protein. While it has been shown that highly labelled proteins were less likely to conjugate to GNPs, it still leaves the quantification average based rather than giving an exact DOL for either the protein or the

constructs. For this reason, the fluorescence intensity $I(t_0)$ was employed when looking at correlative signals of extinction and fluorescence rather than evaluating the N_F of each construct. Additionally, it should be noted, that the presented quantification method is not capable of detecting proteins with no fluorescent label. Given that there is no knowledge of the excess of fluorophore added during protein labelling, the fraction of such proteins can also not be estimated. Because of this, the use of a Poisson distribution to evaluate N_F can be put to question. Poisson distributions that do not have zero values are termed zero-truncated Poisson distributions. This distribution is used when the process being modelled cannot result in a count of zero, which is a key characteristic of the standard Poisson distribution. In the case of this study, zero is a possible outcome but not one that we can measure¹⁴⁷. In a standard Poisson distribution, the probability of zero counts (no events occurring in a fixed interval) is a significant part of the model. The Poisson distribution is used to simulate the number of times an event occurs within a specified time or space interval, and it includes the possibility of having zero occurrences of that event. The normal Poisson distribution will allocate some probability to the occurrence of zero events, thereby skewing the distribution and potentially leading to inaccurate predictions or interpretations if 0 is not actually a possible outcome. In such cases, the model would overestimate the likelihood of zero occurrences and underestimate the likelihood of higher counts. A zero-truncated Poisson distribution corrects this issue by recalibrating the probability distribution to account only for the positive counts (1, 2, 3, ...) ¹⁴⁸. Again, the occurrence of non-labelled proteins cannot be estimated but it seems unlikely that they would not be present within the TfA sample. Therefore, it is hard to say if the normal Poisson distribution was the correct choice or if the zero-truncated distribution would have led to more accurate results. This issue persists in any other methodology to measure fluorophore labelling, as discussed in Section 4.1, as DOLs are always an averaged measure after measuring the protein concentration within a sample and the fluorescence signal separately. Protein concentration determination would include unlabelled proteins, therefore hiding within the average.

4.4.3 Particle size distributions and oddly shaped particles skew N_{NP} quantification

Similar to the variation in fluorophore intensities, the GNP samples exhibited a size fluctuation of approximately 10% in extinction, corresponding to diameters ranging from 17 to 23 nm. Owing to the strong dependency of the extinction cross-section on the GNP size, there is a small potential for misidentification in the analysis: particle dimers formed by two smaller particles could be incorrectly identified as a single, marginally larger particle, whereas dimers comprising two larger particles might be mistaken for triplets. This issue may become more

pronounced with an increasing number of NPs in the same construct, though the varying sizes should theoretically average out in larger particle aggregates. It is important to note that GNP crosslinking is not a desired result in subsequent experiments of this project. Larger constructs are less likely to be internalised due to the size constraints of CME and were only produced under the specific functionalisation conditions to evaluate the developed correlative fluorescence bleaching and extinction techniques for ligand quantification. These methods effectively assess sample quality, as samples with extensive cross-linking should be excluded.

Small deviations were observed between TEM and extinction measurements regarding the average GNP size before functionalisation. TEM indicated an average diameter of 22.7 nm, whereas extinction measurements suggested a mean size of 20 nm. Considering the recent calibration of the TEM setup by the manufacturer, the validity of the extinction analysis was looked at. Upon further investigation, we found out that the MiePlot simulation utilises the gold dielectric function from Johnson & Christy¹⁴⁹, which does not account for surface scattering in small particles¹⁴¹. This could lead to an overestimation of the absorption cross-section by approximately 10-30%, subsequently resulting in a particle size underestimation of 3-10%. This aligns with the scaling of the σ_{ext} with particle volume in the small size regime. The observed size difference between the two methods falls within this range, providing a plausible explanation, bringing all observed effects into agreement.

4.4.4 Scatter plots of correlative fluorescence and extinction allow construct quality determination at a glance

Different regions within the construct scatter plots provide a rapid evaluation of construct sample quality at a glance, as each area offers insights into crosslinking and ligand density (Figure 4.16). Constructs made from a single GNP and a single fluorophore typically scatter within the unfunctionalised particles' size distribution on the y-axis and within the bleaching step size distribution on the x-axis. Fluorescence intensities extending towards higher x values suggest GNP labelling with multiple fluorophores, up to a theoretical limit set by steric crowding on the GNP surface. Conversely, constructs that extend out in the y direction indicate multiple GNPs crosslinked by the same protein, with an upper limit determined by the number of available ASs on the protein.

Additionally, if constructs consistently attach to the same average number of proteins but occasionally to the same protein, this results in a linear relationship between extinction and fluorescence signals, which is also observable in these scatter plots. The intermediate areas between these distinct regions may consist of constructs with a few particles functionalised with

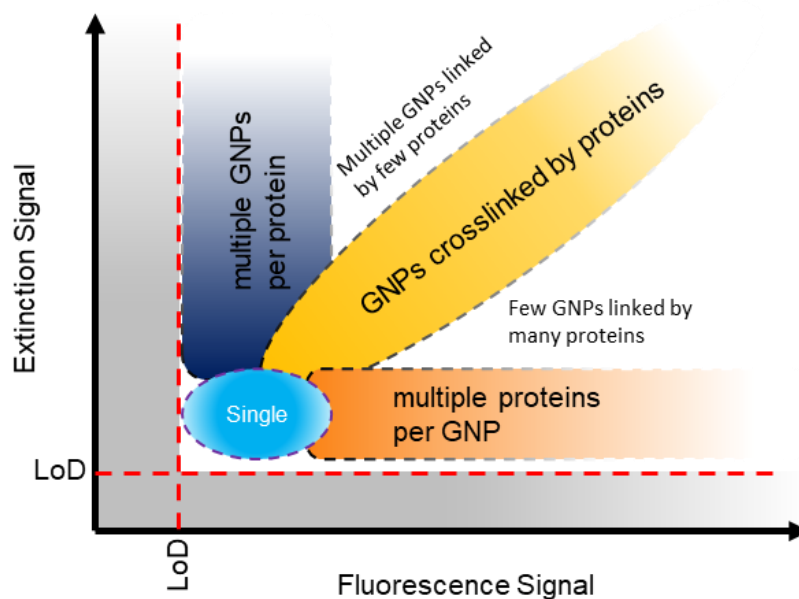


Figure 4.16 | Scatter Plots of GNP-Protein Constructs for Sample Quality Determination at a Glance. Representation of the different areas of a scatter plot of correlative fluorescence and extinction and how to interpret them.

numerous fluorophores, or a cluster of GNPs functionalised with just a few proteins. When comparing Figure 4.16 to Figure 4.15 it appears that constructs consisting of a few GNPs and many proteins have a higher probability of forming than constructs that consist of many particles but few proteins. This can be attributed to the likelihood of GNP crosslinking via the same protein, which is influenced by both the number of available binding sites per protein for the GNP to attach to, and the accessibility of these binding sites. It is possible that these factors are more limiting than the available surface area on a GNP. Furthermore, there is a possibility that clusters of proteins might attach to a single GNPs, further contributing to the positioning of these constructs in the area of the scatter plot where constructs made of few GNP and many proteins are found. Typically, GNP applications aim to avoid all groups except for single-particle clusters functionalised with either one or multiple proteins, if multivalency is critical to the experiment.

Future methodologies need to be developed to separate these different construct clusters. This will ensure that even if the functionalisation mechanism does not yield high-quality samples, the desired constructs can still be isolated and utilised effectively. Such methods would solve the presence of unfunctionalised GNP and unconjugated proteins, which are not shown on these scatter plots. Good starting points to separate particle clusters and unconjugated protein might be density gradient centrifugation¹⁵⁰ or diafiltration¹⁵¹. It is also possible that other functionalisation methods result in less unreacted constituents, which will be explored in Chapter 6.

4.5 Conclusions

We have developed a novel strategy for the quantitative analysis of the functionalisation of GNPs decorated with fluorescently labelled proteins on a particle-by-particle basis, by means of optical microscopy on GNP-protein constructs sparsely deposited onto a glass surface. The number of proteins per particle is assessed using widefield fluorescence microscopy combined with an analysis of the fluorescence bleaching step from single fluorophores, which enables us to quantify the number of fluorophores per single protein, and in turn the number of proteins per single particle. The presence, size and number of GNPs is quantitatively characterised using extinction microscopy. The cross-correlative analysis of fluorescence and extinction microscopy gives a quantitative measure of the fraction of single GNPs conjugated to fluorescent proteins, versus unconjugated proteins and GNPs, and the formation of GNP multimers suggesting crosslinked particles. Albeit demonstrated here with spherical GNPs and transferrin proteins, our technique is expected to be widely applicable to plasmonic nanostructures of various shapes and materials functionalised with fluorescent biomolecules. The method is based on relatively simple and easy-to-use widefield microscopy instrumentation, lending itself for widespread adoption of the technique to improve the characterisation of nano-formulation systems. The technique can be further simplified by combining fluorophore photobleaching and extinction microscopy on the same imaging system, removing the need for post-acquisition alignment.

5 Establishing Four-Wave-Mixing imaging in living cells

5.1 Introduction

The ability to monitor and analyse the interaction, localisation, and dynamics of GNPs within cellular environments can help to understand cellular processes at the nano-scale, improving the fields of drug delivery and photothermal therapy using GNPs¹⁵². The importance is not only limited to knowing the GNPs location, but also their accumulation and concentration at a specific location to assess whether therapeutically relevant concentrations are reached where they are needed. Accurate tracking of GNPs within mammalian cells can provide insights into cellular uptake, intracellular trafficking, and exocytosis mechanisms. By revealing the dynamics of these processes, the details of cellular pathways can be characterised. GNPs can serve as direct labels rather than just pure delivery vehicles, and can potentially allow tracking at an unprecedented resolution, especially because GNPs neither blink nor bleach, and can therefore be tracked for their entire trajectory on a single NP level. The methodology permits observations over an extensively long duration without necessitating a trade-off between the exposure time per point and the total observation window. Essentially, it allows for the tracking of complete GNP trajectories. Fluorescence on the other hand is also capable of tracking entire trajectories but it requires a compromise between exposure time and time intervals to optimally allocate the "photon budget" before the onset of fluorescence bleaching.

In this chapter, Four Wave Mixing imaging (FWMi) is introduced as a visualisation method for GNPs, and I will explore the optimisation of acquisition settings to allow both 3D cell analysis, and live cell imaging. The development and implementation of a live cell imaging chamber allowed the analysis of GNP trafficking in live cells. In this project, fluorescent labels were consistently used, even though FWMi is capable of tracking GNPs without requiring additional labels. In the short term, fluorescent labelling serves to validate this relatively new technique by comparing it to established methodologies. Once FWMi is recognised as a standard microscopy approach, the long-term objective is to eliminate the use of fluorescent labels entirely.

5.2 Results and discussion

5.2.1 2D image analysis of FWMi data and proof of GNP signal

FWMi is a technique that has been developed within the Biophotonics & Quantum Optoelectronics group at Cardiff University⁴⁸. As this method is not widely established, an

explanation of the data it can acquire is laid out before elaborating on the system's further development for live-cell imaging.

FWMi is a technique that identifies changes in a probe's transmission due to pump-probe interactions. This process begins with focusing a beam, that can be adjusted in x, y, and z dimension, onto a targeted area. The wavelength of this beam is chosen to be in resonance with spherical GNPs, which exhibit significant electronic responses to multiphoton excitation by the laser. The GNPs react to the laser beam by generating a hot electron gas. This alters the optical properties of the GNP, as described in Section 3.2.2. If another beam interacts with these excited GNPs before these electronic dynamics dissipate as heat into the surroundings, the change in their dielectric function is measurable. This is measured by epi-detecting the reflected probe beam and evaluating its amplitude and phase shifts relative to a reference beam that has not interacted with the sample^{47,48}.

Since multiphoton excitation is required for FWM, the imaging modality is inherently capable of optical "sectioning", as the high photon densities needed to achieve multiphoton excitation are only reached at the focal point of where the laser is focused. Apart from measurements of the modulated FWM amplitude (FWM^A), the technique also detects the reflected probe field (REFL) via its interference with the external reference beam. REFL essentially represents interferometric reflectometry data, which arises from variations in sample or cellular thickness and refractive index heterogeneity. These interactions of the reflected probe beam and the reference beam allow the reconstruction of the cell's three-dimensional structure.

The dynamics of the FWM process, as indicated earlier, are time sensitive, i.e. the probe pulse needs to arrive and interact with the GNP before the electronic and lattice response has reached equilibrium, and the pump-induced change has vanished. For GNPs with a diameter of 20 nm, the electronic response peaks approximately 0.5 picoseconds ($\tau = 0.5$ ps) after the pump interaction. This temporal evolution of the GNP's electron response to a pump pulse is schematically presented in Figure 5.1A along with an example measurement⁴⁹.

In this set of experiments, HeLa cells were serum-starved for 30 min to reduce their Tf levels. The cells were then treated with GNP-protein constructs for another 30 min, washed, fixed with 4% PFA, and subjected to FWMi to evaluate GNP-TfA binding to the cells. Figure 5.1B provides a DIC image of a HeLa cell for orientation, together with images of REFL and FWM^A , captured with the pump pulse train set to a delay of 0.5 ps ($\tau = 0.5$ ps), as shown in Figure 5.1C and D, respectively. REFL reveals information about cellular attachment and shape. The cell's shape and its adherence to the culture dish are visible in Figure 5.1C.

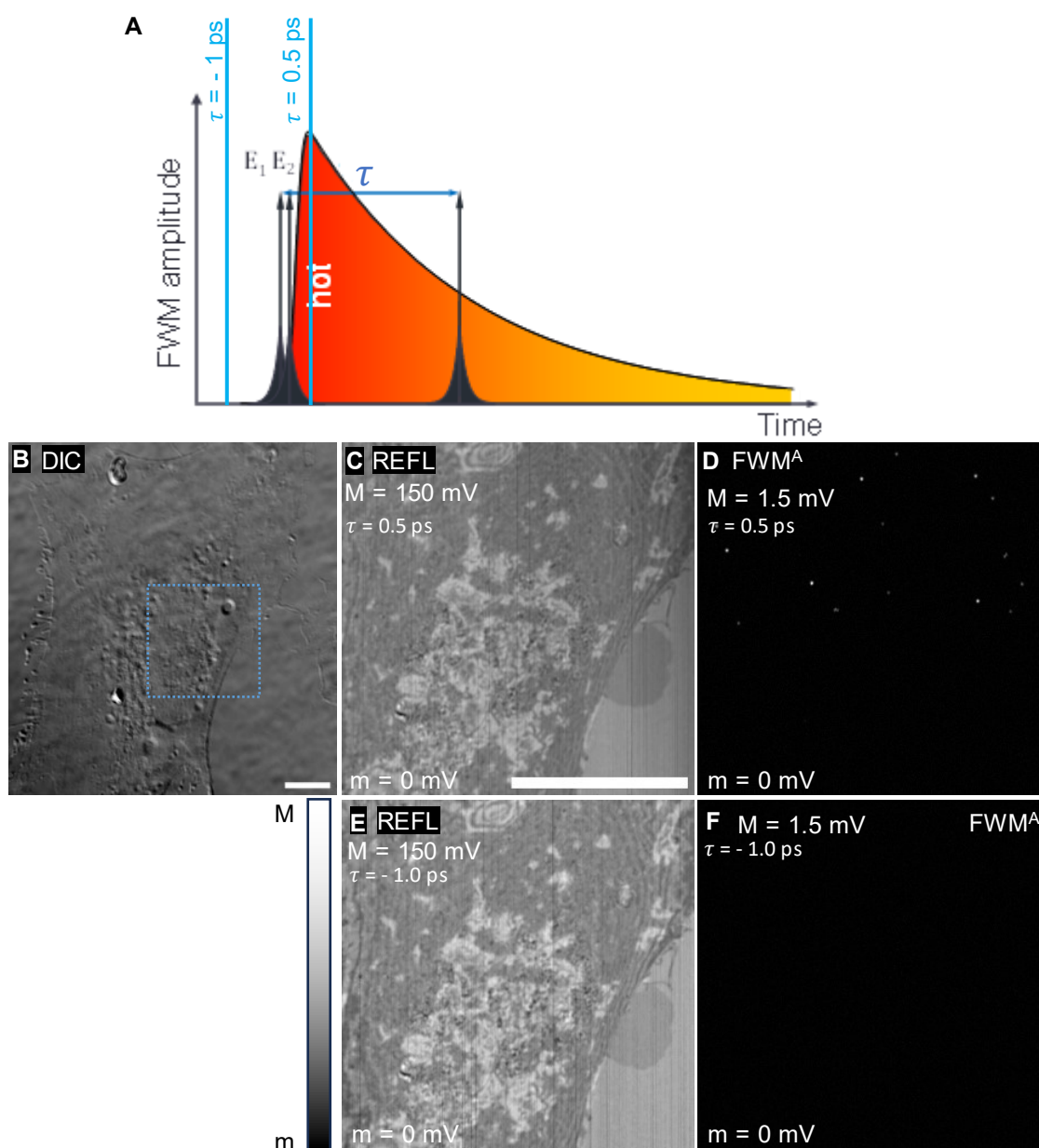


Figure 5.1 | 2D FWMi Images Reveals Cell Attachment to the Dish Surface and Localisation of GNPs.

(A) Schematic illustration of the temporal progression of the electronic response of a GNP after multiphoton excitation adapted from Masia *et al.*⁴⁴ (B) DIC image of a fixed HeLa cell after exposure in a pulse-chase experiment with a 30 min serum-starvation step, 30 min GNP-Tf treatment, and fixation in 4% PFA. The area marked by the blue dotted square underwent FWMi under two conditions: firstly, with the probe beam arriving 0.5 ps after the pump, displaying the (C) REFL and (D) FWM^A results at the coverslip surface showing GNP signals in D. The second measurement was conducted with the probe beam preceding the pump by 1 ps, showing the (E) REFL and (F) FWM^A with no GNP signals due to the absence of an electronic response from the GNPs. Nominal pump/probe powers before entering the microscope: 60/30 μ W. Scale bars: 20 μ m.

Adherence can be inferred from variations in gray values observed within a single z-plane. Regions where the probe beam encounters more refractive index changes appear darker in the image. Conversely, lighter areas at the substrate interface indicate that the cell is attached to the dish in these regions. In such cases, the probe beam undergoes only three refractive index transitions: from oil to glass, glass to the cell membrane, and subsequently into the intracellular environment. In areas where the cell is not fully attached, the probe beam encounters additional refractive index transitions - specifically, from glass to cell culture media, media to the membrane, and then into the cell. These additional changes result in darker image regions. This approach also allows for the identification of intracellular structures surrounded by membranes, as these structures introduce further refractive index changes. Figure 5.1D displays the FWM^A for the same region, showing 16 distinct FWM signals. Variations in amplitude among these signals suggest differences in their z-positions, sizes, or the possibility of multiple GNPs within the focal volume.

The specificity of the GNP signal of FWMi microscopy can be established by adjusting the time delay between the pump and probe pulses. For instance, if the probe pulse precedes the pump by 1 picosecond ($\tau = -1.0$ ps), no change in the electronic response from the GNPs can be detected because it has yet to be stimulated. This is shown in the resulting REFL and FWM^A images shown in Figure 5.1E and F. The REFL remains unaffected by these temporal dynamics because it is dominated by the direct probe reflectance, independent of the pump excitation. However, the FWM^A does not detect any change since the GNPs have not yet been excited by the pump, and long-lived photothermal effects from previous pump pulses in the train are negligible. This lack of signal when the probe arrives too early demonstrates the presence of GNPs; no other cellular components produce a detectable response under these conditions. This not only indicates the presence of GNPs, but also that nothing else within the cell generates FWM signals, therefore making this technique background free³². This characteristic is particularly beneficial for the unambiguous detection and analysis of GNPs within cellular environments.

5.2.2 3D image analysis of FWMi

Due to the inherent optical sectioning capability of FWMi and REFL, it is possible to identify the location of MNPs associated with a cell in three dimensions. In terms of drug delivery studies this may give important information as to whether a particular formulation has made it to the cell surface, has been internalised, or has made it through to the target organelle. In order to explore this further, we now turn our attention to 3D FWMi of HeLa cells treated with GNP-TfA conjugates. Figure 5.2A provides a DIC image for orientation alongside a series of REFL

images captured at progressing z-levels, with 400 nm increments and spanning a z-range from 0 μm -3.2 μm (Figure 5.2B-J). The REFL image at $z = 0$ gives information about cellular attachment and refractive index variations within the cell. As mentioned previously, refractive index changes within a cell occur in various components such as the nucleus, organelles, lipid droplets, and the cell membrane, due to differences in composition and density¹⁵³.

Furthermore, by examining the REFL field progression through a z-stack, one can discern cell morphology. This is achieved by observing the contrast lines that extend along the periphery to the top of the cell(s) under investigation. These lines are similar to topographic contours on a mountain map, delineating the height profile across the cellular landscape. The bright/dark line pattern originates from the interference between probe reflections at multiple layers, specifically between the bottom glass-cell and top cell-water interfaces. Depending on the distance between these surfaces, and therefore the cell height, constructive/destructive interference fringing appears.

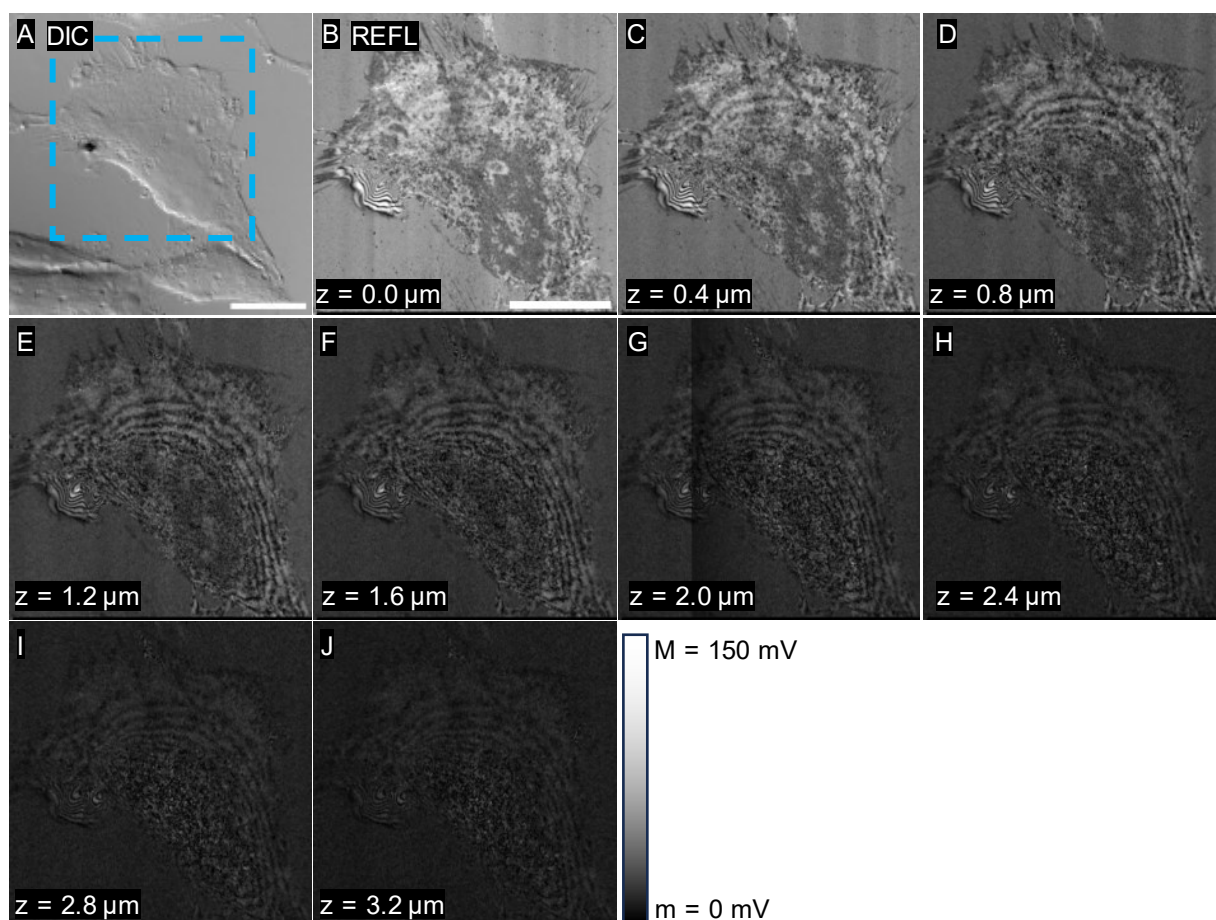


Figure 5.2 | 3D REFL Field Reveals the 3D Morphology of Cells. (A) DIC image of an exemplary fixed HeLa cell after exposure in a pulse-chase experiment with a 30 min serum-starvation step, 30 min GNP-Tf treatment, and fixation in 4% PFA. The area marked by the blue dotted square underwent z-stack measurement in FWMi in steps of 400 nm over an axial range. (B-J) Acquired REFL data over an axial range of 0 to 3.2 μm . The ascending lines can be used to infer cell morphology – similar to topographical maps of mountains. Nominal pump/probe powers before entering the microscope: 60/30 μW . $\tau = 0.5$ ps. Scale bars: 20 μm .

Z-stack imaging of the FWM^A provides comprehensive three-dimensional insights into the localisation of GNPs, as depicted in Figure 5.3, which corresponds to the data shown in Figure 5.2. Progressing through the z-stack in FWM^A reveals individual GNP signals (Figure 5.3A-J). In this thesis, these data sets are typically presented as either maximum intensity projections (MIPs, Figure 5.3J) to display the xy-information of all GNPs throughout the stack as colour-coded MIPs (ccMIPs, Figure 5.3K), to retain z-axis information, or as orthogonal views to visualise GNP internalisation. However, it's important to acknowledge that ccMIPs depict the lowest z-values in purple and blue, which may not stand out against a dark background.

Orthogonal projections were used to enable a more detailed interpretation of these data sets, as they offer a quick visual assessment of the z-position of GNPs (Figure 5.3L). Orthogonal views also reveal the relatively large PSF of the FWMi set-up. A section from the data in Figure 5.3L

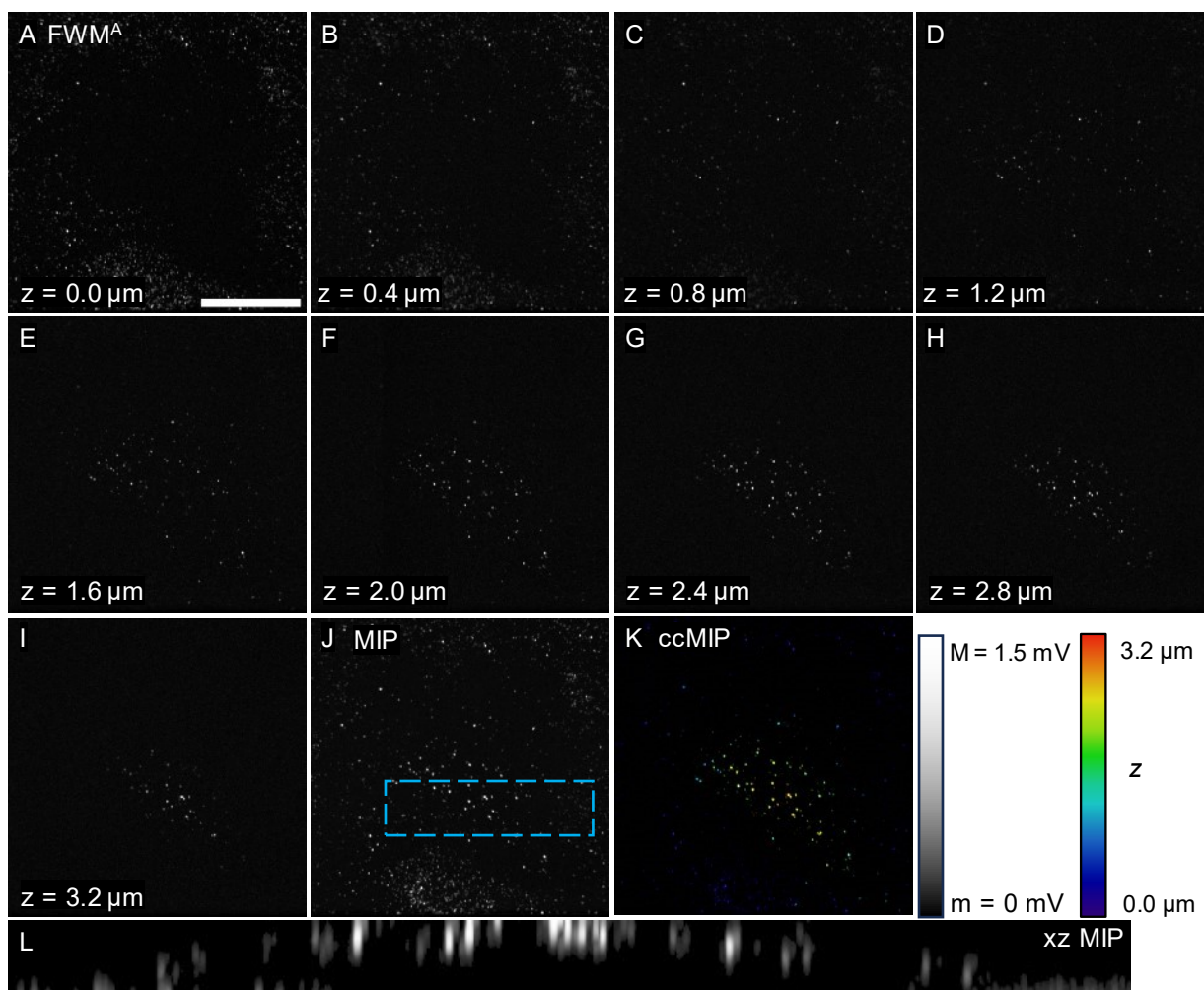


Figure 5.3 | 3D FWM^A Data Reveals GNP Localisation in the z-axis. Z-Stack FWM^A data of a fixed HeLa cell after exposure in a pulse-chase experiment with a 30 min serum-starvation step, 30 min GNP-Tf treatment, and fixation in 4% PFA over an axial range of (A-I) 0 to 3.2 μm in steps of 400 nm showing GNP positions. (J) Maximum intensity projection (MIP) of the images shown in A-I for representation of all signals in the FOV across the z-stack. (K) Colour-coded MIP (ccMIP) of the data shown in A-I while additionally retaining z-information. (L) Orthogonal view of the area marked by the blue dotted square in J. Nominal pump/probe powers before entering the microscope: 60/30 μW . $\tau = 0.5$ ps. Scale bars: 20 μm .

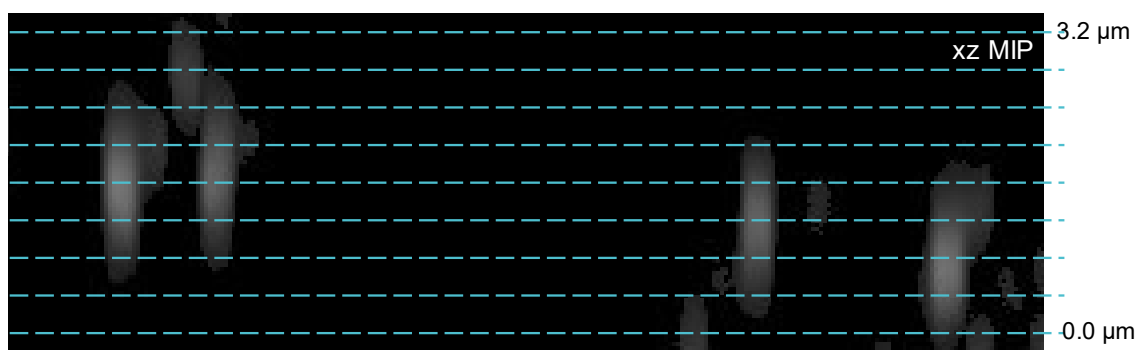


Figure 5.4 | The FWMi PSF is Elongated. FWMi measurement of a fixed HeLa cell after exposure in a pulse-chase experiment with a 30 min serum-starvation step, 30 min GNP-Tf treatment, and fixation in 4% PFA. FWM^A acquired in z with steps of 400 nm, represented as xz MIP. The figure is cut out from Figure 5.3L to evaluate the z-resolution of the FWMi PSF. The blue dotted lines represent the individual z-planes, showing a PSF of 1.2 – 2.0 μm .

was extracted and displayed in Figure 5.4 to enhance the visibility of the particle signals in xz. Here, the blue dotted lines indicate the z-plane images taken along the z-axis, enabling the assessment of the z-resolution. The signal PSF in z spans between values of 1.2 to 2.0 μm , which is notably broad. While deconvolution could potentially optimise this resolution, it was not applied to FWM^A data within the scope of this project. The signal intensity was sufficient to deduce the z-position and identify the centre of each signal, which met the requirements for the experiments conducted as the current level of detail was adequate for the purposes of this research project.

5.2.3 Improving FWMi acquisition settings on fixed samples

Typically, optimisation efforts in microscopy are focused on sample health, temporal resolution, spatial resolution, signal to noise ratio (or contrast), and the size of the FOV. Adjusting any one of these parameters typically causes compromises in others. This is a commonly known obstacle for all fields focussing on improving microscope set-ups, commonly known as the pyramid of frustration¹⁵⁴. For instance, increasing illumination to improve spatial resolution or contrast can affect specimen health, while enhancing temporal resolution to capture fast-moving processes might cause loss of information in spatial detail or increase phototoxicity risks. Therefore, optimisation of acquisition requires a balanced approach that meets the specific requirements of the study while minimising harmful effects on the specimen. To follow internalisation events of single GNPs, multiple settings need to perform together in the best way possible.

Initial acquisition settings of fixed cell experiments employed a nominal 60/30 μW pump/probe power, with 2.0 ms pixel dwell time and 63 nm sample step size (SSS, also pixel size). These power levels, as well as higher ones, have previously been utilised by our group and demonstrated to be non-destructive for fixed cell samples^{32,121}.

Figure 5.5 illustrates the impact of prolonged acquisition times on data quality on the FWMi set-up. It shows a MIP of a fixed HeLa cell treated with GNP-TfA imaged in z. The dataset comprises 26 frames captured sequentially at 250 nm intervals in the z-dimension, covering a z-range of 0 – 6.25 μm . With a pixel dwell time of 2 ms and 63 nm SSS for a 40 μm^2 area, each frame required an acquisition period of 13:23 min. Acquiring a data set as shown in Figure 5.5 took 348 min (5.8 hours), excluding additional time for microscope setting adjustments such as z-value modification and checking for z-drift before starting the measurement. The extensive acquisition duration led to noticeable xy drift. This drift is particularly evident in the intensity profile presented in Figure 5.5B, which displays distinct steps of intensity across the frames.

It should be noted, that following the regularisation of the FWMi data, the processed data are stored as bitmaps utilising a predefined grey scale range (in this instance, minimum $m = 0$ mV and maximum $M = 1.5$ mV). Subsequently, the intensity values within this range are converted to grey values spanning 0 to 255. Therefore, the y-axis in the graph presented in Figure 5.5B denotes these arbitrary units, as opposed to millivolts. As discussed previously, the FWMi PSF is elongated and therefore GNPs are visible throughout multiple frames in Figure 5.5A and the intensity plot in Figure 5.5B. Together with the long acquisition times and the drift, a single GNP signal is visible up to four times within the presented image. To mitigate this, samples were imaged at larger z-steps (400nm) to accelerate scanning while preserving z-resolution.

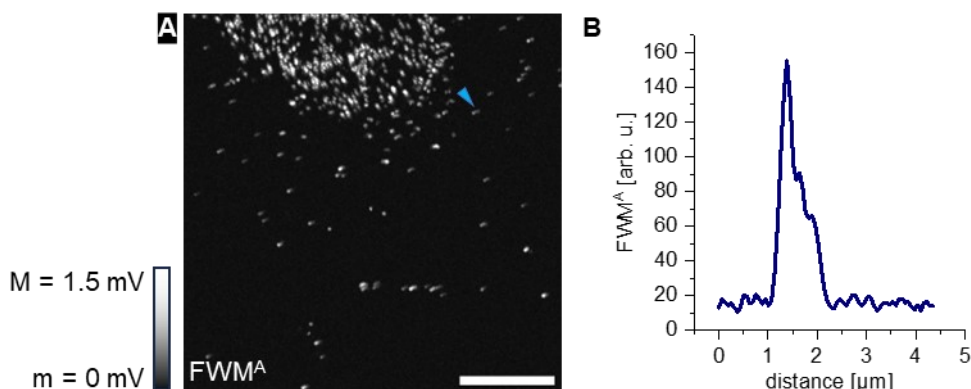


Figure 5.5 | Long Acquisition Times Cause Visible Drifts in FWMi. Early z-stack FWMi data of HeLa cells after exposure in a pulse-chase experiment with a 30 min serum-starvation step, 30 min GNP treatment, and fixation in 4% PFA. The image was acquired with long acquisition settings, resulting in a total acquisition time of 5.8 h for 26 frames with visible drifts. (A) MIP of the acquired data with visible drift. To visualize this drift, one of the signals was chosen (blue arrow) to (B) plot the measured FWM^A intensity over a line across 4.5 μm . Nominal pump/probe powers before entering the microscope: 60/30 μW . $\tau = 0.5$ ps. Scale bar: 10 μm .

In an effort to enhance acquisition speed, the impact of modifying the SSS settings in conjunction with pixel dwell time was evaluated. The control software for the setup permits adjustments to the SSS for the x and y axes separately, enabling a balance between rapid scanning and adherence to the Nyquist criterion for spatial measurements. The Nyquist criterion in spatial measurements determines that the sampling interval must be sufficiently small to accurately capture an image¹⁵⁵. The sampling interval should be at least half the size of the smallest feature that can be resolved. This ensures that spatial variations are sampled adequately to reconstruct the original signal without loss of detail. Not meeting this criterion in spatial measurements can lead to misrepresentation or loss of information. This is similar to undersampling in time-based measurements, where an event can only be resolved if the scanning is at least twice as fast as the event or mechanism of interest.

To test various integration times and SSS settings, a fixed HeLa sample treated with GNP-TfA was measured. Figure 5.6A provides a DIC image for orientation with a blue dotted square indicating the area measured in FWMi. Figure 5.6B and C show the REFL and FWM^A of this area, respectively, and Figure 5.6D-L displays multiple images of an area within this FOV (orange dotted square) to demonstrate the effects of varying integration times (2 ms, 1.5 ms, and 1 ms) and SSS settings of 63 nm, 95 nm, and 189 nm (same settings in x and y axes) on GNP imaging. While all of these step sizes fulfill the Nyquist criterion for the wavelength used on a diffraction limited set up (225 nm), a higher sampling rate should be preferred to increase the reliability of the acquired signals. Additionally, a table details the total acquisition time per frame for a 40 μm^2 area (such as the area depicted in Figure 5.5A).

Increasing the SSS significantly decreased acquisition times as visible within the table of Figure 5.6. However, it also impacted the quality of the measurement. At a SSS of 63 nm, the image was clear (Figure 5.6D, G, and J), but increasing the SSS by a factor of 1.5 or 3 resulted in decreased resolution and worse signal to noise ratio (Figure 5.6E, H, and K), (Figure 5.6F, I, and L). Such a decrease in resolution and image quality could obstruct the analysis of signals and the quantification of GNP uptake. Therefore, a SSS of 63 nm was maintained to not sacrifice resolution for speed. Experiments to test faster acquisition times than those presented in Figure 5.6 were conducted on a separate sample.

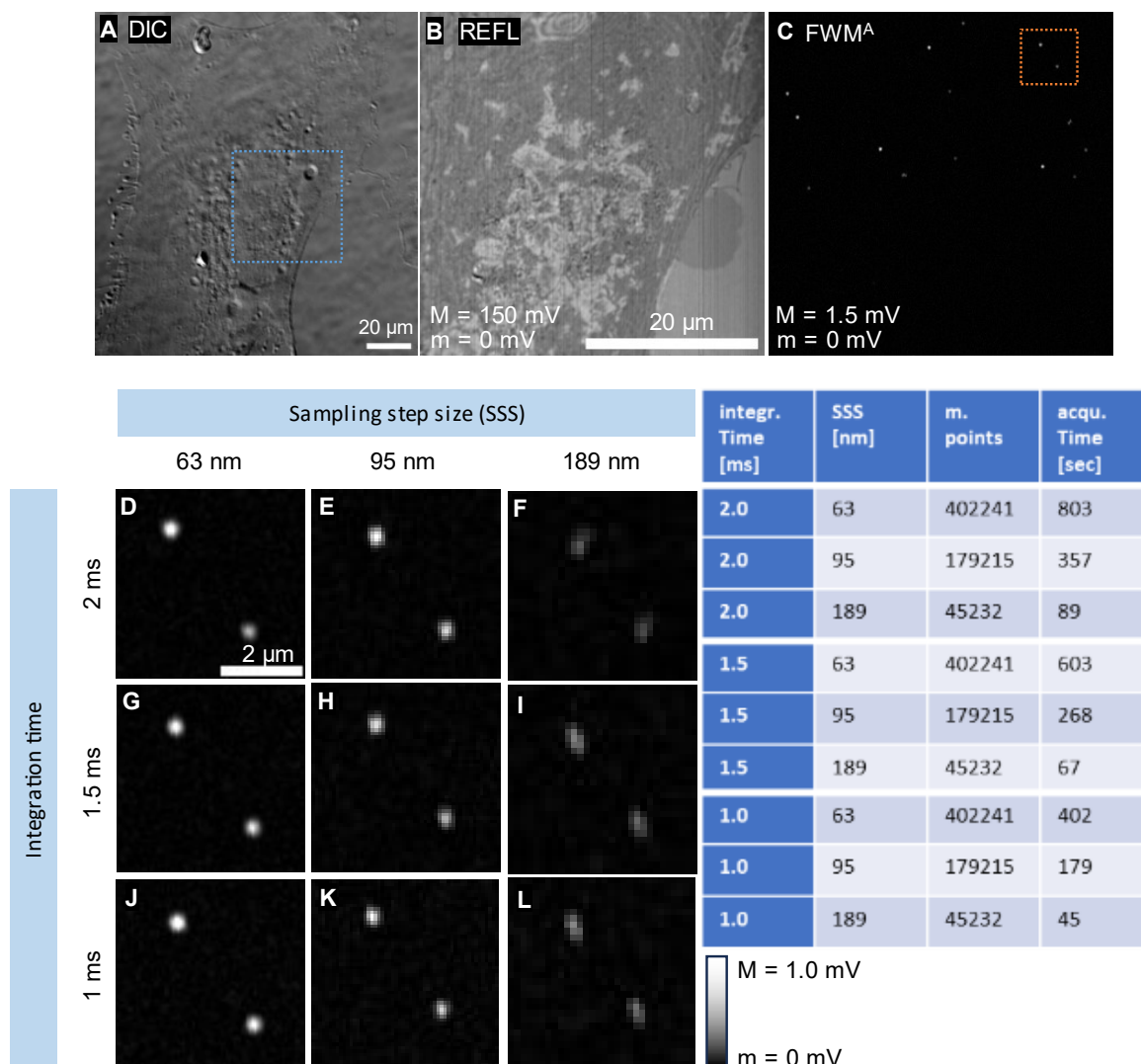


Figure 5.6 | Enhanced Scanning Speed Through Reduced Samples per Row Impacts Data Quality More Significantly Than Shorter Integration Times. FWMi of a fixed HeLa cell after exposure in a pulse-chase experiment with a 30 min serum-starvation step, 30 min GNP-Tf treatment, and fixation in 4% PFA. Cells were measured under varied scanning settings for the sampling step size (SSS) and integration time. (A) A DIC of a fixed HeLa for orientation. Images of (B) REFL and (C) FWM^A depict the area of interest marked by a blue dotted square in (A). Data from FWMi with a 2.0 ms, integration time at different SSS settings: at 63 nm (D), at 95 nm (E), and at 189 nm SSS (F). Further imaging of the same region at a 1.5 ms pixel dwell time at 63 nm (G), at 95 nm (H), and at 189 nm SSS (I), and again at a 1.0 ms pixel dwell time with 63 nm (J), 95 nm (K), and 189 nm SSS (L) settings. These measurements were conducted to assess the effects of sampling per row and acquisition speed on the resulting image quality of FWMi. The table provides more detailed information about how these settings affected the number of measurement points (m. points) and the acquisition time. The stated acquisition times refer to the acquisition time for the complete FOV of 40x40 μm . Nominal pump/probe powers before entering the microscope: 60/30 μW . $\tau = 0.5$ ps.

In continuation of prior investigations, fixed HeLa cells treated with GNP-TfA conjugates were imaged using the FWMi set-up. A DIC image of the targeted area is presented in Figure 5.7A, with the FWMi measured region marked by a blue dotted square. An additional adjustment in these experiments involved varying the SSS along the x and y axes, specifically maintaining the x-resolution at 63 nm and adjusting the y-resolution to 95 nm. This adjustment was made to preserve high resolution along one axis while significantly reducing acquisition time by sacrificing resolution in the other. Figure 5.7B and C display the resulting REFL and FWM^A images to give an overview of the entire area that was measured.

To assess how these acquisition settings influenced the FWM^A at integration times of 0.5 ms and 0.2 ms, the section highlighted by an orange dotted square in Figure 5.7C was enlarged and examined. The results are depicted in Figure 5.7D and E, respectively. The comparison shows a reduction in the signal-to-noise ratio for the shorter integration time, but not to a degree that would impede the use of these settings (i.e. 0.2 ms acquisition time, 63 nm SSS in x, 95 nm in y) in subsequent experiments, considering the significant reduction in acquisition times from 100 seconds to 40 seconds for a 40 μm^2 FOV.

While the emphasis on acquisition speed is less critical for fixed cell samples, the objective of these developments within the project was to refine the acquisition settings for live cell imaging, where rapid scanning is essential for studying internalisation mechanisms. With the current adjustments to the z-stepping of 400 nm, a pixel dwell time of 0.2 ms, and resolution settings of 63 nm SSS in x and 95 nm in y, a measurement as presented in Figure 5.5 would require a total measurement time of 625 sec, i.e. 10 min and 25 sec as compared to the initial 20,880 sec (5.8 hours), resulting in a 48-fold increase in acquisition speed. The possibility of further optimisations of the imaging speed by targeting smaller areas poses another option. Future live cell FWMi measurements are set to determine the necessity of such adjustments. The current 40 sec acquisition speed is likely still too slow to follow GNPs in live cell imaging. To give weight to this argument, actual live cell imaging was necessary.

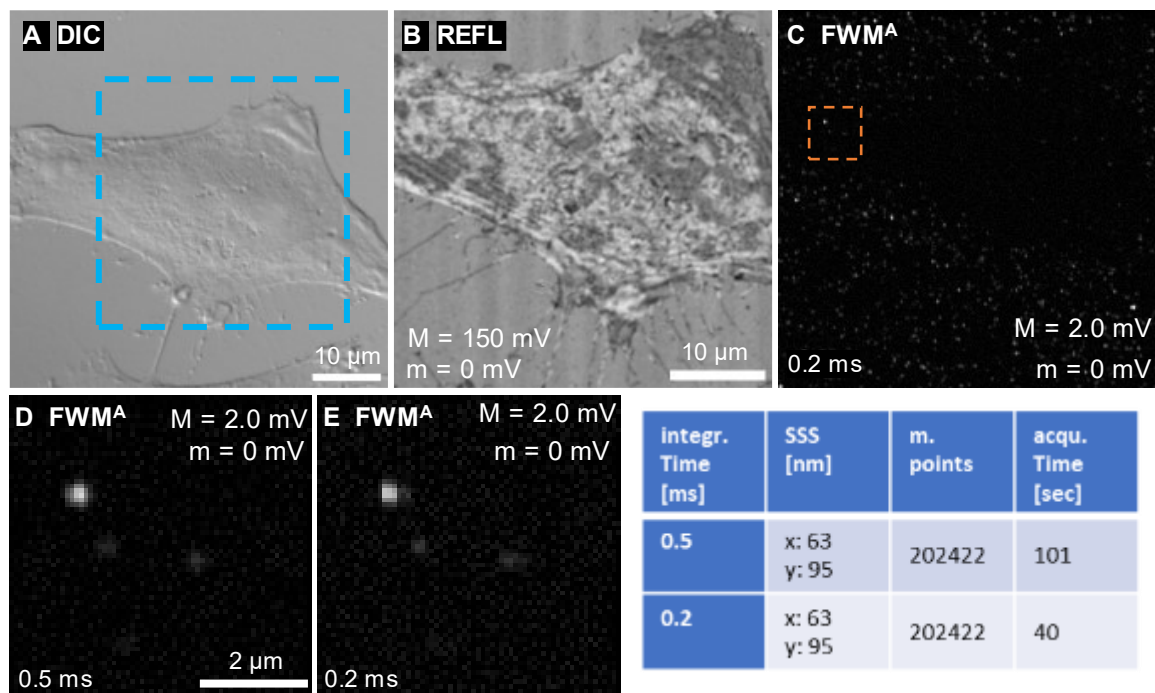


Figure 5.7 | Optimised Fast Scanning in FWMi Utilising Rapid Integration Times and Reduced SSS Settings Along One Axis. FWMi measurements of a fixed HeLa cell after exposure in a pulse-chase experiment with a 30 min serum-starvation step, 30 min GNP-Tf treatment, and fixation in 4% PFA. Measurement settings were set to $x = 63 / y = 95$ SSS across varying integration times to assess their impact on image quality in FWMi. (A) DIC image for sample orientation, with the blue dotted line indicating the area measured with FWMi, resulting in (B) REFL and (C) FWM^A images. This region underwent imaging twice, with integration times of (D) 0.5 ms and (E) 0.2 ms, specifically focusing on the section highlighted by the orange dotted square in (C). An accompanying table details the impact of these settings on measurement points and acquisition time for the complete $40 \mu\text{m}^2$ FOV. Nominal pump/probe powers before entering the microscope: 60/30 μW . $\tau = 0.5$ ps.

5.2.4 Live cell imaging chamber set-up

Maintaining cell line viability during measurements requires a sample chamber that closely controls the ambient environment of the cells. This involves the consideration of several factors, starting with temperature control. Cells generally thrive at a stable temperature that mirrors physiological conditions, typically around 37°C for human cells¹⁵⁶. The control of the atmosphere conditions is equally important. HeLa cells, as most human cell lines, need to be maintained at a specific pH, which in cell culture is regulated by the use of specific carbon dioxide levels, usually around 5%. This requires an incubation chamber equipped for CO₂ regulation¹⁵⁶. Furthermore, high humidity levels are needed to prevent the culture medium from evaporating, which could alter its supplement concentration and pH, affecting the health of the cells negatively. Furthermore, when updating a microscope for live cell imaging, the stage needs to be able to hold an appropriate growth substrate such as a cell culture dish. The introduction of a heated element onto a microscope introduces the potential of thermal drifts of the focus as well, which need to be mitigated by allowing enough time for the microscope elements to come to temperature.

The FWM microscope was updated to allow live cell imaging taking the mentioned factors into account. The installed parts are shown in Figure 5.8. This upgrade involved the installation of a heated stage capable of holding a 35 mm glass bottom cell culture dish (Figure 5.8A) with a ring attachment to heat the sides of the cell culture dish (Figure 5.8B and C). To maintain cell viability for extended periods of time, a heated lid with a glass top was integrated to provide uniform heat distribution and to allow for clear, unobstructed imaging (Figure 5.8D). Heating of the glass top was implemented to mitigate condensation on the glass surface, which could potentially interfere with image acquisition using DIC microscopy, though FWMi remains unaffected by the presence of such droplets on the lid due to its epi-detection geometry. Tube connectors were attached to the heated lid to enable a continuous flow of CO₂ (Figure 5.8D). The CO₂ was humidified in a heated humidification tube to prevent cell media evaporation and maintain a consistent microenvironment and pH (Figure 5.8E). A heating strip was attached to the imaging objective to prevent localised cooling in the area under observation, as illustrated in Figure 5.8F. The control units for the heating elements are displayed in Figure 5.8G and H.

Control Unit 1, depicted in Figure 5.8G, regulates the temperature of the humidification chamber to 45°C. This temperature setting accounts for the thinness of the heating strip relative to the tubing and takes into account that there will be slight cooling of the humidified CO₂ as it travels through the tubing to the live-cell imaging chamber. The culture dish itself was set to be heated at 43°C. While this temperature may appear high, only the dish's side walls were heated.

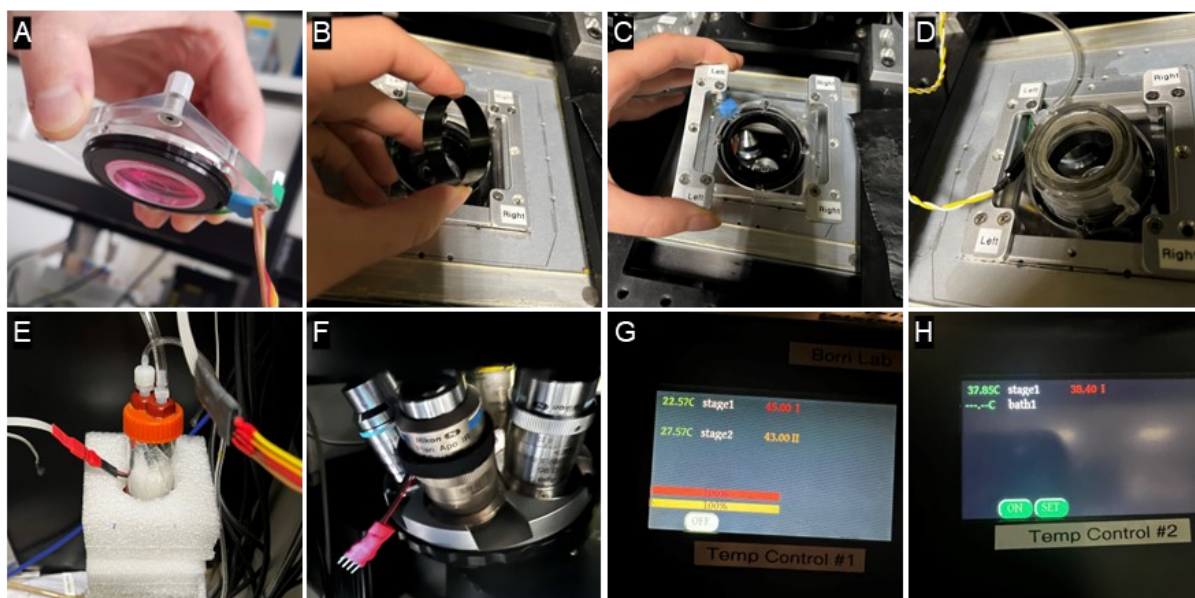


Figure 5.8 | Live Cell Imaging Chamber Components. (A) Heated stage holder designed for a 35 mm glass bottom dish, ensuring the specimen remains at a constant temperature. (B) Circular heating ring to distribute heat uniformly across the cell culture dish's perimeter. (C) Assembly of the components mentioned above. (D) Heated lid equipped with a glass top and tube connectors, facilitating CO₂ circulation. (E) Humidification chamber with an inlet for CO₂ supply from a gas bottle and an outlet for the humidified CO₂ to prevent evaporation of the cell culture media. (F) A heating strip used to heat the objective to prevent cooling of the chamber due to contact with a cold immersion oil objective. (G) Temperature control unit for regulating the heating strips around the humidification chamber (stage1, preset to 45°C) and the heated stage (stage2, preset to 43°C). (H) Second temperature control unit responsible for the heating strip around the objective (stage1, set to 38.4°C), providing an additional layer of temperature stability for the imaging process.

The temperature of the media was measured at 36.9°C using a miniature temperature probe (TC-TP, Bioscience Tools) placed in the centre of the dish. Temperature Control Unit 2, shown in Figure 5.8H, heats the objective to 38.4°C. This ensures that the sample does not cool during imaging without risking damage to the objective.

To evaluate the live cell chamber's functionality, live HeLa cells were subjected to prolonged imaging using DIC prior to FWMi measurements to assess their viability. This approach ensured that any potential adverse effects on cell health could be attributed to the imaging chamber environment, rather than to the intensity of laser illumination used. A representative FOV from these measurements is depicted in Figure 5.9A, showing multiple live HeLa cells over time. More specifically, three cells were observed undergoing division – indicated by a blue arrow at 30 min in Figure 5.9B, an orange arrow at 52 min in Figure 5.9C, and a navy arrow at 122 min in Figure 5.9E – followed by successful reattachment of the cells to the culture dish as shown in Figure 5.9F. The occurrence of cell division within the FOV served as an indicator of cell culture conditions being maintained, confirming the live cell chamber's functionality in preserving cell viability during extended imaging sessions. With the temperature of the cell culture media at 36.9°C at the centre of the dish and no visible

discoloration of the phenol red-supplemented media during measurement sessions, indicating a stable pH, no further optimisation of the temperature settings was conducted.

Subsequently, the cells were subjected to FWMi without the addition of a GNP sample. At this point of the project, confocal fluorescence imaging was integrated into the beam path. Confocal fluorescence data will allow correlative fluorescence and FWMi when needed. The fluorescence signal is excited by the same laser beam employed for FWMi and is then epi-detected. It is then spectrally separated from FWM fields by a dichroic mirror, as detailed in Section 3.2.2. This integration enabled the simultaneous acquisition of FWMi and confocal fluorescence data.

As mentioned previously, fluorescent labelling was included within the project as it serves to validate the GNP tracking capability of FWMi by comparing it to established methodologies. Once FWMi is further developed and reconised as reliable tracking technique for plasmonic NPs, the long-term objective is to eliminate the use of fluorescent labels entirely.

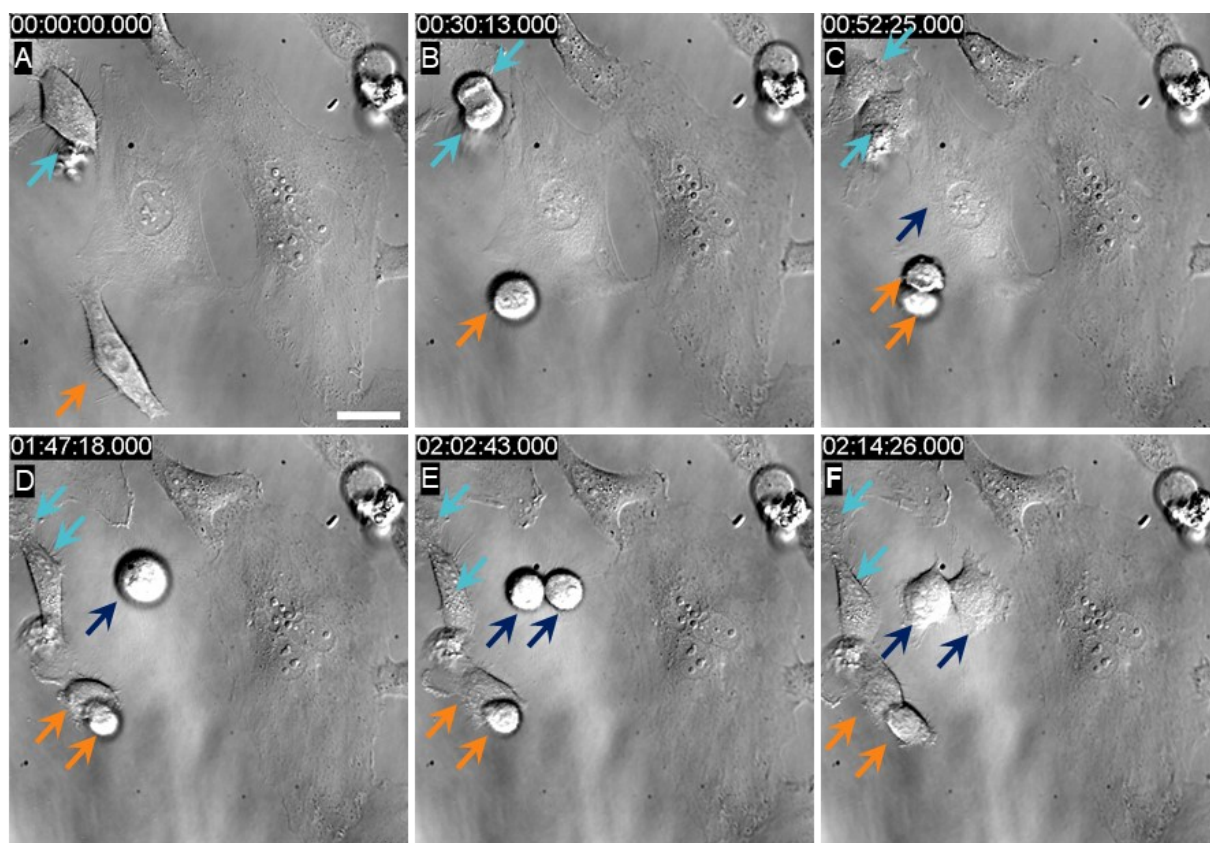


Figure 5.9 | DIC Microscopy Shows that HeLa Cells Viability is Maintained Throughout Extended Imaging Sessions Within the Live Cell Imaging Chamber. DIC images from the multimodal imaging setup demonstrate the live cell chamber's ability to sustain live HeLa cells over time. (A) Displays four live HeLa cells imaged in the live cell imaging chamber. (B) Highlights a cell entering division (blue arrow) 30 min into the measurement. (C) Shows another cell (orange arrow) initiating division after 52 min of imaging. (D) Shows both cells after successful division and reattachment to the culture dish at 1 h and 47 min, while (E) a third cell initiates division 2 h and 2 min into the session. (F) Concludes with all cells reattached after 2 h and 14 min of continuous imaging. Time format: hh:mm:ss. Scale bar: 20 μm .

Figure 5.10 illustrates live cell FWMi of untreated HeLa cells, and demonstrated no observable adverse effects to laser illumination over the course of the experiment. It furthermore proves that nothing within the cell generates FWM signals, even when the pump-pulse train is set to induce FWM dynamics. Figure 5.10A-H shows REFL data of this measurement, highlighting observable cellular movements. The FWM^A in Figure 5.10J confirmed the absence of background signals, consistent with observations from fixed cell FWMi. Confocal fluorescence images captured at the start and end of the measurement are presented in Figure 5.10K and L,

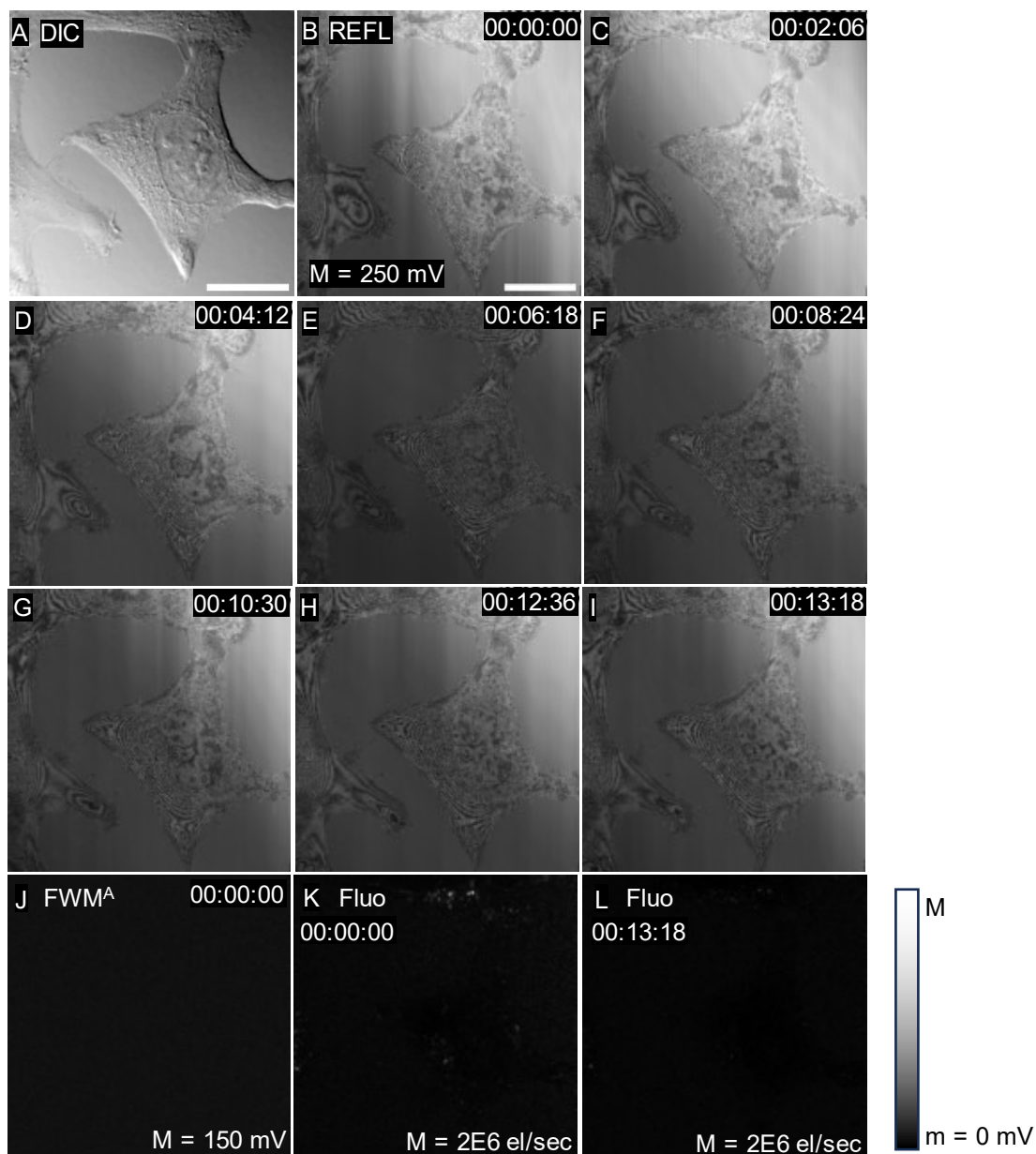


Figure 5.10 | Live Cell FWMi Shows No Adverse Effects on HeLa Cells. This figure depicts a time series of untreated live HeLa cells under laser illumination at the settings used for FWMi imaging to illustrate their viability during FWMi measurements. (A-H) REFL field, capturing subtle cellular movements over the time of observation. (I) MIP of the FWM^A from the same FOV. (J) Confocal fluorescence image at the beginning of the measurement in comparison to (K) the last confocal fluorescence image of the time series. Nominal pump/probe powers before entering the microscope. $\tau = 0.5$ ps. Time format: hh:mm:ss. Scale bar: 20 μ m.

which revealed intrinsic cellular fluorescence, which appeared to undergo photobleaching over time. This finding suggests that the applied laser powers, while low enough to preserve cell viability, were sufficiently intense to cause noticeable fluorescence bleaching within the FOV.

Photobleaching was particularly visible after capturing a subsequent FWMi image with a slightly shifted FOV, immediately following an initial FWMi acquisition, as depicted in Figure 5.11. It shows that photobleaching affected not only the intracellular fluorescence but also the phenol red indicator in the cell culture medium.

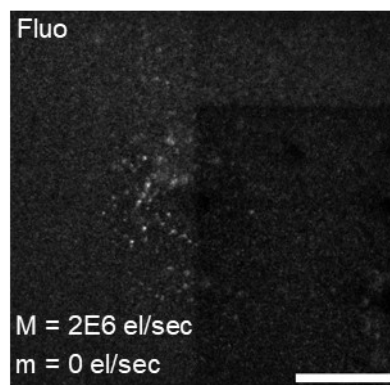


Figure 5.11 | FWMi Laser Illumination Bleaches Intrinsic Fluorescence of Cells and the Cell Culture Medium. Confocal fluorescence of an untreated HeLa cell, showing a FOV immediately adjacent to an area that had just been imaged, showing clear signs of fluorescence bleaching. Nominal pump/probe powers: 60/30 μW . $\tau = 0.5$ ps. Pixel dwell time: 0.2 ms. Scale bar: 20 μm .

5.2.5 Following GNP internalisation events with the help of live cell FWMi

In an initial experiment, GNP-TfA conjugates were introduced directly into the culture dish to evaluate their detection in the FWM^A channel. Figure 5.12 shows representative live FWMi data as false colour overlays, REFL depicted in greyscale, FWM^A in green, and confocal fluorescence in red. To allow the evaluation of their pathways, two GNP trajectories are highlighted with blue and orange lines within the images, indicating their apparent intracellular trafficking over time. This assumption of trafficking was based on the directional movement of the GNP signals, which diverges from random Brownian motion. Although the displayed data shows an area of 17x18 μm , it was originally recorded over a larger field of 30 μm^2 and subsequently cropped during image analysis to more effectively highlight the signals of interest.

Irrespective of whether the observed signals represented actual trafficked or free GNPs or not, this first test confirmed the capability of live cell FWMi to track particles live. Therefore, to study GNP trafficking further, live HeLa cells were once again supplemented with GNP-TfA in a pulse-chase experiment, with continuous measurements taken 400 nm above the glass substrate to capture internalisation events. Pulse-chase experiments are used to study protein behaviour within cells, such as trafficking and degradation¹⁵⁷. Initially, cells are exposed to a short "pulse" of a (usually fluorescently or radio-) labelled molecule of interest. This is followed by a "chase" phase, where cells are washed to remove remaining labelled compounds. The cells are then incubated with the native form of the molecule, usually in complete media, allowing normal cellular processes to continue. The samples can then be imaged at different time points

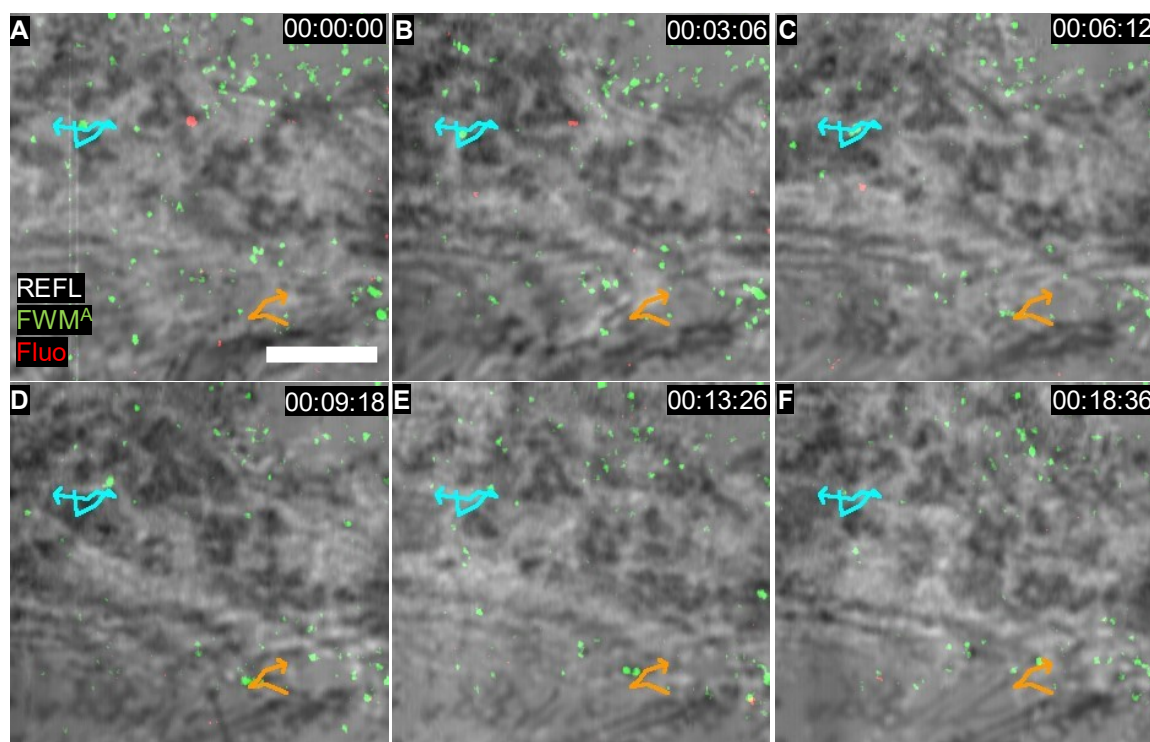


Figure 5.12 | Initial Evidence of Successful GNP Internalisation Captured in Live FWMi. False colour overlays of an FWMi session of a live HeLa cell treated with GNP-Tf after 30 min of serum starvation and subsequent GNP-Tf addition on the set up (no washing off). The presented images combine REFL in greyscale, FWM^A in green, and confocal fluorescence (fluor) in red, to present dynamic live cell FWMi and GNP tracking. Two distinct trajectories of GNP signals illustrate the directional movement of GNPs within the cellular environment (highlighted with blue and orange lines). Nominal pump/probe powers before entering the microscope: 60/30 μ W. $\tau = 0.5$ ps. Pixel dwell time: 0.2 ms. Acquisition time per frame: 62 sec. Time format: hh:mm:ss. Scale bar: 5 μ m.

after the pulse live or they can be fixed at those time points for later imaging. By evaluating the localisation of the signals of the labelled compounds, conclusions about trafficking, endocytosis, or degradation dynamics of the labelled molecules can be drawn.

Figure 5.13 illustrates such an occurrence, showing particle movement over time with exemplary time frames of REFL superimposed with FWM^A from the particle (Figure 5.13A-C). The vesicle the GNP is moving in is also visible in the REFL depending on its z-depth (Figure 5.13D-F). The GNP appears predominantly stationary within the first 30 min of the measurement and exhibits slight shifts in the xy-direction. This conclusion was drawn from the plots showing the GNP displacement over time (Figure 5.13G), the resulting speed of the particle over time (Figure 5.13H), as well as the sum intensity of the signal over time (Figure 5.13I). These plots have been created using the TrackMate plugin available for ImageJ¹²². The sum intensity value was calculated within a mask of a 10-pixel diameter around the centre of the particle. The pattern of movement suggested the GNP's location within an organelle or possibly at the cell membrane.

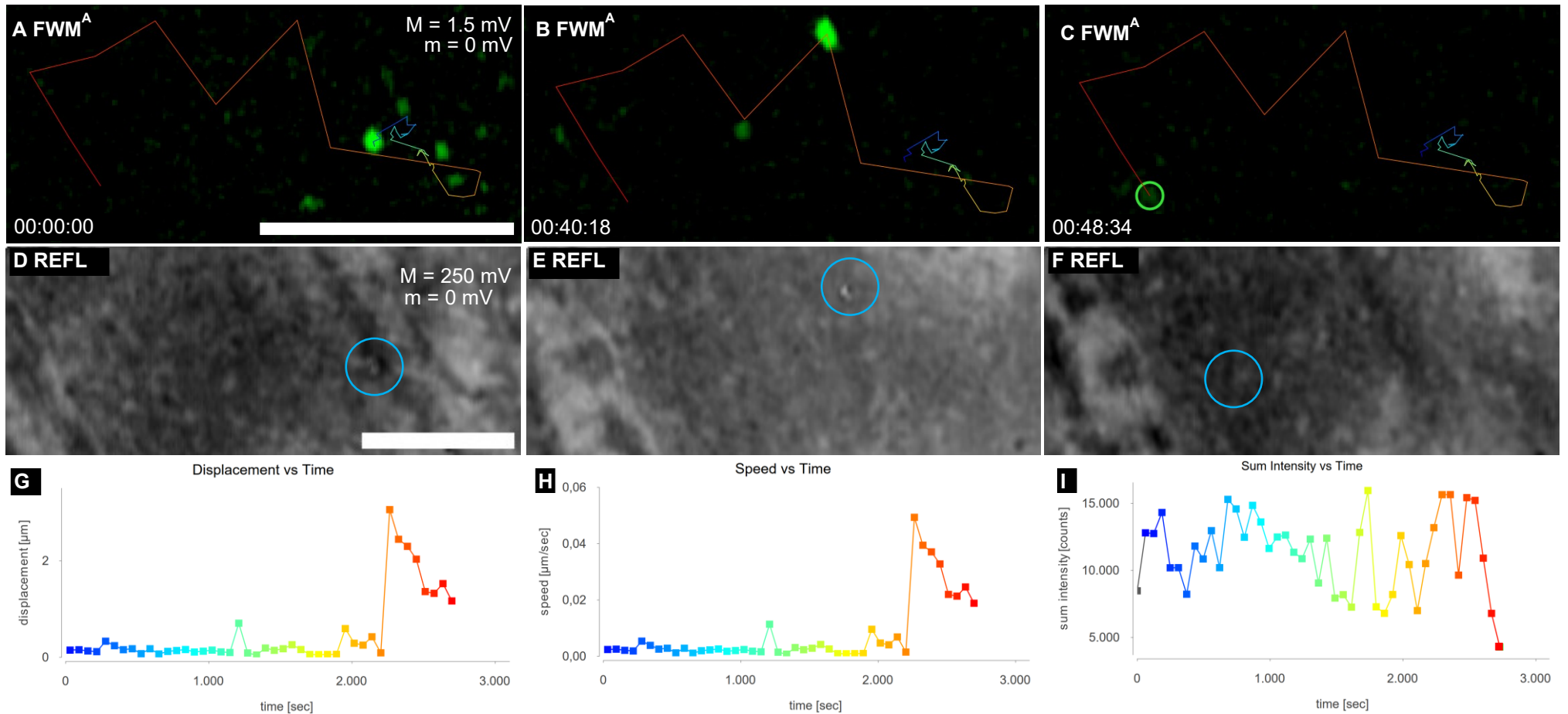


Figure 5.13 | Trafficking Speed Analysis Through Particle Movement in Live Cell Imaging. This dataset depicts live cell FWMi of a HeLa cell treated with GNP-Tf after 30 min of serum starvation and subsequent GNP-Tf addition on the set up (no washing off). (A-C) FWM^A signal of a GNP as it traverses the cellular environment or undergoes possible exocytosis, captured over sequential time points. The green circle in (C) denotes the masked area used for sum intensity calculation. (D-F) illustrate the corresponding REFL at identical time points, revealing vesicular structures within the cell. (G) Displacement over time graph for the duration of the observation before the particle left the FOV (50 min), highlighting a notable shift in particle movement at the 32-minute mark (1920 seconds). This is complemented by (H) a speed versus time plot, providing insight into the changes in GNP trafficking speed. Additionally, (I) shows the sum intensity of the tracked FWM^A signal within a 5-pixel radius from the centre of the signal. Nominal pump/probe powers before entering the microscope: 60/30 μ W. $\tau = 0.5$ ps. Pixel dwell time: 0.2 ms. Acquisition time per frame: 62 sec. Time format: hh:mm:ss. Scale bars: 5 μ m.

Vesicles and organelles, such as endosomes and lysosomes, often remain stationary when docked or tethered at specific sites in the cell. Once engaged with motor proteins, these vesicles transition into active transport along microtubules. For example, vesicle trafficking may involve the movement of cargo between early and late endosomes or from the Golgi apparatus to the plasma membrane. Motor-protein-driven transport along microtubules occurs at speeds typically ranging from 0.5 to 2 $\mu\text{m/s}$ ^{22,158,159}.

Endocytic vesicles formed via clathrin-mediated or caveolin-mediated endocytosis can initially remain near the plasma membrane and stay stationary at their site of internalisation. Subsequently, they engage with motor proteins and are transported along microtubules toward early or recycling endosomes. The transport speed of these vesicles is typically around 0.5 to 1 $\mu\text{m/s}$ ^{158,160}, which is approximately an order of magnitude faster than the displacement shown in (Figure 5.13H). However, it is important to note that this figure represents only the xy displacement, and if movement in the z-axis were resolved, additional displacement might be observed. Similarly, secretory vesicles in exocytosis often remain docked at the plasma membrane for several minutes. If fusion does not occur, these vesicles may disengage and undergo retrograde transport back into the cytoplasm toward the Golgi apparatus or recycling endosomes. This transport is also mediated by motor proteins and occurs at speeds of approximately 0.5 $\mu\text{m/s}$ ¹⁶¹. The exact time of entry into the organelle remains undetermined, as the GNP was already present at this location at the beginning of the measurement. The particle's stationary behaviour changes noticeably 32 min into the measurement, moving closer towards the nucleus. Subsequently, the particle either re-descends in the z-axis to a different intracellular location or possibly it underwent exocytosis at the 32 min mark and drifted away from the cell, which is assumed based on the weaker intensity of the GNP before it left the FOV.

The particle under study expressed movement characteristics associated with a particle that is being trafficked. To give this argument more weight, an additional GNP within the observed FOV that exhibited characteristics consistent with Brownian motion was investigated more closely. The distinction is examined in Figure 5.14, where the behaviours of a directionally moving GNP (dGNP) and a randomly moving particle (rGNP) are compared. The sum intensity of the dGNP remains relatively stable, contrasting with the rGNP, which shows significant fluctuations (as seen in Figure 5.14A and C). This suggests pronounced displacement in the z-direction for the rGNP, leading to notable variability in the FWM^A intensity. The analysis is further enhanced by examining the displacement plots over time, where the dGNP demonstrates minimal lateral movement until a significant change in its trajectory occurs 32 min into the

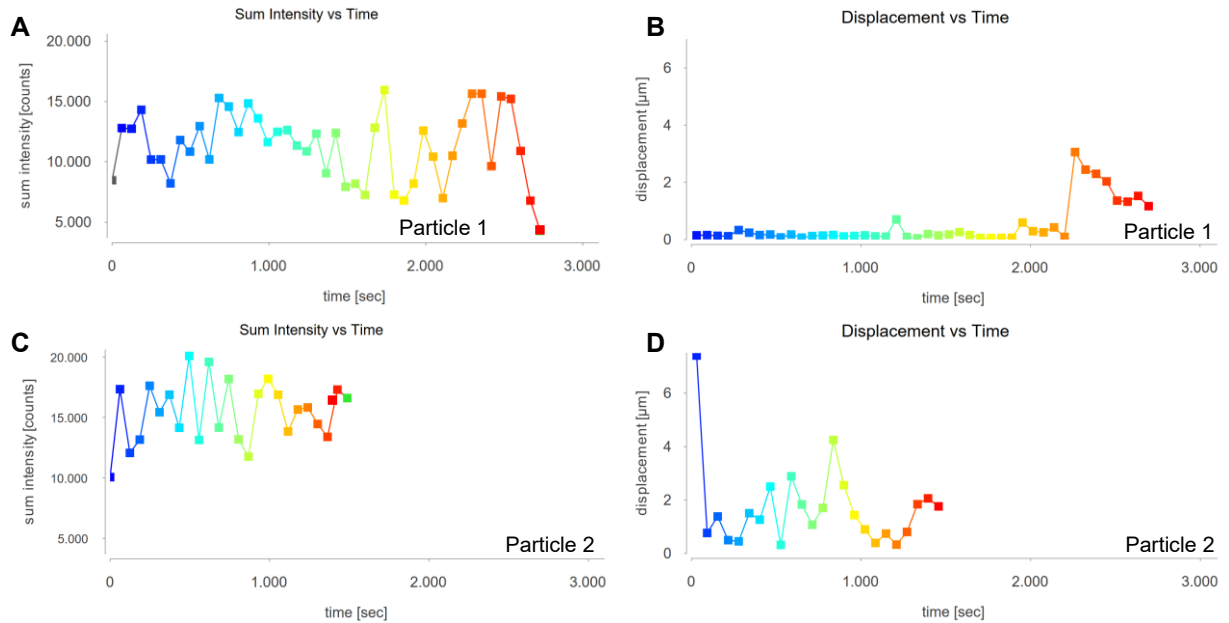


Figure 5.14 | Differential Analysis of GNP Movement: Trafficking versus Brownian Motion. This figure contrasts the behaviour of a GNP undergoing active trafficking with that of a GNP exhibiting Brownian motion. Utilising FWM^A data, the analysis includes plots of (A) mean intensity, and (B) particle displacement over time for the actively trafficked GNP, compared against a particle displaying Brownian movement, represented in plots (C) and (D), respectively. Both particles were identified within the same measurement session, but at distinct time points during the measurement, providing a unique opportunity to compare the dynamics of directed cellular trafficking with random motion. The plots presented in (A) and (B) are the same as the ones shown in Figure 5.13 but with adjusted axes to allow direct comparisons between the two GNPs.

observation. Conversely, the rGNP exhibits substantial displacements between frames, reinforcing the hypothesis that it is not anchored to any structures on or within the cell, supporting the distinction between directed trafficking and random Brownian movement.

Live cell FWMi is a novel technique that needs further foundational research to enable the identification of cellular organelles using REFL data. The potential to identify organelles can be seen in the same data set that has been used to analyse the GNP trafficking event. More specifically, highly dynamic tubular structures were visible throughout the measurement, appearing as a light grey and constantly moving group of small tubes (see Figure 5.15, blue circle). These structures can be found beneath the area where the above-described distinctive particle movement was observed. The behaviour of these structures suggests that these could be tubular endosomes, or mitochondria if they are assumed to be located in the intracellular space, or they could be filopodia if they are located on the extracellular space (membrane), though it is hard to determine whether these signals come from the intra- or extracellular space with certainty. A sorting endosome is an organelle that serves as a key station within the cell's endocytic pathway, where internalised materials from the cell surface are initially received and sorted. It determines the fate of these materials, directing them either back to the cell membrane for recycling, to lysosomes for degradation, or to other destinations within the cell for further

processing. The observed behaviour of the GNP might indicate that it was located within a sorting endosome, with potential outcomes aligning with either the typical recycling pathway of TfA, or receptor crosslinking leading to lysosomal trafficking. Validating the localisation and trafficking patterns of GNPs with additional insights from REFL data still needs more in-depth investigation but shows great potential for further insights into cellular dynamics.

Additionally, further investigations are needed to interpret the mechanisms behind the observed contrast inversions from black to white in the REFL data of the trafficked particle, as illustrated in Figure 5.16. This figure presents three consecutive frames from the same data set discussed in Figure 5.13 and Figure 5.15, highlighting the vesicle encapsulating the

GNP and exhibiting contrast inversion behaviour (Figure 5.16A-C). Additionally, the plot of the maximum intensity over time of the FWM^A is provided once more (Figure 5.16D), which indicates that the particle becomes progressively brighter over the presented frames. This, in turn, suggests that the GNP gets progressively closer to the imaging plane, though the precise trajectory of the particle into the focal plane, whether from above or below, remains uncertain. The signal appears blurry and white with a dark edge when outside the focal plane, turning black as it reaches the focal point and transitioning to a clear white as it exhibits maximum signal strength in FWM^A. While these observations serve as a preliminary basis for analysis, they require confirmation through additional measurements of similar nature.

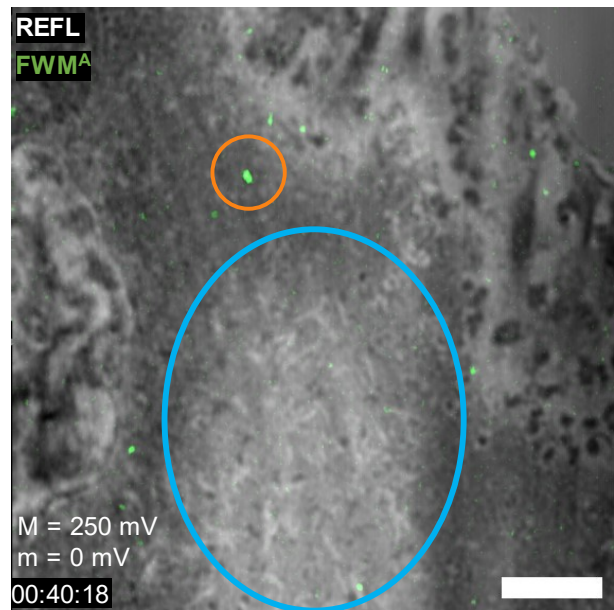


Figure 5.15 | Expanded Field of View for GNP Tracking Suggests Localisation within a Sorting Endosome. This figure combines REFL data, presented in greyscale, with FWM^A signals in green, to illustrate dynamic, elongated tubular structures indicative of sorting endosomes, delineated by a blue circle. The depicted data, collected for the purpose of GNP trafficking analysis, identifies the GNP previously shown in Figure 5.13, highlighted in orange, highlighting its association with sorting endosomal pathways. This image highlights the capability of REFL data to infer information of cellular structures. Nominal pump/probe powers before entering the microscope: 60/30 μW . $\tau = 0.5$ ps. Pixel dwell time: 0.2 ms. Acquisition time per frame: 62 sec. Time format: hh:mm:ss. Scale bar: 5 μm .

In subsequent experiments, specific GNP trafficking events like the one described were not consistently captured, partly due to the limited FOV of FWMi that requires 'being in the right place at the right time' to observe such dynamics. Challenges also arose from the quality of GNP-TfA constructs, which often exhibited off-target binding, either adhering excessively to the culture dish or binding to cell surfaces without being internalised. It should be noted that particle movement is not immediately noticeable while data is acquired due to the slow frame rate, therefore every data set needed to be processed before it was clear whether an internalisation event was observed within the FOV. Therefore, the probability of conducting measurements with low quality GNP-TfA conjugates can lead to entire measurement sessions without meaningful GNP tracking data. To address these challenges, a comprehensive evaluation of various functionalisation techniques has been conducted to allow studies on GNP-TfA trafficking, which is the focus of the next chapter of this work.

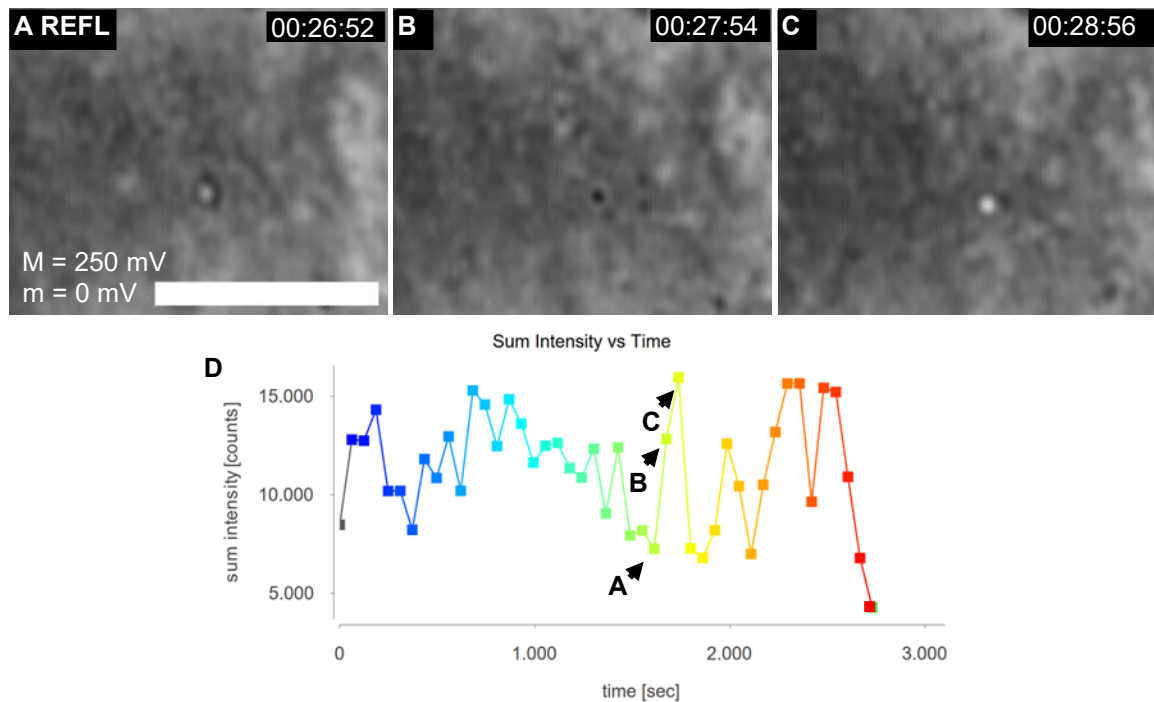


Figure 5.16 | Contrast Inversions in REFL Signal as Indicators of Vesicle Position Relative to the Focal Plane. (A-C) Three sequential frames REFL data, capturing a GNP as it transitions into focus during FWMi imaging of a live HeLa cell treated with GNP-Tf after 30 min of serum starvation sample addition on the set up (no washing step). These frames demonstrate notable contrast inversions from white to black, and then back to white, suggesting changes in the vesicle's proximity to the focal plane. (D) Intensity over time plot for the FWM^A channel, correlating with the observed time points, thereby providing insights into the dynamic intensity variations associated with the vesicle's movement. Nominal pump/probe powers: 60/30 μ W. $\tau = 0.5$ ps. Pixel dwell time: 0.2 ms. Acquisition time per frame: 62 sec. Time format: hh:mm:ss. Scale bar: 5 μ m.

5.3 Limitations and Future Considerations

5.3.1 Live cell FWMi needs further development for faster image acquisition

The implementation of live FWMi has highlighted its potential for measurements of GNPs as they traverse the intracellular environment. This technique shows great potential to reveal more details of the pathways and interactions of GNPs within live cells. However, the temporal resolution of image acquisition needs improving.

The frame rates achieved during these experiments, while sufficient to track GNP movement, have limited the ability to make real-time judgements during the imaging session, as GNP movement could only be identified during post-processing of the FWMi data. This limitation sometimes resulted in prolonged imaging sessions where the selected area did not yield insights on GNP trafficking. Therefore, faster frame rates would not only aid in revealing GNP trafficking pathways in more detail, but they would also allow an immediate evaluation of the imaging process, allowing adjustments during imaging sessions in real-time. This would not only enhance the efficiency of data collection but also ensure the optimal use of resources and time. In its current configuration, FWMi requires 46 s to acquire a $80 \times 80 \mu\text{m}$ frame. This temporal resolution was sufficient to reveal slower processes such as vesicle docking, endosomal maturation, and clathrin mediated endocytosis^{162,163}. However, it was inadequate for tracking intracellular vesicle transport along microtubules, which occurs at speeds of $0.5 - 2 \mu\text{m/s}$ and requires a temporal resolution of 10–100 ms per frame to accurately resolve vesicle movements¹⁶⁴. Diffusion over $10 \mu\text{m}$ occurs within 1-10 s within mammalian cells¹⁵⁹.

Receptor recycling, which typically takes 5–15 minutes, can be tracked with a frame rate of 10–30 seconds per frame to capture different stages of the transport process¹⁶⁵. For events requiring higher temporal resolution, such as fast vesicle transport, FWMi can achieve faster frame rates by reducing the frame size. However, this approach requires precise positioning to ensure that the region of interest is captured at the right moment, as the smaller field of view increases the risk of missing key events.

To address these challenges, our research group has initiated plans to further develop the FWMi technology. Two upgrades are being considered, i) galvo-mirror beam-scanning FWMi (as opposed to the existing sample stage scanning), and ii) wide-field illumination and camera-based FWM detection. Both advancements promise to mitigate the limitations of slower frame rates. Regarding the use of galvo mirrors, they will allow to speed up the laser scanning process (~few microseconds per point), as compared to using the piezo nanostage which is significantly

limited by its mechanical response time (~10 ms). Beam-scanning will require to collect FWM in a “de-scanned” configuration, to enable its overlap with the external reference.

5.3.2 The live cell imaging chamber does not create a sterile environment

The live cell chamber environment on the FWMi set-up is not sterile and therefore presents an additional source of consideration when planning experiments. While none of the experiments conducted during the course of this project have been affected by cell culture infections following imaging in the live cell chamber, the risk remains a concern. Possible solutions for this are the addition of antibiotics to the cell culture medium to prevent infections, adding a filter into the CO₂ line, or using a sterile lid on the sample that allows DIC imaging. Samples exposed to live FWMi were discarded after an imaging session. Should future research require longer measurement periods, upgrades to the current imaging chamber would be necessary.

5.3.3 A better GNP-Tf conjugate quality is needed for meaningful studies

The GNP-TfA conjugates used in this study up to this point have shown significant adherence to the culture dish and, as outlined in Chapter 4, contained a substantial proportion of unconjugated components (free TfA and unlinked GNPs). This, in conjunction with prolonged acquisition times, considerably complicated real-time decision-making during imaging sessions, leading to inefficient utilisation of both time and resources. Although published functionalisation protocols, which are elaborated upon in the subsequent chapter, were adopted to synthesise GNP-TfA conjugates, these protocols originally used GNPs as drug delivery vehicles and not as imaging agents, but rather focused on fluorescently labelled proteins as secondary label of the NPs. The observed low incidence of particle internalisation events might suggest that previous studies have mistakeably categorised crosslinked proteins as internalised GNPs more frequently than was accurate.

For similar projects to the one detailed in this thesis, it is important to explore and establish functionalisation techniques that minimise non-specific interactions of GNPs and develop a purification strategy that effectively isolates GNP-protein conjugates from free reaction constituents. Such advancements are important for enhancing the specificity and effectiveness of GNPs as imaging labels in biological research, facilitating more accurate and reliable observations of NP behaviour within cellular environments.

5.3.4 Further assessments of REFL and FWM^A are necessary to better interpret the data

FWMi has successfully demonstrated its capability to capture not only the temporal dynamics of GNP movement but also the structural dynamics occurring within or on the surface of cells. This pioneering data introduces new possibilities that require detailed foundational analysis. Structures in motion have been observed in REFL data. However, their precise nature remains to be determined. A targeted investigation could entail the recording of multiple untreated cells at small z-intervals to thoroughly analyse identifiable structures. REFL is particularly sensitive to structures enveloped by membranes, as it relies on variations in the refractive index to generate contrast. Enhancing this data with live recordings taken at incremental z-steps, while pausing at each z-plane to gather extended information on the movement of these structures, could significantly enrich the understanding of cellular dynamics recorded by FWMi.

Interpreting the directional movement of vesicles and particles along the z-axis presents an additional challenge, specifically whether they ascend or descend through the focal plane. Previous reports suggest that analysing the phase of GNPs could provide insights into their movement direction, utilising FWM^A data as a basis for this analysis. Although this aspect was not explored within the scope of the current work, it highlights an important area for future research when using a FWMi set up. Collectively, integrating these approaches promises to refine the ability to accurately identify cellular structures and understand their dynamics. Developing methodologies to identify the directional movement of intracellular vesicles and particles will be important for advancing FWMi as a strong microscope in the field of nanobiotechnology that combines the capabilities of a number of different separate microscopes.

5.4 Conclusions

Within this segment of the research, the introduction of a live mode for FWMi has been effectively realised, demonstrating the capability to maintain HeLa cells in a viable state throughout the measurement process while simultaneously capturing REFL, FWM^A, and confocal fluorescence data. This advancement allows the detailed tracking of GNP and vesicle dynamics within the cellular environment and has been proven within this chapter.

Conclusively, while live FWMi stands as a formidable technique for exploring NP interactions in living cells, future enhancements are necessary to address existing challenges. These include improving frame rates to enable more dynamic observations, ensuring sterility to prevent contamination, refining the quality of GNP-protein conjugates for more precise targeting, and deepening the fundamental comprehension of data acquired in live cell mode. Preliminary

directions for the advancement of both the setup and analytical methodologies have been outlined, laying a solid foundation for subsequent innovations in acquisition speed and the analytical depth of live-cell imaging data.

This work not only allows further research of particle dynamics but also enables subsequent data analysis methods, offering methodologies for particle movement analysis and three-dimensional cellular visualisation. Identifying GNP functionalisation techniques that consistently produce high-quality conjugates are a focus of this study explored next, thereby enhancing the specificity and effectiveness of FWMi in live cell studies.

The introduction of live mode FWMi significantly enhances the available scientific toolkit, enabling real-time analysis of GNP dynamics and cellular processes. This breakthrough has broad implications across cell biology, pharmacology, and nanotechnology, offering insights into cellular mechanisms and NP interactions on a new level of detail, as FWMi has been shown to resolve rotational dynamics during measurement on top of the already discussed capabilities⁴⁷. Live FWMi within live cells can clarify details of pathways for drug delivery, enhancing the design of targeted therapeutic systems and contributing to safer nanotechnology applications by understanding NPs' intracellular behaviour.

6 Establishing a GNP functionalisation procedure

6.1 Introduction

Many GNP functionalisation procedures have been published and are frequently used to study GNP uptake and trafficking in cells, tissues, or animal models using fluorescence microscopy¹⁶⁶. Prior research has indicated that GNPs and fluorescent markers do not always colocalise^{31,32}. With the developments within the project so far, we have shown that we can validate that fluorescence colocalises with GNPs on spin coated construct samples (Chapter 4), and we have developed a 3D live cell FWMi system (Chapter 5) that can detect GNPs in biological samples. These two developments would allow the characterisation of developed formulations, assess their physico-chemical characteristics, and enable us to follow their trafficking within live cells. In anticipation of these developments, alongside this work we explored functionalisation procedures with the aim of developing a GNP-ligand construct capable of receptor crosslinking at the cell surface, that would be subsequently internalised into the cell. It should be noted that functionalisation procedures were tested from the onset of the project, when FWMi training had yet to be conducted. The validation of experiments was initially solely based on epi-fluorescence microscopy until fixed cell FWMi was introduced, followed by live cell FWMi.

In this part of the project, our objective was to identify functionalisation methods that enhance GNP internalisation into HeLa cells, ideally through receptor crosslinking, to allow more detailed investigations of this mechanism via FWMi, which will be discussed in the following. Here, we explored established functionalisation strategies targeting carboxyls, amines, and thiols. The experiments included GNPs with pre-attached stabilising polymers and those in which the stabilising polymer was appended in-house.

The in-house methods presented in the following involved two approaches: either coating the GNPs with the polymer before TfA conjugation or conjugating the stabilising polymer to the protein first and then attaching this conjugate to the GNPs. Our findings showed that GNPs with pre-attached polymers were not effective in achieving cellular internalisation. Although fluorescence imaging suggested successful binding or internalisation, FWMi indicated minimal to no actual GNP uptake. In contrast, constructs created through in-house polymer decoration demonstrated significantly improved internalisation. Specifically, constructs made using PEG-TfA conjugates for GNP decoration resulted in markedly improved uptake compared to untargeted control GNPs.

6.2 Results and discussion

6.2.1 Functionalisation of GNPs with pre-attached polymers

GNPs are available with a range of pre-attached terminal groups, facilitating the conjugation of proteins through the mechanism of choice. This versatility significantly enhances the adaptability of GNPs for diverse applications and eliminates the time-consuming steps involved in selecting and applying stabilisation protocols. However, the use of pre-attached groups introduces certain challenges, particularly due to the lack of transparency from suppliers regarding the properties of the stabilising polymers used within their products. The undisclosed nature and length of these polymers can obscure the true hydrodynamic radius of the GNPs after conjugation and, by extension, their cellular internalisation capabilities¹⁶⁷. Misinterpretations of experimental outcomes, such as attributing failed internalisation to non-functional proteins, may arise when the actual issue lies in the oversized GNPs. Selecting the optimal strategy for a given application involves balancing considerations such as time efficiency, simplicity of functionalisation, and the degree of control over the conjugation process, to achieve desired outcomes without compromising on the scientific integrity of the experiments.

At the start of the project, GNPs pre-conjugated with a stabilising polymer were utilised as they allow an easy entry point to GNP functionalisation, potentially reducing time and resources spent on doing the entire functionalisation in-house. For initial experimental procedures EDC-NHS and sulfo-SMCC, the two predominantly utilised crosslinking chemistries were selected⁵⁷. The reaction mechanisms of these are explained in detail in Sections 3.1.1.2 and 3.1.1.3. These reactions required the use of GNPs terminated with carboxyl and thiol groups, respectively. The reactions employing EDC-NHS and sulfo-SMCC chemistries were performed according to the procedures described in Section 3.1.1 with two distinct TfA concentrations for each functionalisation method. This was done to test which concentration of TfA appeared to be more promising in inducing receptor crosslinking and then adjust concentrations, if necessary, after the analysis of these construct samples. The concentrations chosen for the first experiments were a ratio of 100 TfA to 1 GNP, and 1000 TfA to 1 GNP. Following the vendor's recommendation for GNPs, a protein to GNP ratio of 100:1 was suggested. Hence, this concentration, along with a level an order of magnitude higher, was evaluated. This approach aimed to determine the protein density that allows effective cell internalisation, ensuring efficient coverage and functional activity of the GNPs. The vendor states a labelling of 2 ASs per nm² GNP surface. GNPs of 20 nm diameter have a surface area of 1256 nm², equating to roughly 2500 ASs per GNP. This corresponds to 0.04 and 0.4 TfA/AS, respectively.

To aid the line of discussion, constructs functionalised with TfA using EDC-NHS are denoted as 0.04-NHS-GNP and 0.4-NHS-GNP, respectively, while those functionalised with sulfo-SMCC will be denoted 0.04-SMCC-GNP and 0.4 SMCC-GNP.

As first line of particle functionalisation validation, UV-Vis spectra of the GNP samples were measured (Figure 6.1). UV-Vis spectroscopy is an important technique for analysing GNP samples, particularly when evaluating functionalisation success and sample quality. This method exploits the SPR of GNPs, which shifts in response to changes in particle size, shape, and their surrounding medium¹⁶⁸. A red shift in the SPR peak typically signifies the attachment of biomolecules or ligands to the GNPs, altering their local refractive index and therefore indicating functionalisation, though the shifts are usually small for spherical GNPs (2-5 nm)¹⁶⁹. The UV-Vis spectra also provide insights into the aggregation state of GNPs. A broadened SPR peak suggests aggregation, whereas a sharp peak indicates a well-dispersed sample. Additionally, the peak width offers clues about the uniformity of the GNP size distribution. Comparative analysis of UV-Vis spectra before and after functionalisation can confirm ligand attachment and NP stability. For further information, one can refer to Mauriz *et al.*¹⁷⁰ and Conde *et al.*⁵⁶. When assessing UV-Vis spectra, the optical density (OD) of the GNP sample can also be used to assess sample quality prior to and after functionalisation. A change in OD after functionalisation can indicate the success of biomolecule attachment to the NP surface, again by altering the GNP's SPR properties due to the changed surrounding dielectric environment¹⁷¹. Stable or increasing OD values suggest successful functionalisation and maintained NP concentration, indicating that the GNPs are well-dispersed and stable. Conversely, a decrease

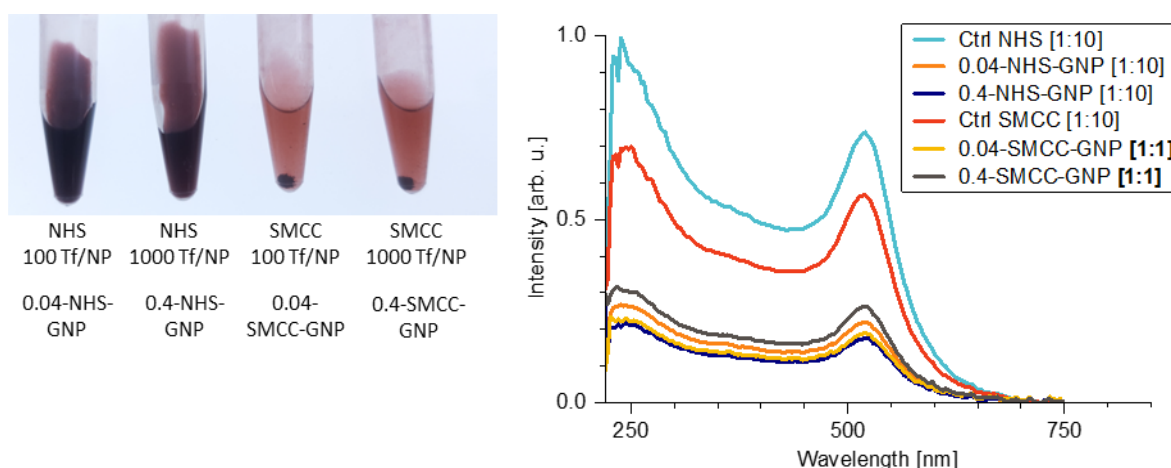


Figure 6.1 | Sulfo-SMCC and NHS Functionalisation Induce Aggregation and Destabilisation in GNPs. The photo shows the different constructs after functionalisation, with sulfo-SMCC reactions showing clear signs of aggregation (loss of OD). The UV-Vis spectra of the resulting constructs show a reduction in OD₅₂₀ between samples functionalised with EDC-NHS reaction chemistry at a ratio of 0.04-NHS-GNP (orange, OD₅₂₀ 0.22, 1:10 dil.) and 0.4-NHS-GNP (navy, OD₅₂₀ 0.176, 1:10 dil.) compared to particles prior to functionalisation (blue, OD₅₂₀ 0.737, 1:10 dil.). Loss of GNP is especially evident in sulfo-SMCC reactions in 0.04-SMCC-GNP (yellow, 0.191, no dil.) and 0.4-SMCC-GNP (grey, 0.263 no dil.) in comparison to the GNP solution prior to functionalisation (red, 0.566, 1:10 dil.).

in OD may signal NP aggregation or loss, highlighting potential issues in the functionalisation process. As such, monitoring OD serves as a straightforward, non-destructive quality control measure^{56,172}. In practice, a loss of particles will occur during GNP functionalisation reactions, as not every particle is pelleted during centrifugation, and some will be lost during the removal of supernatants and resuspension. Centrifugation is a necessary and standard practice to remove unconjugated reaction constituents from the sample¹⁷³. If the correct centrifugation speeds are applied, the GNPs will pellet, and the free polymers and proteins will remain in the supernatant.

The original stock solution of GNPs with proximal primary carboxyl groups (Ctrl NHS) had an optical density at the LSPR wavelength of 520 nm (OD_{520}) of 7.37, while the OD_{520} for the constructs was measured at 2.20 for 0.04-NHS-GNP and at 1.76 for 0.4-NHS-GNP constructs. This corresponds to a GNP loss of 60% and 76%, respectively. This reduction in GNP quantity seems too high to solely be attributed to GNP loss during repeated decantation, suggesting that colloidal instability during functionalisation is a contributing factor. This colloidal instability was especially pronounced in samples functionalised using sulfo-SMCC reaction chemistry, showing significant aggregation of the GNPs, as depicted in Figure 6.1 visible as aggregates after resuspension in the storage buffer PBS. The initial OD_{520} of the stock solution of GNPs with proximal primary amine groups (Ctrl SMCC) was 5.6, while the OD_{520} values registered at 0.191 for the 0.4-SMCC-GNP and at 0.263 for the 0.04-SMCC-GNP constructs. This signifies a reduction of 93% and 90% in the GNP quantity, respectively, relative to unfunctionalised GNPs. Although the majority of this particle loss can be attributed to colloidal instability stemming from the reaction conditions, it was observed that the GNPs adhered to the tube walls after sulfo-SMCC activation. This adhesion persisted, and the GNPs did not re-enter into solution during subsequent functionalisation stages nor sonication. Additionally, there was no shift in the LSPR peak after functionalisation (Figure 6.1). This could indicate that the GNPs were not functionalised, though it is also possible that no LSPR shift is detectable due to the pre-attached polymer corona. As mentioned above, the LSPR shift signifies a change in the refractive index surrounding the GNP. The thickness of this corona is not known and therefore it is not clear if the conjugated protein is close enough at the GNP surface to change the dielectric environment of the particle significantly enough to be registered as a shift in the LSPR peak of the functionalised sample.

The suspended constructs were isolated from aggregates that settled at the tube's base and all samples were subsequently subjected to pulse-chase experiments. As previously described in Section 5.2.5, pulse-chase experiments are used to study protein behaviour within cells, such as trafficking and degradation¹⁵⁷. Initially, cells are exposed to a short "pulse" of a labelled

molecule of interest. This is followed by a "chase" phase, where cells are washed to remove remaining labelled compounds. The cells are then incubated with the native form of the molecule allowing normal cellular processes to continue. The samples can then be imaged at different time points after the pulse live or they can be fixed at those time points for later imaging. By evaluating the localisation of the signals of the labelled compounds, conclusions about trafficking, endocytosis, or degradation of the labelled molecules can be drawn.

In this experiment, HeLa cells were subjected to a 30 min pulse with either the construct or free TfA to assess their trafficking profile by fluorescence microscopy, shown in Figure 6.2. On HeLa cells, GNP-TfA constructs were examined for TfA trafficking that resembled the pathway of receptor crosslinking which has been characterised by Moody *et al.*, who showed how receptor crosslinking affects Tf recycling¹⁶ (refer to Section 1.2). In this line of pulse-chase experiments, we would expect the intracellular presence of unconjugated TfA to be markedly reduced after a longer chase period (e.g. 2h). Specifically, we would expect to find that the quantity of free TfA remaining within the cell would constitute approximately 1% of the level observed at the 0 chase time point¹⁷⁴. On the other hand, we would expect the GNP-TfA

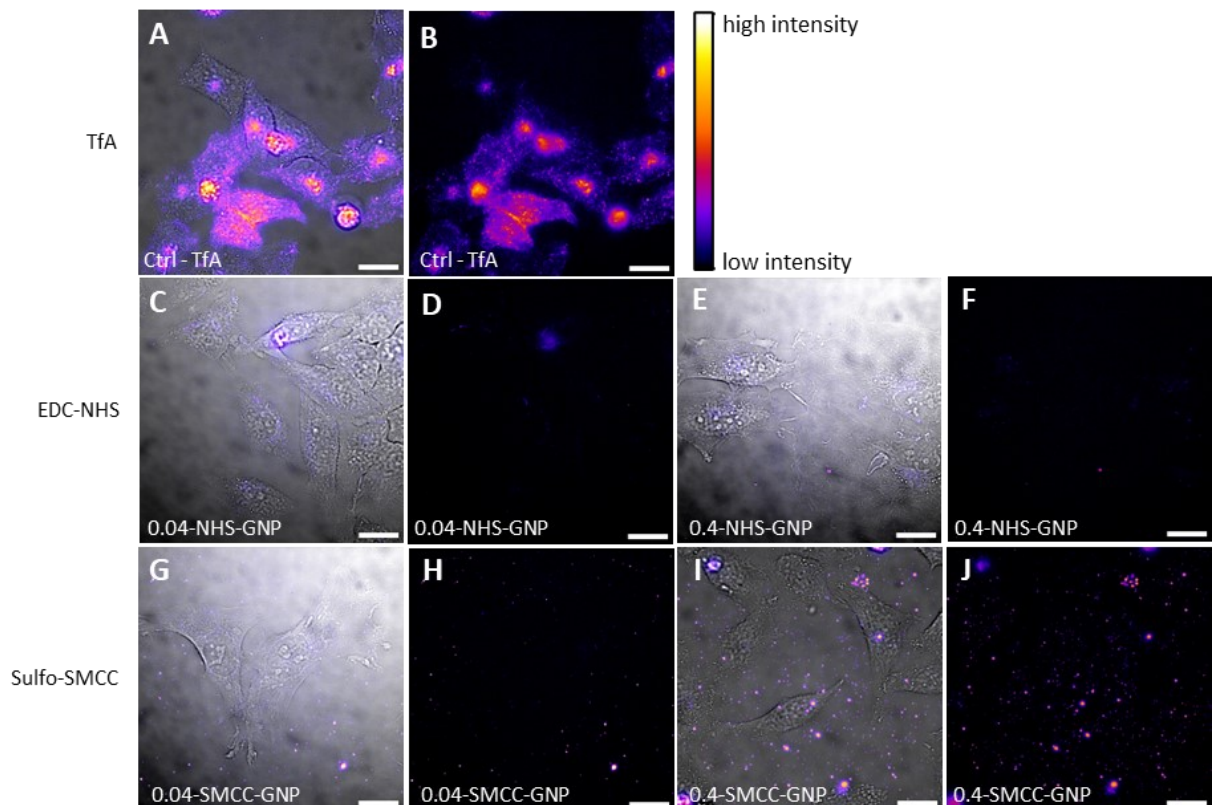


Figure 6.2 | Differential Binding Patterns of SMCC-GNP and NHS-GNP-TfA Constructs to HeLa Cells. Brightfield and z-stack fluorescence images, shown as MIPs, display the interaction of live HeLa cells with various constructs after exposure in a pulse-chase experiment with a 30 min serum-starvation step, 30 min GNP treatment, after a 2 h chase: (A-B) TfA, showing good levels of internalisation. (C-D) 0.04-NHS-GNP and (E-F) 0.4-NHS-GNP, both demonstrating minimal to no internalisation; in contrast, (G-H) 0.04-SMCC-GNP and (I-J) 0.4-SMCC-GNP reveal notable binding to both the cell surface and the Petri dish. Scale bars: 20 μm .

construct signals to accumulate within the cells at specific regions over time without loss of overall intensity, if receptor crosslinking was in fact induced (Section 1.2). As visible in Figure 6.2A and B, free TfA was readily taken up by the cells and was distributed throughout. NHS-GNP-TfA constructs appeared to show no internalisation nor binding to the HeLa cells (Figure 6.2C-F), suggesting that the reaction mechanism did not work under the conditions applied during functionalisation, rendering the recording of further time points not useful due to low sample quality. Cross-correlative studies of the NHS-GNPs later revealed that there was no correlation of GNP and fluorescence signals, validating the assumption of a failed functionalisation (see p. 118 and Figure 6.7). The most common issue with EDC-NHS reaction chemistries is the fast hydrolysis of the NHS group, suggesting that shorter incubation times might solve the issue⁸¹. Further experiments have been conducted using GNPs with a pre-attached PEG-corona terminated with carboxyl-residues while varying the incubation times, pH, or applying various ratios of GNPs to protein but, again, none showed internalisation. The SMCC-GNP constructs predominantly bound to the dish with no visible cell-binding of the 0.04-SMCC-GNP construct (Figure 6.2G-H). It is unclear whether the particles bound the petri dish itself or if they bound compounds secreted by the HeLa cells, or serum components from the cell culture media. The observed stickiness of the particles was likely due to exposed hydrophobic maleimide residues. According to the manufacturer, the surface of the 20 nm GNPs was densely packed with 2 amine sites per nm², providing a lot of sites for sulfo-SMCC attachment. While the small size of sulfo-SMCC may allow efficient coupling to these amine-terminated stabilising polymers, the steric constraints of large molecules such as Tf prevent all maleimide-activated ends from engaging in successful conjugation. This leaves many maleimide groups exposed, increasing nonspecific interactions and promoting aggregation in biological media. To address this issue, reducing the density of sulfo-SMCC during the functionalisation process and capping unreacted maleimide groups with small thiol-containing molecules, such as L-cysteine or mercaptoethanol, could minimise nonspecific binding.

When evaluating internalisation, axial colour-coded representations can be used to distinguish between cell-surface binding and internalisation. Figure 6.3 schematically shows how the uptake of internalising and non-internalising constructs can be assessed using these 2D representations of 3D data. Panels A-D of Figure 6.3 detail the characteristics of non-internalising constructs. These constructs adhere to the cell surface but are not internalised (Figure 6.3A), as the fluorescence signals (or later FWM signals) align with the topography of the cells (Figure 6.3B). This alignment is visible as a colour gradient that closely follows the contours of the cell (Figure 6.3C). Panels D-F schematically depict internalising constructs,

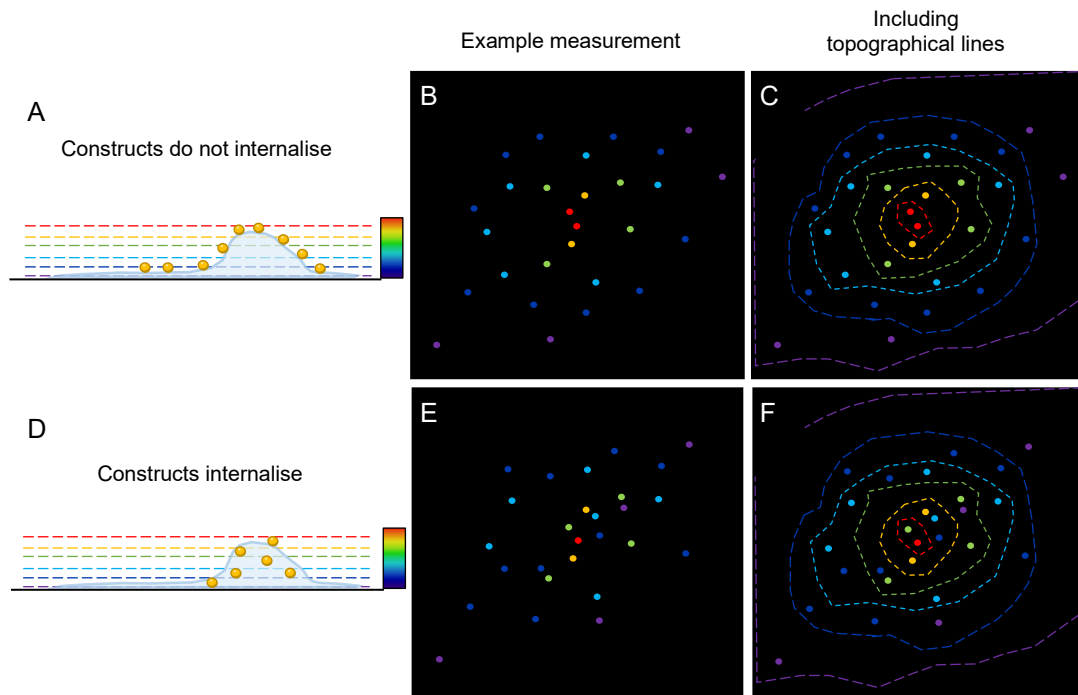


Figure 6.3 | Comparative Analysis of GNP Construct Internalisation in Cells Using Axial Colour-Coded Representations of Fluorescence or FWMi Data. This figure presents a schematic comparison of non-internalising and internalising GNP constructs within cellular environments using axial fluorescence (or later FWMi data) represented as ccMIPs. Sections (A-C) display non-internalising constructs adhering to cell surfaces with fluorescence/GNP signals mirroring cell topography, evident as a colour gradient following cell morphology. Conversely, panels (D-F) illustrate internalising constructs, characterized by a random colour distribution within the gradient, independent of cell morphology. The addition of topographical lines in panels (C, F) further accentuates the axial colour progression in relation to cell structure in both cases.

characterised by the random distribution of colour within the gradient that does not follow the cell's morphological structure. This allows a visual differentiation from surface-bound and internalised constructs. The addition of topographical lines indicating the schematic cell morphology in panels C and F emphasise the variance in axial colour progression relative to cell morphology between non-internalising and internalising constructs.

To assess whether the signals in Figure 6.2I and J show internalised or surface-bound particles, the data of the control (Figure 6.4A-D) and the 0.4-SMCC-GNP construct (Figure 6.4E-H) are further depicted as axial ccMIP and a XZ representation (Figure 6.4D and H). The XZ projections verified internalisation of free TfA, but suggested cell surface association with minimal internalisation of the construct. The constructs appeared to align with the expected topography of a HeLa cell with no notable variation of z-localisation of neighbouring fluorescence signals. The construct signals were in contrast to those of free TfA, as shown in Figure 6.4D which dispersed uniformly throughout the intercellular space. The size of the construct signals suggested either accumulation of multiple GNPs at the same spot, or potential crosslinking between the GNPs. To address this, the concentrations of TfA were increased in subsequent functionalisation attempts to combat potential crosslinking.

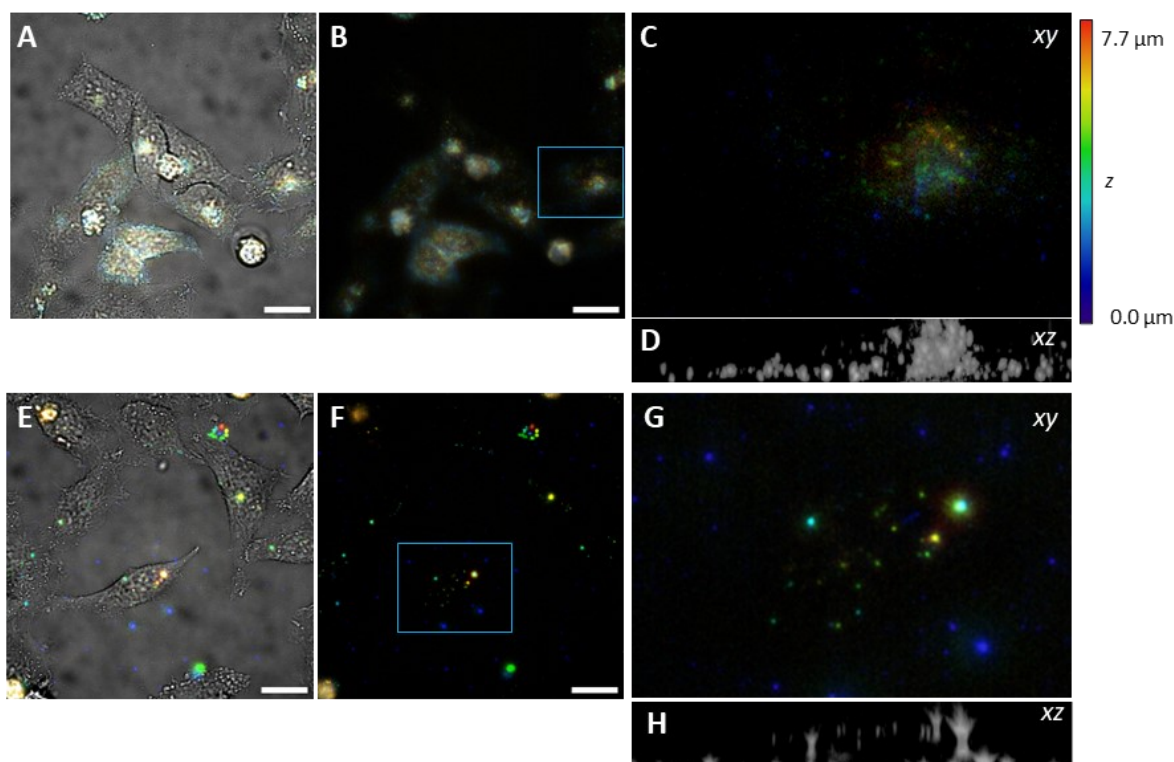


Figure 6.4 | 0.4-SMCC-GNP Constructs Bind Live HeLa Cells But Do Not Internalise. (A) False-colour-overlay of brightfield and axial epifluorescence data presented as an axially color-coded MIP (shown in B) of HeLa cells after exposure in a pulse-chase experiment with a 30 min serum-starvation step, 30 min TfA (A-D) or SMCC-GNP (E-I) treatment. (C) shows an additional zoom of B that is further depicted as an XZ representation (D) to assess Tf internalisation. (E) False-colour-overlay of brightfield and fluorescence data of HeLa cells treated with SMCC-GNP presented as a color-coded MIP (shown in F) and (G) an additional zoom of the color-coded MIP that is further depicted as (H) an XZ representation. Scale bars: 20 μm .

Particle adhesion to reaction tube walls, pipette tips and the cell culture dish was observed after the initial maleimide activation step, which led to the hypothesis that residual unreacted maleimide groups might be responsible for the stickiness of the constructs. Therefore, mercaptoethanol was used to quench any remaining maleimide residues. The resulting constructs of the functionalisation with higher ratios of TfA to GNP (0.4 TfA/AS, 1 TfA/AS and 4 TfA/AS, denoted as 0.4-SMCC-GNP, 1-SMCC-GNP and 4-SMCC-GNP, respectively) were tested again in pulse-chase experiments (Figure 6.5). Free TfA showed the earlier postulated decrease of TfA intensity over time (Figure 6.5A-C) with high signal intensities at 0 min chase and a strong decrease of intracellular signal at 2 h and 4 h chase.

At 0 min chase, SMCC-GNP constructs were evenly distributed within the cellular environment (Figure 6.5D, G, and J). However, a gradual increase in fluorescence signal intensity was observed, accumulating at distinct regions either located in the intracellular environment or on the cell surface. None of the samples show substrate binding, suggesting that mercaptoethanol-quenching was successful and that unreacted maleimide groups on the particles were indeed the cause of the previously reported stickiness. The lack of significant signal intensities at the beginning of the assays suggests minimal crosslinking between the GNPs.

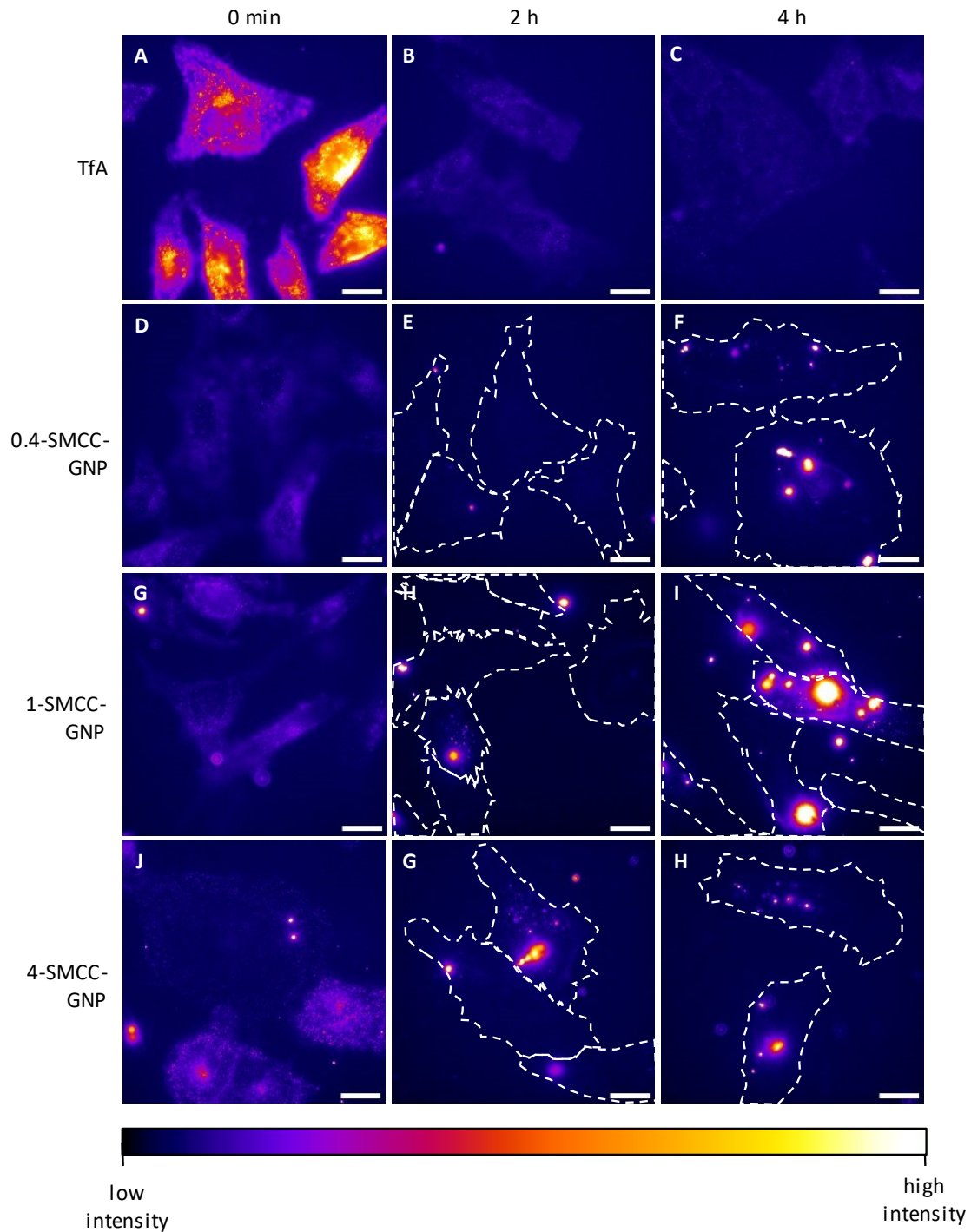


Figure 6.5 | Mercaptoethanol-Quenched SMCC-GNP Constructs Exhibit Binding and Accumulation in Live HeLa Cells. Epifluorescence imaging captures the interaction between live HeLa cells and mercaptoethanol-quenched SMCC-GNP-TfA constructs after exposure in a pulse-chase experiment with a 30 min serum-starvation step, 30 min SMCC-GNP treatment, imaged at timepoints of 0 min, 2h, and 4h, with free TfA serving as a control. (A-C) TfA, and (D-F) 0.4-SMCC-GNP, (G-I) 1-SMCC-GNP, and (J-L) 4-SMCC-GNP, with an increasing accumulation of signal intensities at specific spots in or on the cells. White dotted lines delineate the HeLa cells within the FOV. Scale bars: 20 μ m.

Therefore, it was assumed that the observed accumulation was attributed to cellular trafficking processes, potentially accumulating either within intracellular compartments or on the cell membrane.

The images presented in Figure 6.5 are extracted from time-lapse measurements that highlight the behaviour of the observed signals. Temporal ccMIPs of these data sets reveal that high-intensity signals not associated with a cell exhibit Brownian motion, while signals of similar magnitude and intensity that are cell-associated remain stationary (Figure 6.6, white signals). In contrast, smaller signals of lower intensity display directional movement, signifying intracellular trafficking processes. This suggests a variability in either ligand valency on the GNPs, or there was indeed some crosslinking between the constructs that wasn't initially visible at early time points of the pulse-chase experiment.

To further investigate both SMCC-GNP and NHS-GNP constructs, the samples underwent characterisation by correlative single fluorophore bleaching and extinction microscopy. It should be noted that in cases in which a high level of functionalisation was achieved (Figure 6.7A), identifying spatially correlating signals of fluorescence and extinction was a facile and fast process in which the three particles spanning a triangle across the entire FOV were chosen as reference points for the image transformation software (see Figure 6.7C-E, blue circles), which was explained in detail in section 3.5.6 and 4.2.6.

Generally, correlation between fluorescence and extinction signals was seen for all samples functionalised using sulfo-SMCC. A high variability was found in both characteristics: ligand valency on the constructs as well as varying amounts of construct crosslinking. This can be seen in the analysis of GNP-crosslinking described in Section 4.3.2, which described these specific SMCC-GNP samples. It furthermore showed that there was still a significant fraction of unconjugated TfA present within the sample, complicating the interpretation of the pulse chase experiments.

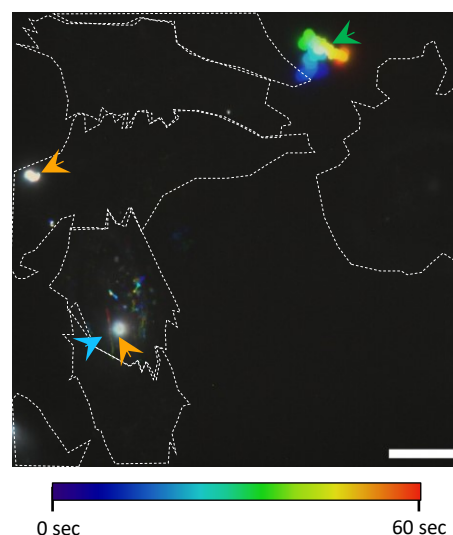


Figure 6.6 | Size- and Intensity-Differentiated Movement of SMCC-GNP-TfA Constructs Within HeLa Cells. A temporal colour-coded MIP of epifluorescence measurements of live HeLa cells after exposure in a pulse-chase experiment with a 30 min serum-starvation step, 30 min GNP treatment, and immediate imaging at the 2h timepoint shows the dynamics of construct movement on or within HeLa cells. Larger, high-intensity signals linked to cells (indicated by orange arrows) remain stationary, while smaller, low-intensity signals (highlighted by blue arrows) exhibit directional movement. Conversely, a large, high-intensity signal unassociated with cells (marked by a green arrow) displays Brownian motion, highlighting the distinct behaviours of SMCC-GNP constructs based on their size, intensity, and cellular association. Scale bar: 20 μm .

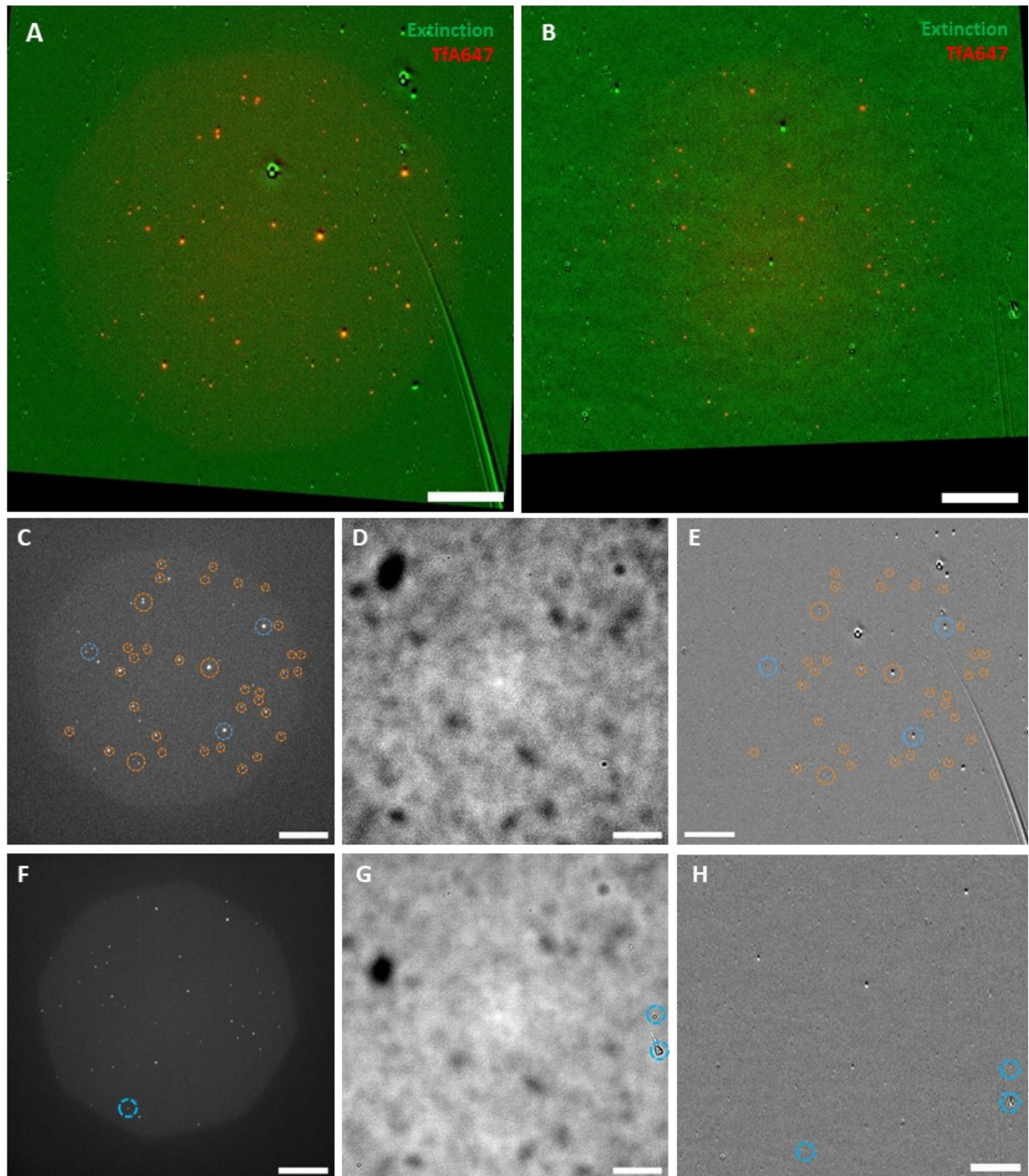


Figure 6.7 | Correlating Structures Across Fluorescence, Brightfield, and Extinction Modalities. False-colour overlays integrate fluorescence (red) and transformed extinction signals (green), contrasting samples with (A) high functionalisation yield (sulfo-SMCC) against (B) low yield (EDC-NHS). In cases of high functionalisation efficiency, correlative analysis between structures was achieved using (C) fluorescence and (E) extinction data directly, bypassing the need for alignment with (D) brightfield images. Conversely, for samples exhibiting minimal functionalisation, correlation of structures required the inclusion of both (F) fluorescence and (G) brightfield data to accurately align with (H) extinction signals. Orange circles highlight areas where fluorescence and extinction signals coincide, coordinates of signals outlined in blue were used as references for image transformation. Scale bars: 20 μm .

NHS-GNP constructs, on the other hand, showed no correlation (Figure 6.7B). In these cases, brightfield and fluorescence measurements needed to be taken into account simultaneously to find common features in both imaging modalities (Figure 6.7F-H). Brightfield images were acquired at each FOV subsequent to bleaching to serve as a reminder of the shape of the scratch (described in section 4.2.5) and to help with recognising the region of interest in extinction. Despite these additional points of validation, none of the samples based on EDC-NHS reaction chemistries returned correlating fluorescence and extinction signals. It remains unclear if this was an issue of conducting the functionalisation correctly or if there was a problem with the preliminary attached polymer corona. Due to the repeated findings of no internalisation nor cell surface binding in cell experiments and no correlation of fluorescence and extinction signals in correlative studies, NHS-GNP constructs made with GNPs with a preliminary stabilising polymer were no longer used in further experiments, in order to focus on samples with more potential for the intended internalisation studies, such as the SMCC-GNP constructs.

At this stage of the project, FWMi was introduced as a tool to investigate GNP internalisation. Therefore, the pulse-chase experiments were repeated using HeLa cells cultivated on coverslips, with cell fixation occurring at various intervals following the pulse to assess the dynamics of SMCC-GNP internalisation. Figure 6.8A shows a fixed HeLa cell treated with 1-SMCC-GNP constructs and in a pulse-chase experiment at the 4h chase timepoint recorded by FWMi. FWM^A data revealed a single GNP signal within the cell (Figure 6.8B-D). Other areas of this sample and all other SMCC-GNP constructs showed two particles at most, indicating that the high intensity signals seen in the previous experiments stemmed from crosslinked proteins, rather than GNP-TfA constructs. Following these results, we transitioned to relying

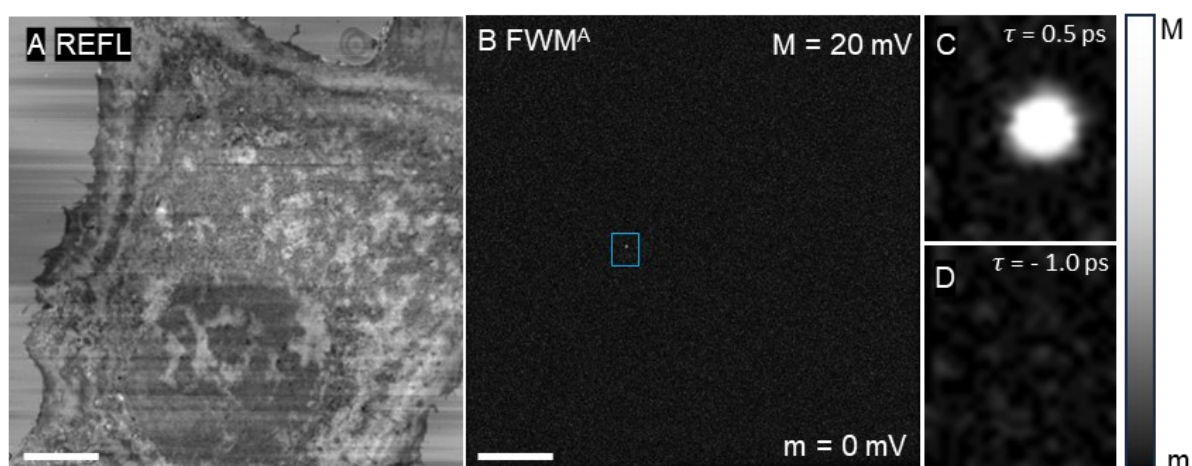


Figure 6.8 | FWMi Analysis Indicates Lack of Internalisation of SMCC-GNP Constructs into HeLa Cells. FWMi of a fixed HeLa cell after 30 min of serum starvation, and a subsequent treatment with mercaptoethanol-quenched 1-SMCC-GNP constructs 4-hours after incubation, showing minimal GNP internalisation. (A) REFL and (B) FWM^A images. (C) Depicts a magnified view of the area marked by the blue square in (B) using a positive pump-probe delay, while (D) presents the same region under a negative pump delay, confirming the signal's origin from a GNP. Scale bars: 5 μ m.

almost exclusively on FWMi to validate construct internalisation in subsequent experiments. This shift was driven by the risk to potentially misinterpret fluorescence signals on and inside the cells originating from residual free TfA as GNP constructs, requiring a more precise technique to assess the presence and localisation of GNP.

In light of the outcomes observed from the EDC-NHS reactions and the extensive protein crosslinking during sulfo-SMCC reactions, subsequent experiments focused on in-house GNP functionalisation reactions including a PEGylation step for stabilisation. This approach was adopted to assess whether the issues encountered were attributable to the pre-attached polymer coating applied by the supplier. The nature of this coating is not disclosed by the vendor and introduces a considerable degree of uncertainty that complicates the subsequent analysis and interpretation of results. At this stage, the reactions seemed to take place between the proteins and the crosslinkers rather than indicating GNP functionalisation. This assumption is drawn based on the comparison between the fluorescence data shown in Figure 6.5 in comparison to the FWMi data shown in Figure 6.8. The interpretation of GNP internalisation in fluorescence data was challenged by the subsequent absence of corresponding GNP signals in FWMi, casting doubt on the effectiveness of GNP functionalisation. While this does not conclusively negate the possibility of functionalisation in general, it raises concerns regarding the sample's quality, suggesting it may not be suitable for conducting meaningful studies on internalisation processes.

6.2.2 Functionalisation of citrate-capped GNPs

While the in-house functionalisation with stabilising polymers introduced a more time-consuming workflow, it awarded a higher level of control of the length of the stabilising polymers as well as the use of more than one form of polymer. PEGylation, the process of attaching PEG chains to GNPs, significantly enhances their utility in drug delivery applications⁷¹. By coating GNPs with PEG, their biocompatibility is increased, reducing potential immunogenicity and minimising recognition and clearance by the immune system. PEGylation improves the solubility and stability of GNPs in biological fluids, facilitating their traversal through biological barriers and increasing their payload's bioavailability⁷².

For GNPs that underwent complete in-house stabilisation and functionalisation, dithiol groups anchored to 5 kDa PEG chains were selected as anchoring agents. Namely, dithiol(diS)-PEG-NHS and OPSS-PEG-NHS (OPN) (Figure 6.9) were chosen as they were proven to effectively internalise to GNPs for applications on cells^{36,175,176}. Thiols are the most widely utilised anchoring-group to attach proteins, polymers, and oligonucleotides to GNPs⁵².

The gold-sulphur interface is intensely studied as it gives way for all fields that make use of functionalised gold surfaces such as nanoscience, material science, and inorganic chemistry. These monolayers can be formed by monothiols (RSH), thioethers (RSR), or disulfides (RSSR) with R representing either an alkyl or an aryl group and the bonds are considered covalent⁵².

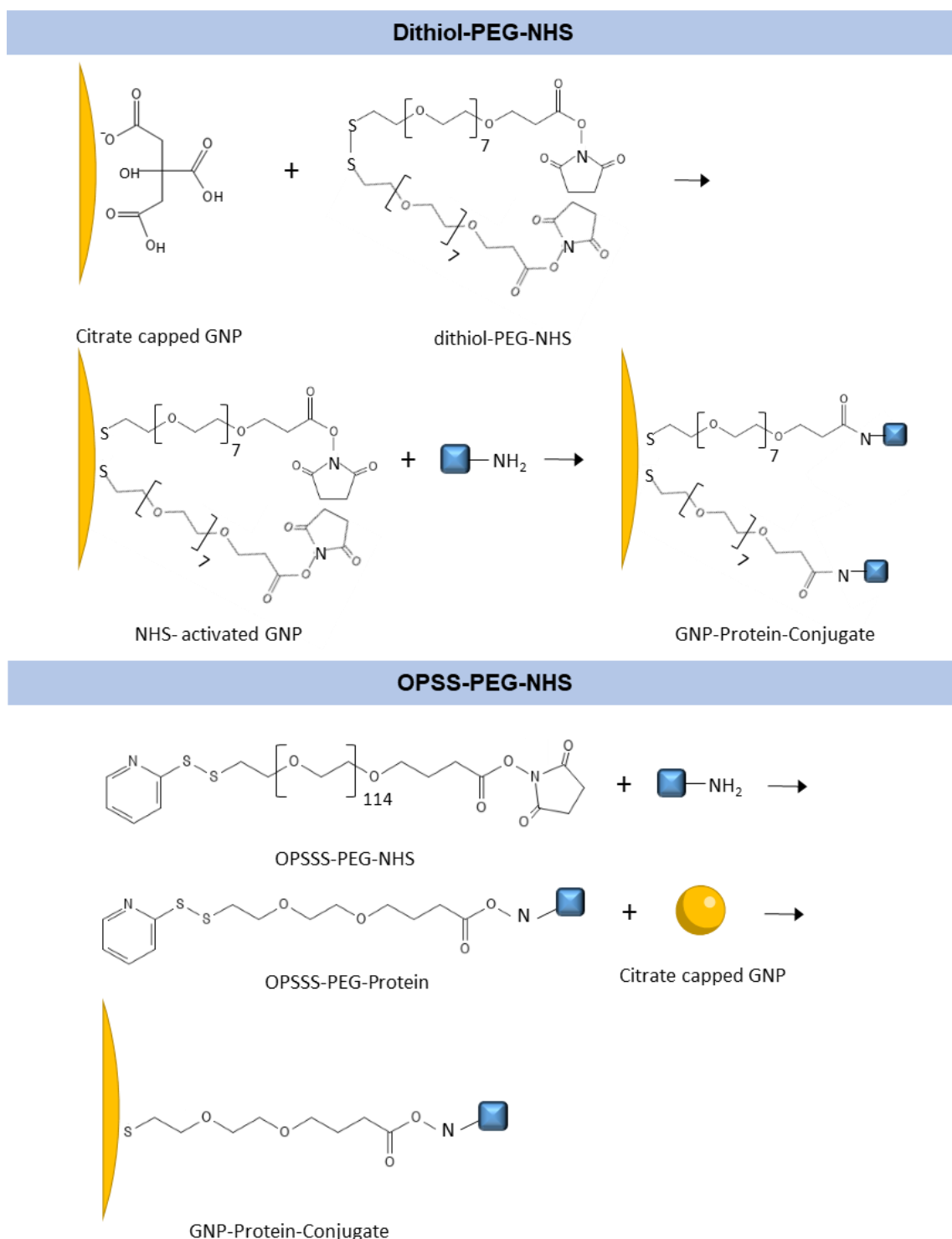


Figure 6.9 | Schematic Overview of Protein Conjugation to GNPs via diS-PEG-NHS and OPSS-PEG-NHS. Schematic illustration of the functionalisation process of diS-PEG-NHS and OPSS-PEG-NHS. diS-PEG-NHS contains a central dithiol group flanked by two PEG chains with proximal NHS groups. OPSS-PEG-NHS has an NHS group on one and an OPSS group at the opposite end. The primary distinction of these approaches lies in the order of functionalisation: diS-PEG-NHS is initially attached to the GNP followed by protein conjugation, whereas OPSS-PEG-NHS is first bound to a protein before facilitating GNP functionalisation.

6.2.2.1 diS-PEG-NHS

Functionalisation of GNPs with TfA was carried out using diS-PEG-NHS, as detailed in the methods section. First functionalisation attempts following the functionalisation mechanism as published by Chen *et al.*³⁶ resulted in irreversible particle aggregation (see Figure 6.10). This method required the use of citrate-capped GNPs, which cannot withstand the high salt concentrations needed for functionalisation reactions. Because of this, the first step of the reaction, i.e. the PEGylation of the GNPs with diS-PEG-NHS, is usually conducted with the GNP suspended in dH₂O rather than using PBS, the suspension buffer of TfA.

Following the conjugation reaction, the particles were centrifuged to eliminate unreacted diS-PEG-NHS and then

resuspended in PBS containing TfA. It was during this functionalisation step that aggregation occurred again, visible by a colour shift in the particle solution from red to blue, or in some cases, to colourless (Figure 6.10). This aggregation was assumed to be a result of the sudden change in salt concentration, which could potentially disrupt the arrangement of PEG strands on the particle surface and additionally hydrolyse the NHS group. To mitigate this, a modified approach was adopted where the particles were first resuspended in DMSO after purification from their citrate storage buffer and the first reaction step was carried out in DMSO. Subsequently, TfA was diluted in dH₂O rather than PBS to allow salt-introduction at a later stage. PBS was used as storage buffer to allow optimal storage conditions and therefore functionality of the conjugated proteins. UV-Vis spectra of the functionalisation reactions with the first step in dH₂O and DMSO, respectively shown in Figure 6.11, revealed a less pronounced broadening of the LSPR peak in the DMSO/dH₂O-based reactions. This suggests a decrease in cross-linking and aggregation of GNPs during stabilisation in DMSO. Additionally at this stage, various concentrations of diS-PEG-NHS were evaluated to determine the optimal diS-PEG concentration for particle stabilisation. The concentrations tested included 0.2 mM (approximately 2 PEG strands per nm²), 2 mM (20 strands/nm²), 4 mM (40 strands/nm²), and 20 mM (200 strands/nm²). The 2 mM concentration exhibited the least broadening of the LSPR peak and the highest OD in both functionalisation strategies, indicating it as the most effective

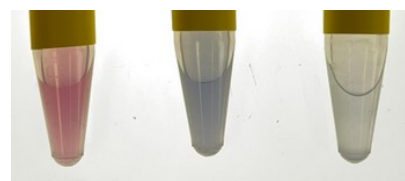


Figure 6.10 | Stages of Particle Aggregation in GNP Functionalisation. The image displays samples treated with diS-PEG-NHS across various stages of particle aggregation: (left) exhibits a red hue at the onset of the reaction, signifying no or minor aggregation; (middle) transitions to blue after PEGylation, marking partial aggregation; and (right) becomes colourless following the final purification step, indicative of irreversible GNP aggregation.

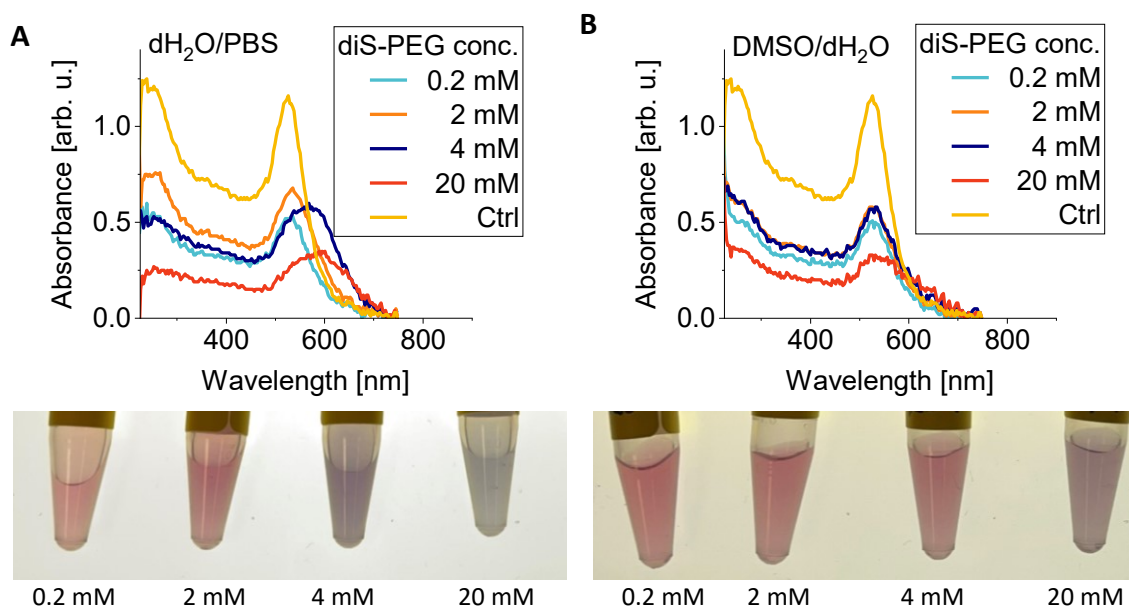


Figure 6.11 | DMSO/dH₂O stabilises GNP more effectively than dH₂O/PBS during Functionalisation using diS-PEG-NHS. UV-Vis spectra of diS-GNP-TfA constructs prepared with different concentrations of diS-PEG-NHS and with the subsequent TfA conjugation reaction in (A) PBS and (B) in dH₂O to assess if hydrolysis of the NHS groups could be prevented by carrying out the functionalisation in a non-aqueous environment. All samples show a reduction in their OD both in the PBS reaction (blue, 0.2 mM diS-PEG-NHS: 0.53; orange, 2 mM: 0.67; navy, 4 mM: 0.60; red, 20 mM: 0.35) as well as in the reaction that was conducted in DMSO (blue, 0.2 mM diS-PEG-NHS: 0.51; orange, 2 mM: 0.58; navy, 4 mM: 0.58; red, 20 mM: 0.32) but there is less broadening of the LSPR peak in B, indicating less aggregation/crosslinking between the particles. Ctrl (yellow): 20 nm GNPs prior to functionalisation with an OD of 1.16. The photos show the respective samples after all steps of functionalisation with the GNPs suspended in PBS.

concentration for particle stabilisation out of the ones tested in these experiments. The loss of GNPs during functionalisation is still extensive in this functionalisation procedure, reducing the GNP content in the sample by 50% (from OD₅₂₀ 1.16 to 0.58).

In following experiments, diS-GNPs were always prepared using DMSO/H₂O. The resulting constructs, referred to as diS-GNPs (when functionalised with TfA) and PEG-GNPs, were employed in fixed-cell pulse-chase experiments with a 30 min pulse. These experiments, with chase durations of 0 minutes and 2 hours, aimed to evaluate the diS-GNP binding and uptake by HeLa cells, in comparison to particles that were PEGylated using the same cross-linker without the addition of TfA. FWM images, as shown in Figure 6.12, depict both diS-GNP constructs and diS-PEGylated GNPs at 0 min chase. At this timepoint, there was minimal to no GNP internalisation observed (Figure 6.12A-D). This assumption is based on the axial color-coded representation of particle localisation within the cells. Specifically, the GNP signals presented in Figure 6.12D, L, and P conform to the topographical contours of HeLa cells. This is supported by the observation of purple and blue signals predominantly at the cell peripheries. As the signals approach the vicinity of the nucleus (in respect to their x,y-position on the 2D

images), they ascend on the colour scale in the axial color-coded representation, a pattern that suggests a surface-bound state of the constructs that is particularly visible in the areas in proximity to the nucleus. The extensive binding of PEGylated GNPs could stem from conjugation of the GNPs to serum proteins that are deposited on the dish surface. The conjugation might be a result of the proximal NHS group of the stabilising polymer with amines. This would suggest that the reported fast hydrolysis dynamics of NHS-groups are incorrect^{81,177}. At the 2h time point, there are clear differences in the uptake of PEG-GNPs and diS-GNP (Figure 6.12E-H, and M-P). The FWM^A signals of the constructs do not ascend on the axial colour scale, in contrast to diS-GNP-PEG, and appear to be randomly distributed within the cell, suggesting internalisation and trafficking to different localisations.

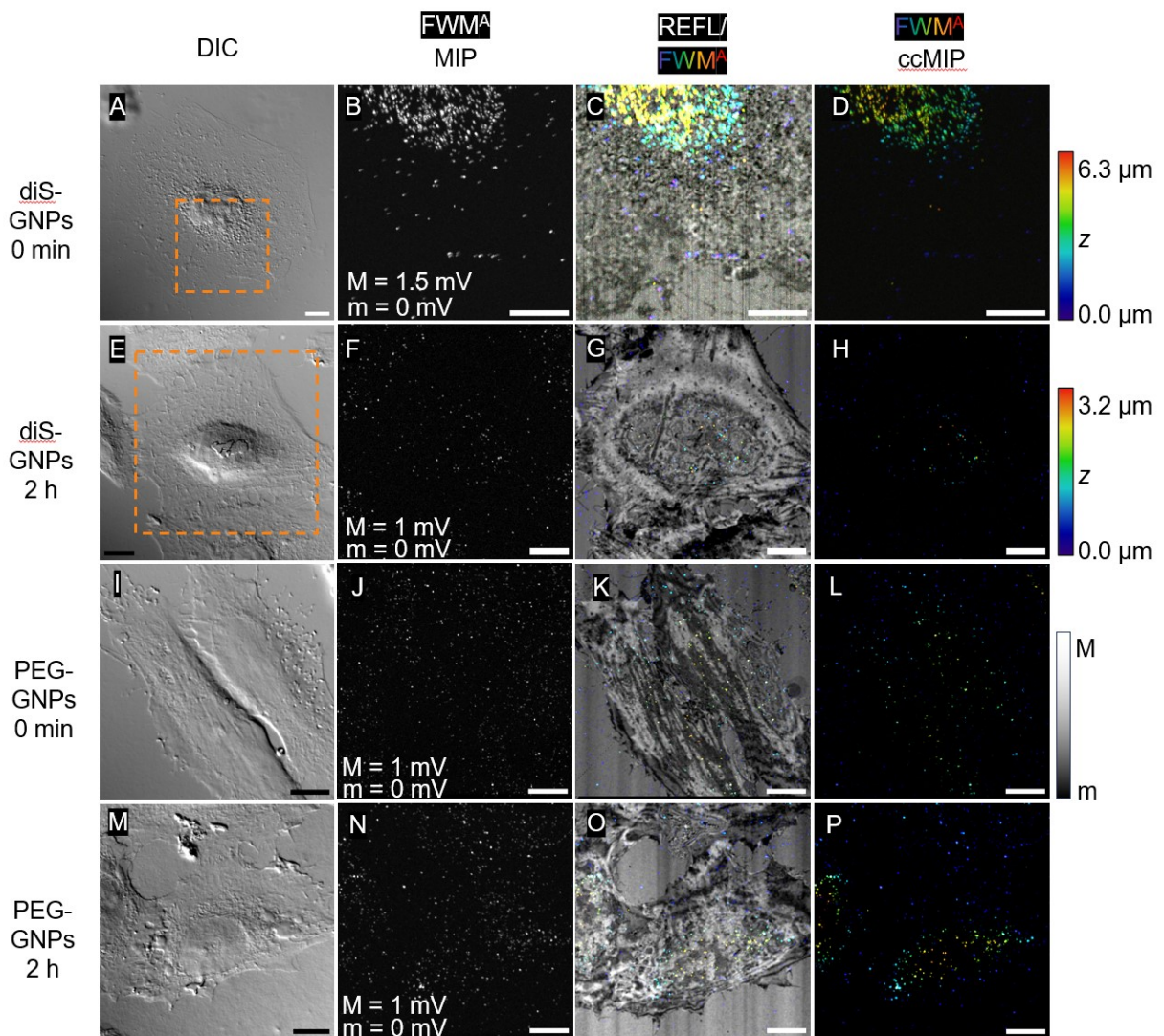


Figure 6.12 | Binding and Internalisation of diS-PEG-NHS Functionalised GNPs in HeLa Cells. Fixed cell FWMi measurements of HeLas treated with diS-GNP-TfA (A-H) and diS-GNP (I-P) at 0 min and 2h after exposure in a pulse-chase experiment with a 30 min serum-starvation step, 30 min GNP treatment, and fixation in 4% PFA represented as MIPs. Included are (DIC) DIC images illustrating the FOV and (FWM^A MIP) MIPs of FWM amplitude (FWM^A) measurements. To preserve z-information, (REFL/FWM^A) false-colour overlays of the REFL field alongside a ccMIP of FWM^A, and (FWM^A ccMIP) cc MIPs of FWM^A are provided. Z-stack images are contrast-enhanced to allow assessment of construct localisation. Scale bars: 10 μm .

A more detailed visualisation of this is provided in Figure 6.13, which revisits the FWM^A data from Figure 6.12 (shown in panels A-D of Figure 6.13) and includes detailed zoom-ins on panels B and D (marked with orange squares, panels G and H), alongside orthogonal views (indicated by blue rectangles, panels I-J). The difference in colour scale progression between PEG-GNP (Figure 6.13G) and diS-GNP (Figure 6.13H) is highlighted when comparing them against the schematic illustrations of non-internalising (Figure 6.13E) and internalising (Figure 6.13F) constructs. Panels I and J verify that the PEG-GNP signals aligned with the cell's morphology, indicating a lack of internalisation. Similarly, diS-GNPs at 0 min chase demonstrate no internalisation (Figure 6.13K), yet signals observed at the 2h time point clearly indicate internalisation as signals are visible throughout the cell rather than just at the periphery (Figure 6.13L). However, the presence of significant unspecific binding observed with both PEG-GNPs and diS-GNPs (visible in Figure 6.12F, J, and N) highlighted the need for further

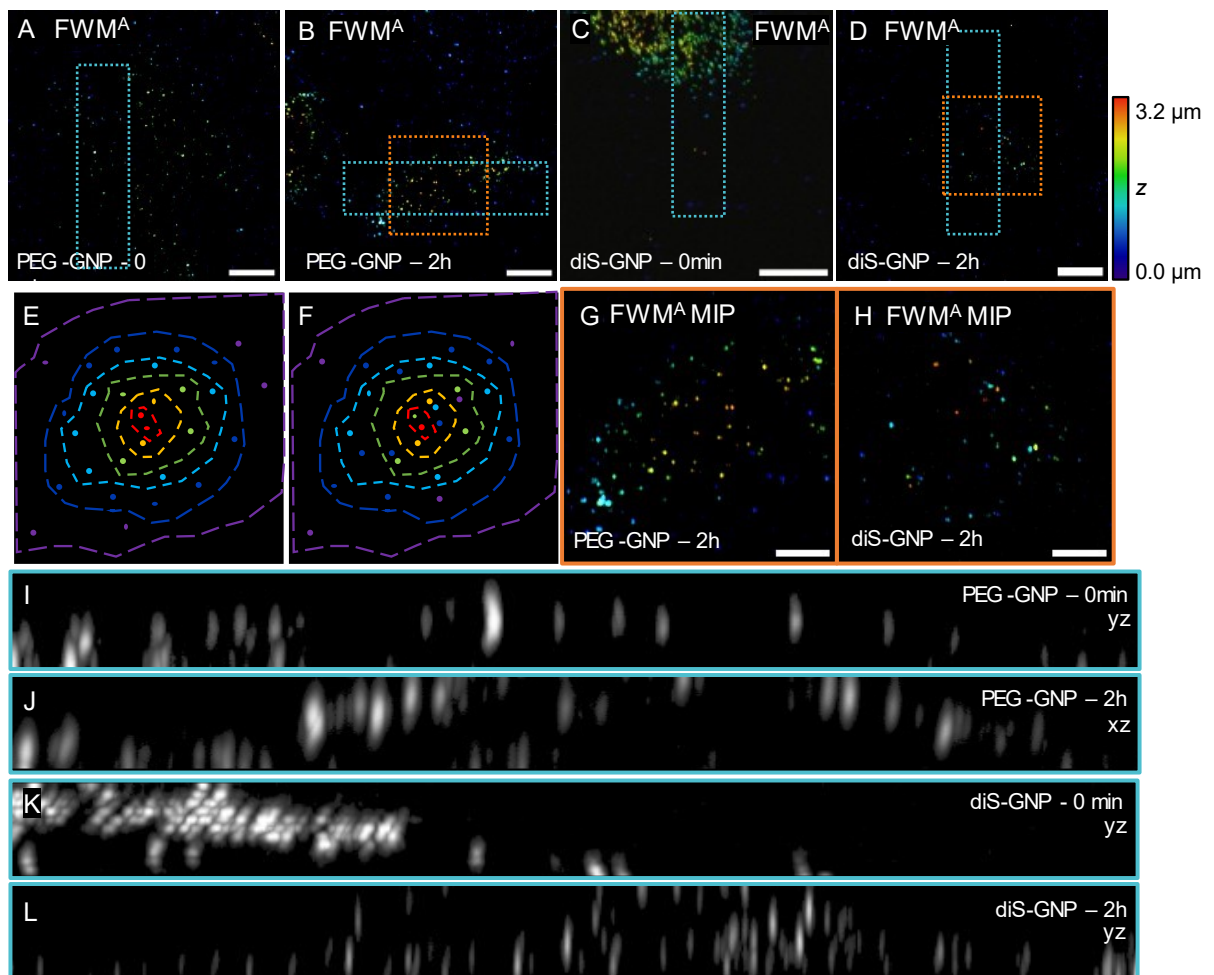


Figure 6.13 | Orthogonal Views of FWM^A verify non-Internalisation of PEG-GNPs and Internalisation of diS-GNPs. (A-D) FWM^A data from fixed HeLa cells, highlighting internalisation observed in Figure 6.12 through a colour-scale analysis, with panels (E) and (F) providing schematic representations of non-internalising and internalising constructs. (G) and (H), marked by orange squares in the FWM^A data, offer zoomed views at the 2 hour chase point for PEG-GNPs and diS-GNPs, respectively. (I) and (J) show MIPs of the xy or xz direction for PEG-GNPs at the initial 0-minute and the 2-hour time points, respectively, while (K) and (L) illustrate the same for diS-GNPs, demonstrating the absence and presence of internalisation respectively. Scale bars: 10 μm .

optimisation. The aim was to refine the synthesis process to produce GNP constructs with minimal off-target interactions. Specifically, the binding behaviour of PEG-GNPs suggested that not all the NHS groups on the diS-PEG-NHS underwent reaction, leading to the stickiness previously seen in particles with a pre-attached stabilising corona.

It should be mentioned that the FWMi data shown in Figure 6.12 and Figure 6.13 was created during acquisition setting optimisation of FWMi measurements that was detailed in Section 5.2.3. Therefore, the pixel dwell time as well as the sample/resolution settings differ between the images. That data in Figure 6.12A-D was one of the first FWMi data acquired in this project and took 5.8 hours to acquire, which is the origin of the extensive lateral drift visible in the data discussed in Section 5.2.3. Subsequent FWMi data was recorded with improved settings that allowed to record a fixed HeLa cell in z within 6 min. In light of persistent dish binding issues, an alternative functionalisation strategy was evaluated, involving the initial conjugation of PEG to proteins, followed by the attachment of the resulting protein-PEG conjugate to GNPs. This allowed the purification of unreacted PEG, thereby eliminating reactive terminal groups from the reaction mixture.

6.2.2.2 OPSS-PEG-NHS

OPN functionalisation was chosen as it was the only functionalisation method among the tested mechanisms that allowed PEG-functionalisation with TfA prior to GNP functionalisation (creating OPT). Prior to GNP-conjugation, the OPT sample was purified by dialysis, separating unconjugated polymer and TfA in preparation for the next reaction steps. Subsequently, the purified OPT was conjugated to the GNP (creating OPT-GNP) at a ratio of 1 OPT/40 nm² GNP surface area, equating to 32 TfAs per particle for a 20 nm GNP sample. The construct was then back-filled with 2 kDa mPEG-SH at 4 mPEG/nm² GNP surface area to further stabilise the particles. The back-filling of functionalised GNPs was previously reported to provide additional stabilisation for GNPs¹⁷⁸. The mPEG was also used to create stabilised control-particles at 5 mPEG/nm² during functionalisation. As visible in UV-Vis spectra of this reaction (Figure 6.14), there was no broadening of the LSPR peak of OPT-GNPs and mPEG-GNPs as compared to particles prior to functionalisation. The OD of these samples was higher than that of the control. As described in Section 6.2.1, an increase in the OD of GNPs after functionalisation can indicate successful functionalisation. Furthermore, the LSPR peak of mPEG-GNPs and OPT-GNPs shifted from 520 to 523 nm, further indicating a change in their dielectric environments after functionalisation. The resulting construct was first tested on HeLa cells in

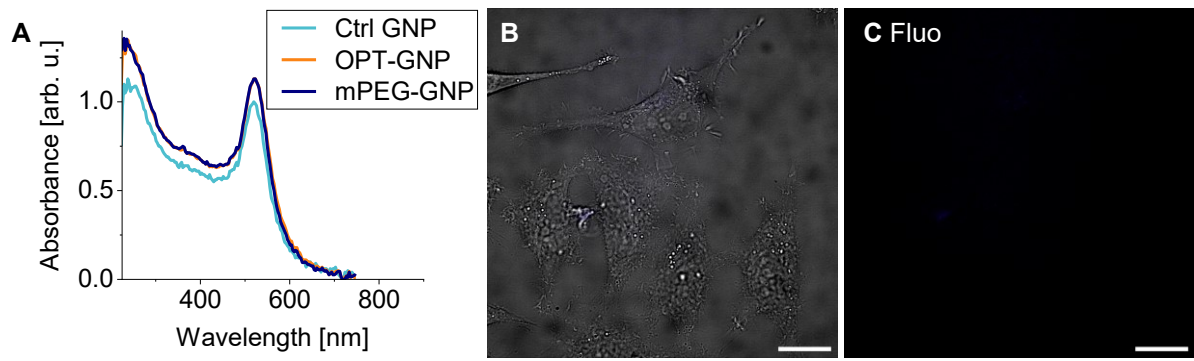


Figure 6.14 | Stabilisation of GNPs by OPN-Based Functionalisation Evidenced by UV-Vis, Yet Lacking Internalisation in HeLa Cells according to fluorescence imaging. UV-Vis spectroscopy reveals the stability of 20 nm GNPs after functionalisation: (A) (blue) GNPs prior to functionalisation exhibit an OD of 0.99, while (orange) OPT-GNPs show an increased OD of 1.13, mirroring the OD of (navy) GNPs PEGylated with mPEG at 1.13. Despite the stabilisation, OPT-GNPs subjected to a pulse-chase assay on live HeLa cells, with a 30-minute pulse and immediate post-pulse imaging, displayed no significant fluorescence signal in (B) brightfield and (C) epi-fluorescence images, indicating an absence of internalisation. Scale bars: 20 μm .

brightfield and epi-fluorescence mode to check if there was any visible fluorescence. The sample showed no fluorescence signal distinguishable from fluorescent background (Figure 6.14B and C).

At this point, live cell FWMi was fully established and allowed for simultaneous confocal fluorescence imaging. Therefore, dextran-Alexa568 was introduced to label lysosomes to assess whether the GNP sample might be trafficked through the endo-lysosomal route. Fluorescently labelled dextran is used to study endocytosis by providing a marker that can be tracked as it is internalised and trafficked within live cells. When cells are exposed to fluorescent dextran, it is taken up through various endocytic pathways, allowing the observation of this process in real-time using fluorescence microscopy. The patterns of dextran uptake, its accumulation in endocytic vesicles, and subsequent trafficking through the cell provide valuable insights into the mechanisms of endocytosis and vesicle trafficking. When using dextran in pulse-chase experiment with long chase times, dextran gets trafficked through to endocytic end-points which allows the determination of accumulation and retention of a second labelled molecule within the cells¹⁷⁹.

To test the OPT-GNP constructs on living cells, HeLa cells were subjected to three different treatments: no treatment (control), treatment with mPEG-GNP, and treatment with OPT-GNP, as part of a pulse-chase experiment. Initially, the cells were incubated with Dextran568 for 4h followed by a 14h chase. The cells then underwent serum starvation for 30 min. Subsequently, the cells were incubated with the constructs for 30 min after which the cells were washed and incubated in pre-warmed imaging medium before immediate measurement using the live FWMi

setup. Figure 6.15 shows representative images captured in live FWMi, illustrating a striking difference in GNP uptake between targeted and non-targeted constructs.

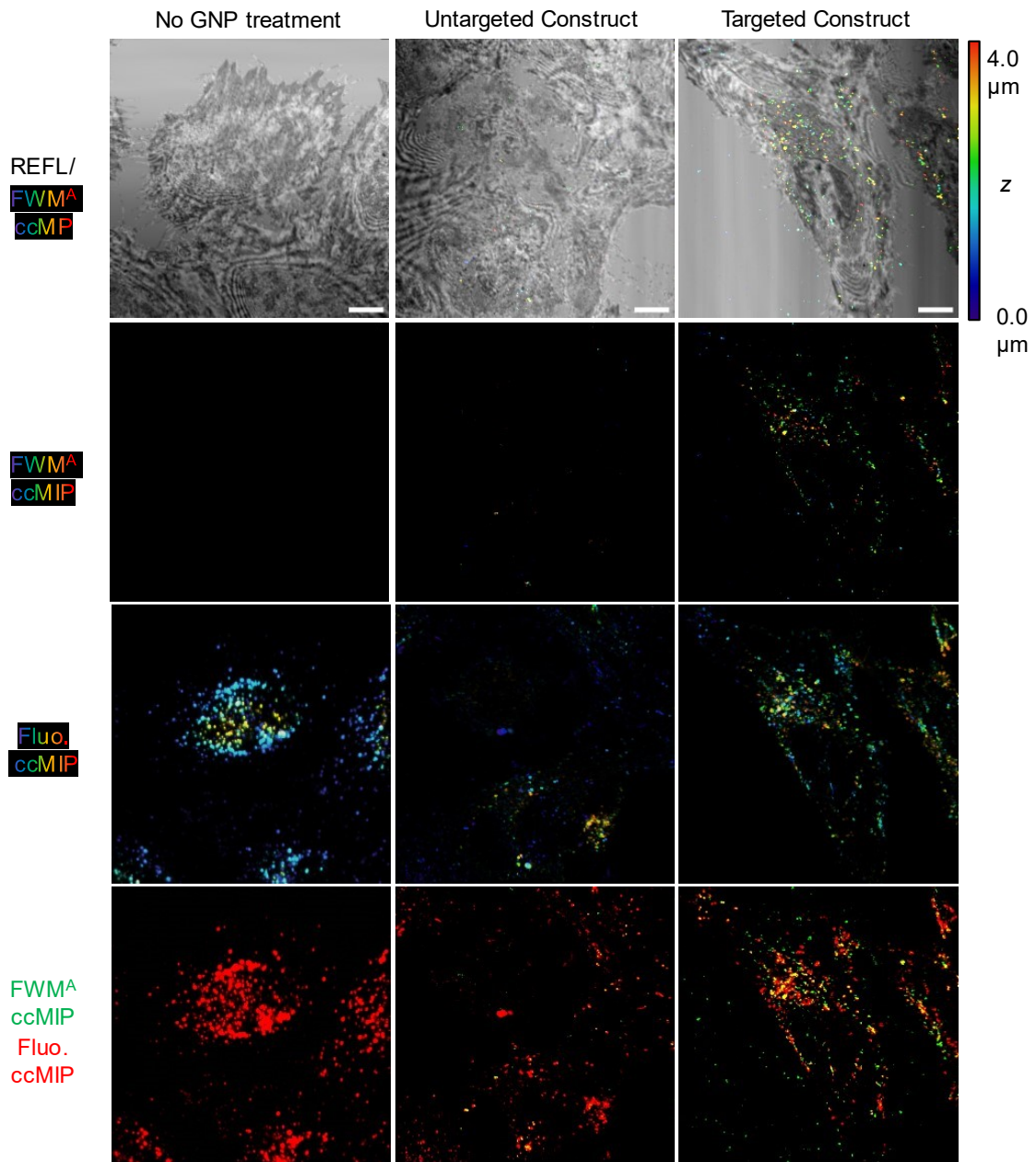


Figure 6.15 | OPT-GNP Demonstrates Tf-Specific Trafficking and Uptake Variations in HeLa Cells. The figure illustrates the cellular trafficking of GNP constructs in a pulse-chase experiment of live HeLa cells with three different treatments: untreated (control), treated with mPEG-GNP, and treated with OPT-GNP. Prior to treatment, cells were incubated with Dextran568 for 4 hours with by an overnight chase. After serum starvation (30 min), cells were exposed to GNPs for 30 min, followed by washing and immediate FWMi measurement in pre-warmed imaging medium. Displayed data represent the 4h chase timepoint and include a false-colour overlay of the reflected FWM field and axial ccMIP of REFL over an axial stack of 4 μm recorded in steps of 400 nm. Separate depiction of axial FWM^A ccMIP is provided for clarity. Confocal fluorescence is shown as ccMIP. Comparative localisation assessment is realised by a false-colour overlay of confocal fluorescence (red) and FWM^A signal (green). Scale bars: 10 μm .

For quantitative comparison, the count of FWM^A signals located 1.2 μm above the surface within the cells, and on the surface ($z = 0.0 \mu\text{m}$) outside of the cells was determined (see Table 6.1). The targeted OPT-GNP construct demonstrated a significantly higher uptake rate, averaging approximately 3000 signals/ mm^2 (area occupied by a cell), compared to the non-targeted, PEGylated particles, which showed around 650 signals/ mm^2 . This indicates a 4.6-fold increase in the uptake of OPT-GNP over PEG-GNP. It is important to acknowledge that this experiment was conducted only once, as the project concluded shortly thereafter.

To validate statistical significance, further repetitions of this experiment are necessary. It is important to note that the measurement unit employed here is signals/ mm^2 , as there has been no amplitude analysis of FWM^A signals to determine the actual number of GNPs within the focal volume in this experiment. The FWM^A signals from OPT-GNPs internalised within cells generally show a higher intensity than those from PEGylated GNPs, suggesting that the actual disparity in GNP density per mm^2 of cell-covered area could be more pronounced. Similar to earlier samples utilising different functionalisation techniques, the OPT-GNPs demonstrated binding to the dish (approx. 1600 signals/ mm^2). This data confirms the theory of the previous sections in this chapter, where it was assumed that the unreacted proximal NHS- (and sulfo-SMCC-) groups might cause particle binding as there is no detectable binding of PEGylated GNPs (0 signals/ mm^2). The dish-binding of OPT-GNP is assumed to be caused by serum proteins deposited on the cell culture dish. This hypothesis is further supported by the complete absence of dish binding exhibited by the PEGylated GNPs. In light of these results, we wanted to characterise this construct further, integrating all methodologies developed throughout this project.

Table 6.1 | Quantitative 20 nm OPT-GNP and mPEG-GNP uptake by HeLa cells.

	area covered by cells [mm^2]	FWM ^A signals inside cells	Signals/ mm^2	area not covered by cells [mm^2]	FWM ^A signals outside cells	Signals/ mm^2
OPT-GNP, area 1	0.03602	151	4192	0.02798	55	1966
OPT-GNP, area 2	0.05071	128	2524	0.01329	29	2182
OPT-GNP, area 3	0.02199	61	2774	0.01859	12	646
PEG-GNP, area 1	0.05406	36	666	0.00994	0	0
PEG-GNP, area 2	0.02951	24	813	0.00613	0	0
PEG-GNP, area 3	0.05688	31	545	0.00712	0	0

6.2.3 Correlative single fluorophore bleaching, extinction, and FWMi

6.2.3.1 Data transformation

To comprehensively characterise the OPT-GNP constructs and generate comparable samples without replicating the experiments detailed in Chapter 4.3, OPT-GNP constructs of two different sizes were functionalised with OPT, as opposed to altering their TfA ratio. Therefore, GNPs with diameters of 20 nm and 60 nm were functionalised and will be referred to as 20-OPT-GNP and 60-OPT-GNP in the following, respectively. The functionalisation maintained a consistent ratio of one TfA per 40 nm² of GNP surface area. This would, in theory, result in 32 TfAs per 20 nm particle (with a surface area of 1260 nm²) and 283 TfAs per 60 nm particle (11,310 nm²). Following functionalisation, these samples were spin-coated, measured, and analysed by the methods developed and described in Chapter 4, with the additional step of acquiring FWMi data for the spin-coated samples on the same setup that was used for extinction measurements. As described in Chapter 4, single fluorophore bleaching and extinction were conducted on two different set-ups with different sensor sizes and binning settings, requiring image transformation based on common features within the data sets to allow a false-colour-overlay for correlative analysis.

To evaluate the consistency of the transformation process, the transformation parameters across different samples for FWMi, fluorescence and extinction data were compared. These parameters, if the transformation is reliable, should exhibit no significant variation. The specific parameters under consideration are elaborated upon in Section 4.2.6 and are detailed for this dataset in Table 6.2. As the extinction and FWMi data were acquired using the same set-up, no rotational adjustment was necessary for data transformation (angle adjustments of -

Table 6.2 | Transformation parameters of extinction and fluorescence to FWMi data on varying samples.

Parameters	20 nm [pixel]	40 nm [pixel]	60 nm [pixel]	Avg [pixel]
Extinction				
Error S	0.0	0.0	0.0	0
scale x	1.026	1.024	1.029	1.026
scale y	1.104	1.103	1.106	1.104
angle x	-0.024	-0.022	-0.019	-0.022
angle y	0.026	0.026	0.024	0.025
Parameters	20 nm [pixel]	40 nm [pixel]	60 nm [pixel]	Avg [pixel]
Fluorescence				
Error S	0.0	0.0	0.0	0
scale x	2.057	2.053	2.066	2.058
scale y	2.214	2.222	2.223	2.220
angle x	-0.079	-0.081	-0.074	-0.078
angle y	0.082	0.087	0.083	0.084

0.022 and 0.025 pixels in the x and y axes, respectively). The transformation scaling was minimal, at 1.026 in the x-axis and 1.104 in the y-axis, which implies a slight distortion in the FWMi data, as indicated by the 8% discrepancy between the x- and y-scaling factors. This distortion is also reflected in the x- and y-scaling parameters required for the transformation of the fluorescence data. The distortion might originate in the way the FWMi data was regularised. Regularisation is the term used to generate images from the acquired FWMi data, which is

detailed in Section 3.5.7.3. The 2x2 binning in the fluorescence dataset required a scaling factor that is twice that required for the transformation of extinction data. These findings are consistent with those from previous comparisons of the transformation processes between extinction and fluorescence data described within this work.

6.2.3.2 Determination of number of fluorophores per TfA and number of TfAs per GNP

The bleaching step size I_B was determined for both 20- and 60-OPT-GNP and plotted in a histogram in Figure 6.16A. The distribution of I_B appeared similar to previously reported data within this project (refer back to Figure 4.5), with a marginal increase in outliers towards a larger I_B . For a more detailed statistical analysis, additional box plot representations of the data are provided. The 20 nm GNP-OPT exhibited an average I_B of 224 ± 112 pe s^{-1} , the 60 nm OPT-GNP at 227 ± 151 pe s^{-1} , and free TfA at 195 ± 102 pe s^{-1} . The median values for these samples were 215 pe s^{-1} , 169 pe s^{-1} , and 169 pe s^{-1} , respectively, with a consistent statistical mode of 153 pe s^{-1} across all three samples. These statistical measures can be interpreted in various ways. For instance, using the average I_B as a reference, both the 20- and 60-OPT-GNP could be argued to amplify the fluorescence signal by 15% (fluorescence enhancement factor, FEF, of 1.15). However, the slightly higher average I_B of the 60-OPT-GNP is influenced by the presence of statistical outliers. Considering the median value, only the 20-OPT-GNP demonstrated fluorescence intensity amplification with a FEF of 1.27. When focusing on the statistical mode, all samples exhibit an I_B of 153 pe s^{-1} . Given that the standard deviation is approximately 50% of the average, none of these differences are statistically significant. The 20 nm GNP and TfA are separated through a 5 kDa PEG chain, creating distances between the

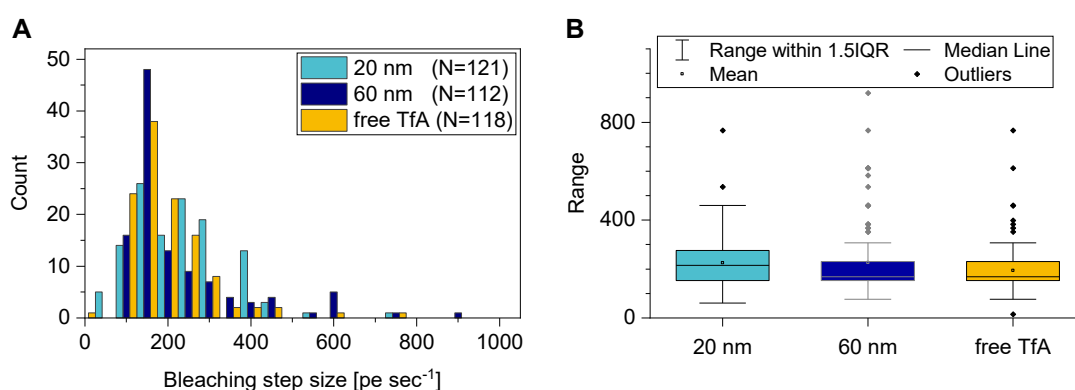


Figure 6.16 | Determination of Bleaching Step Size of TfA on OPT-GNP. Histograms of bleaching step sizes I_B of Alexa 647 attached to (blue) 20 nm OPT-GNP, (navy) 60 nm OPT-GNP, and (yellow) free TfA. The data is additionally displays box plots to further showcase the statistics of the signal distributions. 20 nm GNP-OPT showed a I_B (mean \pm standard deviation) of 224 ± 112 pe s^{-1} , 60 nm OPT-GNP of 227 ± 151 pe s^{-1} and free TfA 195 ± 102 pe sec^{-1} . The median of the samples is 215 pe s^{-1} , 169 pe s^{-1} , and 169 pe s^{-1} , respectively. The statistical mode of all three samples is the same at 153 pe sec^{-1} . IQR: Interquartile range.

two constituents that have been reported to enhance fluorescence intensity by other groups (19.7 nm GNP have been shown to express a FEF of 1.5 with a 14.3 nm spacer¹⁸⁰).

In order to confirm that the visible fluorescence signals did not originate from fluorescent impurities on the glass substrate, a dH₂O sample was included in the fluorescence analysis together with unfunctionalised particles to validate that the particles neither produce fluorescence themselves and that they do not enhance signals of fluorescence of fluorescent debris. For visual comparison epifluorescence data of TfA, the OPT-GNP of 20 and 60 nm diameter and the respective controls are shown in Figure 6.17. The distribution of the initial fluorescence intensity values $I(t_0)$ at the start of the bleaching experiment analysis are depicted in the histograms presented in Figure 6.18. The figures should be read as follows: Upper histograms (white background) represent initial fluorescence intensity values $I(t_0)$ of functionalised GNPs of 20 nm (blue) and 60 nm (navy) diameter, as well as $I(t_0)$ values from unconjugated TfA (yellow). The lower histograms (grey background) represent $I(t_0)$ values that have been measured on their respective control samples of unfunctionalised 20 and 60 nm GNPs, and spin coated dH₂O (red). To calculate N_F , the statistical mode of the samples' I_B was chosen (153 pe sec^{-1}) to allow the use of a single scale for all samples for easier comparison, though the implications of this will be further discussed below.

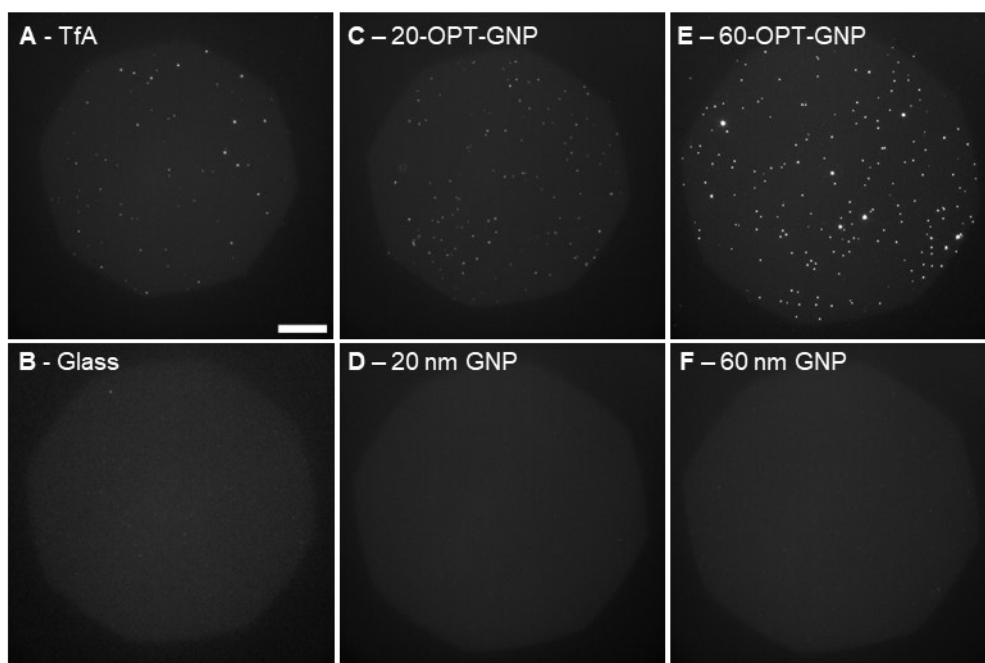


Figure 6.17 | Initial Fluorescence Intensity Indicates Successful GNP Functionalisation. This figure displays initial fluorescence intensities ($I(t_0)$) from time-lapse experiments in epifluorescence mode, differentiating between spin-coated samples of OPT-functionalised GNPs and their unfunctionalised equivalents. Controls include (A) free TfA and (B) spin-coated dH₂O. The comparative analysis includes GNPs of varying sizes: (C) 20 nm GNPs functionalised with OPT alongside (D) unfunctionalised 20 nm GNPs; (E) 60 nm GNPs with OPT functionalisation compared to (F) unfunctionalised 60 nm GNPs. Scale bar: 20 μm .

The distribution of GNP construct fluorescence was observed to be comparable to the fluorophore distribution of free TfA within the range of 1-9 attached fluorophores with the bulk of both distributions located within 1-4 fluorophores attached to 20-OPT-GNP and free TfA, respectively. However, free TfA exhibited several signals indicative of labelling with up to 20 fluorophores. The absence of similar high-intensity signals in the 20-OPT-GNP samples suggests that the likelihood of GNPs conjugating to highly labelled proteins is reduced. This reduction seems plausible considering that both, OPN and Alexa647, target lysines via NHS-chemistry. Proteins with a high degree of labelling are less likely to have free primary amines available for OPN attachment. GNPs with diameters of 20 nm and 60 nm exhibit a difference in surface area by a factor of nine. The majority of fluorescence signals from 60-OPT-GNP samples were found to fall within a range of 4-11 fluorophores per construct, although the range extended from 1 to 90 fluorophores for constructs comprising of a single GNP. In contrast, the 20-OPT-GNP samples displayed a labelling range of 1-8 fluorophores, mirroring the available surface area of the GNPs with the respective diameters. Had the mean I_B been utilised to calculate the degree of labelling, the ratio observed would have remained the same. However,

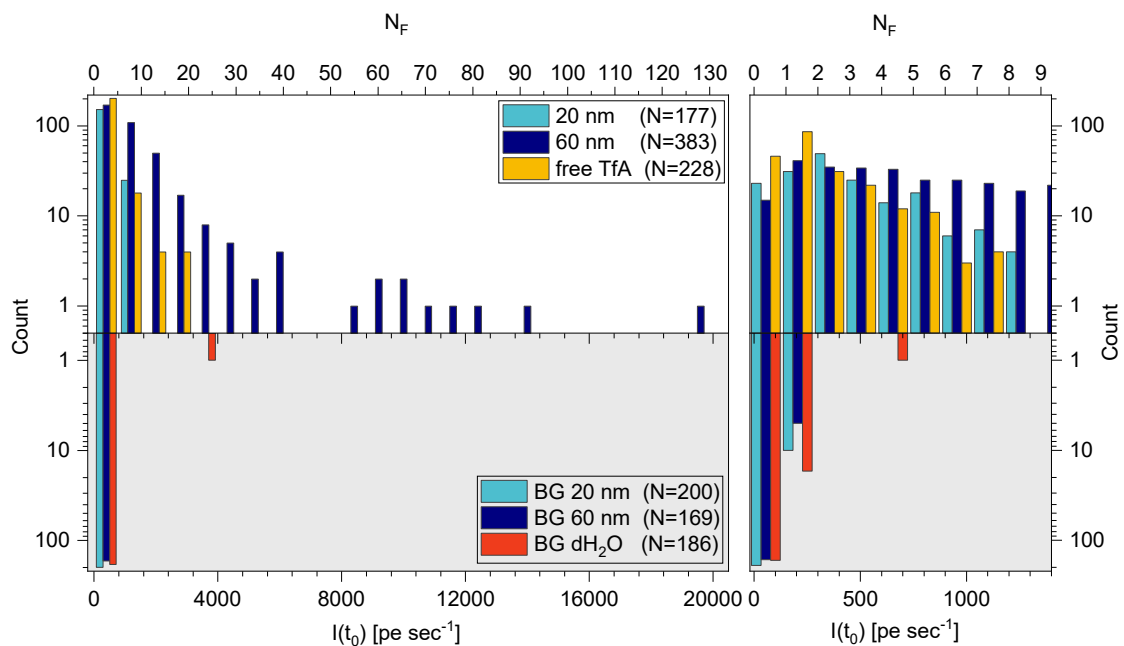


Figure 6.18 | Distributions of $I(t_0)$ on free TfA and GNP-TfA constructs. Distribution of $I(t_0)$ for (yellow) free TfA and GNP-TfA constructs of (blue) 20 nm and (navy) 60 nm diameter using a bin size of 800 pe s^{-1} (right histograms). Data show initial fluorescence rates from time course experiments in epifluorescence mode (from the first frame with 3 sec integration time) to assess the DOL of OPT-GNP constructs. BG fluorescence was acquired by measuring samples of spin-coated GNP prior to functionalisation in epi fluorescence mode using the same settings as for the constructs and is shown flipped with the same bin settings. Additionally, one sample was spin coated with (red) dH_2O that was used for all steps of functionalisation, dilution, and production of buffers. For additional resolution, a zoom of $I(t_0)$ in the range of 0-1400 pe sec^{-1} is provided with a bin size of 150 pe s^{-1} . Lower axes represent $I(t_0)$, upper axes represent the corresponding N_F ($I(t_0)$ divided by I_B). Seven especially large signals found for 60-OPT-GNPs are not shown on this histogram. They show $I(t_0)$ values of 114,820 pe sec^{-1} , 128,203 pe sec^{-1} , 135,389 pe s^{-1} , 184,514 pe sec^{-1} , 254,805 pe sec^{-1} , 320,829 pe sec^{-1} , and 431,671 pe sec^{-1} .

employing the median I_B values would indicate a labelling degree of 1-6 for 20-OPT-GNP and 1-82 for 60-OPT-GNP. Although these values still align with the available surface area, they do not reflect the proportional relationship as precisely.

Background fluorescence signals from samples containing unfunctionalised particles and dH₂O exhibited comparable $I(t_0)$ distributions in respect to one another, indicating that any fluorescent impurities present on the glass substrate were not amplified by the presence of GNPs. The intensity of these background signals was comparable to what might be interpreted as a GNP with a single attached fluorophore. However, none of these background signals colocalised with an extinction signal, suggesting that the colocalising extinction and fluorescence signals can be confidently interpreted as successfully functionalised constructs. It is important to acknowledge that the variable N in Figure 6.18 represents the total number of fluorescent emitters analysed by the ESM. On certain occasions, some signals were in close proximity to each other, activating the proximity restriction of the ESM protocol. As a result, the intensity of these signals was not evaluated. However, these constructs were identifiable as successfully functionalised and were subsequently incorporated into the assessment of sample fractions. These fractions include free TfA, unconjugated GNPs, and successfully functionalised GNPs as will be described in the following sections. Therefore, the value of 'N' exhibits variation across different figures, despite the overall number of successfully functionalised GNPs remaining consistent.

6.2.3.3 Determination of construct size distribution

To assess the size of the constructs the samples were imaged using correlative widefield extinction microscopy and analysed using ESM. The results of this analysis are presented in Figure 6.19. The unfunctionalised particles with diameters of 20 and 60 nm exhibited average σ_{ext} of $378 \pm 110 \text{ nm}^2$ (corresponding to 18 nm diameter GNPs) and $18,186 \pm 7189 \text{ nm}^2$ (corresponding to 60 nm diameter particles), respectively. These values are within the expected range for size variation in GNP samples. For the functionalised particles, the average σ_{ext} values were calculated as $526 \pm 205 \text{ nm}^2$ for 20-OPT-GNP (equivalent to a 20 nm diameter GNP), and $22,023 \pm 25,117 \text{ nm}^2$ for 60-OPT-GNP (equivalent to 66 nm diameter GNPs). The discrepancy between the 20 nm GNPs and their corresponding constructs was minimal, with both measurements not differing significantly.

Regarding the 60-OPT-GNP, the substantial standard deviation indicates that the outliers in this sample contribute to an elevated average σ_{ext} . Excluding the eight largest particles from the analysis reduces the mean σ_{ext} to $19,605 \pm 12,073 \text{ nm}^2$, corresponding to a GNP diameter of

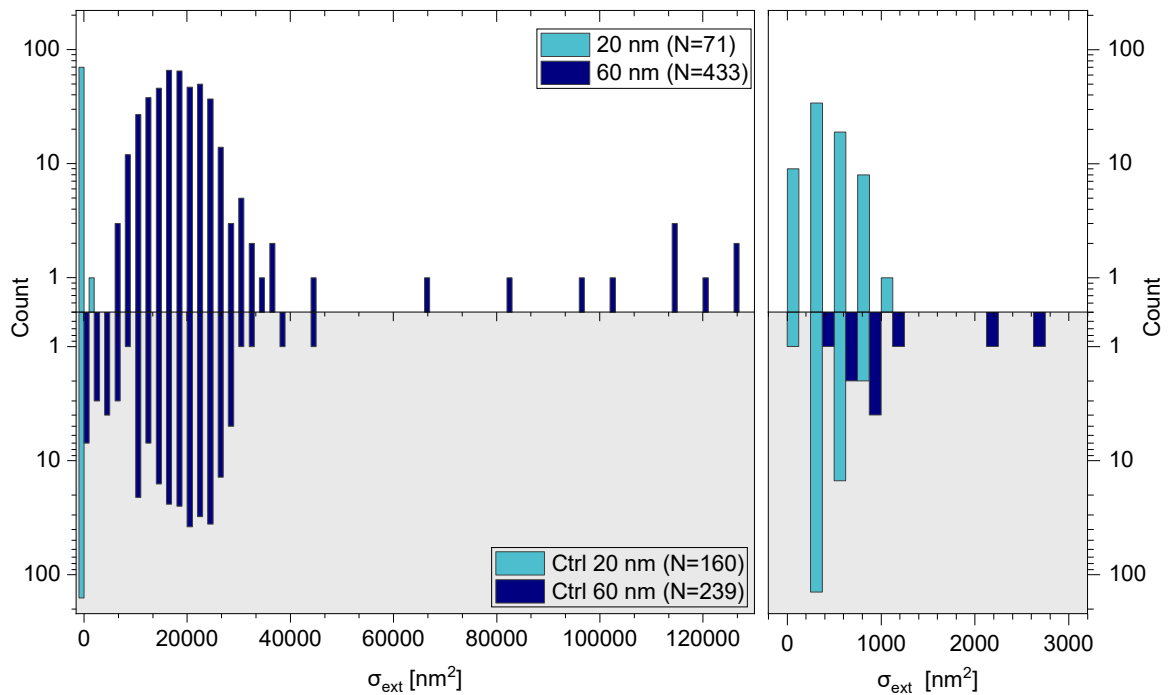


Figure 6.19 | Extinction Cross Sections of Unconjugated GNPs and GNP-TfA Constructs. Histogram of σ_{ext} measured on unconjugated (blue) 20 and (navy) 60 nm diameter (top) GNP-TfA constructs and (bottom, flipped) GNPs prior to functionalisation with a bin size of 2000 nm^2 . For better resolution, an additional zoom of the histogram in the range of 0 and 3200 nm^2 with a bin size of 250 nm^2 was added (left). The functionalised particles exhibit average diameters of $526 \pm 205 \text{ nm}^2$ for 20-OPT-GNP (20 nm diameter GNPs) and $22,023 \pm 25,117 \text{ nm}^2$ for 60-OPT-GNP (corresponding to 66 nm diameter). Unfunctionalised GNPs show average σ_{ext} values of $378 \pm 110 \text{ nm}^2$ for 20 nm (approximating 18 nm diameter particles) and $18186 \pm 7189 \text{ nm}^2$ for 60 nm (corresponding to 60 nm diameter particles). Three exceptionally large particles with σ_{ext} values of $171,164 \text{ nm}^2$, $204,471 \text{ nm}^2$, and $256,776 \text{ nm}^2$ are excluded from this histogram (all found in the 60-OPT-GNP sample).

62 nm. However, the average σ_{ext} of unfunctionalised 60 nm GNPs is skewed towards lower values by GNPs with values between $500\text{-}10,000 \text{ nm}^2$, which are notably absent in the construct sample of the same size. The most likely cause of this are the varying centrifugation speeds employed to centrifuge GNPs of different diameters. When purifying stock GNP samples of different sizes, different centrifugation conditions are applied as larger particles sediment faster than smaller particles and therefore, 60 nm GNPs are spun down at 900 rcf, and 20 nm GNPs at 10,000 rcf (see Methods section)¹⁷³. This introduces an inherent separation of small GNPs for the 60 nm GNP stock solution, as the small particles don't precipitate at the applied centrifugation conditions and are removed when exchanging reaction buffers. Apart from the removal of these small GNPs, the distribution of 60-OPT-GNPs mirrors that of unfunctionalised particles apart from a few outliers. 2 % of all 60-OPT-GNP σ_{ext} values show exceptionally large values, corresponding to constructs made of 6-13 GNP of 60 nm diameter. Given that more OPT can attach to the larger surface area, the probability of a protein conjugated to more than one OPN molecule is higher, leading to a higher probability of larger aggregates consisting of multiple particles.

6.2.3.4 Correlation of fluorescence and extinction signals

Further insights into the functionalisation process can be drawn when looking at a correlative analysis of fluorescence and extinction signals. This involves evaluating the extinction cross-sections against $I(t_0)$ on a single-particle basis, as depicted in Figure 6.20. The correlation analysis reveals that the majority of constructs from all samples (represented by blue squares) align with the size range of unfunctionalised GNPs (indicated by yellow diamonds) in panels A-C. This observation suggests that OPN chemistry does not lead to extensive crosslinking of GNP-constructs.

This trend holds true for most 60-OPT-GNP constructs as well, although there is a subset of notably larger constructs. Generally, there is an extensive variability in the number of fluorophores per construct in the 60-OPT-GNP sample that fall within the size range of a single GNP, ranging between a DOL of 1 to 40. However, this DOL seems low when considering that the functionalisation ratio was at 283 OPT per GNP. The σ_{ext} values of the notably large constructs range from approximately $65,500 \text{ nm}^2$ to $256,800 \text{ nm}^2$. When these σ_{ext} values are divided by the average σ_{ext} of unfunctionalised GNPs to calculate the number of particles in the construct, the implication is that these larger constructs consist of 3-14 GNPs though it should be noted that the size distribution of the 60 nm GNPs was quite broad to begin with so the constructs might consist of slightly less or slightly more GNPs. The unfunctionalised 60 nm GNPs show a broader size distribution than the 60-OPT-GNP constructs when comparing the

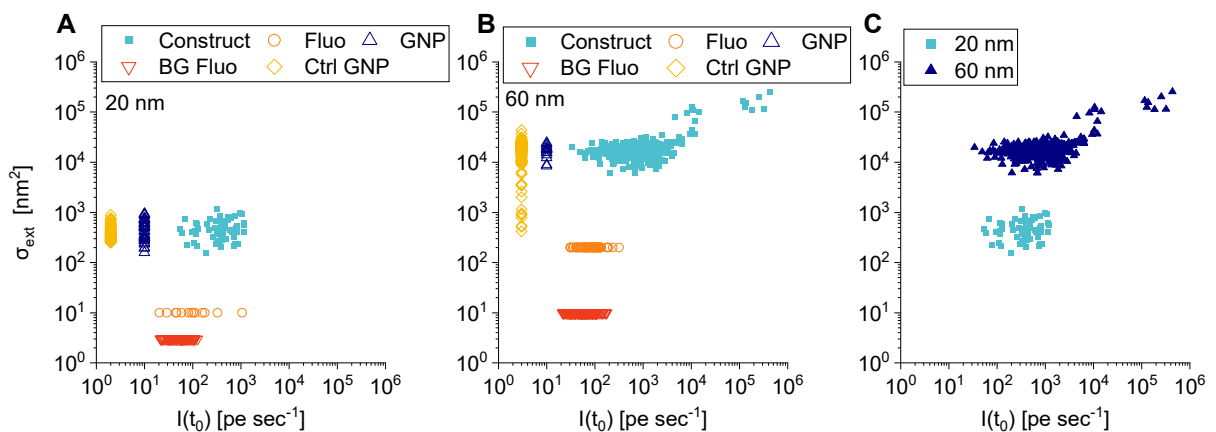


Figure 6.20 | Correlation Between Extinction Cross-Section and Fluorescence Rates in GNP-TfA Constructs. Correlation of extinction cross-section and fluorescence rates for GNP-TfA constructs of (A) 20 nm and (B) 60 nm diameter. In each panel, the data points are represented as follows: blue squares for construct signals, hollow orange circles for fluorescence signals not associated with an extinction signal within the construct sample assigned an arbitrary σ_{ext} value, hollow navy triangles for GNPs not associated with a fluorescence signal within the construct sample with an assigned arbitrary fluorescence intensity, hollow red triangles for fluorescence signals from control samples of unfunctionalised GNPs of the same size assigned an arbitrary σ_{ext} value, and hollow yellow diamonds for σ_{ext} distribution of GNPs of the same size with an arbitrary fluorescence value. (C) All constructs deriving from (blue squares) 20-OPT-GNPs, and (navy triangles) 60-OPT-GNP.

distribution of the blue squares and the yellow circles in Figure 6.20B, which has been linked to the centrifugation conditions as described in section 6.2.3.3.

The initial fluorescence intensity values $I(t_0)$ of 60-OPT-GNP range between 4428 – 43,1671 pe sec^{-1} , equating to 29-2,823 fluorophores per construct. These values are further detailed in Table 6.3. The DOL of these constructs varies significantly, ranging from 6 to 349 fluorophores per GNP. A DOL of 349, while high, is possible

Table 6.3 | Large 60-OPT-GNP Constructs. Values of σ_{ext} values are given in nm^2 , $I(t_0)$ in pe sec^{-1} .

σ_{ext}	$I(t_0)$	GNP	FI	FI per GNP
65 589	12 079	3-4	79	26 (3)/20 (4)
81 984	4 428	4-5	29	7 (4)/6 (5)
96 041	8 256	5	54	11
102 562	14 312	5-6	94	19 (5)/16 (6)
113 496	10 691	6	70	12
126 219	10 395	7	68	8
113 496	184514	6	1206	201
114 996	32 0829	6	2097	349
125 706	128 204	7	838	120
155 131	135 389	8-9	885	111 (8)/98 (9)
171 164	114 820	9-10	750	83 (9)/75 (10)
204 471	254 804	11	1665	151
256 776	431 671	14	2823	202

considering the functionalisation ratio of 283 OPT per particle. The DOL of 349 fluorophores per GNP corresponds to 1 OPT per 32 nm^2 of a 60 nm GNP surface. Theoretically, a density of 1-2 OPN per nm^2 is possible. The variation of I_B of fluorophores can be significant, meaning that the actual DOL of the GNPs is likely narrower. It is unclear why there is a notable gap between the larger 60-OPT-GNPs, creating a small subpopulation that stands out within the scatter plot in Figure 6.20B (and C). It should also be noted, however, that these larger constructs constitute outliers, accounting for only 2% of the total 60-OPT-GNP construct population. Their size might enable their purification from the rest of the ensemble through gel electrophoresis. While their size renders cellular internalisation unlikely, they may still interact with the TfR on the cell surface.

A significant proportion of the construct fluorescence and fluorescence signal from unconjugated protein (represented by orange circles) falls within the range of the background fluorescence for all samples, as represented by red triangles in Figure 6.20A-B. As previously mentioned, background fluorescence in control samples did not colocalise with GNPs, lending confidence to the assumption that colocalising intensities of fluorescence and extinction measured on OPT-GNP samples are indeed attributable to successfully formed GNP-Tf constructs. However, background fluorescence on the glass substrate might lead to an overestimation in the proportion of free TfA within the overall construct population.

The surface area of the 60-OPT-GNP is approximately an order of magnitude greater than that of the 20-OPT-GNP. This disparity is also mirrored in the DOL, which differs by an order of magnitude between these two samples, as evidenced in Figure 6.20C. The observed trend is further exemplified in the analysis of sample fractions depicted in Figure 6.21. For both 20- and 60-OPT-GNP constructs, the fraction representing successfully functionalised GNPs constitutes the largest fraction, accounting for 64% and 85% respectively. The composition of the remaining fractions comprises 28% unfunctionalised GNP and 7% free OPT for the 20-OPT-GNP, whereas the 60 nm sample

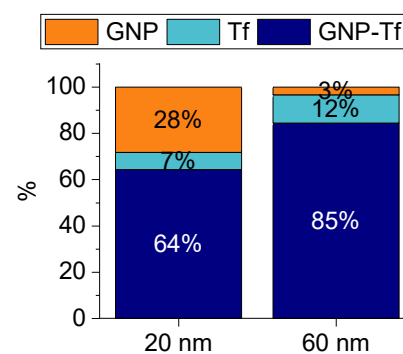


Figure 6.21 | Sample Quality of OPT-GNP Samples. Fractions of unbound protein (light blue), unconjugated particles (orange), and successfully TfA-conjugated GNPs (dark blue) of each sample. Presented here are the fractions of 20-OPT-GNP (N=337), 40-OPT-GNP (N=294), and 60-OPT-GNP (N=633).

includes 12% unfunctionalised GNP and 3% free OPT. Previous research has demonstrated that OPN detaches from cell surfaces over time, with desorption dynamics typically accelerating for larger particle sizes¹⁸¹. This phenomenon seems to be verified in the present study, as evidenced by the higher fraction of free OPT observed in the 60-OPT-GNP constructs. Another argument could be that extended incubation times during the functionalisation process might result in larger fractions of successfully formed constructs. In both samples, one of the two remaining fractions of unconjugated components is notably smaller, indicating the potential for the unreacted component to lack sufficient time to find reaction partners.

6.2.3.5 Zeta potential measurements for validation of functionalisation

Lastly, the OPT-GNP samples were further characterised by measuring their zeta (ζ) potential. The ζ potential is a measure in colloid chemistry, defining the average net electric charge of charged particles in suspension within a solution (see Figure 6.22). It quantifies the potential difference across the boundaries of solids and liquids¹⁸², specifically at the slipping plane, which is the juncture where loosely attached ions no longer move with the particle. When ligands attach to a GNP, they form what's known as the Stern layer¹⁸³. This layer carries a charge which, in turn, attracts a surrounding layer of solvent ions, producing what's

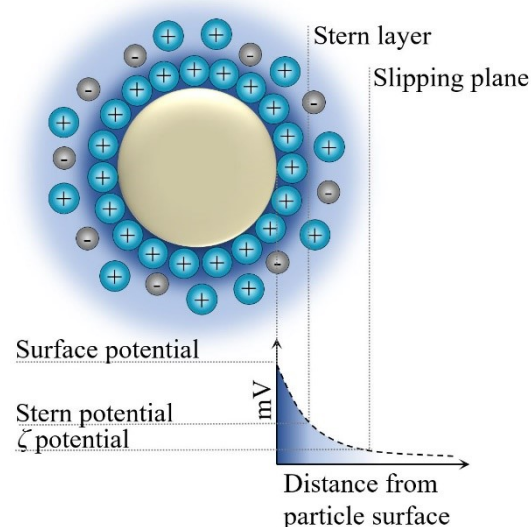


Figure 6.22 | ζ potential of a Particle with Positive Surface Charge. The diagram depicts the potential difference according to the distance from a charged surface of a particle in a dispersion medium.

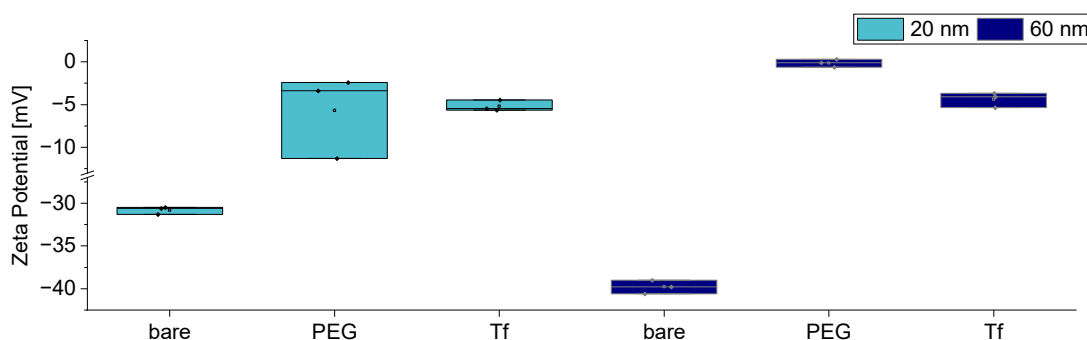


Figure 6.23 | Zeta Potential of GNPs. ζ potential over three measurements of the same sample of (blue) 20 nm, (orange) 40 nm, and (navy) 60 nm GNP before functionalisation, after PEGylation, and after OPT-conjugation. The mean ζ potential of the samples was: -30.8 mV (20 nm bare), -5.7 (20 nm PEG), -5.1 mV (20 nm OPT), -33.3 mV (40 nm bare), -2.9, mV (40 nm PEG) -4.1 mV (40 nm OPT), -39.8 (60 nm bare), -0.1 mV (60 nm PEG), -4.4 mV (60 nm OPT). Measurement conditions: dH₂O for bare GNPs, PBS for PEGylated and OPT-functionalised particles, 25°C.

referred to as an electrical double layer bound to the particle. The boundary between this double layer and the surrounding free liquid defines the slipping plane. The ζ potential can be experimentally determined through the electrophoretic mobility of a particle, which measures the speed at which a charged particle moves under the influence of an external electric field. Therefore, negatively charged particles gravitate towards a positively charged electrode, with their velocity being directly proportional to the ζ potential of the particle¹⁸⁴.

The unfunctionalised GNPs exhibited a negative ζ potential due to their citrate group decoration, which has a negative charge. The ζ potential was more negative as the size of the GNP increased, attributable to the larger surface area accommodating more citrate groups (which are negatively charged). The measured ζ potentials were -30.8 mV for 20 nm GNPs and -39.8 mV for 60 nm GNPs (Figure 6.23). In contrast, the mPEG used in these samples is methyl-terminated and therefore not charged. This characteristic is evident in the ζ potential measurements of the PEGylated particles, with 20 nm GNPs showing a ζ potential of -5.7 mV, and 60 nm GNPs -0.1 mV. The diminished negative charge suggests successful PEGylation, but also indicates the quality of PEGylation achieved. The neutral charge of the 60 nm GNPs implies a more effective PEGylation compared to the 20 nm GNPs which indicates a suboptimal PEG density. Under the measurement conditions (PBS at pH 7.4), Tf has been previously reported to possess a slight negative charge¹⁸⁵. This was reflected in the measurements, as the OPT-functionalised GNPs exhibited a slightly more negative ζ potential compared to their PEGylated counterparts, measured at -5.1 mV for 20 nm GNPs and -4.4 mV for 60 nm GNPs. The outcomes of the ζ potential assessment indicated that particle functionalisation was successful.

6.3 Limitations and Future Considerations

6.3.1 GNP Functionalisation is Characterised by Significant Variability

Throughout this project, numerous iterations of various reaction mechanisms have been extensively tested. On occasion, identical reaction mechanisms were conducted using the same buffers and GNPs, but in different reaction tubes on the same day, leading to markedly different outcomes in the resulting constructs. The concentration of added particles to cell samples was consistently maintained at an OD of 0.01, ruling out high sample concentration as a causative factor for these discrepancies. In the project's initial stages, 20 nm GNPs from various vendors were employed, as well as GNPs purchased at different times before and during the course of the project from the same vendor. Although some consistency was observed within identical batches, GNPs of the same size, stabilised with the same polymer and stored in identical buffers, displayed varying levels of stability, particularly evident during medium exchanges from citrate to dH₂O. Given that the primary focus of this project was to develop constructs for assessing GNP internalisation and their intracellular pathways, there was limited opportunity to investigate the variability in construct samples under consistent reaction conditions. Detailed studies addressing this variability would be valuable to the broader scientific community, especially for those employing functionalised GNPs in applications with medical relevance.

6.3.2 The Order of Functionalisation is likely more Important than the Functionalisation Mechanism

Within this project, two primary reaction mechanisms were explored: maleimide chemistry targeting thiol groups in proteins and NHS chemistry focusing on primary amine groups, with EDC employed for anchoring via carboxyl groups. The use of GNPs with pre-attached stabilising polymers introduced complexities in discerning the specific causes of issues encountered during functionalisation, which frequently resulted in sticky particles. This stickiness were found to stem from unreacted reactive groups binding to cell remnants on the dish or interacting with tube walls, as observed in sulfo-SMCC reactions.

The reduced internalisation of GNPs with pre-attached polymers compared to those functionalised in-house may be attributed to differences in surface chemistry, steric hindrance, and charge distribution. Pre-attached polymers often obscure the nanoparticle surface properties, with unknown polymer composition potentially increasing the hydrodynamic radius. This can limit close interactions with the cell membrane and prevent uptake¹⁸⁶. Additionally, dense polymer coatings may sterically hinder the efficient functionalisation of GNP attachment

sites (e.g., with Tf), reducing the effectiveness of targeting ligands and impacting cellular internalisation¹⁸⁷.

The dense presence of hydrolysed NHS groups, carboxyl groups, or amine groups on the NP surface further influences their ability to interact with mammalian cells. Hydrolysed NHS groups convert to carboxyl groups, which have a negative surface charge⁵⁷. This charge creates electrostatic repulsion with the negatively charged cell membrane, reducing the likelihood of non-specific uptake and receptor-mediated endocytosis¹⁸⁶. Particles with pre-attached carboxyl groups face these same challenges.

In contrast, particles with a high density of amine groups exhibit a positively charged surface, enhancing electrostatic interactions with the negatively charged cell membrane. This can promote uptake through non-specific endocytosis or adsorptive-mediated mechanisms¹⁸⁸. However, an excessive number of amine groups can result in an overly high surface charge, which can lead to cytotoxicity, membrane disruption, or aggregation in biological media¹⁸⁹. These observations demonstrate that in-house functionalisation allows for better control over the density and type of functional groups on the NP surface.

Conducting the entire functionalisation process in-house offered enhanced control over the procedure, even though it introduced additional potential sources of error, particularly for less experienced experimenters. Two main functionalisation approaches were tested: firstly, attaching the stabilising polymer to the GNP, followed by the targeting protein, or alternatively, conjugating the stabilising polymer to the protein before functionalising the GNP with this complex. In this study, stabilising polymers were initially attached to the GNP surface, anchoring via a dithiol group. The proximal groups employed were sulfo-SMCC, which is directed towards thiol groups. Conversely, OPN polymers, conjugated first to primary amine residues in Tf, were then anchored onto the GNP using a dithiol group within the OPSS structure. The results from the OPN-based experiments were notably better in quality, characterised by reduced dish binding and more effective internalisation. This success was attributed to the filtration step in the initial step of conjugating stabilising polymer with protein. Through dialysis, unbound stabilising polymer was extracted from the sample. The amount of unconjugated TfA was mitigated by adding an excess of OPN. Nonetheless, the presence of unbound TfA is unlikely to attach to the GNP. This introduces an additional degree of control in the functionalisation process, enabling the incorporation of OPT at controlled concentrations, and thereby avoiding excessive surface crowding that could impede the interaction between Tf and TfR.

It is possible that a similar outcome might have been attained with sulfo-SMCC polymers, provided they had been initially conjugated to the proteins and subsequently filtered. Sulfo-SMCC particles showed enhanced cell internalisation compared to their PEGylated counterparts. However, their tendency to adhere to tube walls and cell culture dishes persisted as a complication. Assuming that this adhesiveness was a consequence of unreacted sulfo-SMCC, the dialysis filtering step would likely have fixed this issue. It would be a good addition to look into this further to validate this assumption drawn from the outcomes of the experiments presented in this chapter and would provide further insight into how particle functionalisation works. An additional measure during OPT functionalisation involved the incorporation of a mPEG backfilling step, which contributed to the stabilisation of the constructs. Following the overnight incubation with OPT, mPEG was applied to cover any residual exposed gold surfaces, which could act as seed for irreversible GNP aggregation. This additional step might also have enhanced the quality of SMCC-GNPs. Control samples for SMCC-GNP, which included PEGylated GNPs, were prepared by introducing unconjugated diS-PEG-sulfoSMCC. Considering that unreacted sulfo-SMCC is assumed to be the origin of the observed adhesiveness, this likely resulted in GNPs with increased stickiness.

6.3.3 FWMi aids in identifying GNP constructs in correlative experiments

In this chapter, FWMi has been utilised as a tool for construct localisation. Ideally, FWMi could be utilised to verify the size of GNPs by comparing the FWM^A to the extinction cross section of each construct. This comparison was not conducted with this set of experiments due to unexpected strong sample tilt, which affected the uniformity of the measurement plane across the FOV. Unlike extinction measurements, which were conducted across multiple z-planes to differentiate GNPs from debris, this multi-z-plane imaging was not applied in FWM field acquisition. In Future correlative experiments, FWMi should be recorded at multiple z-planes at the same FOV to account for potential tilt.

Nonetheless, the correlative experiments provided further insights into GNP functionalisation for cell targeting. It was observed that the DOL of GNPs correlated with the available surface area on 20- and 60-OPT-GNPs, reinforcing the reliability of the correlative fluorescence and extinction evaluation methods. An illustrative zoomed FOV of correlative fluorescence, extinction and FWMi is presented in Figure 6.24, where both extinction and fluorescence data have been transformed to align with the FWMi data. It also proves the capability of FWMi to resolve single GNPs.

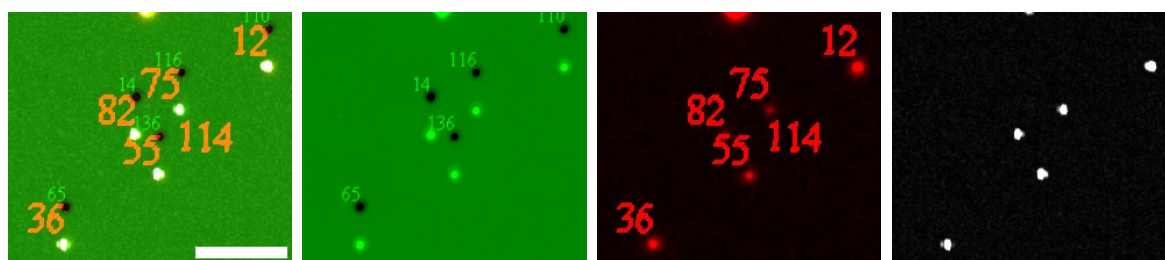


Figure 6.24 | Correlative Analysis of Extinction, Single Fluorophore Bleaching, and FWMi in Spin-Coated OPT-GNP Constructs. An exemplary area of a 60 nm OPT-GNP sample processed by spin-coating is presented. From left to right, (panel 1) a false-colour overlay illustrates (panel 2) extinction, (panel 3) fluorescence captured in epi-fluorescence mode, and (panel 4) FWMi amplitude. Both extinction and fluorescence data have undergone transformation for alignment with the FWMi data, facilitating correlative analysis. Scale bar: 5 μm .

6.3.4 Fluorescence intensities of the constructs differ in cell applications and in single fluorophore bleaching

A notable discovery was that fluorescence generated by the constructs was visible in single fluorophore bleaching experiments but absent in live cell applications. Other research groups have reported the use of additional fluorescently labelled mPEG for PEG-backfilling of their constructs to generate sufficient fluorescent signals in cell experiments, indicating that the sole use of fluorescently labelled proteins does not generate constructs capable of producing visible fluorescence intensities strong enough to be detected by most standard fluorescence microscopes^{175,181,190}. These microscopes, unless specifically designed or optimised to detect single-molecule fluorescence, typically lack the sensitivity required to pick up such low-intensity signals. This suggests that while labelled GNPs may produce fluorescence, the intensities are insufficient for practical imaging in many experimental setups, requiring alternative strategies such as fluorescent PEG-backfilling to enhance signal visibility. A likely explanation for the variance in signal intensity observed may be attributed to the nature of fluorescence emission in spin-coated constructs. These constructs, being static emitters, produce a consistent photon flux towards the detector from a fixed position over a duration of three seconds, thereby yielding a higher signal-to-noise ratio. In contrast, constructs that are freely diffusing within a solution during live cell epi-fluorescence experiments exhibit movement. This mobility, coupled with a shorter integration time of one second, results in diminished signal intensity. While the movement of the constructs in solution might be the main contributing factor to the lack of distinguishable fluorescence signal observed in cellular applications of GNP-constructs, it is unclear how measuring fluorescence of such constructs in air compares to measuring fluorescence of the same construct in a polar solution such as cell culture media.

This difference in measurement environments raises questions about the inherent fluorescence properties of the constructs and how they are influenced by their surroundings. In air, the absence of a solvent medium may lead to different interactions between the fluorescent labels and the GNPs, potentially affecting the fluorescence intensity or spectral characteristics. In a polar solution on the other hand, solvent molecules could interact with the fluorescent labels or the GNPs, potentially quenching the fluorescence or altering its properties in other ways. H₂O has been shown to quench organic fluorescent labels, especially those emitting in the red, whereas their fluorescence intensity could be restored in deuterated solvents¹⁹¹. Works focussing on comparisons of different solvents to air in this regard have not been found. Future research should focus on exploring these discrepancies to develop a more comprehensive understanding of the fluorescence behaviour of GNP-constructs under varying environmental conditions.

6.4 Conclusions

In this chapter, established functionalisation mechanisms and reactions were tested for their quality in internalisation studies, employing TfR-targeted GNP-protein constructs as primary imaging labels. This involved:

- 1) Utilising live and fixed cell brightfield, epi-fluorescence, and FWMi with simultaneous confocal fluorescence, to assess the uptake of GNP constructs into HeLa cells.
- 2) Applying correlative extinction and single fluorophore bleaching in conjunction with FWMi on spin-coated GNP constructs, to determine the fluorescence DOL and the overall quality of the construct samples.
- 3) Conducting ζ potential and UV-Vis spectroscopy measurements for an in-depth characterisation of the resulting constructs.

These experiments were initiated following the observation of inconsistent colocalisation between fluorescence and GNP signals in cellular applications of GNP-TfA constructs developed using previously published methodologies. The findings indicate that fluorescence alone can be an unreliable indicator of GNP localisation. To address this, further investigations were undertaken to discern the distinctions among various functionalisation mechanisms, primarily to identify a method that yielded targeted constructs with high specificity and minimal retention at the cell surface. It was established that employing sulfo-SMCC and NHS reaction chemistries lead to the formation of GNP-TfA conjugates capable of efficient cellular internalisation. A critical aspect was the order of functionalisation, specifically with the conjugation of the protein to the stabilising polymer as the first step, followed by purification

to separate unconjugated polymers with reactive NHS groups. These conjugates could then be attached to GNPs, resulting in samples of high quality and functionalisation yield. FWMI proved effective in validating the localisation of GNPs, offering insights into the intracellular trafficking pathways in HeLa cells, improved by simultaneous confocal fluorescence measurements to localise fluorescently labelled endo-lysosomal compartments.

7 Thesis conclusions

7.1 Fluorescence is not necessarily a faithful reporter of GNP localisation

Previous works have shown that the labelling of proteins with fluorophores alters their behaviour, toxicity and trafficking pathway within living cells^{192,193} and furthermore it has been shown that there is little to no colocalisation between fluorophore and GNP signals^{31,32}. As illustrated in Chapters 4 and 6 of this thesis, fluorescence signals may fail to accurately report the localisation of GNPs within biological systems, which could lead to potential inaccuracies in conclusions drawn about NP function, distribution, and behaviour.

The analysis combining epifluorescence and extinction microscopy, detailed in Chapter 4, revealed that GNP-protein constructs, purified using the widely accepted method of centrifugation, contained a significant proportion of unconjugated proteins. This finding highlights the limitations of conventional purification techniques in separating GNPs that are fully conjugated to proteins from the reaction constituents, suggesting that a substantial fraction of the proteins does not attach to the GNPs as intended. As a result, fluorescence signals in such systems may (in a worst case scenario predominantly) arise from free, unconjugated proteins rather than the GNP-protein constructs being studied. This can lead to significant misinterpretations in studies relying on fluorescence alone.

While this thesis does not aim to undermine the utility of fluorescent tagging as a whole, it does advocate for a more cautious and nuanced approach to its use in NP studies. Fluorescent tagging has been employed successfully in numerous studies to accurately report GNP internalisation and behaviour^{194,195}, and its value as a tool for visualising and tracking biological processes is undeniable. However, these findings highlight the importance of complementing fluorescence-based methods with direct NP detection techniques in cases where the intracellular localisation of particles is studied. By integrating fluorescence with methods capable of detecting GNPs directly, such as FWMi, parallax DIC microscopy, and photothermal imaging, a better validation of results is possible, which ensures the accuracy of experimental data interpretations.

Furthermore, concerns of pathway alteration after fluorescent tagging of proteins has been reported^{192,196}. Although relatively few studies have explored this, likely due to a lack of robust non-fluorescent protein tracking methods, the existing evidence suggests that tagging can introduce substantial changes in the biological behaviour of proteins. The developments of this work, especially live FWMi in Chapter 5, can help to provide a more direct and accurate means

Thesis conclusions - For GNP-protein constructs to be used as therapeutics *in vivo*, sophisticated purification methods are still needed to make sure the internalisation pathway of interest is induced of studying the behaviour and trafficking of GNP-protein constructs in living systems without relying on fluorescence. The findings presented in this thesis suggest that this methodology could be an important imaging modality to explore how fluorescent tagging may alter protein trafficking pathways. A future directions project based on this is described in Chapter 8.1.

7.2 For GNP-protein constructs to be used as therapeutics *in vivo*, sophisticated purification methods are still needed to make sure the internalisation pathway of interest is induced

Apart from looking at GNPs as pure labelling agents, they also hold great promise as fundamental tools for understanding cell biology and as drug delivery vehicles. Up to this point, the state of the art for assessing ligand density on GNPs has involved an averaged calculation, where the total protein number is divided by the number of GNPs, assuming a uniform particle size.⁹⁹ However, as shown in Chapter 4, the reality of GNP functionalisation processes significantly deviates from such assumptions. Given the impact of ligand density on the trafficking pathways, especially when multiple ligands induce crosslinking among particles typically functioning independently, developing sophisticated purification techniques that can discernibly separate various construct fractions becomes critical. In the absence of such methodologies, unintended trafficking routes could compromise the utility of GNPs as imaging labels, nanocarriers, or therapeutic agents.

The need to refine NP purification and characterisation methods is important for pushing GNPs in the fields of biomedical research and therapeutic applications. Section 8.1 proposes a project that includes the development of such a purification technique as a milestone. Once a purification method has been developed and validated using particle by particle analysis, for example using the technique from Chapter 4, live cell FWMi (Chapter 5) can be used to specifically test GNPs how ligand valency influences their trafficking, which is proposed in the future directions in Chapter 8.2.

7.3 Specific changes to GNP functionalisation procedures and GNP morphology can be closely monitored with the help of particle-by-particle ligand density determination and FWMi

Controlling, characterising, and understanding all other fabrication parameters of functionalised GNPs will be key to interpreting data obtained from any source, imaging or otherwise. Surface functionalisation along with the size and shape of the NP itself need to be correlated. Addition of physical spikes to the NP shape has been shown to increase internalisation by regulating

Thesis conclusions - Live cell FWMi helps with revealing GNP trafficking in living cells but needs to be improved on speed myosin IIA recruitment at the cell membrane during cellular uptake¹⁹⁷, highlighting that just small changes to NP geometry can impact interactions between NPs and the cell. The combined developments described across Chapter 4-6 open up a validation workflow on how small changes in particle functionalisation affect the constructs and their internalisation or whether the chosen functionalisation protocol yields effective particles at all. Studying additional NP parameters such as morphology and how they affect internalisation are incorporated in the study proposed in Section 2 of Chapter 8.

7.4 Live cell FWMi helps with revealing GNP trafficking in living cells but needs to be improved on speed

In its current configuration, FWMi is capable of detecting single GNPs down to 10 nm diameter with high signal-to-noise ratio in live cellular environments^{32,47,198}. Background signal can only be generated by objects with χ^3 susceptibility, which aren't naturally present in cells, while the FWM signal is only modulated by coherent signals. Therefore, the signal is not affected by autofluorescent background and with an imaging speed of 0.1–1 ms per pixel it allows to follow internalisation events at the single particle level. The main limiting factor of this technique is speed. This is mostly due to its point-scanning configuration, where a single laser beam is focussed on a specific location of the sample and moved in 3D using a nanostage. Using galvo mirrors could significantly speed up the scanning, but the three beams (pump, probe, reference) would need to be aligned perfectly both spatially and temporally. A recent review on NPs from a group of cell biologists however gives an alternative perspective on this problem, in that “the identification of a specific pathway might not always need to be a priority and the focus should instead be on establishing that internalization occurs, its relative efficiency, and showing where in the endocytic pathway internalised NP are located at specific times after endocytosis”¹⁹⁹. Due to the non-invasive, high signal to noise and long timeframes for acquisition available, FWM is ideally placed to be able to answer exactly these questions within cells. For example, understanding GNP trafficking is further complicated by the large variation possible in proteins binding to the surface of NPs as they encounter biological material (i.e. different types of media components). Efforts are being made to understand how the NP surface changes within a biological environment, specifically with the formation of a protein corona²⁰⁰ that can impact and affect the way in which NPs bind to, and traffic within cells.

7.5 Concluding remarks

The objective of this project was to pave the way for a comprehensive analysis GNP trafficking within cells by developing a method for assessing ligand density at an individual particle level,

upgrading the FWM microscope for live cell studies, and evaluating functionalisation techniques to minimise off-target binding.

In Chapter 4, we achieved a more refined evaluation of ligand density through correlative single fluorophore bleaching and single particle detection via extinction microscopy. Although this method allows for the quantification of fluorophores per construct, the calculation of fluorophores per protein remains an average estimate. Despite this, the method offers higher resolution compared to all other available techniques. The estimation is based on the DOL of proteins, which can result in slight over- or underestimations of the exact number of proteins on GNPs. However, this method allows for high-resolution comparisons on a construct-by-construct basis, assessment of sample fractions, and estimations of particle crosslinking. These measures are not provided by any other current method for quantifying ligand density on GNPs.

The uncertainty of DOL on the proteins themselves could be addressed by creating a genetically encoded binding site into the protein such as a fluorescent unnatural amino acid, validating that there is only one fluorophore attached to the protein. It was observed that proteins highly labelled with fluorophores exhibit reduced binding affinity to GNPs, attributed to the saturation of chemical groups involved in both protein labelling and GNP polymer coating functionalisation. This insight is a significant step forward in understanding ligand density, surpassing the capabilities of existing quantification methods which do not account for variable DOLs on proteins.

Chapter 5 demonstrated the capability of imaging GNPs within living HeLa cells, capturing individual endocytosis events over extended periods. However, to achieve statistically significant datasets for internalisation studies, an increase in imaging speed is necessary. FWM microscopy serves as a valuable tool for validating ligand density data as well, either by confirming GNP presence at targeted locations or, when adjusting for sample tilt during measurements, estimating particle size based on FWM signal amplitude.

Chapter 6 revealed that not all GNP functionalisation approaches yield functional constructs and may lead to considerable off-target binding. This phenomenon is likely due to unreacted functional groups on the stabilising polymers, warranting further investigation for validation. Although lower quality samples can in theory be utilised for internalisation studies, their suitability for therapeutic applications is questionable, highlighting the need for a critical evaluation of GNP constructs in medically relevant research. It can generally be questioned if studying GNP constructs in a medically relevant context which won't be fit for use in medically relevant applications in the future is a worthy effort. The findings suggest that initial

functionalisation of the stabilising polymer with proteins, followed by size exclusion purification to remove unreacted polymers, could mitigate the issue of sample quality. Nevertheless, strategies for separating unfunctionalised GNPs after functionalisation require further exploration.

Furthermore, as detailed in Chapter 6, epifluorescence imaging was employed to explore the trafficking pathways of fluorescently tagged GNP constructs within cells. Initial observations suggested altered trafficking patterns. However, upon employing FWMi it became apparent that the actual internalisation of GNPs was negligible. This discrepancy between the fluorescence imaging and FWMi outcomes highlights the challenges in using fluorescence-based methods to track GNP localisation and behaviour accurately within cellular environments. The findings from this project reveal the need for more reliable and precise methodologies for studying GNP-protein constructs in cells. The apparent discrepancy in fluorescence imaging results calls for a reevaluation of current assumptions regarding the behaviour of GNPs in biological systems. It emphasises the potential of live cell FWMi, described and developed in Chapter 5, as a superior alternative for accurately determining the fate of GNPs in cells, offering a clearer understanding of their interactions and mechanisms of action at the cellular level.

In essence, the project's findings lay a foundational framework for the next steps in the optimisation of GNP constructs and for a more detailed analysis of internalisation pathways. By pinpointing the limitations of current practices and proposing actionable solutions, this research contributes significantly to the field of nanotechnology in medicine. The ultimate goal is to refine GNP functionalisation and purification techniques to a degree that ensures their effectiveness and safety in clinical settings, thereby realising the full potential of GNPs as versatile tools in biomedical research and therapy.

8 Future Directions

This chapter gives suggestions for two future studies based on the results of this work. This work has shown that different functionalisation mechanisms, while seemingly all cause GNP uptake when using fluorescence microscopy for validation, do not result in the same sample quality and level of protein labelling as widely assumed. Furthermore, live cell FWMi can now be used to track GNPs as they are being trafficked throughout the cell.

8.1 Influence of fluorescent labels on the trafficking profile of proteins

Background: As highlighted repeatedly in this thesis, various studies indicate that fluorescent tags can alter the trafficking pathway of proteins and that fluorescent signal and GNPs do not necessarily colocalise^{31,32}. Given that fluorescent tags are predominantly used for studying cellular processes, it's important to verify their reliability as reporters in live cell applications. Previous research within our group focused on fixed cell samples, leaving uncertainty around whether the observed effects were due to inadequate fluorescence intensity of the construct or disintegration of the complex within the cell, possibly due to degradation. Employing live cell FWMi offers an opportunity to elucidate the impact of fluorescent labelling on protein trafficking, providing valuable insights into the accuracy and effectiveness of these commonly used biological markers.

Main objective of this study: to determine whether fluorescent labelling alters the trafficking pathway of fluorescently tagged GNP-proteins. This objective would need to validate a few points to answer this question. 1) Is the functionalisation of GNPs reproducible enough to assume that constructs made using the same functionalisation approach result in the same sample quality? 2) Do GNPs functionalised with fluorescently labelled proteins traffic differently through a mammalian cell than their native counterparts? 3) Are there any differences between fluorescent tags of different molecular structure?

Approach: 1) Investigate the consistency of functionalising GNPs with fluorescently labelled proteins using the protocol detailed in Chapter 6. This functionalisation can be applied under various conditions. These include functionalisation on the same day in different tubes or on different days, using different batches of GNPs or proteins. The aim is to determine if the functionalisation consistently yields similar constructs, as assessed by the methodology developed in Chapter 4. This step is crucial for validating that native protein-GNP constructs differ from their fluorescently labelled counterparts solely in the absence of the fluorescent label. This validation is important, considering the limitations in analysing non-fluorescently

labelled constructs on a particle-by-particle basis, which isn't possible with the technique developed in Chapter 4. If the functionalisation outcome is similar every time, the same could be assumed when swapping out the labelled proteins for native proteins. 2) Compare the trafficking of GNP constructs functionalised with fluorescently labelled proteins against those with native proteins. Any observed differences in trafficking will be closely examined, particularly in relation to the various cellular compartments the constructs traverse. To achieve this, different cellular compartments will be co-labelled to discern the specific trafficking pathways. This analysis will be conducted using live cell FWMi, as described in Chapter 5, to trace the construct's journey through the cell. 3) GNPs can be functionalised with red fluorophores or dyes of different molecular structures, which can either be sourced from multiple vendors or synthesised in-house. If opting for commercially available tagged proteins, it's recommended to select those conjugated using the same reaction chemistry. This ensures that any potential alterations in trafficking are not attributed to the labels being attached to different residues. The trafficking of these differently labelled constructs will then be monitored using FWMi, providing further insights into the impact of fluorescent labelling on protein behaviour within cells.

Expected results: Should the existing literature prove accurate in suggesting that fluorescent tags modify protein trafficking profiles, we anticipate detecting these differences in uptake using live cell FWMi^{192,196}. An intriguing aspect of this investigation would be to simultaneously track the fluorescent tag and the GNP to determine if and when the complex disintegrates. While FWMi typically leads to rapid bleaching of the fluorophores, rendering this simultaneous tracking challenging, an exploratory approach could involve reducing the laser intensity. The objective of this adjustment would be to prolong the visibility of the fluorescent signal, thereby potentially allowing us to observe these processes in greater detail.

Possible Limitations: If fluorescent tags are found to influence protein trafficking, it's plausible to consider that GNPs might have a similar effect. Given the distinct chemistries of GNPs and fluorophores involved, it's worthwhile to investigate whether GNPs impact protein behaviour differently. The main limiting factor of success for this project would be ensuring the reproducibility of GNP functionalisation. Consistent functionalisation across experiments is essential to infer that the resulting constructs are of similar quality, which is important as the correlative fluorophore bleaching and extinction evaluation is not possible with non-fluorescently labelled protein-GNP constructs. Hence, this uniformity in construct formation is a key factor in reliably determining whether any observed changes in protein trafficking are due

to the presence of fluorophores or other experimental variables. Establishing this consistency will be a fundamental step in validating the influence of fluorophores on protein trafficking.

Significance: This research project is designed to enhance the understanding of the impact of fluorescent tagging on protein trafficking, particularly investigating if various tags affect this process differently. This study aims to determine the reliability of fluorophores in accurately reporting GNP localisation and, if discrepancies exist, to quantify these variations. To achieve this, the project will employ systematic experiments to compare the effects of different fluorescent tags on GNP-protein behaviour and track any resultant changes in their trafficking pathways. By doing so, the research will provide insights into the reliability of fluorescent tagging in biological studies where GNPs are used, potentially guiding the selection of appropriate tagging methods for accurate GNP-protein localisation.

8.2 Trafficking of mono- and multivalent GNPs in living cells

Background: This study focuses on investigating the mechanism of receptor crosslinking. A key aspect would be to distinguish between receptor crosslinking and non-crosslinking internalisation pathways. This differentiation suggests that GNPs targeting the same receptor, but with either monovalent or multivalent constructs, would exhibit distinct trafficking profiles. Additionally, the study considers how the size and shape of GNPs can influence their interaction with the cell membrane. Since different sizes and morphologies present ligands in varying manners to a cell membrane, it is hypothesised that these physical attributes might significantly impact the uptake of GNPs by cells. The investigation will therefore include a comparative analysis of GNPs of different sizes and shapes to assess how these factors influence receptor-mediated internalisation and trafficking within the cells. Through these analyses, the study aims to gain a deeper understanding of the intricate processes governing receptor crosslinking and GNP internalisation, contributing to the broader knowledge of cellular interaction mechanisms.

Main objective of this study: **The research aims to determine whether multivalency affects the trafficking of GNPs and to identify if there is a specific multivalency threshold that may cause GNPs to adhere to the cell surface.** The main questions of this project include 1) Is it possible to separate constructs from their reaction constituents as well as based on their DOLs? 2) What constitutes the minimal receptor count required for inducing the receptor crosslinking pathway, and is there a specific receptor threshold that controls the rate of construct internalisation, either accelerating, decelerating, or preventing it entirely? 3) In what manner does the morphology of the construct impact these processes and which parameter causes more significant changes: valency or shape?

Approach: 1) The development of effective purification methods is important for separating different sample fractions of GNP-protein constructs with different valences. As briefly mentioned in Section 4.4.4, density gradient centrifugation, diafiltration and gel electrophoresis are potential starting points for isolating particle clusters and unconjugated proteins. These techniques have been shown to be capable of separating GNPs of varying shapes. The efficiency of the developed purification method will be assessed using correlative fluorophore bleaching and extinction microscopy techniques, as detailed in Chapter 4. The OPT functionalisation mechanism discussed in Chapter 6 could be tweaked to ratios that make the formation of certain fractions more likely by adjusting the ratios of GNP to OPT in each reaction. 2) The project would involve separating the constructs into distinct fractions, such as monovalent, divalent, and so on. Separate pulse chase experiments should be conducted with these fractions to measure their trafficking dynamics using live FWMi, as described in Chapters 5 and 6. The aim is to discern any differences in the trafficking and retention of these constructs across various cellular compartments. This analysis should include co-labelling of cell compartments to allow comparison. The study can explore the mechanisms of endocytosis by employing specific blockers to inhibit different endocytosis pathways, thereby determining the role of these mechanisms in the uptake and trafficking of the constructs. 3) To further the research, the experiments can be repeated with GNPs of different morphologies. This will allow for a comparative analysis of their trafficking and retention profiles using live FWMi. By examining GNPs of various shapes and sizes, the study seeks to understand how these physical characteristics influence the cellular interaction and behaviour of GNPs, contributing to a more comprehensive understanding of NP-cell interactions.

Expected results: Assuming successful separation of constructs with varying valences is achievable, this study could reveal more details regarding the mechanism of receptor crosslinking. This insight could enhance our understanding of targeted delivery of therapeutic payloads into specific cellular compartments. The research anticipates that receptor crosslinking may require a certain threshold of crosslinked receptors to be effectively induced. The verification (or disproof) of this hypothesis is a key objective of this study. Furthermore, previous research has shown that GNPs of different morphologies are internalised by cells differently. Building on this understanding, it is anticipated that constructs of different morphologies and valences will demonstrate further discrepancies in terms of their uptake. By comparing the internalisation of GNPs with different sizes, shapes, and valences, the study aims to provide a more comprehensive understanding of the factors influencing receptor-mediated endocytosis and the potential for targeted intracellular delivery of therapeutic compounds.

Possible Limitations: Even with the successful development of methods to separate constructs based on the number of ligands per GNP, it remains a challenge to definitively confirm that all these ligands are presented to the cell membrane in a manner that enables simultaneous binding. To investigate this aspect thoroughly, a substantial number of samples would be required to provide statistically significant data. This necessity stems from the complexity of ligand-receptor interactions and the variability in how ligands on a single GNP may engage with cell membranes.

Significance: Developing a purification method capable of effectively separating constructs of functionalised GNPs could significantly benefit the scientific community, particularly those focusing on targeted therapeutic applications. Currently, it remains uncertain whether suppliers offering monovalent GNPs employ specific purification processes that distinguish between mono- and multivalent GNPs or if their production relies primarily on controlling the protein-to-GNP ratio. If the latter is true, the introduction of a purification method capable of this would not only be of scientific interest but also hold substantial value for industrial partners. Such a method would enable more precise control over the targeting capabilities of GNPs, enhancing the potential for targeted drug delivery and other therapeutic applications. Additionally, a better understanding of the receptor crosslinking mechanism could lead to more effective strategies for directing therapeutic agents to specific organelles within cells. In essence, refining the process of functionalising GNPs with a controlled number of ligands would be an advancement, contributing to both the fundamental understanding of NP-cell interactions and the practical application of GNPs in biomedicine.

9 Bibliography

- (1) Gavas, S.; Quazi, S.; Karpiński, T. M. Nanoparticles for Cancer Therapy: Current Progress and Challenges. *Nanoscale Res Lett* **2021**, *16*, 173. <https://doi.org/10.1186/s11671-021-03628-6>.
- (2) Xu, L.; Xu, M.; Sun, X.; Feliu, N.; Feng, L.; Parak, W. J.; Liu, S. Quantitative Comparison of Gold Nanoparticle Delivery via the Enhanced Permeation and Retention (EPR) Effect and Mesenchymal Stem Cell (MSC)-Based Targeting. *ACS Nano* **2023**, *17* (3), 2039–2052. <https://doi.org/10.1021/acsnano.2c07295>.
- (3) Sun, R.; Xiang, J.; Zhou, Q.; Piao, Y.; Tang, J.; Shao, S.; Zhou, Z.; Bae, Y. H.; Shen, Y. The Tumor EPR Effect for Cancer Drug Delivery: Current Status, Limitations, and Alternatives. *Advanced Drug Delivery Reviews* **2022**, *191*, 114614. <https://doi.org/10.1016/j.addr.2022.114614>.
- (4) Santos, E. da S.; Nogueira, K. A. B.; Fernandes, L. C. C.; Martins, J. R. P.; Reis, A. V. F.; Neto, J. de B. V.; Júnior, I. J. da S.; Pessoa, C.; Pettrilli, R.; Eloy, J. O. EGFR Targeting for Cancer Therapy: Pharmacology and Immunoconjugates with Drugs and Nanoparticles. *International Journal of Pharmaceutics* **2021**, *592*, 120082. <https://doi.org/10.1016/j.ijpharm.2020.120082>.
- (5) Fernández, M.; Javaid, F.; Chudasama, V. Advances in Targeting the Folate Receptor in the Treatment/Imaging of Cancers. *Chem. Sci.* **2018**, *9* (4), 790–810. <https://doi.org/10.1039/C7SC04004K>.
- (6) Koneru, T.; McCord, E.; Pawar, S.; Tatiparti, K.; Sau, S.; Iyer, A. K. Transferrin: Biology and Use in Receptor-Targeted Nanotherapy of Gliomas. *ACS Omega* **2021**, *6* (13), 8727–8733. <https://doi.org/10.1021/acsomega.0c05848>.
- (7) Afsharzadeh, M.; Hashemi, M.; Mokhtarzadeh, A.; Abnous, K.; Ramezani, M. Recent Advances in Co-Delivery Systems Based on Polymeric Nanoparticle for Cancer Treatment. *Artificial Cells, Nanomedicine, and Biotechnology* **2018**, *46* (6), 1095–1110. <https://doi.org/10.1080/21691401.2017.1376675>.
- (8) Krasteva, N.; Georgieva, M. Promising Therapeutic Strategies for Colorectal Cancer Treatment Based on Nanomaterials. *Pharmaceutics* **2022**, *14* (6), 1213. <https://doi.org/10.3390/pharmaceutics14061213>.
- (9) Fenton, O. S.; Olafson, K. N.; Pillai, P. S.; Mitchell, M. J.; Langer, R. Advances in Biomaterials for Drug Delivery. *Advanced Materials* **2018**, *30* (29), 1705328. <https://doi.org/10.1002/adma.201705328>.
- (10) Sun, M.; Wang, T.; Li, L.; Li, X.; Zhai, Y.; Zhang, J.; Li, W. The Application of Inorganic Nanoparticles in Molecular Targeted Cancer Therapy: EGFR Targeting. *Frontiers in Pharmacology* **2021**, *12*.
- (11) Mitchell, M. J.; Billingsley, M. M.; Haley, R. M.; Wechsler, M. E.; Peppas, N. A.; Langer, R. Engineering Precision Nanoparticles for Drug Delivery. *Nat Rev Drug Discov* **2021**, *20* (2), 101–124. <https://doi.org/10.1038/s41573-020-0090-8>.
- (12) Connor, E. E.; Mwamuka, J.; Gole, A.; Murphy, C. J.; Wyatt, M. D. Gold Nanoparticles Are Taken Up by Human Cells but Do Not Cause Acute Cytotoxicity. *Small* **2005**, *1* (3), 325–327. <https://doi.org/10.1002/sml.200400093>.
- (13) Kelly, K. L.; Coronado, E.; Zhao, L. L.; Schatz, G. C. The Optical Properties of Metal Nanoparticles: The Influence of Size, Shape, and Dielectric Environment. *J. Phys. Chem. B* **2003**, *107* (3), 668–677. <https://doi.org/10.1021/jp026731y>.

- (14) Lee, K.-S.; El-Sayed, M. A. Gold and Silver Nanoparticles in Sensing and Imaging: Sensitivity of Plasmon Response to Size, Shape, and Metal Composition. *J. Phys. Chem. B* **2006**, *110* (39), 19220–19225. <https://doi.org/10.1021/jp062536y>.
- (15) Sanvicens, N.; Marco, M. P. Multifunctional Nanoparticles--Properties and Prospects for Their Use in Human Medicine. *Trends Biotechnol.* **2008**, *26* (8), 425–433. <https://doi.org/10.1016/j.tibtech.2008.04.005>.
- (16) Moody, P. R.; Sayers, E. J.; Magnusson, J. P.; Alexander, C.; Borri, P.; Watson, P.; Jones, A. T. Receptor Crosslinking: A General Method to Trigger Internalization and Lysosomal Targeting of Therapeutic Receptor:Ligand Complexes. *Molecular Therapy* **2015**, *23* (12), 1888–1898. <https://doi.org/10.1038/mt.2015.178>.
- (17) Shi, J.; Kantoff, P. W.; Wooster, R.; Farokhzad, O. C. Cancer Nanomedicine: Progress, Challenges and Opportunities. *Nat Rev Cancer* **2017**, *17* (1), 20–37. <https://doi.org/10.1038/nrc.2016.108>.
- (18) Silva, J.; Fernandes, A. R.; Baptista, P. V. Application of Nanotechnology in Drug Delivery. In *Application of Nanotechnology in Drug Delivery*; Sezer, A. D., Ed.; InTech, 2014. <https://doi.org/10.5772/58424>.
- (19) Doherty, G. J.; McMahon, H. T. Mechanisms of Endocytosis. *Annu. Rev. Biochem.* **2009**, *78* (1), 857–902. <https://doi.org/10.1146/annurev.biochem.78.081307.110540>.
- (20) Kaksonen, M.; Roux, A. Mechanisms of Clathrin-Mediated Endocytosis. *Nat Rev Mol Cell Biol* **2018**, *19* (5), 313–326. <https://doi.org/10.1038/nrm.2017.132>.
- (21) Matthaeus, C.; Taraska, J. W. Energy and Dynamics of Caveolae Trafficking. *Frontiers in Cell and Developmental Biology* **2021**, *8*.
- (22) Rennick, J. J.; Johnston, A. P. R.; Parton, R. G. Key Principles and Methods for Studying the Endocytosis of Biological and Nanoparticle Therapeutics. *Nat. Nanotechnol.* **2021**, *16* (3), 266–276. <https://doi.org/10.1038/s41565-021-00858-8>.
- (23) Sharma, A.; Vaghasiya, K.; Ray, E.; Verma, R. K. Lysosomal Targeting Strategies for Design and Delivery of Bioactive for Therapeutic Interventions. *Journal of Drug Targeting* **2018**, *26* (3), 208–221. <https://doi.org/10.1080/1061186X.2017.1374390>.
- (24) Trouet, A.; Deprez-de Campeneere, D.; De Duve, C. Chemotherapy through Lysosomes with a DNA-Daunorubicin Complex. *Nat New Biol* **1972**, *239* (91), 110–112. <https://doi.org/10.1038/newbio239110a0>.
- (25) Erickson, H. K.; Park, P. U.; Widdison, W. C.; Kovtun, Y. V.; Garrett, L. M.; Hoffman, K.; Lutz, R. J.; Goldmacher, V. S.; Blättler, W. A. Antibody-Maytansinoid Conjugates Are Activated in Targeted Cancer Cells by Lysosomal Degradation and Linker-Dependent Intracellular Processing. *Cancer Res* **2006**, *66* (8), 4426–4433. <https://doi.org/10.1158/0008-5472.CAN-05-4489>.
- (26) Luzio, J. P.; Hackmann, Y.; Dieckmann, N. M. G.; Griffiths, G. M. The Biogenesis of Lysosomes and Lysosome-Related Organelles. *Cold Spring Harb Perspect Biol* **2014**, *6* (9), a016840. <https://doi.org/10.1101/cshperspect.a016840>.
- (27) Settembre, C.; Fraldi, A.; Medina, D. L.; Ballabio, A. Signals for the Lysosome: A Control Center for Cellular Clearance and Energy Metabolism. *Nat Rev Mol Cell Biol* **2013**, *14* (5), 283–296. <https://doi.org/10.1038/nrm3565>.
- (28) Jones, S.; King, P. J.; Antonescu, C. N.; Sugiyama, M. G.; Bhamra, A.; Surinova, S.; Angelopoulos, N.; Kragh, M.; Pedersen, M. W.; Hartley, J. A.; Futter, C. E.; Hochhauser, D. Targeting of EGFR by a Combination of Antibodies Mediates Unconventional EGFR

- Trafficking and Degradation. *Sci Rep* **2020**, *10*, 663. <https://doi.org/10.1038/s41598-019-57153-9>.
- (29) Radford, D. C.; Yang, J.; Doan, M. C.; Li, L.; Dixon, A. S.; Owen, S. C.; Kopeček, J. Multivalent HER2-Binding Polymer Conjugates Facilitate Rapid Endocytosis and Enhance Intracellular Drug Delivery. *Journal of Controlled Release* **2020**, *319*, 285–299. <https://doi.org/10.1016/j.jconrel.2019.12.049>.
- (30) Li, L.; Yang, J.; Soodvilai, S.; Wang, J.; Opanasopit, P.; Kopeček, J. Drug-Free Albumin-Triggered Sensitization of Cancer Cells to Anticancer Drugs. *Journal of Controlled Release* **2019**, *293*, 84–93. <https://doi.org/10.1016/j.jconrel.2018.11.015>.
- (31) Miles, B. T.; Greenwood, A. B.; Benito-Alifonso, D.; Tanner, H.; Galan, M. C.; Verkade, P.; Gersen, H. Direct Evidence of Lack of Colocalisation of Fluorescently Labelled Gold Labels Used in Correlative Light Electron Microscopy. *Sci Rep* **2017**, *7* (1), 44666. <https://doi.org/10.1038/srep44666>.
- (32) Giannakopoulou, N.; Williams, J. B.; Moody, P. R.; Sayers, E. J.; Magnusson, J. P.; Pope, I.; Payne, L.; Alexander, C.; Jones, A. T.; Langbein, W.; Watson, P.; Borri, P. Four-Wave-Mixing Microscopy Reveals Non-Colocalisation between Gold Nanoparticles and Fluorophore Conjugates inside Cells. *Nanoscale* **2020**, *12* (7), 4622–4635. <https://doi.org/10.1039/C9NR08512B>.
- (33) Gu, Y.; Di, X.; Sun, W.; Wang, G.; Fang, N. Three-Dimensional Super-Localization and Tracking of Single Gold Nanoparticles in Cells. *Anal. Chem.* **2012**, *84* (9), 4111–4117. <https://doi.org/10.1021/ac300249d>.
- (34) Wu, Y.; Ali, M. R. K.; Chen, K.; Fang, N.; El-Sayed, M. A. Gold Nanoparticles in Biological Optical Imaging. *Nano Today* **2019**, *24*, 120–140. <https://doi.org/10.1016/j.nantod.2018.12.006>.
- (35) Wang, G.; Sun, W.; Luo, Y.; Fang, N. Resolving Rotational Motions of Nano-Objects in Engineered Environments and Live Cells with Gold Nanorods and Differential Interference Contrast Microscopy. *J. Am. Chem. Soc.* **2010**, *132* (46), 16417–16422. <https://doi.org/10.1021/ja106506k>.
- (36) Chen, K.; Gu, Y.; Sun, W.; Bin Dong; Wang, G.; Fan, X.; Xia, T.; Fang, N. Characteristic Rotational Behaviors of Rod-Shaped Cargo Revealed by Automated Five-Dimensional Single Particle Tracking. *Nat Commun* **2017**, *8* (1), 887. <https://doi.org/10.1038/s41467-017-01001-9>.
- (37) Qian, W.; Huang, X.; Kang, B.; El-Sayed, M. A. Dark-Field Light Scattering Imaging of Living Cancer Cell Component from Birth through Division Using Bioconjugated Gold Nanoprobes. *JBO* **2010**, *15* (4), 046025. <https://doi.org/10.1117/1.3477179>.
- (38) Fairbairn, N.; Christofidou, A.; Kanaras, A. G.; Newman, T. A.; Muskens, O. L. Hyperspectral Darkfield Microscopy of Single Hollow Gold Nanoparticles for Biomedical Applications. *Phys. Chem. Chem. Phys.* **2013**, *15* (12), 4163–4168. <https://doi.org/10.1039/C2CP43162A>.
- (39) Ueno, H.; Nishikawa, S.; Iino, R.; Tabata, K. V.; Sakakihara, S.; Yanagida, T.; Noji, H. Simple Dark-Field Microscopy with Nanometer Spatial Precision and Microsecond Temporal Resolution. *Biophysical Journal* **2010**, *98* (9), 2014–2023. <https://doi.org/10.1016/j.bpj.2010.01.011>.
- (40) Chithrani, B. D.; Ghazani, A. A.; Chan, W. C. W. Determining the Size and Shape Dependence of Gold Nanoparticle Uptake into Mammalian Cells. *Nano Lett.* **2006**, *6* (4), 662–668. <https://doi.org/10.1021/nl052396o>.

- (41) Warnasooriya, N.; Joud, F.; Bun, P.; Tessier, G.; Coppey-Moisand, M.; Desbiolles, P.; Atlan, M.; Abboud, M.; Gross, M. Imaging Gold Nanoparticles in Living Cell Environments Using Heterodyne Digital Holographic Microscopy. *Opt. Express, OE* **2010**, *18* (4), 3264–3273. <https://doi.org/10.1364/OE.18.003264>.
- (42) Kim, D.; Oh, N.; Kim, K.; Lee, S.; Pack, C.-G.; Park, J.-H.; Park, Y. Label-Free High-Resolution 3-D Imaging of Gold Nanoparticles inside Live Cells Using Optical Diffraction Tomography. *Methods* **2018**, *136*, 160–167. <https://doi.org/10.1016/j.ymeth.2017.07.008>.
- (43) Turko, N. A.; Peled, A.; Shaked, N. T. Wide-Field Interferometric Phase Microscopy with Molecular Specificity Using Plasmonic Nanoparticles. *JBO* **2013**, *18* (11), 111414. <https://doi.org/10.1117/1.JBO.18.11.111414>.
- (44) Vines, J. B.; Yoon, J.-H.; Ryu, N.-E.; Lim, D.-J.; Park, H. Gold Nanoparticles for Photothermal Cancer Therapy. *Frontiers in Chemistry* **2019**, *7*.
- (45) Lasne, D.; Blab, G. A.; Berciaud, S.; Heine, M.; Groc, L.; Choquet, D.; Cognet, L.; Lounis, B. Single Nanoparticle Photothermal Tracking (SNaPT) of 5-Nm Gold Beads in Live Cells. *Biophys J* **2006**, *91* (12), 4598–4604. <https://doi.org/10.1529/biophysj.106.089771>.
- (46) Adhikari, S.; Spaeth, P.; Kar, A.; Baaske, M. D.; Khatua, S.; Orrit, M. Photothermal Microscopy: Imaging the Optical Absorption of Single Nanoparticles and Single Molecules. *ACS Nano* **2020**, *14* (12), 16414–16445. <https://doi.org/10.1021/acsnano.0c07638>.
- (47) Zoriniants, G.; Masia, F.; Giannakopoulou, N.; Langbein, W.; Borri, P. Background-Free 3D Nanometric Localization and Sub-Nm Asymmetry Detection of Single Plasmonic Nanoparticles by Four-Wave Mixing Interferometry with Optical Vortices. *Physical Review X* **2017**, *7* (4). <https://doi.org/10.1103/PhysRevX.7.041022>.
- (48) Masia, F.; Langbein, W.; Watson, P.; Borri, P. Resonant Four-Wave Mixing of Gold Nanoparticles for Three-Dimensional Cell Microscopy. *Optics Letters* **2009**, *34* (12), 1816. <https://doi.org/10.1364/OL.34.001816>.
- (49) Masia, F.; Langbein, W.; Borri, P. Measurement of the Dynamics of Plasmons inside Individual Gold Nanoparticles Using a Femtosecond Phase-Resolved Microscope. *Physical Review B* **2012**, *85* (23). <https://doi.org/10.1103/PhysRevB.85.235403>.
- (50) Khamehchian, S.; Nikkhah, M.; Madani, R.; Hosseinkhani, S. Enhanced and Selective Permeability of Gold Nanoparticles Functionalized with Cell Penetrating Peptide Derived from Maurocalcine Animal Toxin. *Journal of Biomedical Materials Research Part A* **2016**, *104* (11), 2693–2700. <https://doi.org/10.1002/jbm.a.35806>.
- (51) Azarkin, M.; Kirakosyan, M.; Ryabov, V. Microdosimetric Simulation of Gold-Nanoparticle-Enhanced Radiotherapy. *International Journal of Molecular Sciences* **2024**, *25* (17), 9525. <https://doi.org/10.3390/ijms25179525>.
- (52) Häkkinen, H. The Gold–Sulfur Interface at the Nanoscale. *Nature Chem* **2012**, *4* (6), 443–455. <https://doi.org/10.1038/nchem.1352>.
- (53) Bano, A.; Dawood, A.; Rida; Saira, F.; Malik, A.; Alkholief, M.; Ahmad, H.; Khan, M. A.; Ahmad, Z.; Bazighifan, O. Enhancing Catalytic Activity of Gold Nanoparticles in a Standard Redox Reaction by Investigating the Impact of AuNPs Size, Temperature and Reductant Concentrations. *Sci Rep* **2023**, *13* (1), 12359. <https://doi.org/10.1038/s41598-023-38234-2>.

- (54) Fernandes, J.; Kang, S. Numerical Study on the Surface Plasmon Resonance Tunability of Spherical and Non-Spherical Core-Shell Dimer Nanostructures. *Nanomaterials* **2021**, *11* (7), 1728. <https://doi.org/10.3390/nano11071728>.
- (55) Park, J.-W.; Shumaker-Parry, J. S. Structural Study of Citrate Layers on Gold Nanoparticles: Role of Intermolecular Interactions in Stabilizing Nanoparticles. *J. Am. Chem. Soc.* **2014**, *136* (5), 1907–1921. <https://doi.org/10.1021/ja4097384>.
- (56) Conde, J.; Dias, J. T.; Graça, V.; Moros, M.; Baptista, P. V.; de la Fuente, J. M. Revisiting 30 Years of Biofunctionalization and Surface Chemistry of Inorganic Nanoparticles for Nanomedicine. *Front. Chem.* **2014**, *2*. <https://doi.org/10.3389/fchem.2014.00048>.
- (57) Hermanson, G. T. *Bioconjugate Techniques*; Academic Press, 2013.
- (58) Xie, X.; Liao, J.; Shao, X.; Li, Q.; Lin, Y. The Effect of Shape on Cellular Uptake of Gold Nanoparticles in the Forms of Stars, Rods, and Triangles. *Sci Rep* **2017**, *7* (1), 3827. <https://doi.org/10.1038/s41598-017-04229-z>.
- (59) Trono, J. D.; Mizuno, K.; Yusa, N.; Matsukawa, T.; Yokoyama, K.; Uesaka, M. Size, Concentration and Incubation Time Dependence of Gold Nanoparticle Uptake into Pancreas Cancer Cells and Its Future Application to X-Ray Drug Delivery System. *JRR* **2011**, *52* (1), 103–109. <https://doi.org/10.1269/jrr.10068>.
- (60) Xia, Q.; Huang, J.; Feng, Q.; Chen, X.; Liu, X.; Li, X.; Zhang, T.; Xiao, S.; Li, H.; Zhong, Z.; Xiao, K. Size- and Cell Type-Dependent Cellular Uptake, Cytotoxicity and in Vivo Distribution of Gold Nanoparticles. *IJN* **2019**, *Volume 14*, 6957–6970. <https://doi.org/10.2147/IJN.S214008>.
- (61) Hill, H. D.; Millstone, J. E.; Banholzer, M. J.; Mirkin, C. A. The Role Radius of Curvature Plays in Thiolated Oligonucleotide Loading on Gold Nanoparticles. *ACS Nano* **2009**, *3* (2), 418–424. <https://doi.org/10.1021/nn800726e>.
- (62) Daniels, T. R.; Bernabeu, E.; Rodríguez, J. A.; Patel, S.; Kozman, M.; Chiappetta, D. A.; Holler, E.; Ljubimova, J. Y.; Helguera, G.; Penichet, M. L. Transferrin Receptors and the Targeted Delivery of Therapeutic Agents against Cancer. *Biochim Biophys Acta* **2012**, *1820* (3), 291–317. <https://doi.org/10.1016/j.bbagen.2011.07.016>.
- (63) Tortorella, S.; Karagiannis, T. C. Transferrin Receptor-Mediated Endocytosis: A Useful Target for Cancer Therapy. *J Membrane Biol* **2014**, *247* (4), 291–307. <https://doi.org/10.1007/s00232-014-9637-0>.
- (64) Choudhury, H.; Pandey, M.; Chin, P. X.; Phang, Y. L.; Cheah, J. Y.; Ooi, S. C.; Mak, K.-K.; Pichika, M. R.; Kesharwani, P.; Hussain, Z.; Gorain, B. Transferrin Receptors-Targeting Nanocarriers for Efficient Targeted Delivery and Transcytosis of Drugs into the Brain Tumors: A Review of Recent Advancements and Emerging Trends. *Drug Deliv. and Transl. Res.* **2018**, *8* (5), 1545–1563. <https://doi.org/10.1007/s13346-018-0552-2>.
- (65) Doig, K. 8 - Iron Kinetics and Laboratory Assessment. In *Rodak's Hematology (Sixth Edition)*; Keohane, E. M., Otto, C. N., Walenga, J. M., Eds.; Elsevier: St. Louis (MO), 2020; pp 104–116. <https://doi.org/10.1016/B978-0-323-53045-3.00017-9>.
- (66) Turkevich, J.; Stevenson, P. C.; Hillier, J. A Study of the Nucleation and Growth Processes in the Synthesis of Colloidal Gold. *Discuss. Faraday Soc.* **1951**, *11* (0), 55–75. <https://doi.org/10.1039/DF9511100055>.
- (67) Bakshi, M. S.; Sachar, S.; Kaur, G.; Bhandari, P.; Kaur, G.; Biesinger, M. C.; Possmayer, F.; Petersen, N. O. Dependence of Crystal Growth of Gold Nanoparticles on the Capping

- Behavior of Surfactant at Ambient Conditions. *Crystal Growth & Design* **2008**, *8* (5), 1713–1719. <https://doi.org/10.1021/cg8000043>.
- (68) Turkevich, J.; Stevenson, P. C.; Hillier, J. A Study of the Nucleation and Growth Processes in the Synthesis of Colloidal Gold. *Discuss. Faraday Soc.* **1951**, *11* (0), 55–75. <https://doi.org/10.1039/DF9511100055>.
- (69) Niu, Z.; Li, Y. Removal and Utilization of Capping Agents in Nanocatalysis. *Chem. Mater.* **2014**, *26* (1), 72–83. <https://doi.org/10.1021/cm4022479>.
- (70) Arnida; Janát-Amsbury, M. M.; Ray, A.; Peterson, C. M.; Ghandehari, H. Geometry and Surface Characteristics of Gold Nanoparticles Influence Their Biodistribution and Uptake by Macrophages. *European Journal of Pharmaceutics and Biopharmaceutics* **2011**, *77* (3), 417–423. <https://doi.org/10.1016/j.ejpb.2010.11.010>.
- (71) Wang, Y.; Quinsaat, J. E. Q.; Ono, T.; Maeki, M.; Tokeshi, M.; Isono, T.; Tajima, K.; Satoh, T.; Sato, S.; Miura, Y.; Yamamoto, T. Enhanced Dispersion Stability of Gold Nanoparticles by the Physisorption of Cyclic Poly(Ethylene Glycol). *Nat Commun* **2020**, *11* (1), 6089. <https://doi.org/10.1038/s41467-020-19947-8>.
- (72) Lankveld, D. P.; Rayavarapu, R. G.; Krystek, P.; Oomen, A. G.; Verharen, H. W.; van Leeuwen, T. G.; De Jong, W. H.; Manohar, S. Blood Clearance and Tissue Distribution of PEGylated and Non-PEGylated Gold Nanorods after Intravenous Administration in Rats. *Nanomedicine* **2011**, *6* (2), 339–349. <https://doi.org/10.2217/nnm.10.122>.
- (73) Ballou, B.; Lagerholm, B. C.; Ernst, L. A.; Bruchez, M. P.; Waggoner, A. S. Noninvasive Imaging of Quantum Dots in Mice. *Bioconjugate Chem.* **2004**, *15* (1), 79–86. <https://doi.org/10.1021/bc034153y>.
- (74) Perry, J. L.; Reuter, K. G.; Kai, M. P.; Herlihy, K. P.; Jones, S. W.; Luft, J. C.; Napier, M.; Bear, J. E.; DeSimone, J. M. PEGylated PRINT Nanoparticles: The Impact of PEG Density on Protein Binding, Macrophage Association, Biodistribution, and Pharmacokinetics. *Nano Lett* **2012**, *12* (10), 5304–5310. <https://doi.org/10.1021/nl302638g>.
- (75) Liu, H.; Doane, T. L.; Cheng, Y.; Lu, F.; Srinivasan, S.; Zhu, J.-J.; Burda, C. Control of Surface Ligand Density on PEGylated Gold Nanoparticles for Optimized Cancer Cell Uptake. *Particle & Particle Systems Characterization* **2015**, *32* (2), 197–204. <https://doi.org/10.1002/ppsc.201400067>.
- (76) Liu, Y.; Shipton, M. K.; Ryan, J.; Kaufman, E. D.; Franzen, S.; Feldheim, D. L. Synthesis, Stability, and Cellular Internalization of Gold Nanoparticles Containing Mixed Peptide–Poly(Ethylene Glycol) Monolayers. *Anal. Chem.* **2007**, *79* (6), 2221–2229. <https://doi.org/10.1021/ac061578f>.
- (77) Staros, J. V. N-Hydroxysulfosuccinimide Active Esters: Bis(N-Hydroxysulfosuccinimide) Esters of Two Dicarboxylic Acids Are Hydrophilic, Membrane-Impermeant, Protein Cross-Linkers. *Biochemistry* **1982**, *21* (17), 3950–3955. <https://doi.org/10.1021/bi00260a008>.
- (78) Denny, J. B.; Blobel, G. 125I-Labeled Crosslinking Reagent That Is Hydrophilic, Photoactivatable, and Cleavable through an Azo Linkage. *Proceedings of the National Academy of Sciences* **1984**, *81* (17), 5286–5290. <https://doi.org/10.1073/pnas.81.17.5286>.
- (79) Smyth, D.; Blumenfeld, O.; Konigsberg, W. Reactions of N-Ethylmaleimide with Peptides and Amino Acids. *Biochemical Journal* **1964**, *91* (3), 589–595. <https://doi.org/10.1042/bj0910589>.

- (80) Partis, M. D.; Griffiths, D. G.; Roberts, G. C.; Beechey, R. B. Cross-Linking of Protein by ω -Maleimido alkanoylN-Hydroxysuccinimido Esters. *J Protein Chem* **1983**, *2* (3), 263–277. <https://doi.org/10.1007/BF01025358>.
- (81) Grabarek, Z.; Gergely, J. Zero-Length Crosslinking Procedure with the Use of Active Esters. *Analytical Biochemistry* **1990**, *185* (1), 131–135. [https://doi.org/10.1016/0003-2697\(90\)90267-D](https://doi.org/10.1016/0003-2697(90)90267-D).
- (82) Baker, H. M.; Anderson, B. F.; Baker, E. N. Dealing with Iron: Common Structural Principles in Proteins That Transport Iron and Heme. *Proceedings of the National Academy of Sciences* **2003**, *100* (7), 3579–3583. <https://doi.org/10.1073/pnas.0637295100>.
- (83) Wally, J.; Halbrooks, P. J.; Vonnrhein, C.; Rould, M. A.; Everse, S. J.; Mason, A. B.; Buchanan, S. K. THE CRYSTAL STRUCTURE OF IRON-FREE HUMAN SERUM TRANSFERRIN PROVIDES INSIGHT INTO INTER-LOBE COMMUNICATION AND RECEPTOR BINDING. *J Biol Chem* **2006**, *281* (34), 24934–24944. <https://doi.org/10.1074/jbc.M604592200>.
- (84) Eckenroth, B. E.; Steere, A. N.; Chasteen, N. D.; Everse, S. J.; Mason, A. B. How the Binding of Human Transferrin Primes the Transferrin Receptor Potentiating Iron Release at Endosomal pH. *Proc Natl Acad Sci U S A* **2011**, *108* (32), 13089–13094. <https://doi.org/10.1073/pnas.1105786108>.
- (85) James, A. E.; Driskell, J. D. Monitoring Gold Nanoparticle Conjugation and Analysis of Biomolecular Binding with Nanoparticle Tracking Analysis (NTA) and Dynamic Light Scattering (DLS). *Analyst* **2013**, *138* (4), 1212. <https://doi.org/10.1039/c2an36467k>.
- (86) Zheng, T.; Bott, S.; Huo, Q. Techniques for Accurate Sizing of Gold Nanoparticles Using Dynamic Light Scattering with Particular Application to Chemical and Biological Sensing Based on Aggregate Formation. *ACS Appl. Mater. Interfaces* **2016**, *8* (33), 21585–21594. <https://doi.org/10.1021/acsami.6b06903>.
- (87) Janz, A.; Köckritz, A.; Yao, L.; Martin, A. Fundamental Calculations on the Surface Area Determination of Supported Gold Nanoparticles by Alkanethiol Adsorption. *Langmuir* **2010**, *26* (9), 6783–6789. <https://doi.org/10.1021/la9041277>.
- (88) Clément, M.; Ménard, H.; Rowntree, P. A. Determination of the Surface Area of Pd and Nanometric Au Aggregates Supported on a Micrometric Solid Support by Thiol Adsorption and GC–MS. *Langmuir* **2008**, *24* (15), 8045–8049. <https://doi.org/10.1021/la800963u>.
- (89) Modena, M. M.; Rühle, B.; Burg, T. P.; Wuttke, S. Nanoparticle Characterization: What to Measure? *Advanced Materials* **2019**, *31* (32), 1901556. <https://doi.org/10.1002/adma.201901556>.
- (90) Yang, Y.; Liao, S.; Luo, Z.; Qi, R.; Mac Fhionnlaoich, N.; Stellacci, F.; Guldin, S. Comparative Characterisation of Non-Monodisperse Gold Nanoparticle Populations by X-Ray Scattering and Electron Microscopy. *Nanoscale* **2020**, *12* (22), 12007–12013. <https://doi.org/10.1039/C9NR09481D>.
- (91) Gentilini, C.; Evangelista, F.; Rudolf, P.; Franchi, P.; Lucarini, M.; Pasquato, L. Water-Soluble Gold Nanoparticles Protected by Fluorinated Amphiphilic Thiolates. *J. Am. Chem. Soc.* **2008**, *130* (46), 15678–15682. <https://doi.org/10.1021/ja8058364>.
- (92) Sebyy, K. B.; Mansfield, E. Determination of the Surface Density of Polyethylene Glycol on Gold Nanoparticles by Use of Microscale Thermogravimetric Analysis. *Anal Bioanal Chem* **2015**, *407* (10), 2913–2922. <https://doi.org/10.1007/s00216-015-8520-x>.

- (93) Elzey, S.; Tsai, D.-H.; Rabb, S. A.; Yu, L. L.; Winchester, M. R.; Hackley, V. A. Quantification of Ligand Packing Density on Gold Nanoparticles Using ICP-OES. *Anal Bioanal Chem* **2012**, *403* (1), 145–149. <https://doi.org/10.1007/s00216-012-5830-0>.
- (94) Smith, A. M.; Marbella, L. E.; Johnston, K. A.; Hartmann, M. J.; Crawford, S. E.; Kozycz, L. M.; Seferos, D. S.; Millstone, J. E. Quantitative Analysis of Thiolated Ligand Exchange on Gold Nanoparticles Monitored by ^1H NMR Spectroscopy. *Anal. Chem.* **2015**, *87* (5), 2771–2778. <https://doi.org/10.1021/ac504081k>.
- (95) Zhang, D.; Ansar, S. M. Ratiometric Surface Enhanced Raman Quantification of Ligand Adsorption onto a Gold Nanoparticle. *Anal. Chem.* **2010**, *82* (13), 5910–5914. <https://doi.org/10.1021/ac1010124>.
- (96) Hurst, S. J.; Lytton-Jean, A. K. R.; Mirkin, C. A. Maximizing DNA Loading on a Range of Gold Nanoparticle Sizes. *Anal. Chem.* **2006**, *78* (24), 8313–8318. <https://doi.org/10.1021/ac0613582>.
- (97) Slesiona, N.; Payne, L.; Pope, I.; Borri, P.; Langbein, W.; Watson, P. Correlative Extinction and Single Fluorophore Bleaching Microscopy for Ligand Quantification on Gold Nanoparticles. *Advanced Materials Interfaces* **2023**, *10* (34), 2300568. <https://doi.org/10.1002/admi.202300568>.
- (98) Lévy, R.; Shaheen, U.; Cesbron, Y.; Sée, V. Gold Nanoparticles Delivery in Mammalian Live Cells: A Critical Review. *Nano Reviews* **2010**, *1* (1), 4889. <https://doi.org/10.3402/nano.v1i0.4889>.
- (99) Smith, A. M.; Johnston, K. A.; Crawford, S. E.; Marbella, L. E.; Millstone, J. E. Ligand Density Quantification on Colloidal Inorganic Nanoparticles. *The Analyst* **2017**, *142* (1), 11–29. <https://doi.org/10.1039/C6AN02206E>.
- (100) Mie, G. Beiträge zur Optik trüber Medien, speziell kolloidaler Metallösungen. *Ann. Phys.* **1908**, *330* (3), 377–445. <https://doi.org/10.1002/andp.19083300302>.
- (101) Faraday, M. Experimental Relations of Gold (and Other Metals) to Light. *Philosophical Transactions of the Royal Society of London* **1857**, *147*, 145–181. <https://doi.org/10.1098/rstl.1857.0011>.
- (102) Barber, D. J.; Freestone, I. C. An Investigation of the Origin of the Colour of the Lycurgus Cup by Analytical Transmission Electron Microscopy. *Archaeometry* **1990**, *32* (1), 33–45. <https://doi.org/10.1111/j.1475-4754.1990.tb01079.x>.
- (103) Pelton, M.; Bryant, G. W. *Introduction to Metal-Nanoparticle Plasmonics*; Wiley: Science Wise Publishing: Hoboken, New Jersey, 2013.
- (104) Derkachova, A.; Kolwas, K.; Demchenko, I. Dielectric Function for Gold in Plasmonics Applications: Size Dependence of Plasmon Resonance Frequencies and Damping Rates for Nanospheres. *Plasmonics* **2016**, *11*, 941–951. <https://doi.org/10.1007/s11468-015-0128-7>.
- (105) Drude, P. Zur Elektronentheorie Der Metalle. *Annalen der Physik* **1900**, *306* (3), 566–613. <https://doi.org/10.1002/andp.19003060312>.
- (106) Voisin, C.; Del Fatti, N.; Christofilos, D.; Vallée, F. Ultrafast Electron Dynamics and Optical Nonlinearities in Metal Nanoparticles. *J. Phys. Chem. B* **2001**, *105* (12), 2264–2280. <https://doi.org/10.1021/jp0038153>.
- (107) Kolwas, K.; Derkachova, A. Impact of the Interband Transitions in Gold and Silver on the Dynamics of Propagating and Localized Surface Plasmons. *Nanomaterials (Basel)* **2020**, *10* (7), 1411. <https://doi.org/10.3390/nano10071411>.

- (108) Toudert, J.; Serna, R. Interband Transitions in Semi-Metals, Semiconductors, and Topological Insulators: A New Driving Force for Plasmonics and Nanophotonics [Invited]. *Opt. Mater. Express*, *OME* **2017**, *7* (7), 2299–2325. <https://doi.org/10.1364/OME.7.002299>.
- (109) Crut, A.; Maioli, P.; Del Fatti, N.; Vallée, F. Optical Absorption and Scattering Spectroscopies of Single Nano-Objects. *Chem. Soc. Rev.* **2014**, *43* (11), 3921. <https://doi.org/10.1039/c3cs60367a>.
- (110) Bohren, C. F.; Huffman, D. R. Particles Small Compared with the Wavelength. In *Absorption and Scattering of Light by Small Particles*; John Wiley & Sons, Ltd, 1998; pp 130–157. <https://doi.org/10.1002/9783527618156.ch5>.
- (111) Boyd, R. W.; Gaeta, A. L.; Giese, E. Nonlinear Optics. In *Springer Handbook of Atomic, Molecular, and Optical Physics*; Drake, G. W. F., Ed.; Springer Handbooks; Springer International Publishing: Cham, 2023; pp 1097–1110. https://doi.org/10.1007/978-3-030-73893-8_76.
- (112) Boyd, R. W. Chapter 1 - The Nonlinear Optical Susceptibility. In *Nonlinear Optics (Second Edition)*; Boyd, R. W., Ed.; Academic Press: San Diego, 2003; pp 1–65. <https://doi.org/10.1016/B978-012121682-5/50002-X>.
- (113) Payne, L. M.; Langbein, W.; Borri, P. Polarization-Resolved Extinction and Scattering Cross-Sections of Individual Gold Nanoparticles Measured by Wide-Field Microscopy on a Large Ensemble. *Appl. Phys. Lett.* **2013**, *102* (13), 131107. <https://doi.org/10.1063/1.4800564>.
- (114) Borri, P.; Romstad, F.; Langbein, W.; Kelly, A.; Mørk, J.; Hvam, J. Separation of Coherent and Incoherent Nonlinearities in a Heterodyne Pump-Probe Experiment. *Opt. Express* **2000**, *7* (3), 107. <https://doi.org/10.1364/OE.7.000107>.
- (115) Borri, P.; Langbein, W.; Mørk, J.; Hvam, J. M. Heterodyne Pump-Probe and Four-Wave Mixing in Semiconductor Optical Amplifiers Using Balanced Lock-in Detection. *Optics Communications* **1999**, *169* (1), 317–324. [https://doi.org/10.1016/S0030-4018\(99\)00391-0](https://doi.org/10.1016/S0030-4018(99)00391-0).
- (116) Elliott, A. D. Confocal Microscopy: Principles and Modern Practices. *Curr Protoc Cytom* **2020**, *92* (1), e68. <https://doi.org/10.1002/cpcy.68>.
- (117) *Volume Viewer*. <https://imagej.net/ij/plugins/volume-viewer.html> (accessed 2024-02-21).
- (118) Payne, L. M. Extinction Suite Macro, 2013. <http://langsrv.astro.cf.ac.uk/Crosssection/Crosssection.html>.
- (119) *Help Online - Origin Help - Poisson*. <https://www.originlab.com/doc/Origin-Help/Poisson-FitFunc> (accessed 2024-01-22).
- (120) Payne, L. M.; Albrecht, W.; Langbein, W.; Borri, P. The Optical Nanosizer – Quantitative Size and Shape Analysis of Individual Nanoparticles by High-Throughput Widefield Extinction Microscopy. *Nanoscale* **2020**, *12* (30), 16215–16228. <https://doi.org/10.1039/D0NR03504A>.
- (121) Pope, I.; Tanner, H.; Masia, F.; Payne, L.; Arkill, K. P.; Mantell, J.; Langbein, W.; Borri, P.; Verkade, P. Correlative Light Electron Microscopy Using Small Gold Nanoparticles as Single Probes. **2022**. <https://doi.org/10.48550/arXiv.2209.07771>.
- (122) Ershov, D.; Phan, M.-S.; Pylvänäinen, J. W.; Rigaud, S. U.; Le Blanc, L.; Charles-Orszag, A.; Conway, J. R. W.; Laine, R. F.; Roy, N. H.; Bonazzi, D.; Duménil, G.; Jacquemet, G.; Tinevez, J.-Y. TrackMate 7: Integrating State-of-the-Art Segmentation

- Algorithms into Tracking Pipelines. *Nat Methods* **2022**, *19* (7), 829–832. <https://doi.org/10.1038/s41592-022-01507-1>.
- (123) *Total Internal Reflection Fluorescence (TIRF) Microscopy*. Nikon's MicroscopyU. <https://www.microscopyu.com/techniques/fluorescence/total-internal-reflection-fluorescence-tirf-microscopy> (accessed 2024-02-23).
- (124) Fish, K. N. Total Internal Reflection Fluorescence (TIRF) Microscopy. *Curr Protoc Cytom* **2009**, *0 12*, Unit 12.18. <https://doi.org/10.1002/0471142956.cy1218s50>.
- (125) Liu, B.; Li, Y.; Wen, L.; Zhang, X.; Guo, Q. Effects of Hot Pixels on Pixel Performance on Backside Illuminated Complementary Metal Oxide Semiconductor (CMOS) Image Sensors. *Sensors (Basel)* **2023**, *23* (13), 6159. <https://doi.org/10.3390/s23136159>.
- (126) Paschotta, R. Total Internal Reflection. *RP Photonics Encyclopedia*; 2013. <https://doi.org/10.61835/hgk>.
- (127) Tsekouras, K.; Custer, T. C.; Jashnsaz, H.; Walter, N. G.; Pressé, S. A Novel Method to Accurately Locate and Count Large Numbers of Steps by Photobleaching. *Mol Biol Cell* **2016**, *27* (22), 3601–3615. <https://doi.org/10.1091/mbc.E16-06-0404>.
- (128) Bumb, A.; Sarkar, S. K.; Wu, X. S.; Brechbiel, M. W.; Neuman, K. C. Quantitative Characterization of Fluorophores in Multi-Component Nanoprobes by Single-Molecule Fluorescence. *Biomed. Opt. Express* **2011**, *2* (10), 2761. <https://doi.org/10.1364/BOE.2.002761>.
- (129) Steen, P. R.; Unterauer, E. M.; Masullo, L. A.; Kwon, J.; Perovic, A.; Jevdokimenko, K.; Opazo, F.; Fornasiero, E. F.; Jungmann, R. The DNA-PAINT Palette: A Comprehensive Performance Analysis of Fluorescent Dyes. *Nat Methods* **2024**, *21* (9), 1755–1762. <https://doi.org/10.1038/s41592-024-02374-8>.
- (130) Shrestha, D.; Jenei, A.; Nagy, P.; Vereb, G.; Szöllösi, J. Understanding FRET as a Research Tool for Cellular Studies. *Int J Mol Sci* **2015**, *16* (4), 6718–6756. <https://doi.org/10.3390/ijms16046718>.
- (131) Zolmajd-Haghighi, Z.; Hanley, Q. S. When One Plus One Does Not Equal Two: Fluorescence Anisotropy in Aggregates and Multiply Labeled Proteins. *Biophysical Journal* **2014**, *106* (7), 1457–1466. <https://doi.org/10.1016/j.bpj.2014.02.020>.
- (132) Corry, B.; Jayatilaka, D.; Martinac, B.; Rigby, P. Determination of the Orientational Distribution and Orientation Factor for Transfer between Membrane-Bound Fluorophores Using a Confocal Microscope. *Biophysical Journal* **2006**, *91* (3), 1032–1045. <https://doi.org/10.1529/biophysj.106.080713>.
- (133) Chandler, T.; Mehta, S.; Shroff, H.; Oldenbourg, R.; La Rivière, P. J. Single-Fluorophore Orientation Determination with Multiview Polarized Illumination: Modeling and Microscope Design. *Opt. Express* **2017**, *25* (25), 31309. <https://doi.org/10.1364/OE.25.031309>.
- (134) Xu, W.; Liu, W.; Schmidt, J. F.; Zhao, W.; Lu, X.; Raab, T.; Diederichs, C.; Gao, W.; Seletskiy, D. V.; Xiong, Q. Correlated Fluorescence Blinking in Two-Dimensional Semiconductor Heterostructures. *Nature* **2017**, *541* (7635), 62–67. <https://doi.org/10.1038/nature20601>.
- (135) Lakowicz, J. r.; Fu, Y. Modification of Single Molecule Fluorescence near Metallic Nanostructures. *Laser & Photonics Reviews* **2009**, *3* (1–2), 221–232. <https://doi.org/10.1002/lpor.200810035>.
- (136) Acuna, G. P.; Bucher, M.; Stein, I. H.; Steinhauer, C.; Kuzyk, A.; Holzmeister, P.; Schreiber, R.; Moroz, A.; Stefani, F. D.; Liedl, T.; Simmel, F. C.; Tinnefeld, P. Distance

- Dependence of Single-Fluorophore Quenching by Gold Nanoparticles Studied on DNA Origami. *ACS Nano* **2012**, *6* (4), 3189–3195. <https://doi.org/10.1021/nn2050483>.
- (137) Doane, T. L.; Cheng, Y.; Babar, A.; Hill, R. J.; Burda, C. Electrophoretic Mobilities of PEGylated Gold NPs. *J. Am. Chem. Soc.* **2010**, *132* (44), 15624–15631. <https://doi.org/10.1021/ja1049093>.
- (138) Enns, C. A.; Sussman, H. H. Physical Characterization of the Transferrin Receptor in Human Placentae. *Journal of Biological Chemistry* **1981**, *256* (19), 9820–9823. [https://doi.org/10.1016/S0021-9258\(19\)68700-4](https://doi.org/10.1016/S0021-9258(19)68700-4).
- (139) Jeong, Y.; Kook, Y.-M.; Lee, K.; Koh, W.-G. Metal Enhanced Fluorescence (MEF) for Biosensors: General Approaches and a Review of Recent Developments. *Biosensors and Bioelectronics* **2018**, *111*, 102–116. <https://doi.org/10.1016/j.bios.2018.04.007>.
- (140) Striebel, M.; Wrachtrup, J.; Gerhardt, I. Absorption and Extinction Cross Sections and Photon Streamlines in the Optical Near-Field. *Sci Rep* **2017**, *7* (1), 15420. <https://doi.org/10.1038/s41598-017-15528-w>.
- (141) Payne, L. M.; Masia, F.; Zilli, A.; Albrecht, W.; Borri, P.; Langbein, W. Quantitative Morphometric Analysis of Single Gold Nanoparticles by Optical Extinction Microscopy: Material Permittivity and Surface Damping Effects. *The Journal of Chemical Physics* **2021**, *154* (4), 044702. <https://doi.org/10.1063/5.0031012>.
- (142) Bonvin, D.; Chiappe, D.; Moniatte, M.; Hofmann, H.; Ebersold, M. M. Methods of Protein Corona Isolation for Magnetic Nanoparticles. *Analyst* **2017**, *142* (20), 3805–3815. <https://doi.org/10.1039/C7AN00646B>.
- (143) Mohammad-Beigi, H.; Hayashi, Y.; Zeuthen, C. M.; Eskandari, H.; Scavenius, C.; Juul-Madsen, K.; Vorup-Jensen, T.; Enghild, J. J.; Sutherland, D. S. Mapping and Identification of Soft Corona Proteins at Nanoparticles and Their Impact on Cellular Association. *Nat Commun* **2020**, *11* (1), 4535. <https://doi.org/10.1038/s41467-020-18237-7>.
- (144) Park, S. J. Protein–Nanoparticle Interaction: Corona Formation and Conformational Changes in Proteins on Nanoparticles. *IJN* **2020**, *Volume 15*, 5783–5802. <https://doi.org/10.2147/IJN.S254808>.
- (145) Oh, E.; Delehanty, J. B.; Sapsford, K. E.; Susumu, K.; Goswami, R.; Blanco-Canosa, J. B.; Dawson, P. E.; Granek, J.; Shoff, M.; Zhang, Q.; Goering, P. L.; Huston, A.; Medintz, I. L. Cellular Uptake and Fate of PEGylated Gold Nanoparticles Is Dependent on Both Cell-Penetration Peptides and Particle Size. *ACS Nano* **2011**, *5* (8), 6434–6448. <https://doi.org/10.1021/nn201624c>.
- (146) Pereira, M.; Lai, E. P. Capillary Electrophoresis for the Characterization of Quantum Dots after Non-Selective or Selective Bioconjugation with Antibodies for Immunoassay. *J Nanobiotechnol* **2008**, *6* (1), 10. <https://doi.org/10.1186/1477-3155-6-10>.
- (147) Valero, J.; Pérez-Casany, M.; Ginebra, J. On Zero-Truncating and Mixing Poisson Distributions. *Advances in Applied Probability* **2010**, *42* (4), 1013–1027. <https://doi.org/10.1239/aap/1293113149>.
- (148) Li, X.-J.; Sun, Y.; Tian, G.-L.; Liang, J.; Shi, J. Mean Regression Model for the Zero-Truncated Poisson Distribution and Its Generalization. *Computational Statistics & Data Analysis* **2023**, *179*, 107650. <https://doi.org/10.1016/j.csda.2022.107650>.
- (149) Johnson, P. B.; Christy, R. W. Optical Constants of the Noble Metals. *Phys. Rev. B* **1972**, *6* (12), 4370–4379. <https://doi.org/10.1103/PhysRevB.6.4370>.

- (150) Wu, W.; Huang, J.; Wu, L.; Sun, D.; Lin, L.; Zhou, Y.; Wang, H.; Li, Q. Two-Step Size- and Shape-Separation of Biosynthesized Gold Nanoparticles. *Separation and Purification Technology* **2013**, *106*, 117–122. <https://doi.org/10.1016/j.seppur.2013.01.005>.
- (151) Sweeney, S. F.; Woehrle, G. H.; Hutchison, J. E. Rapid Purification and Size Separation of Gold Nanoparticles via Diafiltration. *J. Am. Chem. Soc.* **2006**, *128* (10), 3190–3197. <https://doi.org/10.1021/ja0558241>.
- (152) Hu, X.; Zhang, Y.; Ding, T.; Liu, J.; Zhao, H. Multifunctional Gold Nanoparticles: A Novel Nanomaterial for Various Medical Applications and Biological Activities. *Frontiers in Bioengineering and Biotechnology* **2020**, *8*.
- (153) Baczewska, M.; Eder, K.; Ketelhut, S.; Kemper, B.; Kujawińska, M. Refractive Index Changes of Cells and Cellular Compartments Upon Paraformaldehyde Fixation Acquired by Tomographic Phase Microscopy. *Cytometry A* **2021**, *99* (4), 388–398. <https://doi.org/10.1002/cyto.a.24229>.
- (154) Brameshuber, M.; Klotzsch, E.; Ponjavic, A.; Sezgin, E. Understanding Immune Signaling Using Advanced Imaging Techniques. *Biochemical Society Transactions* **2022**, *50* (2), 853–866. <https://doi.org/10.1042/BST20210479>.
- (155) Lévesque, L. Nyquist Sampling Theorem: Understanding the Illusion of a Spinning Wheel Captured with a Video Camera. *Phys. Educ.* **2014**, *49* (6), 697. <https://doi.org/10.1088/0031-9120/49/6/697>.
- (156) Segeritz, C.-P.; Vallier, L. Cell Culture. *Basic Science Methods for Clinical Researchers* **2017**, 151–172. <https://doi.org/10.1016/B978-0-12-803077-6.00009-6>.
- (157) Hou, T.; Rinderknecht, C. H.; Hadjinicolaou, A. V.; Busch, R.; Mellins, E. Pulse–Chase Analysis for Studies of MHC Class II Biosynthesis, Maturation, and Peptide Loading. In *Antigen Processing: Methods and Protocols*; van Endert, P., Ed.; Methods in Molecular Biology™; Humana Press: Totowa, NJ, 2013; pp 411–432. https://doi.org/10.1007/978-1-62703-218-6_31.
- (158) Doherty, G. J.; McMahon, H. T. Mechanisms of Endocytosis. *Annu. Rev. Biochem.* **2009**, *78* (1), 857–902. <https://doi.org/10.1146/annurev.biochem.78.081307.110540>.
- (159) Shamir, M.; Bar-On, Y.; Phillips, R.; Milo, R. SnapShot: Timescales in Cell Biology. *Cell* **2016**, *164* (6), 1302–1302.e1. <https://doi.org/10.1016/j.cell.2016.02.058>.
- (160) Hirokawa, N.; Noda, Y.; Tanaka, Y.; Niwa, S. Kinesin Superfamily Motor Proteins and Intracellular Transport. *Nat Rev Mol Cell Biol* **2009**, *10* (10), 682–696. <https://doi.org/10.1038/nrm2774>.
- (161) Galli, T.; Haucke, V. Cycling of Synaptic Vesicles: How Far? How Fast! *Science's STKE* **2001**, *2001* (88), re1–re1. <https://doi.org/10.1126/stke.2001.88.re1>.
- (162) Cárdenas, A. M.; Marengo, F. D. Rapid Endocytosis and Vesicle Recycling in Neuroendocrine Cells. *Cell Mol Neurobiol* **2010**, *30* (8), 1365–1370. <https://doi.org/10.1007/s10571-010-9579-8>.
- (163) Sposini, S.; Rosendale, M.; Claverie, L.; Van, T. N. N.; Jullié, D.; Perrais, D. Imaging Endocytic Vesicle Formation at High Spatial and Temporal Resolutions with the Pulsed-pH Protocol. *Nat Protoc* **2020**, *15* (9), 3088–3104. <https://doi.org/10.1038/s41596-020-0371-z>.
- (164) Pathak, D.; Thakur, S.; Mallik, R. Fluorescence Microscopy Applied to Intracellular Transport by Microtubule Motors. *J Biosci* **2018**, *43* (3), 437–445. <https://doi.org/10.1007/s12038-018-9765-2>.

- (165) Jonker, C. T. H.; Deo, C.; Zager, P. J.; Tkachuk, A. N.; Weinstein, A. M.; Rodriguez-Boulan, E.; Lavis, L. D.; Schreiner, R. Accurate Measurement of Fast Endocytic Recycling Kinetics in Real Time. *Journal of Cell Science* **2020**, *133* (2), jcs231225. <https://doi.org/10.1242/jcs.231225>.
- (166) Rachael Goddard, Z.; J. Marín, M.; A. Russell, D.; Searcey, M. Active Targeting of Gold Nanoparticles as Cancer Therapeutics. *Chemical Society Reviews* **2020**, *49* (23), 8774–8789. <https://doi.org/10.1039/D0CS01121E>.
- (167) Zhang, W.; Taheri-Ledari, R.; Ganjali, F.; Shadi Mirmohammadi, S.; Sadat Qazi, F.; Saeidirad, M.; KashtiAray, A.; Zarei-Shokat, S.; Tian, Y.; Maleki, A. Effects of Morphology and Size of Nanoscale Drug Carriers on Cellular Uptake and Internalization Process: A Review. *RSC Advances* **2023**, *13* (1), 80–114. <https://doi.org/10.1039/D2RA06888E>.
- (168) *Introduction to Gold Nanoparticle Characterization*. Cyodiagnosics Inc. <https://www.cyodiagnosics.com/pages/introduction-to-gold-nanoparticle-characterization> (accessed 2024-01-31).
- (169) Palani, S.; Kenison, J. P.; Sabuncu, S.; Huang, T.; Civitci, F.; Esener, S.; Nan, X. Multispectral Localized Surface Plasmon Resonance (msLSPR) Reveals and Overcomes Spectral and Sensing Heterogeneities of Single Gold Nanoparticles. *ACS Nano* **2023**, *17* (3), 2266–2278. <https://doi.org/10.1021/acsnano.2c08702>.
- (170) Mauriz, E. Clinical Applications of Visual Plasmonic Colorimetric Sensing. *Sensors* **2020**, *20* (21), 6214. <https://doi.org/10.3390/s20216214>.
- (171) Sajti, C. L.; Petersen, S.; Menéndez-Manjón, A.; Barcikowski, S. In-Situ Bioconjugation in Stationary Media and in Liquid Flow by Femtosecond Laser Ablation. *Appl. Phys. A* **2010**, *101* (2), 259–264. <https://doi.org/10.1007/s00339-010-5813-y>.
- (172) Raj, V.; Johnson, T.; Joseph, K. Cholesterol Aided Etching of Tomatine Gold Nanoparticles: A Non-Enzymatic Blood Cholesterol Monitor. *Biosensors and Bioelectronics* **2014**, *60*, 191–194. <https://doi.org/10.1016/j.bios.2014.03.062>.
- (173) Balasubramanian, S. K.; Yang, L.; Yung, L.-Y. L.; Ong, C.-N.; Ong, W.-Y.; Yu, L. E. Characterization, Purification, and Stability of Gold Nanoparticles. *Biomaterials* **2010**, *31* (34), 9023–9030. <https://doi.org/10.1016/j.biomaterials.2010.08.012>.
- (174) Ghosh, R. N.; Maxfield, F. R. Evidence for Nonvectorial, Retrograde Transferrin Trafficking in the Early Endosomes of HEp2 Cells. *Journal of Cell Biology* **1995**, *128* (4), 549–561. <https://doi.org/10.1083/jcb.128.4.549>.
- (175) Sykes, E. A.; Chen, J.; Zheng, G.; Chan, W. C. W. Investigating the Impact of Nanoparticle Size on Active and Passive Tumor Targeting Efficiency. *ACS Nano* **2014**, *8* (6), 5696–5706. <https://doi.org/10.1021/nn500299p>.
- (176) Hongbo B. Lu, †; Charles T. Campbell, *; David G. Castner†, §. *Attachment of Functionalized Poly(ethylene glycol) Films to Gold Surfaces*. ACS Publications. <https://doi.org/10.1021/la990221m>.
- (177) Cuatrecasas, P.; Parikh, I. Adsorbents for Affinity Chromatography. Use of N-Hydroxysuccinimide Esters of Agarose. *Biochemistry* **1972**, *11* (12), 2291–2299. <https://doi.org/10.1021/bi00762a013>.
- (178) Dai, Q.; Walkey, C.; Chan, W. C. W. Polyethylene Glycol Backfilling Mitigates the Negative Impact of the Protein Corona on Nanoparticle Cell Targeting. *Angewandte Chemie International Edition* **2014**, *53* (20), 5093–5096. <https://doi.org/10.1002/anie.201309464>.

- (179) Li, L.; Wan, T.; Wan, M.; Liu, B.; Cheng, R.; Zhang, R. The Effect of the Size of Fluorescent Dextran on Its Endocytic Pathway. *Cell Biology International* **2015**, *39* (5), 531–539. <https://doi.org/10.1002/cbin.10424>.
- (180) Chen, J.; Jin, Y.; Fahrudin, N.; Zhao, J. X. Development of Gold Nanoparticle-Enhanced Fluorescent Nanocomposites. *Langmuir* **2013**, *29* (5), 1584–1591. <https://doi.org/10.1021/la3036049>.
- (181) Dai, Q.; Wilhelm, S.; Ding, D.; Syed, A. M.; Sindhvani, S.; Zhang, Y.; Chen, Y. Y.; MacMillan, P.; Chan, W. C. W. Quantifying the Ligand-Coated Nanoparticle Delivery to Cancer Cells in Solid Tumors. *ACS Nano* **2018**, *12* (8), 8423–8435. <https://doi.org/10.1021/acsnano.8b03900>.
- (182) Gumustas, M.; Sengel-Turk, C. T.; Gumustas, A.; Ozkan, S. A.; Uslu, B. Chapter 5 - Effect of Polymer-Based Nanoparticles on the Assay of Antimicrobial Drug Delivery Systems. In *Multifunctional Systems for Combined Delivery, Biosensing and Diagnostics*; Grumezescu, A. M., Ed.; Elsevier, 2017; pp 67–108. <https://doi.org/10.1016/B978-0-323-52725-5.00005-8>.
- (183) Sameut Bouhaik, I.; Leroy, P.; Ollivier, P.; Azaroual, M.; Mercury, L. Influence of Surface Conductivity on the Apparent Zeta Potential of TiO₂ Nanoparticles: Application to the Modeling of Their Aggregation Kinetics. *Journal of Colloid and Interface Science* **2013**, *406*, 75–85. <https://doi.org/10.1016/j.jcis.2013.05.034>.
- (184) Hunter, R. J. *Zeta Potential in Colloid Science: Principles and Applications*, New paperback edition.; Academic Press: London, 1988.
- (185) Martens, U.; Böttcher, D.; Talbot, D.; Bornscheuer, U.; Abou-Hassan, A.; Delcea, M. Maghemite Nanoparticles Stabilize the Protein Corona Formed with Transferrin Presenting Different Iron-Saturation Levels. *Nanoscale* **2019**, *11* (34), 16063–16070. <https://doi.org/10.1039/C9NR04967C>.
- (186) Augustine, R.; Hasan, A.; Primavera, R.; Wilson, R. J.; Thakor, A. S.; Kevadiya, B. D. Cellular Uptake and Retention of Nanoparticles: Insights on Particle Properties and Interaction with Cellular Components. *Materials Today Communications* **2020**, *25*, 101692. <https://doi.org/10.1016/j.mtcomm.2020.101692>.
- (187) Li, Z.; Cheng, E.; Huang, W.; Zhang, T.; Yang, Z.; Liu, D.; Tang, Z. Improving the Yield of Mono-DNA-Functionalized Gold Nanoparticles through Dual Steric Hindrance. *J. Am. Chem. Soc.* **2011**, *133* (39), 15284–15287. <https://doi.org/10.1021/ja205712a>.
- (188) Ojea-Jiménez, I.; García-Fernández, L.; Lorenzo, J.; Puentes, V. F. Facile Preparation of Cationic Gold Nanoparticle-Bioconjugates for Cell Penetration and Nuclear Targeting. *ACS Nano* **2012**, *6* (9), 7692–7702. <https://doi.org/10.1021/nn3012042>.
- (189) Hühn, D.; Kantner, K.; Geidel, C.; Brandholt, S.; De Cock, I.; Soenen, S. J. H.; Rivera_Gil, P.; Montenegro, J.-M.; Braeckmans, K.; Müllen, K.; Nienhaus, G. U.; Klapper, M.; Parak, W. J. Polymer-Coated Nanoparticles Interacting with Proteins and Cells: Focusing on the Sign of the Net Charge. *ACS Nano* **2013**, *7* (4), 3253–3263. <https://doi.org/10.1021/nn3059295>.
- (190) Lin, Z. P.; Ngo, W.; Mladjenovic, S. M.; Wu, J. L. Y.; Chan, W. C. W. Nanoparticles Bind to Endothelial Cells in Injured Blood Vessels via a Transient Protein Corona. *Nano Lett.* **2023**, *23* (3), 1003–1009. <https://doi.org/10.1021/acs.nanolett.2c04501>.
- (191) Maillard, J.; Klehs, K.; Rumble, C.; Vauthey, E.; Heilemann, M.; Fürstenberg, A. Universal Quenching of Common Fluorescent Probes by Water and Alcohols. *Chem. Sci.* **2021**, *12* (4), 1352–1362. <https://doi.org/10.1039/D0SC05431C>.

- (192) Birch, D.; Christensen, M. V.; Staerk, D.; Franzyk, H.; Nielsen, H. M. Fluorophore Labeling of a Cell-Penetrating Peptide Induces Differential Effects on Its Cellular Distribution and Affects Cell Viability. *Biochim Biophys Acta Biomembr* **2017**, *1859* (12), 2483–2494. <https://doi.org/10.1016/j.bbamem.2017.09.015>.
- (193) Zsila, F. Far-UV Circular Dichroism Signatures Indicate Fluorophore Labeling Induced Conformational Changes of Penetratin. *Amino Acids* **2022**, *54* (7), 1109–1113. <https://doi.org/10.1007/s00726-022-03149-1>.
- (194) Haddad, M.; Frickenstein, A.; Wilhelm, S. High-Throughput Single-Cell Analysis of Nanoparticle-Cell Interactions. *Trends Analyt Chem* **2023**, *166*, 117172. <https://doi.org/10.1016/j.trac.2023.117172>.
- (195) Klein, N. D.; Hurley, K. R.; Feng, Z. V.; Haynes, C. L. Dark Field Transmission Electron Microscopy as a Tool for Identifying Inorganic Nanoparticles in Biological Matrices. *Anal. Chem.* **2015**, *87* (8), 4356–4362. <https://doi.org/10.1021/acs.analchem.5b00124>.
- (196) Hedegaard, S. F.; Derbas, M. S.; Lind, T. K.; Kasimova, M. R.; Christensen, M. V.; Michaelsen, M. H.; Campbell, R. A.; Jorgensen, L.; Franzyk, H.; Cárdenas, M.; Nielsen, H. M. Fluorophore Labeling of a Cell-Penetrating Peptide Significantly Alters the Mode and Degree of Biomembrane Interaction. *Sci Rep* **2018**, *8*, 6327. <https://doi.org/10.1038/s41598-018-24154-z>.
- (197) Huang, L.; Mao, X.; Li, J.; Li, Q.; Shen, J.; Liu, M.; Fan, C.; Tian, Y. Nanoparticle Spikes Enhance Cellular Uptake via Regulating Myosin IIA Recruitment. *ACS Nano* **2023**, *17* (10), 9155–9166. <https://doi.org/10.1021/acsnano.2c12660>.
- (198) Pope, I.; Ferreira, N. G. C.; Kille, P.; Langbein, W.; Borri, P. Background-Free Four-Wave Mixing Microscopy of Small Gold Nanoparticles inside a Multi-Cellular Organ. *Appl. Phys. Lett.* **2023**, *122* (15), 153701. <https://doi.org/10.1063/5.0140651>.
- (199) Griffiths, G.; Gruenberg, J.; Marsh, M.; Wohlmann, J.; Jones, A. T.; Parton, R. G. Nanoparticle Entry into Cells; the Cell Biology Weak Link. *Advanced Drug Delivery Reviews* **2022**, *188*, 114403. <https://doi.org/10.1016/j.addr.2022.114403>.
- (200) Ngo, W.; Wu, J. L. Y.; Lin, Z. P.; Zhang, Y.; Bussin, B.; Granda Farias, A.; Syed, A. M.; Chan, K.; Habsid, A.; Moffat, J.; Chan, W. C. W. Identifying Cell Receptors for the Nanoparticle Protein Corona Using Genome Screens. *Nat Chem Biol* **2022**, *18* (9), 1023–1031. <https://doi.org/10.1038/s41589-022-01093-5>.

Publications

Parts of this project were published in the following articles:

1. **N. Slesiona**, L. Payne, I. Pope, P. Borri, W. Langbein, P. Watson, Correlative Extinction and Single Fluorophore Bleaching Microscopy for Ligand Quantification on Gold Nanoparticles. *Adv. Mater. Interfaces* 2023, 10, 2300568.
2. E. Herkert, **N. Slesiona**, M. Recchia, T. Deckert, M. Garcia-Parajo, E. Fantuzzi, A. Pruccoli, I. Ragupathy, D. Gudavičius, H. Rigneault, J. Majer, A. Zumbusch, E. Munger, S. Brasselet, A. Jones, P. Watson, S. A. Boppart, V. Singh, S. Borkar, F. E. Quintela Rodriguez, W. Langbein, V. Petropoulos, N. F. van Hulst, M. Maiuri, G. Cerullo, D. Brida, F. Troiani, C. A. Rozzi, E. Molinari, M. Vengris, and P. Borri, Roadmap on bio-nano-photonics. *Journal of Optics* 2021. 23, 073001

Oral and poster presentations

Parts of this project have been presented at the following conferences:

1. **N. Slesiona**, I. Pope, P.D. Watson, P. Borri, W. Langbein, Four Wave Mixing imaging for biotherapeutic detection, *Oral presentation*, Focus on Microscopy, online (April 2022)
2. **N. Slesiona**, I. Pope, L. Payne, P. Borri, W. Langbein, P.D. Watson, Correlative analysis of extinction microscopy and single fluorophore bleaching for ligand quantification on gold nanoparticles, *Oral presentation*, Focus on Microscopy, online (April 2022)
3. **N. Slesiona**, I. Pope, L. Payne, P. Borri, W. Langbein, P.D. Watson, Correlative analysis of extinction microscopy and single fluorophore bleaching for ligand quantification on gold nanoparticles, *Poster presentation*, Colloids, Lisbon, Portugal (June 2022)
4. **N. Slesiona**, I. Pope, P.D. Watson, P. Borri, W. Langbein, Four Wave Mixing imaging for the detection of gold nanoparticle internalisation into living cells at the single particle level, *Oral presentation*, Raman Nanotheranostics (RaNT), Exeter, United Kingdom (August 2022)
5. **N. Slesiona**, I. Pope, P.D. Watson, P. Borri, W. Langbein, Four Wave Mixing imaging for the detection of gold nanoparticle internalisation into living cells at the single particle level, *Oral presentation*, Women in Photonics, Jena, Germany (November 2023)